Physicochemical and microstructural approaches for modeling the degradations of power electronic component interconnection

Mustafa Shqair

université PARIS-SACLAY

Physicochemical and microstructural approaches for modeling the degradations of power electronic interconnection components

Approche physico-chimique de la dégradation des interconnexions de composants de puissance par une étude microstructurale

Thèse de doctorat de l'université Paris-Saclay

École doctorale n° 575, Electrical, Optical, Bio – Physics and Engineering (EOBE)
Spécialité de doctorat : Génie électrique, électronique, photonique et systèmes
Graduate School : Sciences de l'ingénierie et des systèmes
Référent : Ecole Normale Supérieure Paris-Saclay

Thèse préparée au **SATIE (Université Paris-Saclay, ENS Paris-Saclay, CNRS)**, sous la direction de **Zoubir KHATIR**, Dir. de Recherche, Université Gustave Eiffel, le co-encadrement de **Ali IBRAHIM**, Chercheur à l'Université Gustave Eiffel

Thèse soutenue à Saclay, le 07 Novembre 2022, par

Mustafa SHQAIR

Composition du Jury

Hélène FREMONT, Professeure des Universités, Univ. Bordeaux1	Présidente
Eric WOIRGARD, Professeur des Universités, Univ. Bordeaux1	Rapporteur & Examinateur
Marc LEGROS, Directeur de Recherche, CNRS	Rapporteur & Examinateur
Marie-Laure LOCATELLI, Chargée de Recherche, CNRS	Examinatrice
Zoubir KHATIR, Directeur de Recherche, Univ. Gustave Eiffel	Directeur de thèse

THESE DE DOCTORAT

NNT : 2022UPAST132

Acknowledgments:

During my Ph.D. studies, I have thought a lot about science, but I have never thought about the moment of writing the “acknowledgments” section in my thesis manuscript. After I finished writing all chapters of my thesis, I have realized now that writing this part was probably the most difficult. It is a very special moment that makes it difficult to put all my gratitude into words for everyone who helped me to reach this point. This Ph.D. thesis would not have been accomplished without these people.

First, I would like to express my sincere thanks to my thesis director Mr. Zoubir KHATIR and my co-director Mr. Ali IBRAHIM. I am grateful and honored to have worked under your supervision. I want to express my gratitude to them for their support, interest, optimism, enthusiasm, and the trust they have placed in me throughout these studies. I also thank them for their wise advice that helped a lot to achieve the scientific goals which were targeted in this Ph.D. work. This surely helped me sharpen my scientific thinking. I hope they find, beyond these few words, the testimony of my sincere gratitude and admiration. I also thank Mrs. Mounira BOUARROUDJ for her scientific advice and kind help, as well as Mr. Tayssir HAMIEH who was in fact the linkage between me, during my Masters’ studies at the Lebanese University, and my Ph.D. thesis supervisors when I traveled to France for doing my Masters’ trainee at their laboratory.

I would also like to thank all the members of the jury. I thank Mr. Eric WOIRGARD and Mr. Marc LEGROS, who accepted to be the reporters of my Ph.D. manuscript as well as Mrs. Hélène FREMONT and Mrs. Marie-Laure LOCATELLI for examining my Ph.D. work. I want to thank also Mr. Toni YOUSSEF who came and attended my Ph.D. defense as an invited member.

I also want to thank the SATIE laboratory members at Gustave Eiffel University in Versailles for welcoming me during all this time. The years I spent in the laboratory were among the most exciting, interesting, and instructive in my life so far. During these three years, I worked, interacted, and exchanged with several people. Each of these people helped me in one way or another to complete this research, and it is time to thank them. So thanks too much to all my colleagues. I wish all of you the best in your future.

From the bottom of my heart, I thank everyone who encouraged me during my studies, particularly my parents, who always pushed me, especially in the hard moments. They are also the ones who tried to afford me the best education possible since I was a kid. Without them, I would not reach this point. I want to thank my fiancee Marwa for being beside me all time, she was a true supporter. I also thank my friends who stood beside me during this journey.

Again to all, thank you so much!

université PARIS-SACLAY | DOCTORAL SCHOOL Electrical, Optical, Bio: Physics and Engineering (EOBE)

Titre: Approche physico-chimique de la dégradation des interconnexions de composants de puissance par une étude microstructurale.

Mots clés: IGBT, contacts métalliques, physicochimique-microstructurel, dégradation, fissure, énergie, contrainte

Résumé: Le vieillissement électro-thermique et thermo-mécanique des interconnexions métalliques supérieures des composants de puissance à semi-conducteurs est une de leurs causes de défaillances principales. L'étude s'est concentrée sur le processus de vieillissement du contact métallique entre le film de métallisation des puces et des fils de connexions en aluminium. L'approche suivie dans cette étude est différente des approches traditionnelles précédentes, le problème de la fatigue est étudié ici par un point de vue physico-chimique, en interprétant les changements microstructuraux qui se produisent, et en les reliant aux processus de dégradation. A partir de la littérature et après une analyse de résultats expérimentaux, les effets des évolutions microstructurales et des changements de propriétés des matériaux sur les processus de vieillissement ont été examinés. Ainsi, il est proposé et investigué ici l'hypothèse d'une corrélation entre la cause de la défaillance du dispositif, c-à-d la propagation de fissure, et les principales propriétés physico-chimiques et microstructurales affectant les processus de vieillissement. Des relations reliant les propriétés physicochimiques et de microstructures aux paramètres d'un modèle de zone cohésive (CZM), basé sur l'endommagement, ont été établies. Ce modèle combine à la fois la modélisation multiphysique par éléments finis et les concepts physicochimiques-microstructuraux.

Lors de l'élaboration de cette combinaison, un modèle géométrique bidimensionnel d'un module IGBT a été construit. Des éléments de forme hexagonales ont été répartis dans le modèle géométrique au niveau des extrémités du contact du fil/métallisation afin de représenter la structure granulaire. Des modèles distribués de zones cohésives (CZM) ont ensuite été mis en œuvre à l'interface des hexagones afin de simuler la fissuration à travers la décohésion entre grains d'un point de vue microstructurel. Les paramètres CZM sont distribués selon les propriétés et caractéristiques locales observées de la microstructure. Des simulations électro-thermique puis thermomécanique ont été réalisées pour reproduire l'effet d'un cyclage thermique actif. La simulation thermo-mécanique permet d'estimer les distribution de stress et déformations au niveau de la zone de contact métallique et simuler l'évolution de la fissure qui a lieu au niveau des interfaces entre les éléments hexagonaux. Les résultats de ces simulations ont ensuite été confrontés à des données expérimentales pour voir la validité de ce modèle physico-chimique-microstructural.

Title: Physicochemical and microstructural approaches for modeling the degradations of power electronic component interconnection.

Keywords: IGBT, metallic contacts, physicochemical-microstructural, degradation, crack, energy, stress

Abstract: Electro-thermal and thermo-mechanical aging of topside metallic components of semiconductor power devices are the main reasons behind shortening their lifetimes. This study has been conducted to focus on the aging processes at such metallic contacts, composed of metallization layers connected to bonding wires. The approach followed in this study is not like the previous traditional ones, by which the fatigue problem is studied here in a physicochemical way through interpreting the microstructural changes occurring, and relating them to the degradation processes. The effects of the evolutions in the microstructure and materials properties on aging processes were reviewed from the literature and after applying experimental analysis. Therefore, a correlation was thought about between the device failure's driving force, the crack propagation, and the main physicochemical-microstructural properties affecting the aging processes. Consequently, relationships linking these physicochemical-microstructural aspects to the parameters of the damage-based cohesive zone model were found. As a result, this model combines both finite element multiphysics modeling and physicochemical-microstructural concepts. When the combination was built, a two-dimensional geometrical model of an IGBT module was constructed using the ANSYS APDL software. Hexagons were integrated at the metallic interconnection positions to represent metallic grains. Cohesive zone models were afterward implemented at the edges of the hexagons in order to interpret the crack evolution microstructurally. This results in hexagons associated with different properties in accordance with the characteristics of the local microstructure. Two separate simulations were subsequently applied. The first one is electrothermal to obtain the thermal distribution among the different components of IGBT upon cycling. Thereafter, a mechanical simulation was applied using the thermal data of the electrothermal simulation to see the distribution of constraints at the metallic contact zone and simulate the crack evolution taking place at the hexagonal edges. The results of these simulations were then compared to some experimental data to see the compatibility of this physicochemical-microstructural model.

Table of contents:

Table of figures:

List of tables:

List of abbreviations:

a: crack length	GOS: average grain orientations	XRD: x-ray crystallography
$a_{interatomic}$: interatomic distance	h: convection coefficient	α and β: shape parameters
a^*: scaled atomic separation distance used in the universal binding energy curves	H: hardness	α_{TE}: Thermal expansion coefficient
a_m: distance between atomic surfaces at equilibrium	HAB: high angle boundary	α_s: shear stiffness parameter
$A_{cross\text{-}sectional}$: atomic cross-sectional area	HCP: hexagonal close-packed	β_{hkl}: peak broadening
AC: active current	I: electric current	ε: micro-strain
AFM: atomic force microscopy	IGBT: insulated-gate bipolar transistor	$\varepsilon_{thermal}$: thermal deformation strain
Al: aluminum	IPF: inverse pole figure	Σ: reciprocal density of coinciding sites
Al_2O_3: aluminum oxide	J_c: critical energy release rate	ρ: dislocation density
APD: atomic packing density	K: stress intensity factor	ΔE: energy extra potential
b: burgers vector	K_c: Fracture toughness	ΔE_{eq}: equilibrium binding energy
B: bulk modulus	K_{HP}: Hall-Petch constant	$\Delta_f H^\circ_{g(0K)}$: enthalpy of the formation of gaseous metals at 0 kelvin
BCC: body-centered cubic	K_s: shape factor	$\Delta_f H^\circ_{s(0K)}$: enthalpy of formation of solid metals at 0 kelvin
Bs: brass texture component	l: scaled separation associated with the Thomas-Fermi screening length	Δ_n: normal separation distance
ccn(i): cohesive coordination number of atoms in an i^{th} group	LAB: low angle boundary	Δ_n*: Δ_n after complete shear separation at $T_n = 0$
C_{11}': elastic stiffness constant associated with the direction perpendicular to the interface	LEFM: linear elastic fracture mechanics	$\Delta_{n,max}$: maximal normal separation distance
Cb: cube texture component	MAD: disorientation average deviation	Δ_t: tangential separation distance

CSL: coincident site lattice	Mg: magnesium	$\Delta_{t,max}$: maximal tangential separation distance
CTE (α_i): thermal expansion coefficient	MOSFET: metal-oxide-semiconductor field-effect transistor	ΔK_ε: strain density factor range
CTOD: crack tip opening displacement	n: strain hardening exponent	ΔT_j: junction temperature variation
Cu: copper	n_A: atom density	γ_s: surface energy
CZ: cohesive zone	n-potential: power of the potential function	γ_{gb}: grain boundary energy
CZM: cohesive zone model	N_{cycles}: number of cycles	γ_{us}: staking fault energy
d: grain size	N_f: number of cycles to device's failure	φ_n: normal fracture energy
d_a/d_N: crack growth rate per cycle	PSB: persistent slip bands	φ_t: tangential fracture energy
d_a: atomic diameter	PVD: physical vapor deposition	θ_{hkl}: peak position
d_i: relative atomic distance between the i^{th} group of atoms and a particular inner atom	q: ratio of mode II fracture energy to mode I fracture energy	θ: grain orientation angle
d_{IS}: interplanar spacing	Q: activation energy for atom's motion	Δθ: disorientation angle
d_n: cumulative damage parameter	r: non-dimensional parameter associated with the length scale Δ_n*	λ: wavelength
DC: direct current	r_{ws}: Wigner-Seitz radius	λ_{TF}: Thomas-Fermi screening length
DCB: direct copper bonding	r_σ: stress rate	Ψ: universal binding energy
DPF: direct pole figure	SEM: scanning electron microscopy	σ: stress
DUT: device under test	Si: silicon	$\sigma_{initial}$: initial stress
E: Young modulus	$T_{j\,max}$: maximal junction temperature	σ_0: friction stress
E(a): total energy as a function of the distance between surfaces of metals symbolized by (a)	$T_{j\,min}$: minimal junction temperature	σ_c: critical fracture stress

E_{adh} (a): adhesive binding energy	T_m: mean temperature	σ_{max}: normal cohesive strength
E_{adh}^* (a^*): universal energy function that describes the binding energy curve	$T_{melting}$: melting temperature	σ_m^j: stress at a specific moment
E_{coh}: cohesive energy	T_n: normal traction	σ_{TS}: tensile strength
E_{pair}(i): average cohesive energy between atoms in an i^{th} group and a particular inner atom from which the distances are counted	T_t: tangential traction	σ_{YS}: yield strength
E_{inner}^{total} : bulk cohesion energy	t_{on}: power-on period	σ_x: stress in the x-direction
EBSD: electron backscatter diffraction	t_{off}: power-off period	σ_y: stress in the y-direction
FCC: face-centered cubic	TEM: transmission electron microscopy	σ_{xy}: stress in the xy-direction
FIB: focused ion beam	Ty: taylor texture component	τ_{max}: tangential cohesive strength
G: energy release rate	V: voltage	δ: crack tip opening displacement
G_c: critical fracture energy	V_{CE}: collector-emitter voltage	δ_c: critical crack tip opening displacement
G_d^j: dissipated energy at a specific moment	W_{sep}: work of separation of intersecting surfaces	δ_n: normal characteristic length
Gs: goss texture component	W_n: work of separation done by the normal traction	δ_t: tangential characteristic length
GND: geometrical necessary dislocations density	W_t: work of separation done by the tangential traction	δ_{um}: maximum displacement

RESUME ETENDU

Résumé français étendu:

Depuis quelques années, le domaine de la fiabilité des dispositifs électroniques de puissance à semi-conducteurs connaît un intérêt croissant, lié à l'augmentation de la demande de systèmes électrifiés. Cette demande s'accompagne de la nécessité de fournir des équipements plus efficaces, plus compacts et plus robustes. Parmi les dispositifs de puissance à semi-conducteurs et au cœur des systèmes de conversion se trouvent les modules de puissance, comportant différents types de composants au sein d'une même structure. Les modules de puissance les plus courants sont les transistors IGBTs et MOSFETs et les diodes et l'on commence à voir sur le marché des composants grands-gaps à base de SiC ou de GaN. Les dispositifs au silicium sont aujourd'hui largement utilisés dans de nombreux domaines d'application en raison de leurs divers avantages, notamment leur haut rendement et leurs commutations rapides du courant, ainsi que leur capacité à être utilisés dans des applications à courant et tension élevés.

Ces dispositifs sont soumis au cours de leur fonctionnement à des contraintes environnementales et fonctionnelles, qui conduisent à la dégradation progressive de leur structure, notamment par fatigue thermique. Ces dégradations altèrent le fonctionnement normal du dispositif, conduisant à sa défaillance. Ainsi, il est nécessaire de connaître les principales raisons de la limitation de leur durée de vie afin de les surmonter, permettant de réduire significativement le coût du système. Un des endroits les plus critiques pour les processus de dégradation se trouve aux interfaces d'interconnexion entre les fils (bondings) et les films de métallisation des puces actives. Ces zones sont soumises, lors de leur fonctionnement, à des variations continues de dissipation de puissance qui entraînent des fluctuations de température et la formation de contraintes thermomécaniques cycliques, allant jusqu'à leur dégradation et leur défaillance.

Traditionnellement, le problème de la fatigue des contacts métalliques supérieurs dans les dispositifs de puissance à semi-conducteurs est modélisé mécaniquement à l'aide de modèles de durée de vie physique. La mécanique des fractures est l'un des modèles les plus utilisés qui fournit une interprétation physique approfondie de la défaillance. Grâce à ces modèles, l'évolution de la fissure peut être modélisée. Cependant, ces modèles ne prennent pas en compte les aspects microstructuraux qui changent avec le vieillissement. De même, ils ne tiennent pas compte de l'état microstructural initial des fils de liaison après leur soudage sur la métallisation des puces.

Certaines analyses physico-chimiques ont été réalisées pour étudier le problème de la fatigue des composants métalliques ; cependant, ces études concernaient principalement le cas d'un recuit à des températures élevées et constants uniquement (proches des points de fusion du matériau fatigué). Selon ces études, les processus de diffusion atomique (principalement la diffusion de surface), qui conduisent au rainurage thermique et à la séparation des atomes qui se croisent, sont les causes de la rupture. Cependant, les conditions de ces études sont complètement différentes pour le cas des dégradations dans les composants semi-conducteurs de l'électronique de puissance puisque la température maximale atteinte n'est pas si élevée, en plus d'avoir des fluctuations cycliques de température lors de leur fonctionnement.

Récemment, l'influence des propriétés microstructurales et physico-chimiques sur les processus de dégradation spécifiques aux modules de puissance a suscité l'intérêt de plusieurs travaux. L'assemblage granulaire a été discuté, montrant le comportement des grains composant les matériaux des modules de puissance et les propriétés et caractéristiques des joints de grains. Lors du vieillissement, les évolutions microstructurales entraînent des modifications des propriétés physico-chimiques des matériaux et de leurs propriétés électriques et peuvent conduire à la défaillance de l'assemblage. Elles sont également concomitantes à la formation et à la propagation de la fissure. Dans des travaux antérieurs, il a été démontré que les changements microstructuraux affectent les propriétés mécaniques des matériaux, telles que leur résistance et leur ductilité. En outre, ils ont lié ces changements aux modifications des propriétés électriques, telles que la résistance de la métallisation. Ces changements ont été liés à l'évolution des fissures soit par des modèles théoriques et analytiques, soit par des observations expérimentales.

En fait, cette étude de doctorat réalisée dans le laboratoire SATIE de l'Université Gustave Eiffel est une continuation du travail de la précédente doctorante de notre laboratoire [Dorn19]. Dans ses études, elle a travaillé sur la modélisation de l'accumulation des dommages (spécifiquement l'évolution des fissures au cours du vieillissement) au niveau des contacts métalliques supérieurs dans les dispositifs de puissance à semi-conducteurs IGBT. Pour ce faire, elle a utilisé un élément fini en mécanique de la rupture appelé modèle de la zone cohésive (CZM) en attribuant des paramètres constants aux éléments de ce modèle, comme indiqué dans la littérature. Sur cette base, elle a prédit la durée de vie utile restante (RUL) des modules IGBT. De cette manière, l'effet des dégradations a été pris en compte lors de la prédiction de la RUL. Cependant, des difficultés ont été rencontrées lors de l'établissement du modèle de dégradation utilisant le MCC. Ces difficultés sont i) la nécessité d'étudier l'effet des changements microstructuraux sur l'évolution des fissures et ii) l'identification des paramètres appropriés du modèle d'endommagement. Ces deux points principaux constituent la principale préoccupation de ce travail de doctorat.

L'hypothèse principale de ce travail de doctorat est que l'évolution des paramètres des modèles de mécanique de la rupture utilisés pour prédire la fissuration, tels que le CZM, pourrait être liée à celle de la microstructure locale pendant le vieillissement. Ainsi, les tests expérimentaux de vieillissement d'échantillons d'IGBT qui avaient été réalisés par le précédent doctorant [Dorn19] ont été utilisés pour effectuer des analyses microstructurales supplémentaires au niveau des contacts fil-métallisation aux sites d'évolution des fissures. L'objectif principal de ces analyses est d'étudier s'il existe un lien entre les changements microstructuraux au niveau des contacts métalliques supérieurs et la fissuration. Si ce lien était mis en évidence, il s'agirait alors de rechercher des liens éventuels entre les paramètres des lois de cohésion (énergie et contrainte critiques de rupture) et les propriétés physico-chimiques des matériaux qui évoluent dans la microstructure lors du vieillissement. Cela sert l'objectif principal de ce travail qui est de modéliser et de prédire l'évolution des fissures de fatigue en tenant compte de l'effet des changements de la microstructure et des propriétés des matériaux pendant le vieillissement.

Les travaux réalisés au cours de cette étude de doctorat sont présentés comme suit :

Chapitre I:

Dans le premier chapitre, l'assemblage des modules de puissance est présenté en mettant l'accent sur les contacts fil métallique-métallisation. Le but de cette description est d'expliquer pourquoi et comment les dégradations se produisent. Ces contacts sont les sites des déformations maximales et des formes de dégradation dues à plusieurs causes, telles que leur processus de fabrication, leur géométrie et les propriétés des matériaux. Par conséquent, l'analyse de ces contacts est très importante pour l'étude de la fiabilité des modules de puissance.

Lors du soudage du fil sur la puce de métallisation, des modifications initiales de la microstructure se produisent en raison des forces appliquées par le soudage qui entraînent des déformations plastiques et des modifications de la microstructure au niveau du contact fil-métallisation. Les principaux processus de déformation et de dégradation, y compris la fracture et le décollement du fil, causés par le vieillissement sont ensuite décrits en explorant les principaux aspects physiques qui les sous-tendent.

Parmi ces processus de dégradation, la progression de la fissure au niveau du contact fil/métallisation est l'un des processus les plus critiques qui provoque la défaillance totale des dispositifs de puissance. La progression de ces fissures s'accompagne de changements microstructuraux qui affectent les propriétés physico-chimiques locaux des matériaux. Ces changements sont notés par les processus de reconstruction des grains, qui affectent la structure et les propriétés des grains et peuvent conduire à leur séparation, ce qui entraîne la fissuration. Ces propriétés affectent les propriétés mécaniques des matériaux, donc leur durée de vie. Tous ces éléments sont détaillés dans ce chapitre.

Pour mieux comprendre la corrélation entre l'évolution des fissures et les changements microstructuraux, il faut d'abord interpréter l'évolution des deux processus lors du vieillissement. Ceci

a été mieux décrit dans le deuxième chapitre.

Chapitre II:

Le deuxième chapitre est consacré à une analyse expérimentale permettant d'interpréter les changements microstructuraux qui se produisent et de les relier aux processus de dégradation. Ces données expérimentales sont également essentielles pour construire le modèle physico-chimique-microstructurel permettant de modéliser l'évolution des fissures dans le chapitre suivant.

Des tests de cyclage accéléré ont été appliqués pour obtenir l'évolution de la dégradation pour des conditions données {Température de jonction, période de mise sous tension...}. Les modules IGBT SKIM63 ont été choisis pour être analysés car les seules dégradations observées dans ces modules sont le soulèvement des fils et les processus de reconstruction granulaire au sein du fil et de la puce de métallisation, zone d'intérêt de cette étude.

L'évolution de la dégradation est directement liée aux évolutions microstructurales et aux changements des propriétés physico-chimiques. Des analyses SEM et AFM ont d'abord été réalisées pour observer les changements microstructuraux se produisant à la surface d'interconnexion entre le fil et la couche de métallisation. À l'état initial, la structure cellulaire multi-élémentaire dans la puce de métallisation est observée sous la forme d'un motif en damier. Lors du cyclage, cette structure devient indiscernable sur la surface métalisée qui a une apparence très désordonnée avec une topologie chaotique. En effet, des micro-vallées et des collines à l'échelle de la structure se forment lors du cyclage à la surface des puces de métallisation, en particulier dans les sites proches de l'interconnexion avec le fil de liaison.

La technique d'analyse la plus importante dans nos travaux est l'EBSD. Cette technique analyse les changements microstructuraux dans le fil, qui est appliqué verticalement de la face supérieure du fil vers le contact fil-métallisation. Une telle analyse offre plusieurs avantages, car les principales propriétés microstructurelles qui changent lors du cyclage peuvent être interprétées en observant l'évolution de la taille des grains, des angles de désorientation des grains, de la texture et d'autres caractéristiques. Cette analyse est réalisée sur différents modules cyclés à différents stades de vieillissement afin d'interpréter l'évolution des changements microstructuraux. Des tests de nanoindentation ont aussi été réalisés pour voir l'évolution des valeurs du module d'Young et de la dureté en fonction de l'état de vieillissement par cyclage.

Les analyses EBSD ont permis de déduire que la taille des grains augmente globalement lors du cyclage. En ce qui concerne la texture, on peut déduire que les grains s'orientent pour augmenter leur densité de tassement et diminuer leur énergie de surface. Les composantes de la texture qui nous permettent de savoir si les processus de déformation ou de recristallisation sont dominants ont également été interprétées. On a montré que chacun de ces deux processus affecte le processus de dégradation à sa manière dans le premier chapitre. L'évolution de la propagation des fissures peut également être interprétée avec précision en utilisant les données EBSD. Il a été déduit que la formation des fissures commence à partir des extrémités du contact, en commençant par les positions d'interconnexion du talon et de la pointe, avec une vitesse plus rapide au niveau du talon par rapport à la pointe. Le processus de croissance des grains aux premiers stades du cyclage et la présence de joints à désorientation angulaire faibles ont été déduits comme étant accompagnés de la vitesse maximale de la fissure au stade de l'initiation de la fissure. Le passage de joints à désorientation angulaire faible à joints à désorientation angulaire élevé à des stades avancés du cyclage a été déduit comme étant concomitant avec le ralentissement de la vitesse de propagation des fissures.

Ces interprétations sont très importantes pour la construction du modèle physico-chimique-microstructural qui est décrit dans le chapitre suivant.

Chapitre III:

Après avoir réalisé la dépendance des aspects microstructuraux sur les processus de dégradation, en particulier l'évolution de la fissure, qui provoque la défaillance du module lorsqu'il sépare le fil de la puce de métallisation, un modèle de dégradation physico-chimique-microstructural spécifique aux parties métalliques supérieures d'interconnexion des dispositifs de puissance à semi-conducteurs a été présenté dans le troisième chapitre. Ce modèle offre une description détaillée de l'endommagement qui se produit pendant le vieillissement des contacts métalliques. En utilisant les données expérimentales du chapitre précédent, une modélisation de l'évolution de la fissure est réalisée en mettant en relation les paramètres d'un modèle basé sur l'endommagement, qui est le modèle de la zone cohésive (CZM) d'une part, avec certaines caractéristiques physicochimiques-microstructurales d'autre part.

Le CZM, un modèle de mécanique de la rupture, est utilisé pour prédire l'évolution des fissures dans les métaux ductiles, comme dans le cas des contacts métalliques supérieurs des dispositifs de puissance. Le CZM est basé sur des relations physicochimiques-microstructurales, notamment la théorie de l'énergie de liaison universelle. La CZM comporte plusieurs types et modes. Le type et le mode CZM appropriés ont été sélectionnés pour construire le modèle physico-chimique. Cette sélection est faite avec soin pour s'adapter à la propagation des fissures de fatigue qui se produit au niveau des contacts fil-métallisation de la face supérieure. En outre, ses paramètres doivent être directement ou indirectement liés aux propriétés et caractéristiques physicochimiques et microstructurales.

Par conséquent, le CZM à mode mixte dans le cas des surfaces de décollement a été choisi. La définition de la CZM sélectionnée est basée sur deux paramètres : la contrainte maximale qui doit être atteinte à l'interface pour initier la décohésion et l'énergie qui permet de savoir quand les interfaces en contact seront complètement décollées. Il a été démontré que ces deux paramètres sont liés aux propriétés physico-chimiques et microstructurales. Cette nouvelle façon de relier les caractéristiques physico-chimiques et microstructurelles à la progression de la fissure constitue la nouveauté de ce travail. La contrainte critique pour la rupture était liée à la taille des grains, à leurs valeurs de dureté et à la limite d'élasticité. En revanche, l'énergie de rupture est liée aux énergies de surface et aux joints de grains, aux angles de désorientation des grains et à leur texture.

Après avoir montré comment obtenir les paramètres de ce modèle à l'aide des propriétés physicochimiques et microstructurales, ce modèle est utilisé pour prédire l'évolution des fissures au niveau des contacts supérieurs dans les dispositifs de puissance. À la fin de ce chapitre, la manière d'introduire les propriétés physico-chimiques pour modéliser microstructuralement la formation de fissures au niveau des interconnexions métalliques de la face supérieure a été décrite. Cette modélisation a été réalisée en insérant des hexagones représentant des grains aux bords terminaux des contacts fil-métallisation. Ces bords ont été attribués à des paires de contacts associées à des paramètres CZM localisés conformément aux observations de leurs caractéristiques microstructurelles locales. De cette façon, la décohésion granulaire peut être simulée en étudiant les effets des paramètres microstructuraux sur la formation de fissures. La manière d'introduire ces propriétés pour modéliser la microstructure de la formation de fissures au niveau des interconnexions métalliques de la face supérieure est décrite bien plus en détail dans le chapitre suivant.

Chapitre IV:

Le quatrième chapitre est consacré aux simulations numériques réalisées à l'aide du logiciel ANSYS APDL. L'intérêt de la modélisation est d'illustrer l'utilisation de l'analyse microstructurale faite dans le deuxième chapitre et d'exprimer la dépendance présentée dans le troisième chapitre entre l'approche combinée CZM - physico-chimique et l'évolution de la fissure. Cette approche permet de simuler la décohésion entre grains ayant des propriétés physico-chimiques locales dépendant de la microstructure locale. L'idée étant de prédire à la fois le chemin et la vitesse de propagation au niveau du contact.

Des simulations électrothermiques et thermomécaniques ont ensuite été réalisées pour modéliser les dommages résultant du vieillissement. Les conditions du modèle ont été paramétrées pour avoir les mêmes conditions que pour les tests de vieillissement effectués expérimentalement. Ces

simulations permettent d'estimer les distributions locales de température et de contraintes mécaniques. Elles permettent également de prédire le processus de formation des fissures ayant lieu dans la zone d'interconnexion fil-métallisation.

Plusieurs simulations ont été réalisées, avec des conditions de cyclage différentes, en faisant varier les valeurs de la température de la jonction et de la durée d'auto-échauffement. Ces simulations ont pour but de i) voir quel est le lieu préférentiel du décollement entre le talon et la pointe, ii) prédire la trajectoire de la fissure, iii) examiner l'effet de la seule modification de la valeur de la température de la jonction (ΔT_j) sur les cartes de décollement, et enfin iv) voir l'effet de la modification de la durée d'auto-échauffement (t_{on}) en gardant la même amplitude de variation de la température de jonction (ΔT_j).

Il a été principalement déduit que la température maximale est localisée au niveau du contact fil-métallisation. Ces contacts sont également le centre de concentration des contraintes. Il a été observé que la fissure s'initie à partir des bords terminaux du fil en contact avec la métallisation. La fissure se forme d'abord à la position du talon, où elle continue à se propager à l'intérieur du fil juste au-dessus de la couche de métallisation. La vitesse de la fissure est plus rapide au niveau du talon qu'au niveau de la pointe. La fissuration au niveau du talon se produit principalement durant la phase d'auto-échauffement des cycles, alors qu'au niveau de la pointe, elle se produit principalement pendant la phase de refroidissement des cycles. Le même mode de formation des fissures est observé lorsque l'on diminue seulement la valeur de la température de jonction ; cependant, la vitesse des fissures devient plus lente. En augmentant la durée de la phase d'auto-échauffement tout en conservant le même ΔT_j, on observe que le décollement s'amplifie.

Les résultats de l'évolution des fissures ont ensuite été comparés de manière satisfaisante aux données des tests de vieillissement expérimentaux réalisés dans les mêmes conditions afin de vérifier la compatibilité entre l'approche de modélisation suivie dans ce travail et réalité.

Dans la dernière étape, les principales limitations résultant des simulations numériques ont été exposées. Certaines limitations ont été discutées sur la base d'un point de vue physico-chimique et microstructural en utilisant les données EBSD. La principale limite discutée est l'utilisation de paramètres CZM réduits pour minimiser le temps de calcul dans les simulations. Cette limitation a été discutée en détail en effectuant des simulations supplémentaires.

Conclusions:

Dans cette étude, un modèle original de zone cohésive, dont les paramètres sont basés sur une analyse physico-chimique et microstructurale, pour prédire l'évolution des fissures lors du cyclage a été présenté. Cette approche a été appliquée au niveau des interconnexions supérieures des modules de puissance, constituées des fils et des puces de métallisation.

GENERAL INTRODUCTION

Recently, the field of reliability of semiconductor power electronic devices has been experiencing growing interest, linked to the increasing demand for electrified systems. With this demand comes a need to provide more efficient, compact, and robust equipment. Among semiconductor power devices and at the heart of conversion systems are the power modules, having different types of components within a single structure. The most common power modules are IGBTs and MOSFETs transistors and diodes. Such devices are widely used nowadays in many fields of applications due to their various advantages, especially their high efficiency and fast current switching, in addition to the ability of their usage for high current and voltage applications. These devices are subjected during operation to environmental and functional constraints, which lead to the degradation of their structures. These degradations alter the normal functioning of the device, leading to its failure. Thus, it becomes necessary to know the main reasons behind shortening their lifetimes in order to overcome them, making it possible to reduce the cost of the system significantly. The most critical positions for degradation processes are at the interconnection interfaces between the welded wires and metallization layers beneath them. These positions are subjected upon their operation to continuous electric power densities, which lead to temperature fluctuations and stress formation there, causing their degradation and failure.

Traditionally the fatigue problem of topside metallic contacts in semiconductor power devices is modeled mechanically using physical lifetime models. Fracture mechanics are among the most used models that provide a profound physical interpretation of failure. Using these models, the crack evolution can be modeled. However, these models do not consider the microstructural aspects that change upon aging. Also, they do not take into account the initial microstructural state of bonding wires after they have been welded to metallization chips. Electrical indicators were used when studying the degradation of topside metallic interconnections to monitor the damage during the device's operation and know the end of its life. Some physicochemical analyses were made to study the fatigue problem for metallic components; however, those studies were mostly for the case of annealing at high and steady-state temperatures only (near melting points of the fatigued material). According to these studies, the atomic diffusion processes (mainly surface diffusion), which lead to thermal grooving and the separation of intersecting atoms, are the causes of fracture. Grooving at grain boundary sites is the decrease in local thickness at these boundaries. Its driving force is the difference in surface and interfacial energies of the intersecting grains, the difference in the grains' orientations, and the surface faceting process caused by the growth of specific crystal planes at the expense of others. However, the conditions of these studies are completely different for the case of degradations in semiconductor power electronics since the maximal temperature reached is not so high, in addition to having continuous temperature fluctuations upon the operation of the power devices.

Lately, the influence of the microstructural and physicochemical properties on degradation processes that occur specifically to power modules has been the interest of several scientists. The granular assembly has been discussed, showing the behavior of grains composing the power modules' compartments and the properties and characteristics of the boundaries at the metallic contact interface between intersecting grains. Upon aging, microstructural evolutions cause changes in the physicochemical material properties and their electrical properties and may lead to their failure. They are also concurrent with the formation and propagation of the crack. In previous works, it has been illustrated that microstructural changes affect the mechanical properties of materials, such as their strength and ductility. In addition, they related these changes to the changes in the electrical properties, such as the metallization resistance. These changes were linked to the crack evolution either by theoretical and analytical models or by experimental observations. In this Ph.D. study carried out in the SATIE laboratory at Gustave Eiffel University, the work is concentrated on using such physicochemical-microstructural concepts in order to be able to analyze and predict the degradation processes occurring. The primary outcome of such analysis is to identify the leading causes of the failure problem, then predict their degradation evolution. This study may be used to try improving the material properties of such modules. The work carried out during this Ph.D. study is presented as follows.

Most of the previously established physicochemical or microstructural models model just the crack initiation stages theoretically based on dislocations' activity. Such models are not validated experimentally. Other models, such as crystal plasticity models, are used to model the crack propagation; however for a single

grain, due to the complexity of such models. Indeed, the aging of polycrystalline structures is rarely considered in terms of microstructural changes. In addition, the relation between aging and changes in the physicochemical material properties is so interesting to discuss. Considering the relation between aging from one side and the changes in the physicochemical and microstructural material properties from the other side is the ultimate objective of this work. A model taking into account the experimental observations is aimed to be constructed. This model should provide a deeper understanding of the reliability aspects within the microstructure and overcome previous models' limitations. It also serves to predict the crack propagation process based on the main physicochemical-microstructural changing properties.

Actually, my Ph.D. work is a continuation of the work of the previous Ph.D. student in our laboratory [Dorn19]. In her studies, she worked on modeling the damage accumulation (specifically the crack evolution within aging) at topside metallic contacts in IGBT semiconductor power devices. This was achieved by using a finite element in fracture mechanics called the cohesive zone model (CZM) by assigning constant parameters for the elements of this model as listed in the literature. Based on that, she predicted IGBT modules' remaining useful life (RUL). In this way, the effect of degradations was considered when predicting the RUL. However, difficulties were faced when establishing the damage model using the CZM. These difficulties are i) the need to investigate the effect of microstructural changes on the crack evolution and ii) identifying the appropriate damage model's parameters. These two main points are the main concern of this Ph.D. work.

The main hypothesis of this Ph.D. work is that the evolution of the parameters of fracture mechanics models used to predict cracking, such as the CZM, could be linked to that of the local microstructure during aging. Thus, the experimental aging tests of IGBT samples that were previously done by the previous Ph.D. student [Dorn19] were used to do further microstructural analyses at the wire-metallization contacts at the sites of crack evolutions. The main aim of these analyses is to investigate whether there is a linkage between the microstructural changes at topside metallic contacts and cracking. If this linkage was illustrated, the main thing to be done is to search for possible links between the parameters of cohesive laws (critical fracture energy and stress) and materials' physicochemical properties that change within the microstructure upon aging. This serves the main objective of this work which is modeling and predicting the fatigue crack evolution taking into account the effect of the microstructural and material properties changes during aging.

In the first chapter, the assembly of power modules is presented with a focus on the metallic wire-metallization contacts. These contacts are the sites of maximal deformations and shapes of degradation due to several causes, such as their manufacturing process, geometry, and material properties. Therefore, analyzing these contacts is highly important when exploring the reliability of the power modules. Main deformations and degradation processes, including the wire fracture and lifting-off, caused by aging are then described by exploring the main physical aspects behind them. Among these processes, the crack progress is the most critical process that causes the power devices' total failure. The crack progress is accompanied by microstructural changes that affect the physicochemical properties of the materials. These changes are noted by grains reconstruction processes, affecting the structure and properties of grains and may lead to their separation, which means cracking. These properties undoubtedly affect the mechanical properties of the materials, thus their lifetime. All this information is well described.

The second chapter is then dedicated to do some experimental analysis for interpreting the microstructural changes occurring and relating these changes to degradation processes. These experimental data are also essential for constructing the physicochemical-microstructural model for predicting the crack evolution in the next chapter. SEM and AFM analyses were first applied to see the microstructural changes occurring at the contact area between the wire and the metallization layer. The most important analysis technique is the EBSD. This technique analyzes the microstructural changes in the wire. Such analysis offers several advantages, where the main microstructural properties changing upon cycling can be interpreted through observing the evolution of grains' size, boundary disorientation angles, texture, and other features. This analysis is applied to different modules cycled at different aging stages in order to be able to interpret the evolution of the microstructural features. The crack propagation evolution can be as well interpreted

precisely using the EBSD data. Nanoindentation tests were afterward applied to see the evolution of the values of Young modulus and Hardness upon cycling. This analysis is applied vertically across the wire, starting from the wire's topside towards the wire-metallization contact. All these interpretations are also essential for building up the physicochemical-microstructural model that will be described in the upcoming chapter.

The third chapter presents the physicochemical-microstructural model used to predict the crack progress. This model offers a detailed description of the damage occurring upon the aging of the metallic contacts. Using some experimental data from the previous chapter, the crack evolution modeling is achieved by relating the parameters of a damage-based model, which is the cohesive zone model (CZM) on the one hand, with some physicochemical-microstructural features on the other. Based on fracture mechanics concepts, the CZM is used for predicting the crack evolution in ductile metals, as in the case of the topside metallic contacts in power devices. The CZM is originally based on physicochemical-microstructural relationships, rising from the universal binding energy theory. After showing how to obtain the parameters of this model using physicochemical-microstructural properties, the model is used to predict the crack evolution at topside contacts in power devices. This prediction is well described in the next chapter. In this way, the manner of the crack formation and propagation can be interpreted.

The fourth chapter is devoted to perform numerical simulations using the ANSYS APDL program. The importance of this modeling section is illustrating the microstructural analysis made in the second chapter and expressing the dependency presented in the third chapter between the CZM and the physicochemical and microstructural properties. This was performed by inserting hexagons at the wire edges in contact with the metallization layer to represent grains at those sites. CZM elements were then implemented at the edges of the hexagons which represent the grain boundaries to predict the crack evolution at these sites. Electrothermal and mechanical simulations were subsequently applied to model the damage resulting from aging. The simulations' conditions were parameterized to be the same as those in experimental aging tests. From these simulations, one can know the local distribution of temperature and stress, and in addition, they give the maps of cracks' evolution. The crack evolution results were then compared to the data of experimental aging tests performed under the same conditions to see the compatibility between the modeling approach followed in this work and that occurring in real situations.

A conclusion on the carried out work is provided at the end of this Ph.D. manuscript. This is followed by a discussion about possible perspectives for this study.

CHAPTER I: RELIABILITY OF INTERCONNECTION TECHNOLOGIES WITHIN POWER MODULES

1 INTRODUCTION

In the modern power semiconductor industry, the work concentrates on improving several features in power modules, such as their efficiency, performance, and reliability, which is the main focus of this manuscript. Semiconductor power devices such as IGBTs are widely used nowadays in many fields of applications due to their various advantages, especially their high efficiency and fast current switching, in addition to the ability of their usage for high current and voltage applications.

Topside interconnections in semiconductor power devices consisting of wires bonded to metallization layers are subjected upon their operation to continuous electric power densities, which lead to temperature fluctuations and stress formation concurrently with microstructural changes, resulting in their degradation and failure. This phenomenon is well known as thermomechanical fatigue. The zone of interest considered in this chapter is this topside interconnection between wires and metallization layers.

Since thermal fatigue causes crack formation and propagation that are microstructurally related, the impact of the microstructural and physicochemical changes should be considered when doing reliability studies. Primarily, the manufacture of the metallic interconnections in power module assemblies is explained, with particular attention to the wire welding process that creates initial defects in the microstructure prior to its operation. Thereafter, degradation processes that take place upon cycling, i.e., granular reconstructions and cracks evolution, are detailed. The effects of such degradation processes on the mechanical properties and lifetime of topside metallic elements are afterward shown. Finally, traditional modes of failure and degradation predictions are presented, including well-known physical models such as fracture mechanics models. Based on these models and the microstructural observations mentioned in the literature, the combined fracture mechanics - physicochemical and microstructural model to be used in this work is introduced.

2 TOPSIDE MOST DEGRADED ELEMENTS IN POWER MODULES

A power module is made up of several layers composed of different materials. In the conventional structure, the upper parts of semiconductor power chips are made up of metallization layers connected with bonding wires. Using solder layers, these topside parts are attached to ceramic substrates that lay on a base plate. The cooling system is fixed under the base plate at the bottom using a thermal interface material. In Figure 1, the main elements of a typical power module structure are presented. The region that this study is focusing on is the upper metallic interconnection part, connecting bonded wires with metallization chips. This zone provides the electrical energy necessary for the device's functioning.

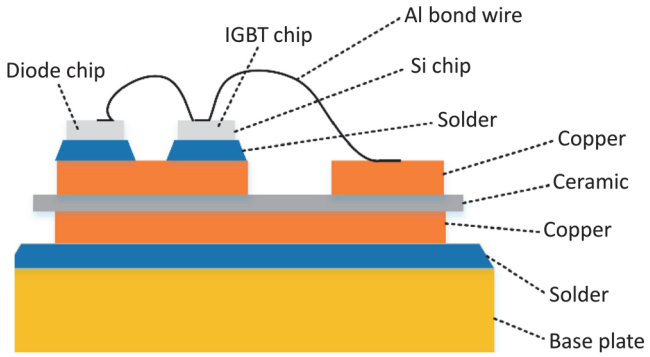

Figure 1: Assembly of a typical power module schema [WHWL20].

As presented previously, the structure of a power module consists of several materials having different thermal expansion coefficients (CTEs) noted by (α_{TE}). When materials have very distant CTEs, this means that they are highly affected by the deformations' generations. This is the case in the upper parts of power

modules, especially between the top aluminum interconnects and the silicon chip (23.5 ppm/K for Al and 4.1 ppm/K for Si). Thermomechanical stresses are created at such positions when the module ages. The thermal deformation strain ($\varepsilon_{thermal}$) resulting from the effect of a temperature swing ΔT_j is most often calculated as follows in equation (1) [Ciap02]. These deformations lead to several degradations, such as the crack propagation at the wire-metallization contact and degradations inside the metallization chips. Such degradation processes lead to several failure shapes like wire fractures and lifting-off.

$$\varepsilon_{thermal} = (\alpha_{TE1} - \alpha_{TE2})\,\Delta T_j \quad (1)$$

Accordingly, the wire welding procedures and bond types will be detailed in the upcoming sections. The factors affecting the wire welding process are then listed. Afterward, as for wires, the structure and the manufacture of metallization layers are detailed.

2.1 BONDING WIRES

In this section, bonding processes and wire types are detailed. The bonding processes are thermo-compression, ultrasonic, and thermo-sonic welding procedures. The procedure of obtaining different wire shapes, balls and wedges, and the main characteristics of each bonding shape are explained. Factors that may affect the wire welding process, such as the bonding force, ultrasonic amplitude, friction between the wire's ball at the contact and the pad, the bond-pad thickness, and the bonding temperature are presented.

- **Wires welding processes:**

For a long time, welds were done in liquid phases by heating materials beyond their melting points. Indeed, this results in permanent changes in their electrical, thermal, and mechanical properties. Solid-phase soldering processes were then developed to bond metallic wires to metallization layers. In a conventional power module structure, wires are majorly welded to metallization layers via the supply of ultrasonic energy, making it possible to keep the materials in a solid phase. Two other classical solid-phase welding processes are also present: thermo-compression and thermo-sonic.

A. Thermo-compression

Thermo-compression bonding technology was used in the first wire-chip interconnections in the mid-1950s. This process was then developed to involve heating and pressuring the assembly enabling the wire to be welded within a few seconds. Thermo-compression welding does not exhibit a liquid phase, where temperatures typically vary between 300-350 °C [Scha73]. These temperature values are below the melting points of the used materials (Al ≈ 660 °C, Si ≈ 1500 °C). Figure 2 presents the thermo-compression welding procedure.

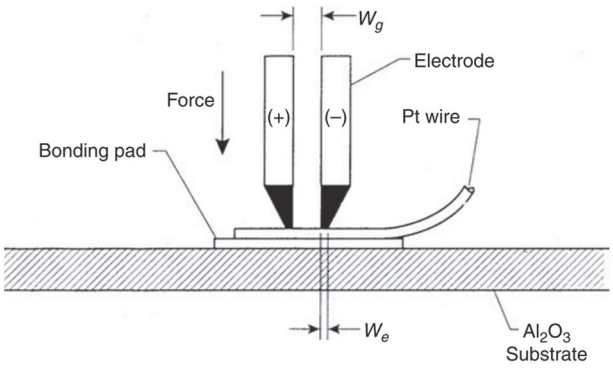

Figure 2: Thermo-compression welding procedure [Harm10].

Ultrasonic welding has now replaced thermo-compression in main applications due to its ease of use and improved performance. Thermo-compression is still used nowadays for specific applications, such as conditioning integrated electronic devices known as wafer-level packaging [TsSS04].

B. Ultrasonic welding

Ultrasonic welding was introduced in 1965 by Robert Soloff [SoLi65]. Unlike thermo-compression welding, this process is performed at low temperatures. Ultrasonic welding has the advantage of being fast and precise. It is widely used in integrated electronic devices, especially in bonding wires in semiconductor chips [Scha73].

Performing an ultrasonic weld relies on a device called a mechanical transducer. This device enables the resonance of the welding system by converting oscillating electrical signals into mechanical vibrations. A generator supplies the necessary electrical energy at a prior defined frequency according to the characteristics of the weld, which is about 60 kHz for bonding wires. Once this electrical energy is transformed into mechanical, a part called sonotrode placed at the output of the transducer allows the amplification and transmission of the ultrasonic mechanical wave to the exact place of the weld. A final device called the capillary adhesion tool maintains the interconnecting wire against the metallization layer while transmitting the ultrasonic energy required for soldering the wire. It moves parallel to the surface to be welded by an amplitude of the order of a micrometer. Performing an efficient weld requires a balance between the ultrasonic power to be delivered, the applied adhesion force applied to the wire necessary to keep it against the metallization without damaging it, in addition to the welding period [Dush71], [Harm10], [Scha73]. Figure 3 shows the ultrasonic welding procedure.

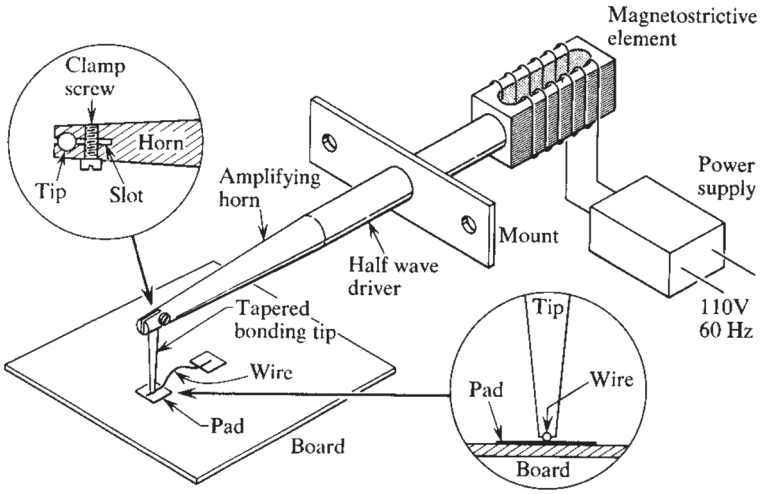

Figure 3: *Ultrasonic welding procedure [Dush71].*

When the wire is subjected to ultrasound, two critical effects should be considered: softening and strain hardening. The metal softening effect appears almost immediately after applying the ultrasonic energy. The latter moves the existing dislocations in the metal from their equilibrium positions and sets them in motion. Thus, the necessary stress to be applied to the metal to deform it plastically will be considerably reduced. The second well-known phenomenon, strain hardening, occurs when a metal is plastically cold-deformed. Strain hardening increases the number of dislocations, causing an increase in yield strength. Therefore, the metal becomes more difficult to be deformed [Harm10], [Lang66].

Additionally, when the wire is brought in contact with the metallization under capillary forces, shear and sliding appear at the interface. These forces play a significant role in breaking the oxide film present at the metallization surface. Thus, impurities will be released, resulting in a clean and energetic metallization surface. More oxides and impurities will be removed when the welding time is greater, accompanied by a greater welded area [Tumm01]. With inter-diffusion, adhesion between the wire and the metallization results [MPBB00]. Consequently, the weld appears first at the periphery of the contact, where the shear and sliding forces are the most significant. An example of an ultrasonic wedge-bond can be observed in Figure 4.

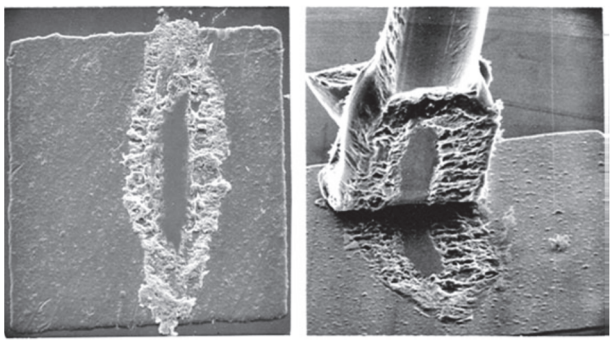

Figure 4: *An ultrasonic wedge-bond made with normal parameters for a manual wedge bonder using 25 µm diameter Al, 1% Si wire. The wire is lifted off to see the bonded area [Harm10].*

C. Thermo-sonic welding

Coucoulas first proposed thermo-sonic welding in 1965 [Harm10]. Today it is of the most widely used welding techniques in the microelectronics industry. It corresponds to the combination of thermo-compression (temperature and pressure) and ultrasonic (ultrasonic energy) weldings [CoLa70]. Coucoulas showed that heating metals significantly reduces the required ultrasonic energy for the wire to obtain a weld, since the presence of temperature counteracts the strain hardening effect. Upon comparing thermo-compression and thermo-sonic weldings, thermo-compression requires the application of a too high temperature; therefore, thermo-sonic welding is a good alternative because the needed temperature does not exceed 220 °C. This is an advantage because when this energy is too high, it can create defects in the semiconductor chip or the substrate.

- **Bond wires types:**

Wire cabling is the most widely used interconnect technology in integrated electronic devices due to its easy implementation. A wire is used to connect the semiconductor chip with the Direct Copper Bonding (DCB) substrate. Depending on the type of components to be supplied and the power to be delivered, the contact between the wire and the metallization can take the form of a ball, then it is called a ball-bond; otherwise, it is called a wedge-bond.

A. Ball-bonds

The ball-bonding process is a process where the shape of the contacting interface looks like a crushed ball. Ball-bond cabling represents more than 90% of wire cablings in microelectronics. In ball-bonding methods, the welding energy is provided by heating the support and by ultrasonic wave (thermo-sonic). Ball-bondings are also subjected to an annealing process before making the metallic contact to limit the appearance of defects during welding, especially in the area above the ball. The time required to make such contact is less than 20 milliseconds.

The main advantage of this ball-shaped technology is that it does not require any alignment or orientation of the wire during its welding, unlike wedge welding. The wires used are generally about 20 µm and are made of 99.99% pure gold. Recently, copper has been considered a gold replacement since it is too expensive. However, copper has a much higher yield point than gold and therefore requires more applied ultrasonic energy and force when welding. This can cause the creation of defaults in the semiconductor chip or the substrate [Harm10]. Besides creating defaults, dislocations' mobility and their density increase in such bonding processes due to the high provided ultrasonic energy values, which also induce strain hardening [Piet10]. In addition, the mechanical constraints resulting from using copper wires should be taken into account. Moreover, copper oxidizes very easily, unlike gold, especially when heated. Thus, the ball-bonding of a copper wire must be carried out in an isolated atmosphere [Harm10]. Consequently, this technique is rather reserved for microelectronics and will not be detailed here. Figure 5 shows the ball-bonding procedure.

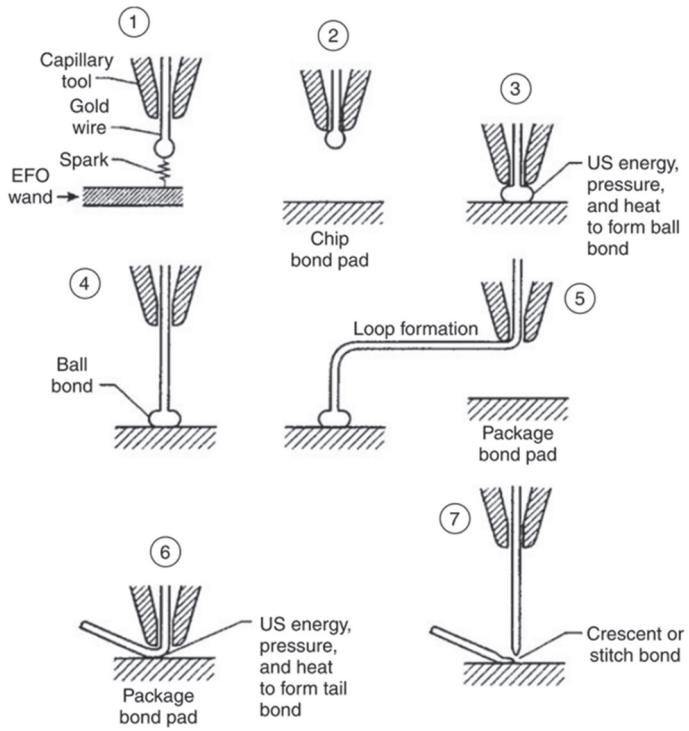

Figure 5: Simplified procedure for making a ball-bond wire *interconnection [Harm10].*

B. Wedge-bonds

The wedge-bond cabling is generally used more for power module interconnections. In such bonds, wires are broader than those for ball-bonds (between 100 µm to more than 0.5 mm) since they must conduct currents in the order of several amperes. They are generally made of aluminum associated with up to 1% silicon. The presence of silicon is essential for increasing the hardness of the wire.

Welding in this procedure is said to be cold because the provided energy is only ultrasonic. The metal is softened by ultrasonic energy through a resonating transducer tool while applying a clamping force, sweeping aside brittle surface oxides and contaminants through this interfacial motion. In this welding type, the wires must be aligned so that their contacts with the metallization and the substrate are not subjected to too much stress [Harm10]. Figure 6 is an example of wedge wire bonding.

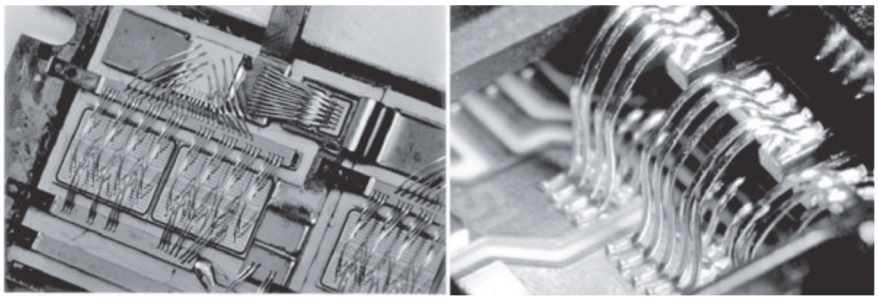

Figure 6: Heavy wire wedge-bonded modules [Harm10].

Like ball-bonding wires, copper is increasingly seen as an alternative to aluminum for wedge-bonding wires within power modules. This is due to its better thermal and electrical conductivities than aluminum, and since its thermal expansion coefficient is nearer to silicon than aluminum. However, copper interconnect technologies face many challenges, mainly the copper's diffusion from the wire into the chip [YXHL19].

- **Factors affecting the bonding process:**

Several factors affect the wire welding quality and the properties of wires and metallization layers. These most essential factors are summed up as follows [BGHS15], [BGHS15], [Harm10].

A. Bonding force:

Generally, to optimize the bonding process, sufficient bonding ultrasonic forces, near begin and end forces, and providing an inversely proportional balance between the power force and the bonding time are essential. For example, in the wire bonding process, static bonding forces lead to cratering. Cratering is a shape of plastic deformations which occurs during the bonding process. The conventional explanation of cratering in wedge-bonded wires, even with low bonding forces, is that the bonding tool might not be held tight enough against the pad. Therefore, it chatters across the top of the wire, producing high-force spikes toward the pad. More cratering will be induced if the bonding force is static and high because more plastic deformations will be present.

B. Ultrasonic amplitude:

The maximal principal stress in the pad below the device increases as the ultrasonic amplitude increases. The maximal von Mises and shear stress values decrease at the beginning of the bonding process. After reaching a certain ultrasonic amplitude, their values increase. The formation of stresses leads to strain generation. In parallel, as the ultrasonic amplitude increases, cratering deformations in the horizontal direction increase, whereas they decrease in the vertical direction.

C. Bonding friction at the contact between the ball/wedge and the pad:

Bonding friction is a complicated multi-physical process at the wire-pad interface. Bonding occurs when the applied energy is enough to overcome the activation energy and surface oxidation energy of the barrier. Another bonding condition is that the wire-pad interface's relative motion must be zero. Increasing bonding friction forces increases deformations, bonding stress, and the stress transferred to silicon. Thus, cratering will be induced.

D. Bond-pad thickness:

Increasing the bond pad thickness is an easy and low-cost way to reduce cratering. When the bond pad thickness increases, no significant reduction results for stresses transferred to silicon. However, the bond pad’s effective plastic strain and plastic strain density reduce rapidly. This means that lower cratering will result.

E. Bonding temperature:

Grains recovery and recrystallization processes are promoted by high bonding temperatures, as shown in Figure 7, leading to the relaxation of residual stresses, along with the reduction or rearrangement in the density of dislocations near the bonding interface.

Recovery is a process when deformed grains reduce their stored energy by removing or rearranging defects in their crystal structure, such as vacancies and dislocations. It is a low-temperature phenomenon that restores some physical properties without any observable changes in the microstructure. Generally, recovery is a process that involves the (a) migration of point defects and dislocations to grain boundaries and (b) the combination of point defects and dislocations. When recovery takes place, vacancies are primarily eliminated. Afterward, some dislocations of opposite signs are annihilated. Usual recovery treatments do not remove the majority of dislocations; however, minor structural changes during recovery pronounce effects on the residual stresses and the electrical properties.

Recrystallization requires higher temperatures than recovery [AwKh19]. In this process, distorted grains are replaced by new strain-free grains. Two mechanisms have been observed in the recrystallization process depending on the metal nature and the degree of deformations. The

first mechanism is the growth of pre-existing grain boundaries, while the second is the growth of sub-grain boundaries resulting from deformations. In the first mechanism, the boundary between a grain with high dislocation density and a grain with low density suddenly grows. This mechanism occurs when boundaries have high grain boundary mobility, such as high angle boundaries. In the second mechanism, the sudden growth of sub-grain boundaries may be due to either boundaries' coalescence or migration. During recrystallization, a sharp decrease in hardness and strength and an increase in ductility occur [BGHS15]. Therefore, recrystallization reduces residual stresses and dislocation densities.

Other effects of bonding the wire at high temperatures can be listed here. It was reported that the mean shear force required to shear the wire bonds increases steadily with increasing the bonding temperature [LCLH07]. It was also deduced that bonds formed at elevated temperatures with low ultrasonic energy could exhibit high bonding strength. This was attributed to the ease of the formation and migration of deformations at the bonding interface and the enhancement of the actual bonded area, resulting in a reduction of voids. Therefore, bonding at higher temperatures increases the lifetime of the bonded wire [ArAJ14], [OnKS00]. Increasing the bonding temperature results in bigger initial grains at the interconnection zones, as observed in Figure 7. This was deduced to reduce the residual stresses and dislocation densities and increase the resistance to crack propagation, as seen in Figure 8. In Figure 8, it is deduced that for room temperature bonded samples, the fatigue crack propagates along the bonded area and eventually shears off the wire bonds after 1500 thermal cycles ($T_{j\,min}$ = -60 °C, $T_{j\,max}$ = +150 °C). For samples bonded at 200 °C, the fatigue crack is much shorter than in 100 °C bonded samples.

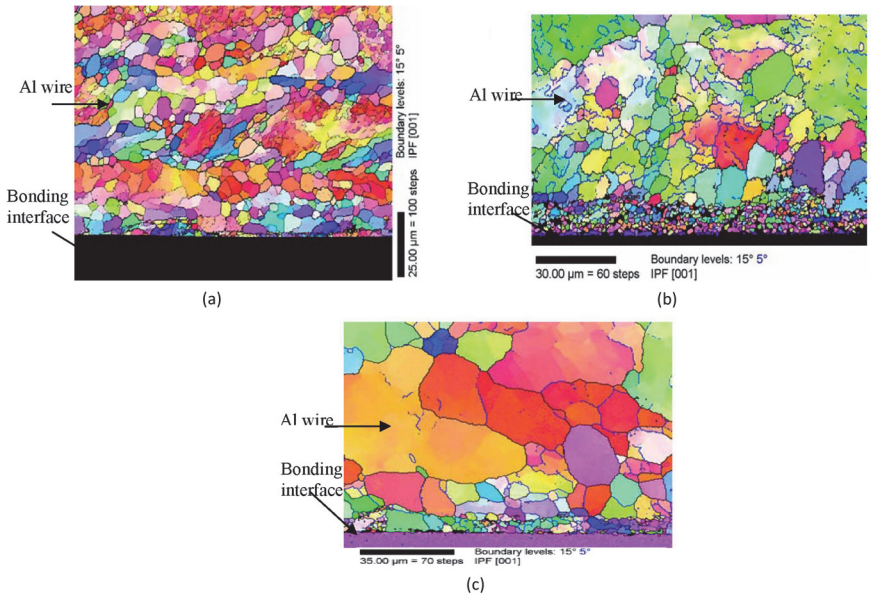

Figure 7: Electron backscattered diffraction (EBSD) analysis for heavy-gauge aluminum wire bonds, bonded at (a) 25 °C, (b) 100 °C, and (c) 200 °C [LCLH07].

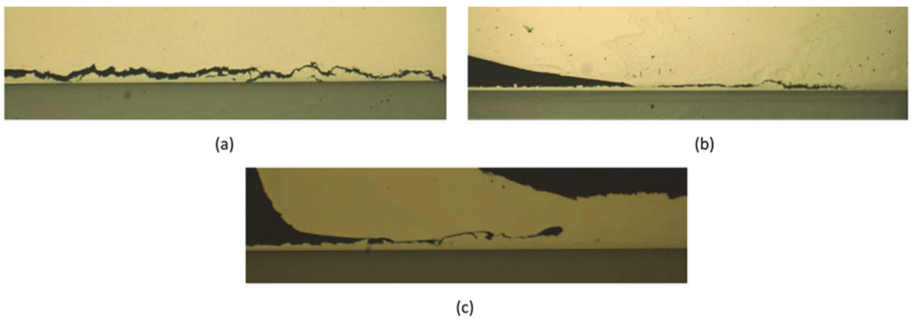

Figure 8: Fatigue crack (magnification x100) after 1500 thermal cycles for wire bonds joined at (a) 25 °C, (b) 100 °C, and (c) 200 °C respectively [LCLH07].

In conclusion, wire cabling with all its shapes and techniques is the classical metallic interconnection technology in the industry. However, it still affects the quality and mechanical properties of the generated bonding wires. As explained, cabling could be in the shape of both ball and wedge-bonds, and could be formed by thermo-compression, ultrasonically, or by using thermo-sonic procedures. Each welding shape is used for specific applications.

2.2 METALLIZATION LAYERS

The metallization layer is generally made up of aluminum or an alloy of aluminum and silicon (1%). It is a thin film, usually about a few microns in thickness. It is the interface between the chip and bonding wires. The metallization layer allows the carryover of bonding wires, uniformly redistributes the current from the chip towards the wires, and can short-circuit the current from each cell undergoing a latch-up phenomenon [PLPB11]. The metallization layer is subjected to high current densities and continuous fluctuating temperatures. It therefore constitutes a critical area of the power module assembly [BPKP16], [Sze08].

The choice of using thin films in power modules is not arbitrary. When the film thickness decreases, its strength increases [ACYL11]. It is reported that when having thinner films, smaller stress-strain hysteresis and higher flow stress result [HePD10]. Additionally, dislocations in metallization films modify their physical behavior, especially the plasticity of crystals. Under the effect of stress, a dislocation can move. This movement allows the sliding of the crystalline planes. Since thin films have more free surfaces than thick films, this enhances dislocation's escape, decreasing their concentration densities and plastic deformations, thus allowing the material's ductility [LeCG09]. This was also deduced by Heinz and others [HePD10], by which when the film thickness decreases, the plastic region decreases. Moreover, it was seen that deformations such as the formation of hillocks are less enhanced when having thinner films [Chu96].

- **Metallization layers manufacture:**

The two main manufacturing processes for metallization layers are detailed here. These processes are the physical vapor deposition (PVD) and sputtering methods.

A. Physical vapor deposition

The physical vapor deposition (PVD) method can be used to manufacture metallization thin films by vacuum deposition. PVD involves heating the material above its melting point in a vacuum chamber. Thus, the resulting evaporated atoms can propagate at a very high speed in the enclosure without colliding with other particles. They are then deposited on the silicon chip to form the metallization chip [Sze08]. Even though this evaporation process has been used for a long time, the sputtering method for manufacturing metallization chips is preferred today.

B. Sputtering

Unlike vacuum evaporation, sputtering does not require heating the material. The sputtering process relies on the ionization of a gas subjected to a strong electric field. The film's source material is attached to the cathode, while the substrate with the silicon chip is positioned near the anode. Both the cathode and the anode are set into an enclosure. When a high voltage source powers the cathode, a plasma is created in the enclosure, where the positively charged ions attract the cathode. When the positive ions collide with the cathode at the position of the source material, source material atoms are crushed as particles due to their kinetic energy. These particles eventually settle on the substrate near the anode to form the metallization.

In semiconductor power electronics, aluminum is used as a source material due to its low resistivity, cheapness, lightness, and good adhesion to silicon dioxide. Aluminum-silicon alloy can be used to limit the interaction between the aluminum particles present in the metallization layer and the silicon in the chip [Sze08]. In sputtering processes, the kinetic energy of aluminum particles is much greater than that in vacuum evaporation processes, resulting in very good adhesion of the

metallization layer. In addition, sputtering provides better coverage and adaptation of the object to be metalized; that is why it is favored over the vacuum evaporation process [Sze08].

As for wires, copper metallization layers have also been considered in recent years. Copper has better electrical conductivity than aluminum. This would make it possible to increase the current densities in the metallization. However, the use of copper is much more complex. Copper has higher diffusivity than aluminum; this can cause diffusion problems upon cycling. Copper is a very effective poison for silicon; therefore, silicon devices must be protected from diffusing copper atoms. If the protection is not applied properly, serious problems result [Lloy98].

The metallization chip has a checkerboard-shaped structure. The checkerboard pattern is obtained due to the presence of a polysilicon passivation layer of silicon dioxide (SiO_2) on the silicon chip [RGTN18]. Figure 9 shows the shape of a metallization chip.

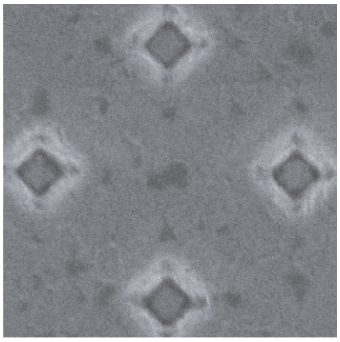

Figure 9: Scanning Electron Microscopy (SEM) images of a healthy IGBT metallization [PØGP15].

To sum up, the metallic interconnection zone constituents were presented, with particular attention to the different interconnection manufacturing technologies. As observed, wire cabling is the most widely used method today due to its ease of implementation and low cost. Metallization sputtering is the most commonly used method to manufacture metallization chips. The main degradations within upper metallic interconnections in the power module are presented in the next part. These degradations are the wire fracture and lifting-off, in addition to grains reconstructions within metallization layers and wires.

3 THE MICROSTRUCTURE OF TOPSIDE METALLIC COMPONENTS

When talking about the microstructure of topside metallic components, two main keywords should be first introduced, the grain and the grain boundary. Grains and grain boundaries have several shapes and characteristics that affect the materials' properties.

3.1 GRAINS PROPERTIES

The grain is a region where atoms align. It is the monomer of polycrystalline structures. Polycrystalline structures such as metallization films and wires consist of various numbers of grains attached to each other, where each grain has its own characteristics. The grain structure has enormous effects on the physical properties of the material. For example, as the grain size decreases, the material's toughness, hardness, and yield strength increase [Wata11]. The main reason behind such augmentations in more refined grains is that they possess more grain boundary areas. According to the Hall-Petch relationship, these areas impede the motion of dislocations [Hall51], [Petc53], [RaRa88]. The Hall-Petch relation has been widely used in face-centered cubic (FCC) lattice metals such as aluminum. This relationship relates the yield strength (σ_{YS}) to the grain size (d), by which the yield strength increases as the grain size decreases and vice versa (from the nano to the microscale). This equation is presented below, where σ_0 is the friction stress (constant), and k_{HP} is the Hall-Petch constant.

$$\sigma_{YS} = \sigma_0 + k_{HP}\, d^{-0.5} \quad (2)$$

In parallel, it was mentioned in reference [DSWN19] that if a material acquires larger grain sizes, it will be more able to have dislocation pile-ups. This drives dislocations to move from one grain to another, as illustrated in Figure 10. Therefore, less force is needed to move a dislocation from a large grain than from a smaller grain. This results in higher yield strength in smaller grains.

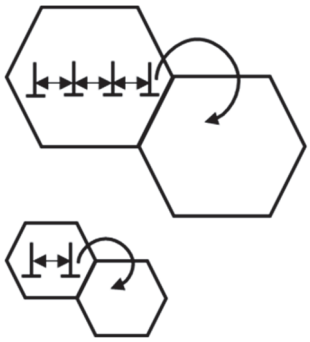

Figure 10: A schematic representation reflecting the effect of dislocation densities on the strength of the grain in the case of small and big grains.

Aluminum atoms acquire FCC crystal lattice type, one of the metal's most famous crystal lattices. The shape of this FCC crystal is shown in Figure 11, where circles represent the positions of atoms. Each lattice of an FCC crystal contains four atoms. The lattice parameter representing the length of the edge of this crystal in aluminum is 4.046 Angstrom. The main crystal orientations are (111), (100), and (101). These orientations can be observed in Figure 12. The highest atomic packing density (APD) among these three orientations in FCC metals is for the (111) orientation, and the lowest is for the (101) orientation. The planar density values representing the number of atoms per μm^2 for the (111), (100), and (101) orientations are listed in equations (3), (4), and (5).

$$Planar\ density_{(111)} = \frac{2\ atoms}{\frac{\sqrt{3}}{2}(4.046 * 10^{-4}\ \mu m)^2} = 1.411 * 10^7\ \ atoms/\mu m^2 \quad (3)$$

$$Planar\ density_{(100)} = \frac{2\ atoms}{(4.046 * 10^{-4}\ \mu m)^2} = 1.222 * 10^7\ atoms/\mu m^2 \quad (4)$$

$$Planar\ density_{(101)} = \frac{2\ atoms}{\sqrt{2}(4.046 * 10^{-4}\ \mu m)^2} = 8.639 * 10^6\ atoms/\mu m^2 \quad (5)$$

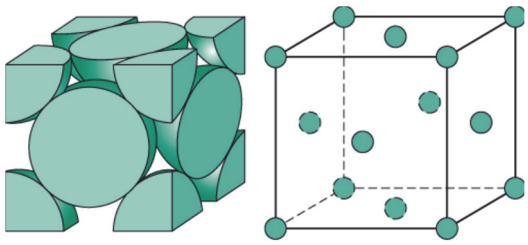

Figure 11: FCC crystal lattice representation.

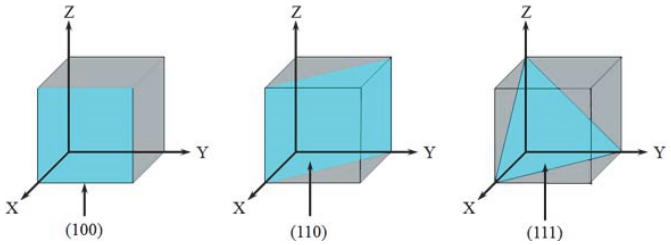

Figure 12: (100), (110), and (111) crystal orientations.

3.2 GRAIN BOUNDARIES CHARACTERISTICS AND TYPES

Grain boundaries separate the grains composing bonding wires and metallization layers. The grain boundary is a planar defect caused by the mismatch of atoms at the boundary separating neighbor grains. In other words, the grain boundary is the position where atoms' repeating patterns stop, and atoms' direction changes. Grain boundaries act as barriers, increasing the strength of the structure. Thus structures with smaller grains have more boundaries, therefore higher strength. This is attributed to two main reasons. The first reason is due to the fact that neighbor grains possess different orientations, then dislocations passing through grains must change their motion direction. This makes their migration more complex, providing an obstruction for crack propagation. The second reason is that the atomic disorder within a grain boundary region will cause a discontinuity of slip planes between neighbor grains [RaRa88]. Figure 13 clarifies the role of boundaries against dislocations. On the contrary, grain boundaries are thought to be stress concentration positions in further cycling because of the formation of dislocations pile-ups.

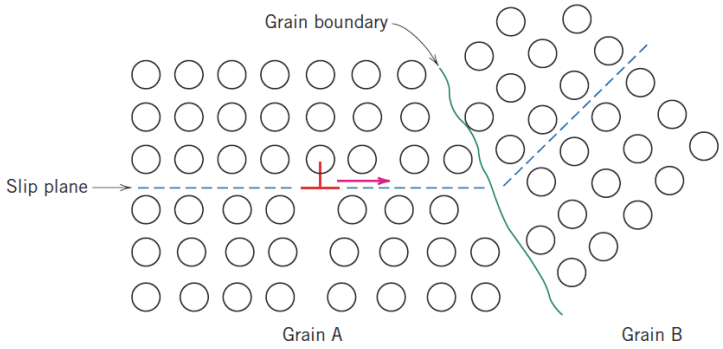

Figure 13: An image showing the role of grain boundaries as barriers to dislocations' motion.

Upon grain boundary migrations, grain boundaries move in a manner that reduces the area they occupy; this reduces the free energy of the system. The mobility of grain boundaries is caused by changes in grains' orientation and inclination, in addition to the grain boundaries' curvature. The curvature leads to the presence of convex and concave grain shapes, as seen in Figure 14. Lower numbers of neighbor atoms are present in convex grains. Consequently, the potential energy of atoms there is slightly greater. This energy extra potential is noted by ΔE, where Q is the activation energy for the atom's motion.

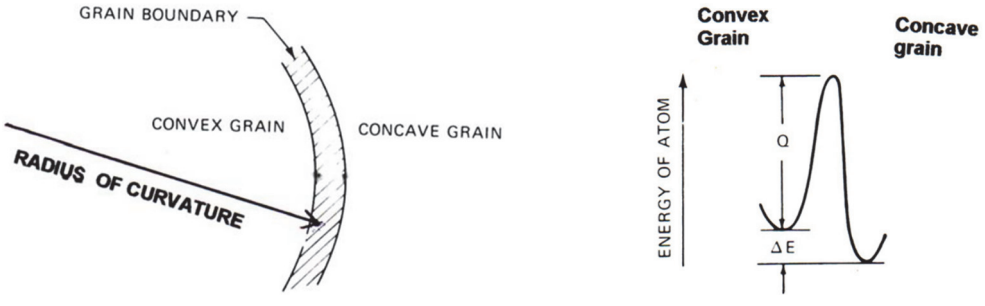

Figure 14. Scheme showing grain boundary curvatures [MoOl76].

Grain boundaries have different properties depending on the shape and nature of disorientation angles between intersecting grains, and the crystallographic orientation of each grain. Several types of grain boundaries exist with different classifications. The classifications are mainly based on the disorientation angle between grains, their rotation axis, and lattice type. These classifications are explained as follows.

- **Classifications based on the disorientation angle (Δθ)**

This classification is the most used. Grains are classified into low and high angle boundaries according to the disorientation angle between them. When the disorientation angle (Δθ) is lower than 15°, it is called a low angle boundary (LAB). However, when it is greater than 15°, it is called a high angle boundary (HAB). The physical reason for the value of 15° lies in the fact that dislocations constituting LABs are discernible, by which they become indiscernible and very close to each other in the case of HABs. Figure 15 presents both boundary types.

HABs differ from LABs in terms of physical and mechanical properties. When HABs are present, less dislocation traversal results, retarding dislocations' movement and causing their accumulation. When dislocations are accumulated, pile-ups are formed. This increases the stress concentration at the boundaries. Upon reaching a specific critical stress concentration value, cracks initiate [SaMS11]. However, since HABs induce more grain boundary sliding, the material's ductility increases; thus, the crack propagation through them is retarded [DSWN19]. On the other hand, dislocations can easily penetrate LABs; then, stress accumulation does not occur. However, if cracks are already formed, and since LABs have poor grain boundary sliding, cracks can easily penetrate them. That is maybe why cracks are easier to propagate through LABs than HABs [BGHS15].

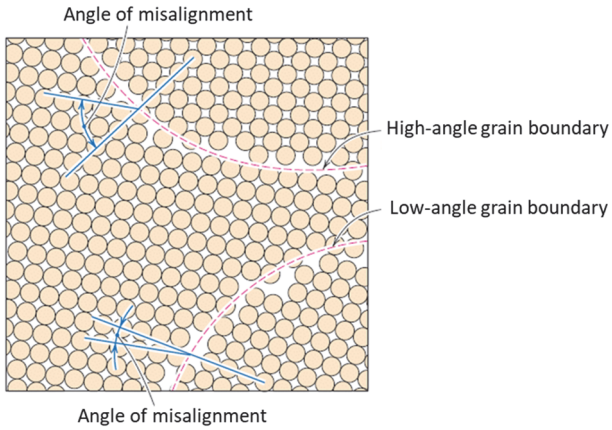

Figure 15: An image showing the difference between low and high angle boundaries (HABs and LABs).

- **Classifications based on the rotation axis**

Upon classifying boundaries according to their rotation axis, two types exist: the tilt and twist boundaries [Zöll16]. When the rotation axis is perpendicular to the normal axis, it is a tilt boundary. However, when the rotation axis is parallel to the normal axis, it is a twist boundary. Figure 16 shows the difference between these two types of boundaries.

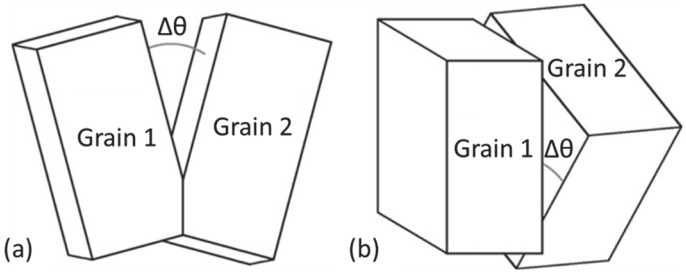

Figure 16: Schemes showing the (a) tilt grain boundary and (b) twist grain boundary [Zöll16].

- **Classifications based on the lattice type for high angle boundaries**

HABs are normally found to be independent of the value of the disorientation angle. One of the main reasons is that when the latter is high, individual dislocations are no more distinguishable, by which they overlap with each other. This occurs for all HABs. Thus, a new classification based on the coincidence site lattice (CSL) has been proposed. CSL theory classifies discrete grain boundary disorientation angles using the factor (Σ), representing the reciprocal density of coinciding sites. The CSL may also be defined as the smallest lattice among the lattices of two intersecting crystals. Figure 17 schematizes the CSL representation [Li17].

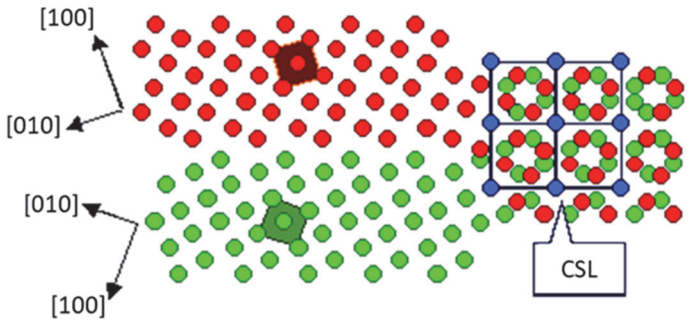

Figure 17: A representation scheme for the coincident site lattice (CSL) [Li17].

A boundary with a value of Σ more than 29 is called a random boundary, whereas it is considered a special boundary when its value is less than 29. The special boundary is a boundary between two crystals that lies close to a crystallographic transformation. Special boundaries are characterized by being more ordered structures, having lower energy and diffusivity than general boundaries, and being able to sustain higher stresses with higher rigidity [Wata11], [WyGr86]. Their presence increases the work hardening rate, where these boundary types act as obstacles for gliding dislocations, providing better ductility and resistance to crack formation [DSWN19].

All the boundary type classifications are summarized in Table 1, by which the main parameters used for classifying them are listed.

Table 1: Types of grain boundaries according to the considered classification criterion.

Classification based on the disorientation angle (Δθ)	Low angle: $\Delta\theta < 15°$
	High angle: $\Delta\theta > 15°$
Classification based on the rotation axis	Tilt: The rotation axis is perpendicular to the normal axis
	Twist: The rotation axis is parallel to the normal axis
	Mixed
Classification based on the lattice for $\Delta\theta > 15°$	Special-CSL: $\Sigma < 29$
	Random-CSL: $\Sigma > 29$

- **Other classifications**

Twinning boundaries are types of boundaries where crystals on one side are located in mirror images with respect to the others; thus, they have very low disorientation angles [CaRe18]. Twinning boundaries are either nucleated due to dissimilar grain boundary mobilities between neighbor grains or a mobile grain boundary intersection with a pre-existing twin boundary [WyGr86]. Figure 18 schematizes twin boundaries.

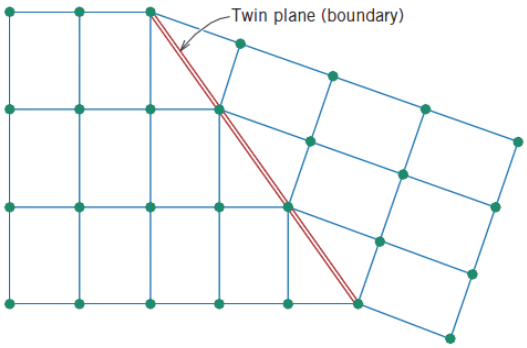

Figure 18: Schematic representation showing a twin boundary with the positions of atoms (coloured circles) [CaRe18].

4 SHAPES OF MICROSTRUCTURAL DEFORMATIONS IN TOPSIDE METALLIC COMPONENTS

This section shows the main forms of deformations taking place in the microscale. These deformations result from both the wire welding process and power cycling. Consequently, they will play a prominent role in the degradation processes in the topside components of power modules.

The dominance of plastic deformation processes when topside metallic parts of power modules are aged can be verified by looking at the aluminum deformation map constructed by Frost and Ashby [FrAs73], shown in Figure 19. When observing the deformation map presented in Figure 19 of aluminum (grains' size ≈ 10 µm) within the temperature range resulting from power cycling ($T_{j\ min}$ ≈ 25 °C to $T_{j\ max}$ ≈ 180 °C), plastic deformations are deduced to be the dominant deformation processes over creep deformations which have very low rates. Thronton [Thor77] also reported that plasticity dominates other deformation processes when the temperature is lower than the melting point temperature, such as $T/T_{melting} < 0.3$.

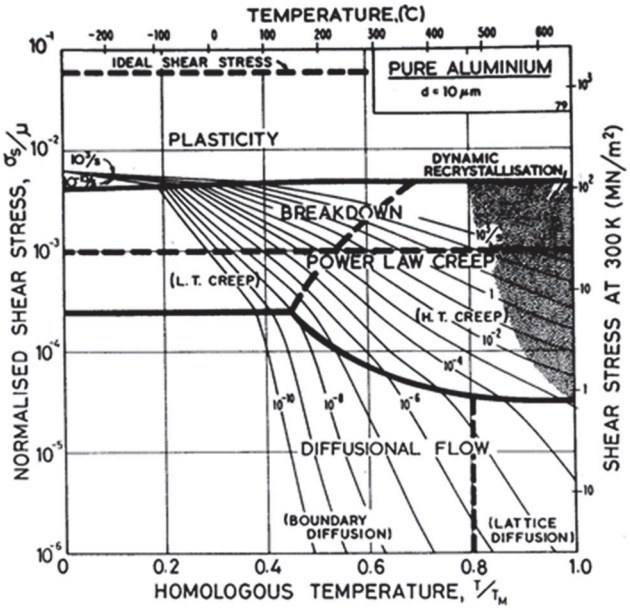

Figure 19: Deformations map of pure aluminum for a grain size of about 10 µm [FrAs73].

Generally, plastic deformations in a single crystal are divided into two types: slipping and twinning. Under the action of shear stress, slipping is the sliding of a crystal part on a specific plane along a particular direction relative to another part. It is caused by a specific dislocations' motion, and is favored in particular crystal directions and planes. On the other hand, twinning occurs when the crystal cannot slip. Twinning is

believed to occur through the glide of partial dislocations having the same magnitudes and directions on successive planes. Under the action of shear stress, some parallel crystal planes in a local area of the crystal produce uniform shearing at a distance relative to each other along a particular direction [YaPa19]. Figure 20 clarifies both deformation processes.

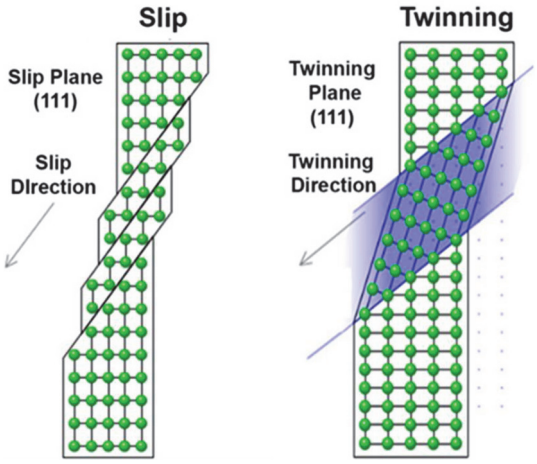

Figure 20: Slipping and twinning deformations in an FCC crystal [YaPa19].

For polycrystalline materials, the same slipping and twinning processes occur; however, not all the crystals are slipped or twinned simultaneously when they are plastically deformed; they are slipped or twinned in batches. In the case of slipping, and due to geometrical constraints, a single slip system in one grain causes more than one activated slip system in the neighboring grains, leading to their rotation. So, slipping occurs first for certain grain crystals, followed by slipping and rotation of their neighbors [RaRa88], [YaPa19].

Based on these general microstructural changes that may face topside metallic components of power modules, the next section presents the main changes that occur upon welding the wire.

5 TOPSIDE METALLIC MICROSTRUCTURAL CHANGES UPON WELDING THE WIRES

Due to the wire welding process, initial plastic deformations and dislocations exist at the metallic contact zones before their aging, as mentioned before. This is due to the high amount of stress caused by the bonding forces when welding the wire to the metallization layer. Such forces are responsible for the decrease in the thickness of the metallic contact areas. High plastic strains caused by the welding forces lead to dislocations' formation and the generation of sub-grains inside initial grains [Ruff17]. Such grain fragmentation does not occur in wire and metallization regions far from the metallic contact region. This is because they are subjected to fewer plastic deformations. An Al-Al metallic interconnection interface is thought to exist at the contact between the wire and the metallization layer, preventing inter-diffusion between the metallization and wire atoms. However, initial imperfections in the shape of small cavities and aluminum oxide residues exist at this interface [Ruff17]. These oxide residues and debris on the metallization surface may hinder metal-to-metal contact. Pores are thought to originate from these regions of partial bonding and coalesce to form larger regions of discontinuity during cycling. Upon bonding the wire, texture development is observed at the metallic contact. Texture change starts when pressure is exerted on the initially oriented grains by activating their preferred dislocations' slip systems and directions. This is assumed to be a combined result of i) enhanced growth of preferred grain orientations to minimize the energy and ii) plastic shear deformations induced by the ultrasonic power [BGHS15].

The bonding temperature affects the initial microstructure, as mentioned previously. It was reported that increasing the bonding temperature results in bigger initial grains at the interconnection zones. The

presence of initial coarser grains along the bonding interface reduces the amount of residual stresses and dislocation densities, and gives rise to much greater resistance to crack propagation. Consequently, it may be concluded that high-temperature bonding can achieve strong and reliable bonds [LCLH07]. Additionally, bonding at higher temperatures will enhance the actual bonding area and decrease the voids and dislocation densities, resulting in strain-free grains. These may be the reasons behind better metallic interconnection characteristics when bonding at high temperatures [OnKS00].

After showing what happens to topside metallic components upon welding the wire, it is time to present the main degradation processes that occur upon cycling.

6 TOPSIDE METALLIC DEGRADATION MECHANISMS AND PROCESSES UPON CYCLING

Cycling tests with actual conditions require long periods. For this purpose, accelerated cycling tests are operated. Accelerated power and thermal cycling tests with various conditions can be performed for power devices to estimate their lifetimes by accelerating their failure modes [KoKS15]. Temperature variations come from power components' self-heating (active cycling) and environmental temperature variations (passive cycling). For example, in power cycling tests, the loading current and both heating and cooling periods are used to control the test conditions [LSSD10]. In switching mode power cycling, a power module is actively heated during the conduction phase by defining the heating period caused by both Joule's effect during the on-state conduction and switching losses. The module is cooled by removing the DC bias during the off-state conduction phase. Thus, power modules are subjected to continuous temperature cycles. More parameters can be used for controlling the cycling tests (current and voltage levels, duty cycles, switching frequency) [MePP07], [MRCL06].

In cycling tests, the topside metallic interconnections are among the most stressed parts. Then, accelerated cycling tests are applied to explore the failure mechanisms at the metallic contacts in a short time. In the following, the shapes of degradations occurring at the interconnection positions are detailed, with particular attention to the crack initiation process forced by the wire welding. This is followed by explaining the crack propagation evolution upon cycling, which is responsible for wires' fracture and lifting-off processes and grains reconstructions. These are the most critical degradation processes occurring in topside metallic parts [Dura15].

6.1 CRACKS INITIATION CAUSED BY WELDING WIRES

Since it is reported that dislocations' accumulation is the leading cause of cracks' initiation inside grains when their density increases, then it is so essential to study their mode of formation and behavior. For example, dislocations' activities may be an important cause of several microstructural changes, especially at the early cycling stages. These changes have crucial impacts on the cracking process. At advanced cycling stages, dislocations' activities decrease because grain boundaries become straighter and closely aligned [Mour12]. In addition, most of the dislocations are adsorbed by grain boundaries upon cycling, increasing the structure's strength and ductility. Figure 21 shows how grain boundaries adsorb dislocations upon cycling.

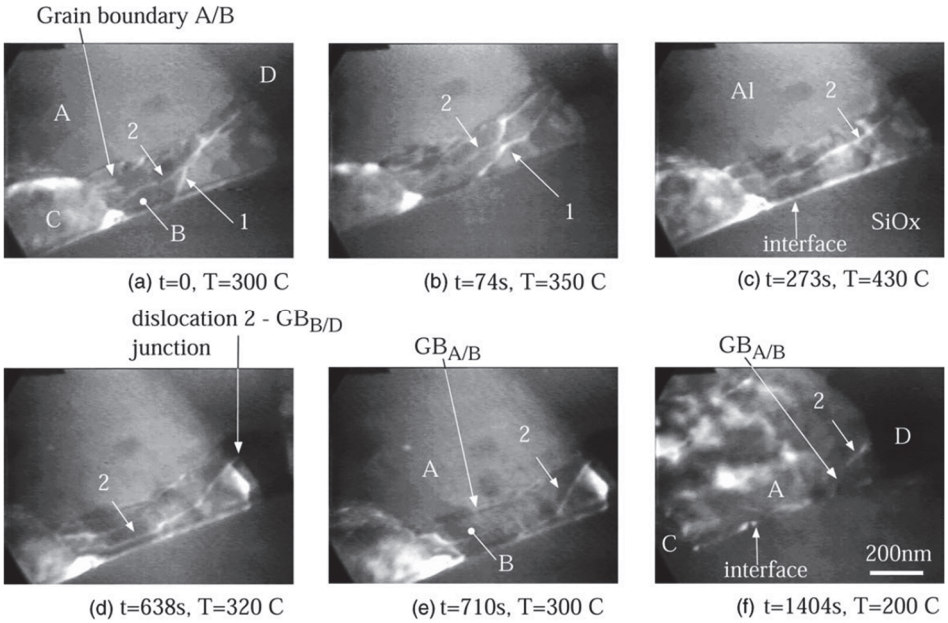

Figure 21: In situ experiment carried out on a 1 µm aluminum layer passivated with 0.5 µm SiOx: (a)–(c) Dislocations 1 and 2 have been emitted from the grain boundary A/B and aim to the Al/SiOx interface during a heating phase. A perpendicular dislocation with residual contrast pins the two parallel dislocations (b) before dislocation 1 reaches the interface (c) and disappears; (d)–(f) Dislocation 2 remains oriented towards the interface even after the temperature gradient is reversed. Dislocation 2 is seen in (f) just before it reaches the interface and disappears. At this point, the entire grain boundary vanishes at the interface [LHGS02].

In fact, during the welding process, grains near the contact are subjected to large plastic deformations that lead to the formation, movement, and multiplication of dislocations. Upon cycling, some new dislocations are generated caused by plastic deformations. Another less common cause for dislocations' creation, different from plastic deformations, is the effect of dislocations' de-pinning. In the case of de-pinning, pre-existing dislocations within grains move along the slip planes until they encounter an obstacle that pins the ends of their dislocation lines. Dislocations attempt to continue moving, forced by the applied stresses. This drives the bending of dislocations in the center. Dislocations can bend as much as they loop around the crystal and cause the pinning process. When looping dislocations touch themselves, new dislocations are created. These new dislocations are free to move away, whereas the pinned dislocations remain trapped. This process of forming new dislocations is repeated several times. The figure below clarifies this phenomenon known as the Frank-Read dislocation's source [Mour12].

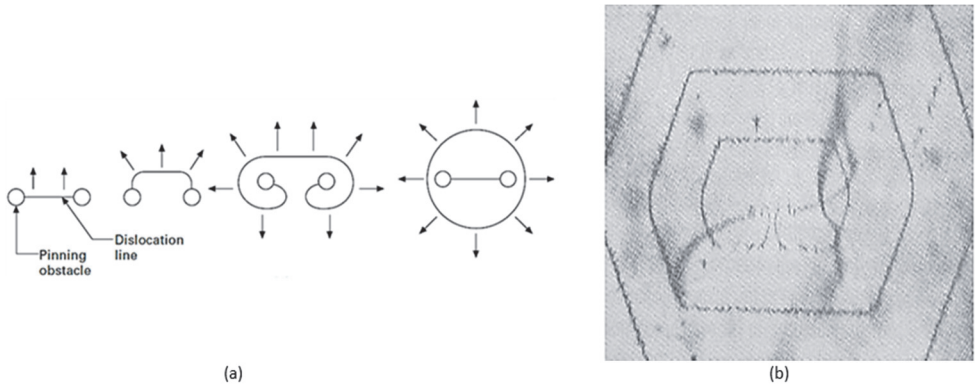

Figure 22: (a) Schematic representation of dislocations formation by the Frank–Read source. (b) High-magnification photograph showing the formation of dislocations [Mour12].

Upon cycling, the number of dislocations inside grains increases, and dislocations pile-ups are formed. This is responsible for the increase in the stress concentration in specific zones. The resulting stress

concentration is relieved by the appearance of extrusions at the grain boundaries and afterward through the nucleation of cracks.

Dislocations' activities are also causes of crystal rearrangements. The driving force of crystals to rearrange themselves under tensile and compressive states is to decrease their total energy. One shape of atoms reordering is the diffusion process. However, diffusion is not so important in the case of power cycling, since the maximum temperature reached is shallow compared to the melting point of the heated material (Aluminum). Nevertheless, diffusion may sometimes exist in lower temperatures, affected by the granular distribution within the microstructure. It may occur due to the presence of point defects and dislocations in the shape of vacancies within crystal lattices.

More important shapes of crystal rearrangements are caused by the high disintegration of dislocations in the heating phases (when the current is switched on upon cycling) and their low disintegration in the cooling phases (when the current is switched off upon cycling). Scientists believe that during the heating phase, most of the dislocations disintegrate. This induces crystal rotations, resulting in textures. Dislocations' behavior is reversed upon cooling, where they are stored. Therefore, the change in orientations during the cooling phase is not pronounced as during heating [HePD10]. Generally, the change of orientations leads to an increase in the surface roughness and the generation of voids, which will later affect the crack evolution process [BWKP18].

6.2 MICROSTRUCTURAL RECONSTRUCTIONS INSIDE METALLIZATION LAYERS AND BONDING WIRES

As mentioned previously, microstructural reconstructions inside wires and metallization chips are among power modules' most potential degradation mechanisms. It is important to mention that due to the wire welding process, initial microstructural reconstructions exist. Upon cycling, microstructural reconstructions are caused by thermomechanical fatigue, due to the difference in CTE values between the aluminum composing wires and metallization layers from one side, and silicon beneath the metallic components from the other side.

Thermomechanical fatigue is enhanced as the temperature swing increases [RMTW99]. Moreover, it is affected by the number of exposed cycles. It is also enhanced in the cases of extreme operating conditions [HSPK91], where wires bend and twist. Other aspects affecting thermomechanical fatigue are related to the material properties, such as the film's and wire's thicknesses. The change in thickness is accompanied by changes in grains' size, orientation, toughness, and resistance to deformations. Materials' purity is also a factor affecting the thermomechanical fatigue of materials.

Upon cycling, significant thermomechanical strains are generated during compression when the power is in the on-state (heating) and during tension when the power is in the off-state (cooling), as seen in Figure 23. A uniform increase in compressive stresses is clearly observed in the first heating steps. Upon cooling, relaxation of stresses occurs through grain boundary sliding or dislocations glide, depending on temperature and stress conditions, where compressive stresses turn into tensile. For example, upon having high junction temperatures, reconstructions in the shapes of grain boundary movements and dislocations glide occur more rapidly compared to when having low junction temperatures. In addition, microstructural reconstructions are stronger at the module's central chips than those at the periphery since the temperature is maximal there. The continuous change from compressive to tensile and vice versa leads to an irreversible alteration of the structure of aluminum films and bonding wires. Thus, several changes in the microstructural topography occur [LHGS02], [MLLD14].

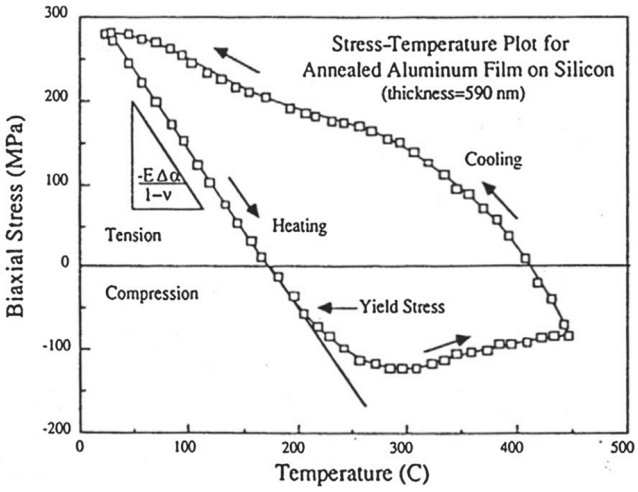

Figure 23: Evolution of the stress as a function of temperature during the heating and cooling phases [MLLD14].

6.2.1 Reconstructions inside metallization layers

Interpreting the changes in the metallization's surface microstructure and topology upon cycling is carried out using Transmission Electron Microscopy (TEM), X-Ray Crystallography (XRD), Focused Ion Beam (FIB), and Scanning Electron Microscopy (SEM) techniques.

Dislocations' accumulation and tangling observed in the TEM images, as shown in Figure 24, reflect the work hardening effect and the increase in residual stresses [KUSM98]. The effect of dislocations on increasing the residual stresses most probably exists in the early cycling stages. On the contrary, since thin films have large surface areas that can act as sinks for dislocations, work hardening is unexpected inside metallization layers. Maybe, since the surface of thin aluminum films is covered by fine oxide layers, such layers could act as barriers to dislocations' annihilation, resulting in the observed work hardening.

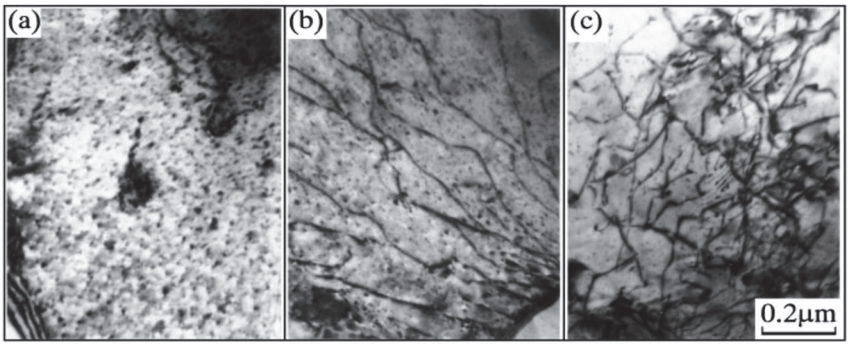

Figure 24: TEM images of thermally cycled films, showing the accumulation of dislocations: (a) before cycling, (b) after the second cycle, and (c) after the twelfth cycle [KUSM98].

From the XRD technique, the dislocation density inside each grain can be calculated [AMST15], [FeRR18]. As mentioned previously, this factor is linked to grains' reconstruction processes [AwKh19], [BGHS15] and the crack initiation process [Mour12], [SaMS11]. The equations relating the grain size to the density of dislocations are given below in equations (6) and (7). To obtain the density of dislocations' value, a graph is primarily plotted, as shown in Figure 25, using equation (6) to calculate the micro-strain value. When micro-strain is calculated, the dislocation density can be deduced using equation (7).

$$\beta_{hkl} \cos\theta_{hkl} = \frac{K_s \lambda}{D} + 4\epsilon \sin\theta_{hkl} \quad (6)$$

$$\rho = 2\sqrt{3(\frac{\epsilon}{Db})} \quad (7)$$

Where β_{hkl} is the peak broadening, d is the crystallite size (grain size), K_s is the shape factor (0.9), λ is the wavelength, ε is the micro-strain, θ_{hkl} is the peak position, ρ is the dislocation density, and b is the burgers vector.

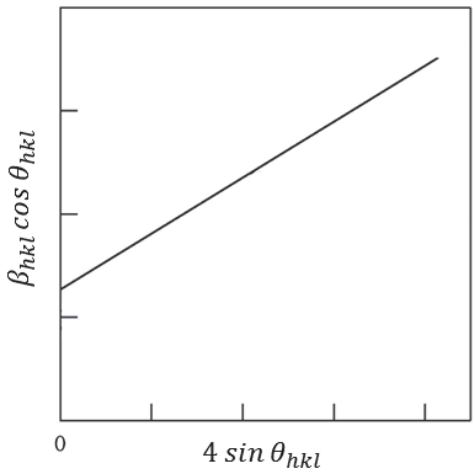

Figure 25: The plot of $\beta_{hkl} \cos \theta_{hkl}$ vs. 4 sin θ_{hkl} used in order to calculate the micro-strain and then obtain the dislocation density parameter [FeRR18].

SEM provides topographic contrasts collected to form a grey-scaled image of the specimen surface. From SEM images, it can also be deduced that the degradation inside the metallization is not uniform. Indeed, reconstructions of the metallization microstructure are more advanced in the areas exposed to the highest temperatures, at the module's central chips in the contact vicinity with the bonded wires [CiMa96], [PLPB11], [YAQZ18]. Reconstructions start with extrusions at grain boundaries, which become broader and denser upon cycling. The rate of extrusions' formation decreases when cycling proceeds. Extrusions' accumulation causes the generation of micro-cracks which may develop into macro-cracks in further cycling. Moreover, before cycling, aluminum grains form the metallization layer's thickness (a few microns). When cycling initiates, grains become numerous and smaller, indicating grains reconstruction processes. After several cycles, the size of grains starts increasing. It was reported that the grain size increases precisely during heating phases [GeKK92]. Figure 26 shows SEM images of a naked metallization layer before and after power cycling.

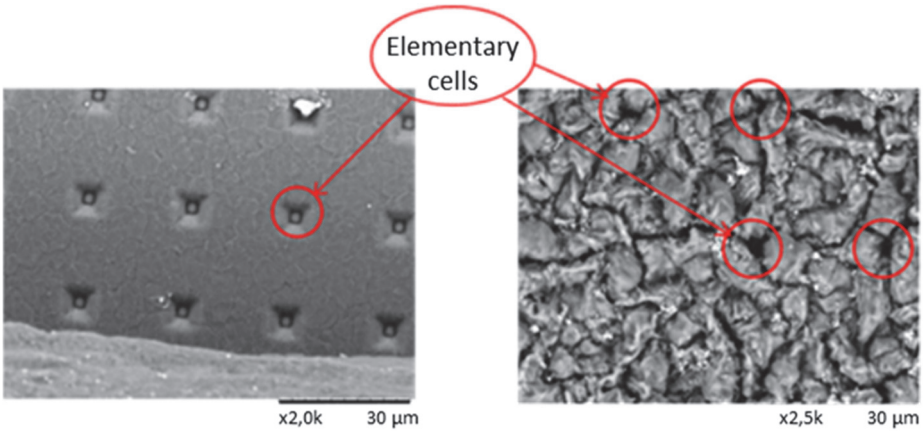

Figure 26: SEM images showing the topside metallization: before and after aging [HaKI18].

When looking at the SEM images for a non-degraded sample, the metallization shows a visible array of elementary chip cells. Once degraded, the metallization surface has a messy appearance associated with cavities. Due to this roughness increase, it is no longer possible to distinguish the cells of the chip. Roughening

greatly affects the chemical stability of the material. When roughening is weak, a greater ability to decrease the surface area results. Thus, the material's stability will be higher. At repeated cycling, surface roughening becomes so high. This reduces the material's ability to rearrange into a lower energy structure; thus, its stability decreases [Sant69].

SEM analysis can also be used to interpret hillocks' activities that may result from specific dislocation movements. Hillocks' formation is affected by the film thickness. Fewer hillocks result as the film thickness is smaller [KaHo97]. In the case of hillocks' formation, aluminum grains are initially extruded to form micro-hillocks at the metallization layer surface. Upon cycling, the longitudinal growth rate of micro-hillocks is higher than their lateral growth rate. This difference in growth rates leads to an uneven surface morphology of the metallization layer. Figure 27 presents SEM images showing the hillocks' formation for the cases of (a) high and (b) low thermal cycling processes. It was deduced that the increase in surface roughness accompanies the rise in the number of hillocks formed. In addition, more hillocks are formed in the case of a low thermal cycle.

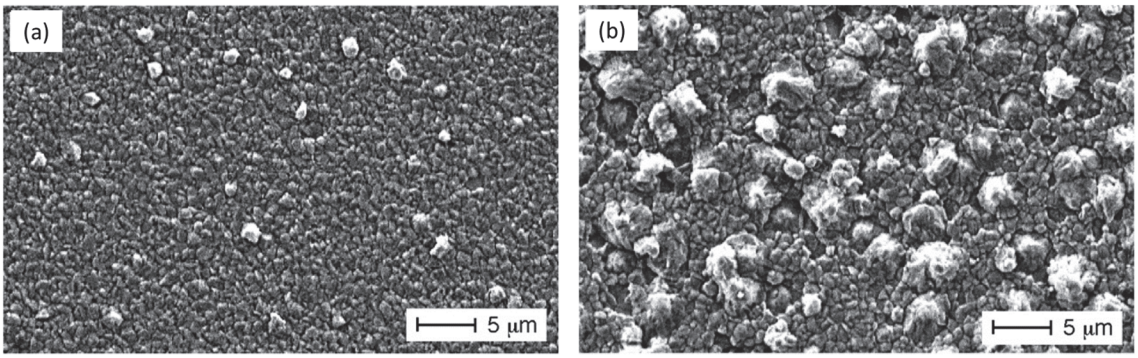

Figure 27: SEM images showing the hillocks formation (a) for a high thermal cycle between 30 and 220 °C after 20,000 cycles with a 12 s interval (the holding time was 2 s), and (b) for a low thermal cycle between 30 and 220 °C after 2000 cycles with a 30 s interval (the holding time was 20 s) [RiSa12].

Micro-section analysis can be used to interpret cracks [BPKP16], [MLLD14]. Cracks may nucleate in severe conditions, due to the opening of grain boundaries and sub-grain boundaries when the power module is subjected to intensive tensile forces during the cooling phase (power-off). Experiments clearly show that metals' surface roughness increases because of the creation of voids and cracks [KPWD11]. Its increase can be considered a driving force for more cracks' formation at advanced cycling stages [RBDL18]. This directly causes changes in the electrical resistance of the degraded material. Cracks reduce the effective contact area between the grains, increasing the on-state metallization resistance [CiMa96]. Metallization resistance increases when the current is no longer perfectly distributed because the topside components of power modules are degraded. This causes the failure of power devices [MLLD14], [PØGP15].

Upon analyzing the microstructural changes and their mechanisms in metallization layers, distinguishing between naked sites and sites directly in contact with the wire must also be considered. These different positions greatly differ in terms of properties and deformations they undergo. Grains in contact with the bonding wire have smaller sizes due to the high initial plastic deformations resulting from the bonding process. In addition, grains in contact with the wire are more constrained upon cycling due to the higher temperature and stress exposure. Therefore, degradation processes are more favored at interconnection sites. After several interpretations, a microstructural degradation metallization model was constructed based on Gao's [GZNT99] and Martineau's [MLLD14] interpretations, as presented in Figure 28.

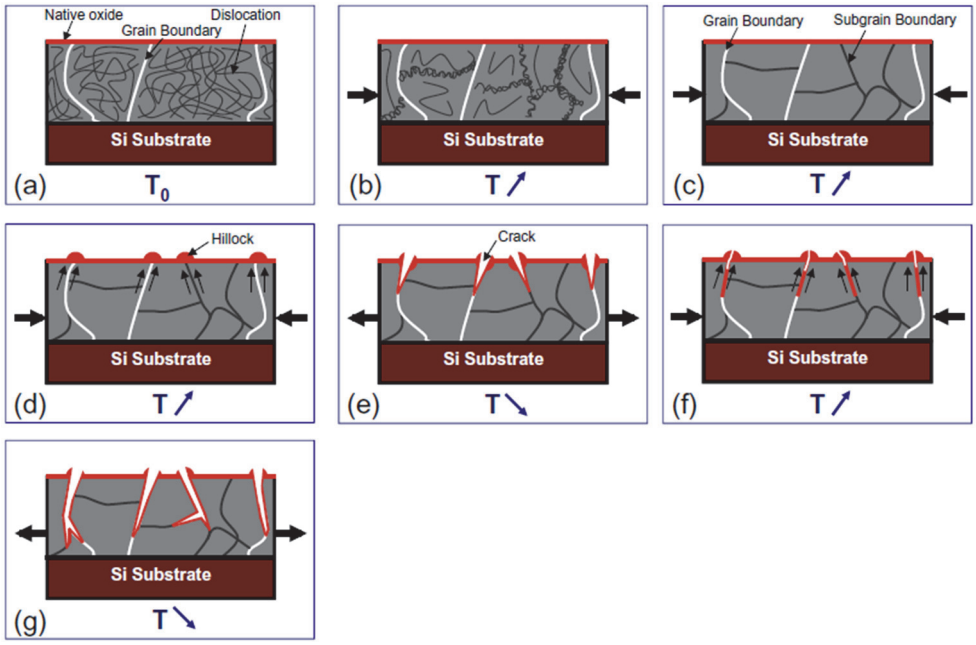

Figure 28: The metallization's degradation model proposed by Martineau [MLLD14], based on the original model of Gao [GZNT99].

As known, deformations inside the metallization layer are constrained by the presence of silicon. During the first cycles, dislocations in large aluminum grains rearrange themselves into cells and sub-grains. Remaining mobile dislocations are absorbed by oxide interfaces and free surfaces such as grain boundaries. When cycling advances and during the heating phase, aluminum atoms get compressed, moving toward free surfaces along grain boundaries, the most rapid paths for diffusion. If the stress is large enough or lasts long enough, atoms can go through the oxide barrier and oxidize when exposed to the atmosphere. Atoms' accumulation creates small-oxidized hillocks. The stress turns tensile during the cooling phase, where boundary grooves and small cracks are formed, and they self-passivate through the oxidized surface. Afterward, the formed cracks and grooves cannot bond again during later compression states due to their oxidation. Over repeated cycles, grooves become deeper cracks. However, the formation of grooves and cracks is less common when the maximum exposed temperature is not so high, especially at naked sites far from the bonding wire.

- **Observations about reconstructions inside naked metallization sites:**

  Aluminum grains away from the bonding wire are not subjected to heavy plastic deformations that could justify the device's failure. This justifies the non-changing texture in the naked metallization sites. However, remarkable changes can be observed in the grains' orientation and disorientation angles, as seen in Figure 29 [BWKP18].

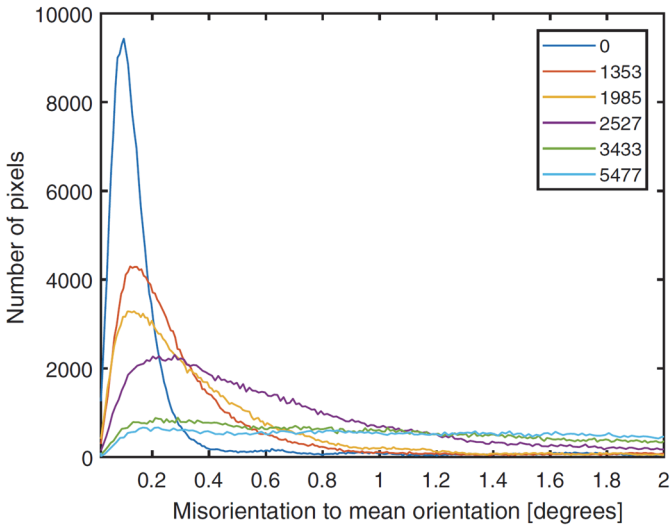

Figure 29: Changes in grains' disorientation angles with increasing the number of cycles. The number of cycles is indicated in the legend [BWKP18].

- **Observations about reconstructions for metallization grains under the connecting wire:**

Grain growth is one of the most crucial microstructural phenomena for metallization grains under the bonding wire. The grain growth process after recrystallization refers to the increase in the average grain size and the development of textured areas [BGHS15]. It occurs because when grains are bigger, they will have lower free energy than smaller ones [Care95], [Thom85]. Smaller crystals having higher energies tend to become a part of larger crystals. Therefore, the driving force of grain growth is energy minimization [Thom00]. Another reported driving force for grain growth is caused by the reduction in the grain boundary curvature. The motion of growing grain boundaries leads to the shrinkage of small grains. At this stage, larger grains will grow at the expense of small ones; therefore, the average size of grains increases [BWKP18].

Grain growth has two types, normal and abnormal. Normal growth results from the migration of many different grain boundaries within a poly-crystal. Abnormal growth is described as a growth process through which some energetically favorable grains overgrow at the expense of fine grains growing at low rates, resulting in bimodal grain size distribution. Abnormal growth is caused by impurities and high anisotropies in surface and grain boundary energies [Zöll16].

Grain growth does not require very high temperatures [NKZG16]. This process is enhanced as much as the material is purer [ACYL11]. This is either due to the grain growth resistance caused by impurities that segregate grain boundaries and hinder the dislocations' movements, or due to the possibility that impurities can act as nucleation sites for new grains during recrystallization [ACYL11]. Grain growth is responsible for reducing residual stresses and dislocation densities.

Another important process that may occur for metallization grains below the bonding wires is the crack formation. This process is considered one of the critical degradation processes. Crack formation is less enhanced in naked sites since more plastic deformations exist at the interconnection sites upon cycling. Cracking starts due to dislocations' activities caused by plastic deformations' accumulation. Dislocations then interact with grain boundaries which adsorb them. This causes the formation of extrusions for relieving stresses [SaMS11]. Created extrusions remain incubated inside the grains unless their density becomes very high. When their density increases, they try to emerge from boundaries, leading to a high rise in the stress concentration, causing cracks' initiation. With aging, cracks propagate through grain boundaries, where cracks' splitting from single cracks occurs, reducing the contact between the wire and the metallization layer [Ruff17].

6.2.2 Reconstructions inside bonding wires

Recrystallization processes occurring inside the wire near the interconnection with the metallization layer are somehow different from those inside the metallization or inside the wire far from the metallic contact. Plastic deformations concentrate inside the wire just above the metallization, especially at the wire's extremities. This is due to the initially present deformations caused by the wire welding process, and the high amount of generated stresses upon cycling. Therefore, recrystallization is much enhanced inside the wire near the metallization.

Dislocations formed by the wire welding process are activated when cycling begins. These dislocations cause the major microstructural changes inside the wire just above the metallization through grains' reconstructions. When aluminum is subjected to significant thermomechanical stresses, dislocations will be set in motion in their sliding planes. Such displacements generate irreversible and permanent plastic deformations. Dislocations then eventually cluster together and form sub-grain boundaries, ultimately leading to the division of aluminum grains into similarly oriented sub-grains. This recrystallization phenomenon seems to saturate quickly and does not explain the presence of cracks and holes since it occurs at early cycling stages [BWKP18], [MLLD14].

Therefore, the first important parameter which can be interpreted inside the grains of the wires just at the metallic interconnection is the density of dislocations. This parameter can be used as an indicator of the occurrence of recrystallization and recovery processes. When low dislocation densities are present, this indicates recrystallization or recovery due to the removal of lattice faults. In contrast, high dislocation densities give evidence for plastic deformations [BGHS15]. An additional indicator for reconstruction and recrystallization processes inside the wires is the change in the disorientation angles between grains caused by grains' rotation. It is reported that the mean disorientation angle between grains mainly increases upon cycling [BWKP18], as previously observed in Figure 29 for grains of thin films.

Another important indication for recrystallization inside the wires is the change in hardness values upon cycling. The hardness represents the material's resistance to deformations. For several reasons, hardness values are much more important to study for the grains of wires than for metallization chips. Due to the wire welding process, high plastic deformations are created inside the wire grains near the metallization, causing significant gaps in terms of grains' size inside the wire for positions near and far from the contact with the metallization. This induces a big gap in hardness values between grains within the same wire. As a result of the grain growth process, a change in grains' texture takes place. The change in grains' texture highly impacts the hardness values, as observed in Figure 30 [BGHS15]. From this figure, it can be deduced that the highest hardness values correspond to textured grains located near the metallic contact. It can also be concluded that the increase in the size of grains decreases hardness. These observations were also deduced by Onuki and others [OnKS00]. At advanced cycling stages, Zhao and others reported that continuous reconstructions highly increase the surface roughness, reducing the contact between neighbor grains. Roughening accompanied by grain growth causes a decrease in the hardness values [ZAFB19].

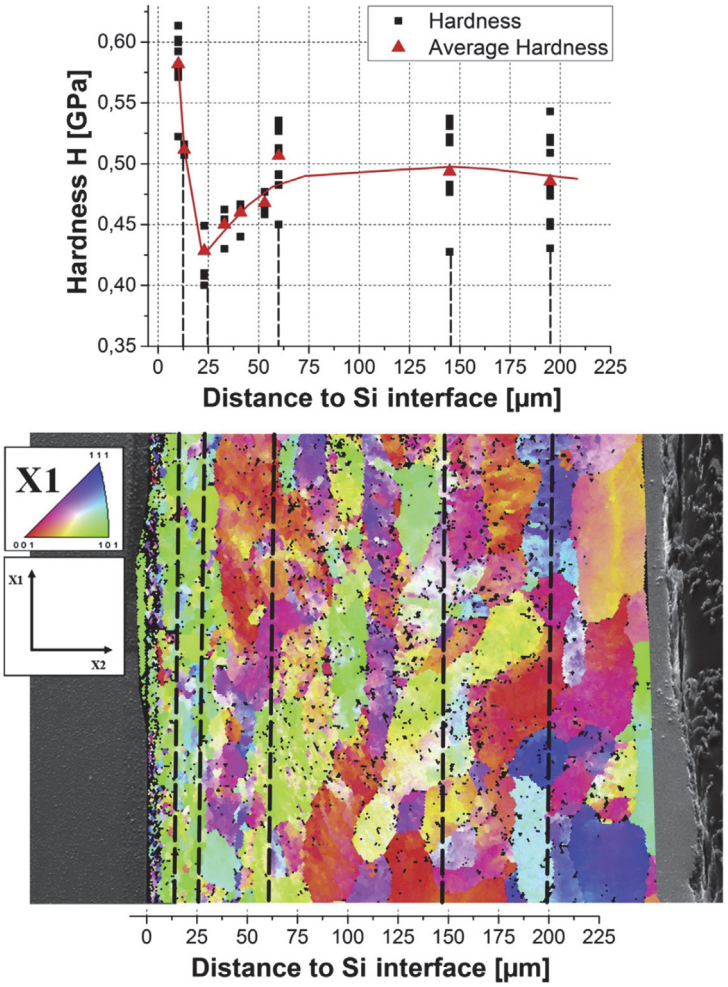

Figure 30: Hardness values obtained by nanoindentation tests overlaid with an Inverse Pole Figure [BGHS15].

6.3 WIRES FRACTURE AND LIFTING-OFF

As presented previously, the welding procedure of wires to metallization layers is mostly ultrasonic. The ultrasonic energy, bonding force, and welding time are the main three parameters to be optimized to obtain good adhesion between the wire and the metallization layer with minimal defects. In most cases, holes and pre-cracks result at the extremities of the wires in contact with the metallization. Stress concentrations cause such defects due to the bending of the wire while it's welding. Upon cycling, these defects start growing; consequently, in this most fragile area degradation begins [ACYL11], [Harm10], [LCLH07]. Two types of degradations are observed at the level of the wires: wires fracture due to cracks' formation and propagation, and wires lifting-off when the wire detaches from the metallization layer [MKSG08], [RaSW00].

6.3.1 Wires fracture

As seen in Figure 31, the heel crack is one of the most famous degradation processes, with rapid initiation speed caused by thermomechanical fatigue. As mentioned previously, fractures and cracks are initially present if the welding process has not been optimized [Ciap02]. It is also observed that the inclination angle of bonded wires affects the wire's strengths, where there is a preferred angle of inclination for having the best-optimized strength [MeVN12]. It is also seen that the geometric ratio of height to length of the wire's loop plays a vital role in the wires' fracture [RaSW00]. Stresses at heel positions are lower when this ratio is high.

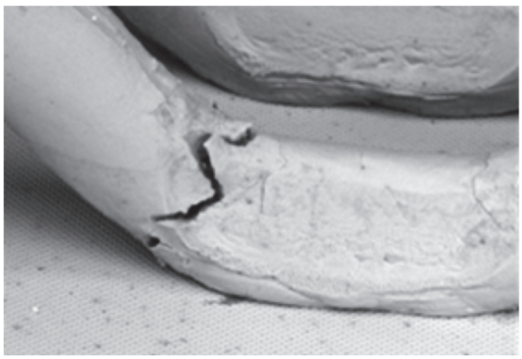

Figure 31: Heel cracks [HaKI18].

The main reason behind the formation of those fractures is the stress concentration gradients generated by the dislocation pile-ups, where high stress results in particular zones, especially the wires' extremities. The number of dislocations in a metal increases upon cycling due to the continuous generation of deformations. Because of the ongoing formation of dislocations and the role of grain boundaries in resisting their motion, as schematized in Figure 32, the density of dislocations increases within grains [ZZYH16]. Consequently, the average separation distance between dislocations decreases; therefore, dislocations will be positioned close to each other. Dislocation–dislocation strain interactions are repulsive; thus, the motion of dislocations is hindered. As the dislocation density increases, the dislocation's motion resistance becomes more pronounced. Therefore, the imposed stress necessary to deform a metal increases. However, the accumulation of numerous dislocations at small zones will cause cracks formation to relieve the high stress concentration [Mour12]. This occurs when a specific critical stress concentration value is reached [Gour02], [KIKT08].

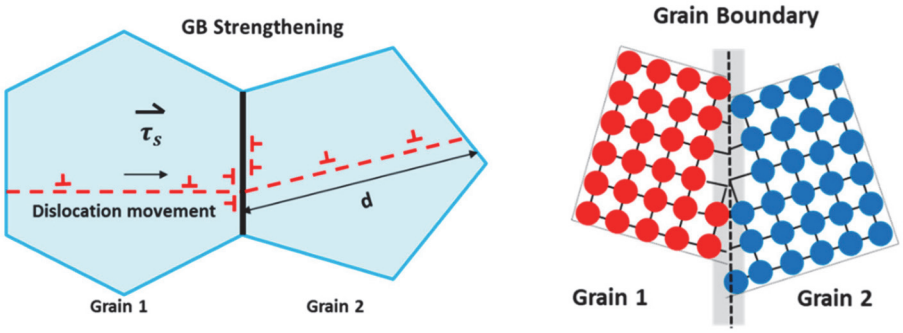

Figure 32: Schematic diagram of grain boundaries [DSWN19].

Smaller grain sizes lead to an increased crack growth resistance due to their higher yield strength values according to the Hall-Petch equation [Hall51], [Petc53]. It was also reported that the crack growth in metals preferably occurs in low Taylor factor areas or grains containing high differences in the Taylor factor [BGHS15]. Taylor factor is frequently used to express the flow stress measured in poly-crystals in terms of critical resolved shear stress in single crystals. It is an average orientation factor, which depends on the texture and the crystallographic nature of the slipping materials. Moreover, it is defined as a first approximation of the stored energy induced by plastic deformations in polycrystalline structures. Grains with low Taylor factors theoretically require low energy to plastically deform by slip activation systems, and therefore are preferred sites for crack growth [BERK09], [BGHS15], [DuWA07].

Upon cycling, fractures develop into cracks that mostly propagate through grain boundaries [ACYL11], [OnKS00]. Cracks at metallic interconnection sites are observed to propagate vertically and horizontally; however, the horizontal direction dominates. Cracks' propagation continues unless cracks face microstructural hindrances. In some cases, grain boundaries themselves are considered microstructural obstructions [DSWN19]. This is because different grain orientations retards the propagation of cracks [ZZYH16].

Sangid and others [SaMS11] mentioned that when dislocations' persistent slip bands are present, their penetration is resisted by HABs; thus, these boundaries are preferred sites for cracks' nucleation. This is because HABs are considered obstacles to the migration of dislocations from one grain to its neighbor, leading to their accumulation around such boundaries. On the contrary, it is reported that HABs induce more sliding, enhancing grains' rotations, resulting in higher ductility and toughness; therefore, the crack propagation through them is inhibited [DSWN19]. It was also mentioned that HABs slow down the crack propagation rate caused by the increase in the energy barrier of dislocations or cracks penetrating these boundaries [ZZYH16]. Therefore, cracks probably initiate from HABs; however, these boundaries are not preferred sites for their propagation.

On the other hand, LABs induced mostly during plastic deformations, especially at the early cycling stages, behave differently with cracks motion. A high population of LABs still exists at the interconnection zone between the wire and the metallization layer, even in advanced cycling stages where HABs are generated [BGHS15]. Dislocations can pass easily through LABs; thus, they are less enhanced sites for cracks' initiation [Gour02], [KIKT08]. However, such boundaries have poor grain boundary sliding. Consequently, if cracks are already formed, they are easier to pass through LABs than HABs [DSWN19].

The strain or work hardening process also increases the strength of grains [YaPa19]. Strain hardening is a process that occurs when a ductile metal becomes harder and stronger as it is plastically deformed. Strain hardening is thought to occur upon cycling. It occurs near room temperature; thus, very high temperatures are unnecessary for such a process [CaRe18]. Besides strain hardening, creating incubation times for cracks upon crossing interfaces makes the propagation harder. Therefore, the crack propagation rate becomes slower, as mentioned by Hussain and others [Huss97]. Moreover, the crack closure phenomenon may take place at advanced cycling stages after the formation of several cracks. It is thought to decrease the crack propagation rate in advanced cycling stages. Crack closure is caused by several factors such as plasticity, roughness, and impurities. Jono and Sugeta [JoSu96] found that the fatigue crack exhibits retardation due to crack closure, especially in the case of long cracks. James and Morris [JaMo83] suggested that the reduced impact of crack closure in small cracks may be the main reason why small cracks propagate appreciably faster than long ones. Dowson and others [DoHB93] suggested that crack closure increases significantly when a crack outgrows a grain boundary. Additionally, it appears that roughness-induced closure plays a vital role in the crack closure phenomenon due to the crack's deflection after crossing the grain boundary.

6.3.2 Wires lifting-off

Wire lifting-off, as seen in Figure 33, is also the result of thermomechanical fatigue as for wires' fracture. It occurs faster than the heel crack evolution [Ciap02]. Cracks start forming at the ends of the metallic contacts due to repeated stresses. Then, they propagate toward the center of the bottom part of the wire just above the metallization layer. When the crack becomes entirely distributed along the bottom wire part, the wire lifts off. After lifting-off, currents are redistributed in the wires at the periphery, leading to an intense increase in current densities, resulting in an open circuit. This causes system failure [Ciap02].

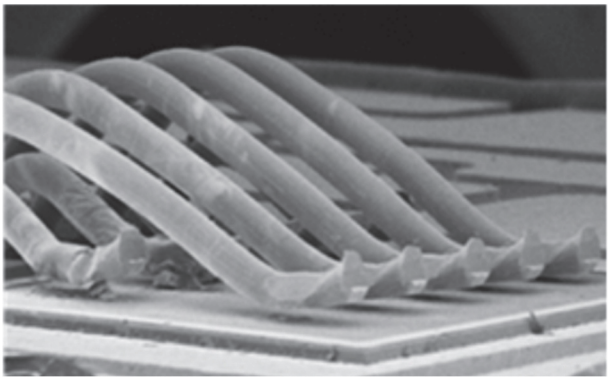

Figure 33: Wire lifting-off [HaKI18].

6.3.3 Microstructural analysis for wires' fracture and lifting-off

The granular structural analysis of the wire carried out mostly using the EBSD method allows us to understand the mechanisms involved in forming these cracks. In this technique, a detector is placed in an SEM, recording the diffraction patterns formed according to Bragg's law during the interaction between the electrons emitted by the column of the SEM and the grating lens of the test specimen. The diffraction pattern recorded by the EBSD detector is representative of the geometry of the crystal lattice, its orientation, and its elastic deformation.

Therefore, the grains' size distribution can be interpreted using EBSD analyses. Once the wire has been welded to the metallization, fine and elongated grains with an average size between 5-15 µm result at the interface, while larger grains with sizes reaching about 60 µm exist inside the wire bulk [RMTW99]. In addition, the existence of different orientations among grains can be deduced by plotting, for example, the Inverse Pole Figures (IPFs). IPF cartographies give information about the spatial distribution of the grains' orientations in the sample. For a cubic crystal lattice such as aluminum, the conventional orientations are noted as (001), (101), and (111) according to the Miller indices. The face of the crystal (100) lies parallel to the surface when red is shown in the normal sample map, the edge of the crystal (110) lies parallel to the surface when green is shown in the normal sample map, and the corner of the crystal (111) lies parallel to the surface when blue is shown in the normal sample map. Each of these indices is associated with a colour in the IPFs, where red, green, and blue colours refer to (001), (101), and (111) orientations respectively. Based on these colours, IPF cartographies show if the grains are oriented in the same manner or not, thus providing information about the grains' texture. If grains are uncolored, this means that they are not oriented.

Figure 34 is an EBSD image showing the grains' size and orientation planes' distribution for a non-cycled wire sample after being welded. Figure 35 shows the evolution of these properties in addition to the crack propagation manner at different cycling stages. Using these data, the crack propagation manner can be interpreted. It was concluded that the crack path is located within a textured area. In addition, grain coarsening and orientation changes accompany the crack evolution [BGHS15].

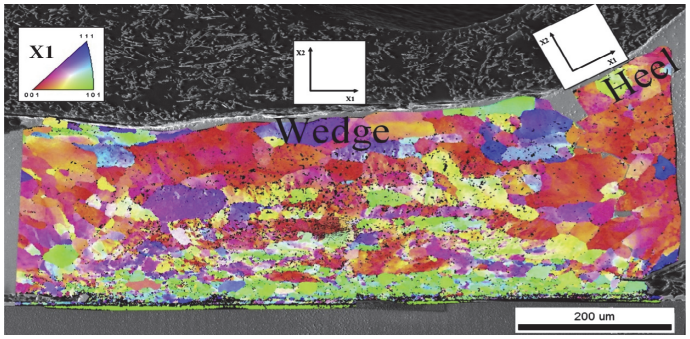

Figure 34: An EBSD image of the microstructure of the aluminum wire-metallization contact after welding the wire [BGHS15].

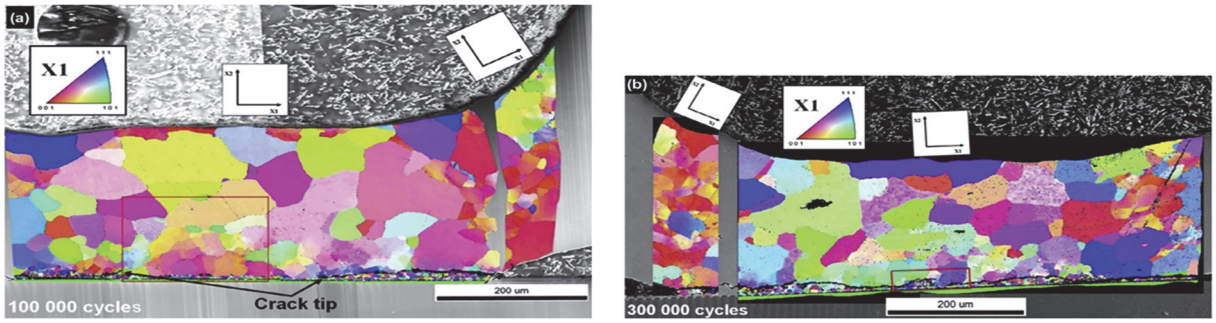

Figure 35: Aluminum wire's microstructure after (a) 100,000 and (b) 300,000 active power cycles (I =10 Amps, each cycle had a period of 2.5–4 s, ΔT_j=90 K starting from 303 K up to 393 K) [BGHS15].

The crack propagation process could be controlled from the wire welding stage, due to the various effects of the welding procedure on the initial microstructure of the wire, as explained previously. Studies showed that increasing the grain size at the metallic interface by applying high welding temperatures or annealing the wire after forming the weld can slow down the crack propagation. It was proposed that when the grains are larger, aluminum is softer and is more able to absorb the deformations [LCLH07], [OnKS00]. In parallel, Loh and others deduced that the force needed to pull the wire from the metallization layer is greater when the welding temperature is higher, as seen in Figure 36 [LCLH07]. This signifies that cracking in such cases is less advanced.

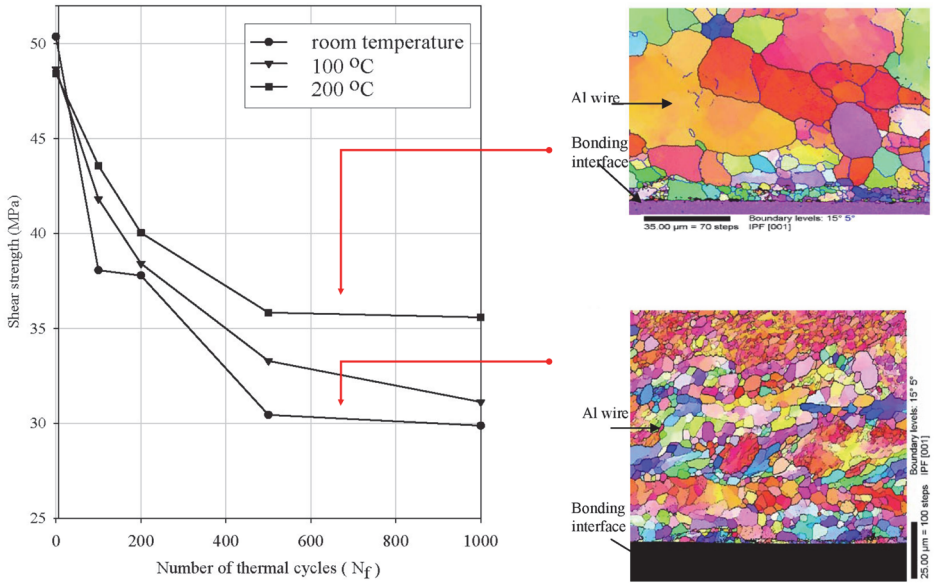

Figure 36: The evolution of shear forces necessary for separating the wire from the metallization at different bonding temperatures. EBSD images corresponding to the wires bonded at 100 °C and 200 °C are presented, where the difference in the grains' size is noticeable [LCLH07].

In conclusion, it has been shown that the degradation mechanisms within power modules generate irreversible structural changes upon cycling, mainly at the interconnection level between metallization layers and bonding wires. These structural changes lead to crack formation and wire lifting-off, causing the device's failure. In the upcoming section, the main physical and microstructural features affecting the mechanical properties of topside metallic contacts are presented.

7 PHYSICAL AND MICROSTRUCTURAL FEATURES AFFECTING THE MECHANICAL PROPERTIES AND LIFETIME OF TOPSIDE METALLIC COMPONENTS IN POWER DEVICES

After detailing the degradation processes, including reconstructions and the direct reasons behind failure, which are the crack propagation and wires lifting-off, the main physical and mechanical properties affecting the mechanical properties and materials' lifetime at the metallic topside contact are shown here.

The first thing to mention when discussing the effect of physical features on materials' properties is the presence of several materials with different characteristics in semiconductor power electronic modules. This causes different temperature and stress distributions. Temperature concentrates in the middle of bonded wires at contact with the metallization. These positions are the most degraded parts of the modules.

Concerning the metallic interconnections manufacturing, the inclination angle of the bonded wire was shown to affect the wire's lifetime since it influences the stress distribution. When the inclination angle increases, the stress concentration increases; thus, the number of cycles to reach failure (N_f) decreases [MeVN12]. In addition, the degree of purity of the components of semiconductor power devices affects grain

reconstruction processes, which greatly influence the shapes of degradations, as seen before. For less pure grains, the grain growth process is weaker.

Upon cycling, several physical features affect the performance and properties of materials. One of the most important factors is the maximum junction temperature value ($T_{j\ max}$). Investigations of wires' microstructure showed a noticeable increase in softening and sub-grain coarsening when cycling with higher $T_{j\ max}$ values [YaAJ13]. Agyakwa and others [ACYL11] concluded that increasing the value of $T_{j\ max}$ enhances the grain boundary migrations, because untangling of dislocations is favored at higher temperatures, as seen in Figure 37. Yamada and others [YTYN07] deduced that increasing the value of $T_{j\ max}$ has a stronger influence on grain growth than increasing the number of applied cycles. Additionally, it was reported by Yang and others [YaAJ13] that bonds subjected to higher $T_{j\ max}$ have slower wear-out rates, thus higher N_f, despite having larger temperature ranges. On the contrary, this interpretation was completely different from the results obtained by Matsunaga and others [MaUe06], who observed that higher $T_{j\ max}$ decreases the N_f, due to the presence of more stress and plastic deformations.

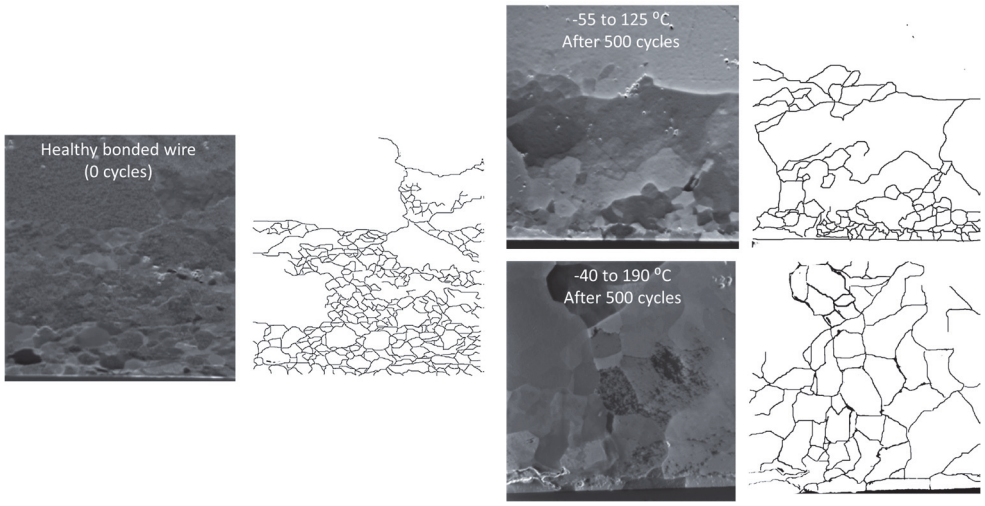

Figure 37: FIB images of 99.999% pure aluminum wire bond interface prior to thermal cycling, after 500 thermal cycles from -55 to 125 °C, and after 500 thermal cycles from -40 to 190 °C [ACYL11].

Other physical factors impacting the properties of materials upon cycling are mentioned as follows. According to Lai and others [LCRX17], upon cycling the IGBT modules, as the temperature swing (ΔT_j) increases, the values of von Mises stresses increase; thus, N_f decreases. The increase in the von Mises stresses is enhanced at higher $T_{j\ max}$ values. Changing the mean temperature (T_m) also affects the lifetime of power modules. According to Murdock and others [MRCL06], upon cycling IGBT modulus, as T_m increases, N_f decreases, even upon having the same ΔT_j. Another factor affecting N_f is the period of the power-on state (t_{on}). The t_{on} parameter is the time of current transmission, whereas the power-off state (t_{off}) corresponds to the time of cutting off the current. Choi and others reported [ChBJ17], [Choi16] that when t_{on} increases, N_f decreases, and the crack evolution enhances. On the contrary, Yang and others [YaAJ13] said that increasing the t_{on} would decrease the total damage; consequently, the material will have better N_f. This is related to the strain hardening effect, where increasing t_{on} seems to have a good effect on the material by enhancing its strength.

On the other hand, the main microstructural features affecting the materials' mechanical properties are listed here. The first factor is the presence of dislocations. Before cycling, and due to the wire bonding forces, different zones of grain sizes form, with tiny grains at the interconnection interface. At early cycling, the size of grains changes due to dislocations' rearrangements. The grain refinement process that occurs at early cycling stages may cause the strengthening of the material by inserting microstructural barriers, which are the grain boundaries. However, grain refinement usually reduces the ductility of the material.

In the early cycling stages, the density of dislocations of each grain increases due to the formation of

dislocations and deformation processes. With the progress of cycling, experiments showed that the density of dislocations decreases, where they escape through surfaces and crystal interfaces [MLLD14]. It is reported that the higher the surface energy is, the more surface defects such as dislocations. It is also deduced that having a higher dislocation density increases the strength of the material due to strain hardening processes. However, cracks develop when many dislocations become entangled in a small forest-zone region. Thus, the presence of dislocations increases the strength of the material; however, it decreases its ductility [Mour12].

Plastic deformations by dislocation glides can result in crystal rotations to improve the material's ductility. Ductility is generally enhanced in HABs and special boundaries such as twin boundaries, while it is less favored in LABs [DSWN19]. In addition, the grain growth process responsible for the change in the size of grains results in a decrease in the material's strength since the frequency of LABs decreases and that of HABs increases. The effect of the grain size on the material strength can also be deduced from the Hall-Petch relationship, by which as the grain size decreases, its strength increases and vice versa [Wata11].

Table 2 sums up the effect of the microstructural changes on materials' properties as follows [DSWN19].

Table 2: The effect of critical microstructural features on materials' properties [DSWN19].

Features	Specifications	Properties	Crack initiation	Crack propagation	Material specifications
Grain size	Ultrafine or nanocrystalline (↑)	Strength (↑) Hardness (↑) Ductility (↓)	Retards	Retards or accelerates, both reported	Brass, stainless steel, ultrafine-crystalline Al-Mg alloy
Low angle grain boundaries	Disorientation angle < 15° (↑)	Ductility (↓) Hardness (↑)	-	-	All polycrystalline metals
High angle grain boundaries	Disorientation angle ≥ 15° (↑)	Ductility (↑) Hardness (↓)	-	-	Ultrafine crystals and non-equilibrium grain boundaries
Dislocations	Generation of pile-ups (↑)	Strength (↑) Hardness (↑) Ductility (↓)	-	-	Nanocrystalline/ultrafine structure
Strain hardening	Magnitude and distribution depth (↑)	Ductility (↓) Hardness (↑)	Retards	Retards or accelerates, both reported	Polycrystalline materials
Compressive residual stresses	Compressive stresses or distribution depth (↑)	Hardness (↑) (little effect)	Retards	Retards (little effect)	Polycrystalline materials

As a result, representative electrical parameters corresponding to degradation processes are used as indicators of aging. Failure criteria associated with these indicators have been defined, serving as references to determine the module's end of life. The following section describes these indicators and the failure criteria associated with them.

8 PREDICTING THE LIFETIME AND DEGRADATION PROCESSES IN TOPSIDE COMPONENTS OF POWER DEVICES

In order to produce methods able to determine the end of life of power modules for the aim of minimizing systems' costs, lifetime and degradation prediction models were established. The purpose of such models is to estimate the remaining lifetime of a device in operation.

8.1 LIFETIME AND DEGRADATION INDICATORS

Generally, the changes inside power modules are associated with electrical or thermal indicators, representatives of the degradation processes. For example, the increase in the metallization resistance is an electrical indicator of reconstructions inside metallization layers and bonding wires, wires fracture, and wires

lifting-off [MLLD14], [PØGP15]. Upon cycling, the resistance evolution often has the same tendency, with three different phases. In the first phase, the resistance does not show any significant increase. In the second phase, a clear and considerable rise in resistance takes place. Finally, in the last phase, a continuous resistance increase to infinity results, with a slower speed than that in the second phase, clueing the existence of an open circuit [MLLD14]. Zhao and others [ZAFB19] showed that the aluminum's metallization resistance increases with the surface roughness evolution in the initial and mid-stages of power cycling. Then, near the ultimate lifetime of IGBT modules, the changes in the resistance value strongly depend on the crack's density.

Additionally, the on-state collector-emitter voltage (V_{CE}) is used as an indicator for degradation processes in metallic topsides of cycled modules [Ciap02], [HJNS97], [PKPU17]. An increase between 5-20% of V_{CE} from its initial values is considered a wear-out failure of power devices [LSSD10]. Regarding the damage at the wire-metallization contact, the sudden increase in the V_{CE} at the end of the module's life has been associated with the detachment of the interconnecting wires from the chip, which is the process known as wire lifting-off [HJNS97], [SFHR13].

Another indicator used for estimating the state of health and determining the lifetime of such components is measuring the temperature inside the module or estimating it using thermal models such as those defined by Cauer and Foster to know the power losses [DrKo03]. Such modeling provides lateral and vertical temperature gradients in the layers of a power module. This helps in knowing the amplitude of the thermal cycles undergone by the module in operation.

8.2 LIFETIME AND DEGRADATION PREDICTION

Lifetime models are the most used degradation prediction models. These models are numerous and are classified according to the following categories: empirical models based on large databases resulting from accelerated cycling tests and physical models invented because empirical models do not consider the degradation mechanisms occurring upon aging. Lately, physicochemical-microstructural degradation interpretation studies have been the primary concern of several scientists. These studies aim to predict the degradation process by relating it to physicochemical and microstructural features inside materials. These main degradation prediction models are presented as follows.

- **Analytical lifetime modules:**

Analytical lifetime modules were first invented. Such models relate the number of cycles to failure to some cycling parameters, such as cycling's duration and frequency, in addition to its minimal and maximal junction temperature values [KoDK10].

A. Coffin-Manson model:

This model defines a power-law relation between the number of cycles to failure and the plastic strain induced per cycle in the case of low-cycle fatigue [MaDo66] [YaAJ13]. Plastic strain values are estimated using finite element modules or numerical calculations of the wire loop's curvature evolution.

The model of Coffin-Manson has been widely used despite its several limitations. This model is built on the assumption that the junction temperature is the sole stressor. In addition, it does not consider the frequency of cycles and heating and cooling times [BHLL08]. Moreover, it does not take into account the twisting and thinning of wires that would occur in real cases. Additionally, it does count for the wire's structure and composition [YaAJ13].

The validation of this model is complex since the plastic strain parameter cannot be measured experimentally. Accelerated mechanical stress tests have been performed to simulate the resulting strain for specific temperature fluctuations; however, such tests do not accurately represent the case of cycling when the loading conditions vary with time upon operation [MKSG08], [RaSW00]. Moreover, compared to experimental data, predicting the number of cycles to failure using the

Coffin-Manson model was inaccurate, especially when varying the cycling parameters it does not consider [HJNS97].

All these limitations make the model unstraightforward, by which the data obtained for one device type is hardly transferable to the same device type operating under different conditions. Several expansions have been made to the Coffin-Manson model to accommodate some of these non-considered factors; however, the junction temperature stills the primary stressor [Buhr18].

B. Norris-Landzberg model:

This model is more developed than the Coffin-Manson by considering the frequency of cycles; however, it neglects the influence of other parameters, such as the heating and cooling times [NoLa69]. Compared to experimental data, it was deduced that the Norris-Landzberg model underestimates the lifetime of power modules.

C. Bayerer's model:

This model is more developed than the Coffin-Manson and Norris-Landzberg models [BHLL08]. It considers several parameters, such as the diameter of the wire, temperature swings, the heating time, and the applied current. Although, compared to experimental data, Bayerer's model was also deduced to be inaccurate in predicting the number of cycles to failure [KoDK10].

In addition to the fact that such models were deduced to be inaccurate for predicting the number of cycles to failure, such empirical methods do not distinguish between failure mechanisms within the different power module positions [HJNS97]. Consequently, physical lifetime models were constructed.

- **Physical lifetime models:**

Physical models were developed after observing the critical limitations that analytical models have [Buhr18], [HLBP14], [PeJi09], [WaLB13]. Physical modeling provides a deeper physical description of the observed failure mechanism, and hence, represents a promising alternative to empirical lifetime models. Physical models are based on analyzing key factors leading to fatigue and failure of materials. In these models, it is essential to know the failure and deformation mechanisms undergone, so that the stress and strain development within the power module assembly can be modeled and directly correlated to the number of cycles to failure. Therefore, such modes rely on the knowledge of stress-strain deformations within the tested modules using SEM and infrared techniques, or by applying stress-strain simulations via computational mechanics like finite element analysis [KoKS15], [KoDK10].

Fracture mechanics models are of the most famous physical models, used especially when estimating the lifetime of aluminum bond wires in power devices [Ciap02], [CiFi00], [GSGL10], [OnKS00], [YaAJ13]. In such models, the crack growth per cycle is governed by a stress or strain intensity factor that controls the magnitude of stress near the crack tip. One of the primary laws utilized for calculating the crack growth rate per cycle (d_a/d_N) using strain density factor range (ΔK_ε) is the Paris law as follows, where C and n are material constants.

$$\frac{da}{dN} = C\ (\Delta K_\varepsilon)^n \tag{8}$$

However, this approach is inaccurate for modeling the crack propagation evolution within the welded wire. The reason is that it does not consider the initial state of wires when welded after being exposed to strong deformations by the bonding tool [YaAJ13]. In addition, it does not take into account the microstructural changes that occur upon cycling, which lead to several degradation processes as shown previously.

- **Previous physicochemical-microstructural degradation interpretations, discussions, and models:**

As shown in the previous models, the failure problem of topside metallic interconnections in semiconductor power devices is discussed electrically and mechanically [CBJI16], [DKCN15], [MeVN12], [OnKS00]. It was deduced that analytical models have several limitations. In physical models, it is still required to obtain a clear understanding of the failure mechanisms, the microstructural changes, and the changes in material properties.

Starting from here, physicochemical-microstructural interpretations of materials' failure problems have been invented. Earlier, physicochemical-microstructural studies were made to interpret the fatigue problem of metallic components, but in the case of annealing at high and steady-state temperatures only (near melting points of the fatigued material) [AkOg17], [AKGG14], [ChKC18], [GeMu93], [Mart07], [Mull61], [RaKS00]. Such models are not helpful if used in the case of cycling for metallic topsides in semiconductor power devices, since their aging conditions are totally different from that of cycling. Upon power cycling, the temperature continuously fluctuates, and its maximal value is so low compared to the melting temperature of the heated material (aluminum). Other limitations exist as well. For example, the interface properties in previous models were assumed to be independent of the crystallographic orientations [RaKS00].

In these previous models, it was deduced that the surface diffusion process driven by the surface curvature is the dominant diffusion process [Rhea63], and it is the driving force of materials' degradation by causing the grain boundary grooving process. The grain boundary grooving is the decrease in the local thickness at the grain boundaries. It occurs due to the difference in the surface and interfacial energies within the same material, the change in grains' orientations, and the faceting of the material's surface. It is also caused by the growth of specific crystal planes at the expense of others. Mullins was the most famous scientist who studied this process [Mull61]. Other works were also done by Genin and others [GeMu93], Martin [Mart07], Rabkin and others [RaKS00], Amram and others [AKGG14], Akyildiz and others [AkOg17], Chakraborty and others [ChKC18] through expanding the field of usage of Mullins work.

Recently, the influence of physicochemical-microstructural properties on the degradation processes, particularly at metallic topsides positions in power modules, has been the work of several scientists. Some important physicochemical-microstructural interpretations are presented as follows. Broll and others [BGHS15] discussed the effect of the bonding procedures on the microstructure of the wire-metallization bonding contact and the impact that the welding process has on the physical properties and reliability of metallic contacts when aged. It was deduced that plastic deformations induced by ultrasonic wire welding power and the grain growth process that occurs upon cycling cause the grains' texture development. The crack was deduced to progress inside texture-developed areas and grown grains.

Loh and others [LCLH07] explained the effect of the wire bonding temperature on the crack formation during aging. Primarily, they reported that for all the bonding temperatures, the mean shear strength of the wire bonds decreases upon cycling due to fatigue crack propagation taking place at topside metallic contacts. The rate of shear strength decrease was higher for wires bonded at lower temperatures because the crack passage speed inside those wires is higher. They also found that the crack propagation is much slower for wires bonded at high temperatures. This is attributed to the changes in the grains' microstructure at the interface when changing the bonding temperature. At higher bonding temperatures, grains at the interface between the metallization and the wire are coarser. The presence of coarser grains along the bonding interface reduces residual stresses and dislocation densities, and gives rise to much more resistance to crack propagation. Consequently, it may be concluded that strong and reliable bonds can be achieved by high-temperature bonding.

Agyakwa and others [ACYL11] mentioned the effect of materials' purity on the evolution of their properties upon cycling, like the hardness and grain size. First, it was deduced that upon cycling, whatever the degree of purity is, the hardness of the interfacial region connecting the wire to the

metallization layer decreases. When the interfacial regions are subjected to higher ΔT_j and $T_{j\,max}$ values, the decrease in hardness is enhanced. Upon comparing the evolution of hardness for samples having a different degree of purity cycled under the same conditions, it was found that the hardness decrease is higher for the purer wire. From this observation, it was thought that upon changing the degree of purity, dislocations' interaction changes, affecting the extent of recrystallization and recovery that take place upon cycling. The grain growth process was deduced to occur more rapidly in purer wires when being cycled under the same conditions. Consequently, the hardness evolution is affected by microstructural properties such as the dislocations' activities and grains' size.

Brincker and others [BWKP18] related the changes in the orientation angles of grains in thin metal films upon cycling to fatigue problems. The change in the orientation angle increases the surface roughness and leads to the generation of voids inside the material. The driving force for the orientation modifications is changing the atomic packing density inside grains to a more stable form. It was also reported that the change in the texture of aluminum grains upon cycling occurs through the increase in the grains' disorientation angles and the change in the grains' sizes.

Pederson and others [PØKG16] related the fatigue problem to the microstructural changes within the metallization and the bonding wire in IGBT power modules. After subjecting the power modules to active thermal cycling, they deduced that wires degrade through the fracturing that develops parallel to the metallization chip's surface. This fracture develops in the shape of cracks that progress across the grain boundaries. In that paper, they concluded that reconstructions facilitate crack propagation and wire lifting-off. Both processes are affected by ΔT_j and $T_{j\,max}$ cycling conditions. These processes were deduced to cause the increase in the electrical resistance that leads to the device's failure.

Martineau and others [MLLD14] explained in detail what happens microstructurally upon the degradation of top metallic components. First, they said that plastic deformations are carried out by the pre-existing mobile dislocations resulting from the wire welding process. These dislocations aggregate inside the metallization chips and form sub-grains. In the second stage, the diffusion of aluminum atoms along grain boundaries, mainly during the heating phase, relieves stress generated from cycling. In the cooling phase, grain boundaries open and oxidize. When cycling is advanced, cracks open, causing physical disconnection of aluminum atoms.

Zhao and others [ZAFB19] estimated correlations between the electrical resistance evolution and the evolution of the aluminum metallization layer's reconstruction. They showed that in the initial and mid-stages of power cycling, the increase in the metallization layer resistance is consistent with the surface roughness evolution. In the initial stages of aging, aluminum grains are extruded from the surface of the metallization layer, resulting in a transformation from a smooth to an extremely rough surface. After a period of cycling, the extrusions grow independently or jointly, with a clearly higher surface roughness in the central area of the chip than that in the peripheral region. The increase in the roughness slows down compared to that in the initial cycling stages. At cycling stages near the ultimate lifetime of the IGBT module, the changes in the resistance values strongly depend on the crack density, not on the microstructure, because at those cycling stages, the microstructure becomes highly reconstructed.

Some important theoretical models for the fatigue crack initiation and propagation and their dependency on the microstructural changes were constructed, such as the Persistent Slip Bands model (PSB model) explained by Sangid and others [SaMS11], [SaMS11] and the model suggested by Zhou and others [ZZYH16]. Starting with Sangid and others [SaMS11], [SaMS11], they explained the PSB model used to predict the crack initiation state. In this model, the crack initiation is related to the material's microstructure, particularly the grain size and orientation angles. The PSB model is a dislocation-based model, where the PSBs are formed when dislocations arrange themselves upon cycling. Since the number of dislocations within the PSB increases when grain boundaries impede

dislocations' movement, pile-ups are formed, increasing the stress concentrations. At this stage, extrusions generate at grain boundaries. This is thought to increase the surface roughness. At further cycling stages, the extrusion's height increases, assisting in the crack nucleation at the PSB-grain boundary interface when the stress concentration reaches a critical value. Figure 38 schematizes the PSB model. The activity of those PSBs decrease when cycling advances. One of the main conclusions deduced by this model is that dislocations within PSB can pass only through LABs; thus, HABs are the preferred sites for the crack initiation.

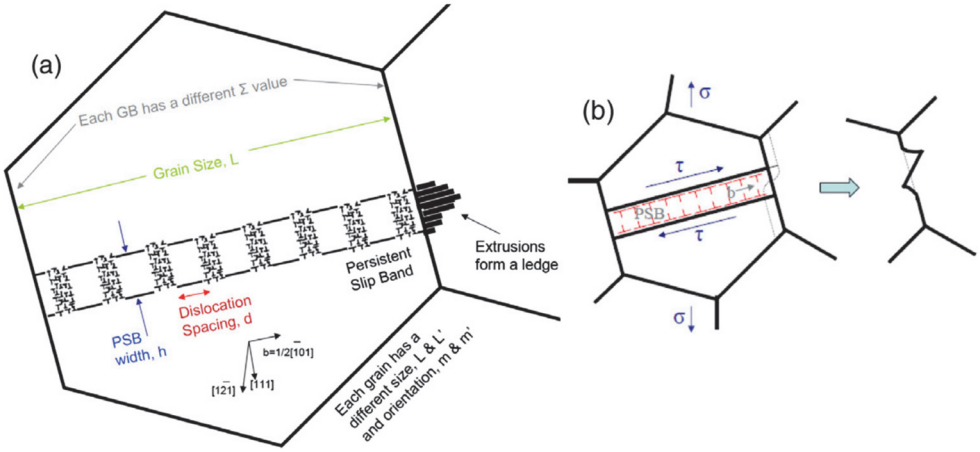

Figure 38: (a) Schematic representation of the PSB geometry and its formation across a grain. (b) Extrusions form across the grain boundary when the number of dislocations within each grain highly increases [SaMS11].

Zhou and others [ZZYH16] showed in their theoretical model the effect of the grain size and the disorientation angle on fatigue crack growth. This model was also dislocation-based, where the crack initiation is due to stress concentrations caused by the deformation and rearrangement of dislocations, leading to the formation of pile-ups. In this model, they deduced that dislocations' penetration is enhanced when the angle between the slip band and the grain boundary interface is minimum, shear stress at the slip band is maximum, and the burgers vector of residual dislocations at the grain boundary is minimum. When these conditions are absent and pile-ups are formed, the crack tip emits dislocations. Grain boundaries resist the motion of these dislocations, where their slip is considered irreversible. With continuous emission of crack tip dislocations, the progressive accumulation of plastic deformation will cause the expansion of the crack tip, resulting in fatigue cracking. In this model, it was deduced that the preferable sites for the crack passage are the grain boundaries. The effects of the evolution of grains' sizes and disorientation angles on crack growth were also discussed in this model. It was observed that the crack evolution rate decreases when the grain size decreases and the disorientation angle between neighbor grains increases.

However, both presented models are theoretical and only used for the crack initiation state. In addition, they can be used only when the formation of dislocations is the dominant deformation process, which is not clear to be the case in power cycling since the temperature reached is not so high (low compared to the melting point of aluminum), even though dislocations pre-exist before cycling due to the wire welding process. It is also unclear whether it can be used for modeling the crack evolution in the case of thermomechanical fatigue at metallic contacts in power devices.

As noted in previous theoretical studies, dislocations at persistent slip bands produce stress concentrations that cause the crack initiation. Wilson and others [WiZD18] suggested that there may be some similarities between the crack growth problem and that of cracks' nucleation. Based on the fact that energy-based methods have been able to predict the crack nucleation sites accurately; therefore, it would be reasonable to apply these methods to predict the crack growth. Crystal plasticity models were developed to model the fatigue crack evolution, taking into account this approach. Such

models can be surely mentioned as advanced physicochemical-microstructural methods for modeling the crack evolution in materials. Among these models, the works of Farukh and others [FZJR16], Wan and others [WaMD16], and Déprés and others [DéRF15] are mentioned.

Farukh and others [FZJR16] have used a critical value for the plastic strain to predict cracking. This value showed a crack growth rate in good agreement with previous works using viscoplastic material models. The crack growth was shown to be dependent on the grain crystallographic orientation. Wan and others [WaMD16] used a maximum principal stress criterion and an energy release rate-based traction-separation response to study the crack growth in ferritic steel microstructures. This work highlighted the importance of including elastic anisotropy to capture the highly-localized stress states at the grain boundaries. A further finding was that the explicit inclusion of grain boundary effects was necessary to capture the crack path correctly. Déprés and others [DéRF15] made 3D simulations to help understanding the persistent slip band's formation and the associated surface extrusion growth mechanisms. A detailed scenario for the crack initiation was proposed. The mechanism for the crack propagation along the slip band was explained and quantified as a function of the grain size. Finally, the crack transmission to the next grain was investigated for diverse crack orientations, showing that the crack plays a major role in developing plasticity in the neighboring grains. Despite the promising results obtained in this study, their simulations have several limitations. The first one is related to the calculation time required for a simulation, which limits the maximum number of simulated cycles. Moreover, neither surface contamination nor diffusion mechanisms are considered in the model. The main limitation is that the simulations were only performed on a single crystal.

Crystal plasticity models are complicated and mostly applied when studying the behavior of a single crystal [DéRF15], [Mlik20]. Representing the microstructure and crystallographic texture of large parts of samples via grain-by-grain maps by applying crystal plasticity finite element for modeling the crack evolution at the wire-metallization interface seems to be so difficult. Additionally, since deformations are studied at different cycling stages, it was reported that crystal plasticity finite element models could not describe self-organizing defects such as dislocations rearrangements and sub-grains formation during deformation [REHT10]. It is also hard to consider the thermal stresses that grains face upon cycling. Consequently, the effect of grain properties changes upon cycling on the crack evolution is so difficult to configure, especially when considering the entire wire-metallization interface. Moreover, it was also reported in the literature that a more detailed comparison between crystal plasticity predictions and their corresponding experiments is necessarily required [REHT10].

- **The physicochemical-microstructural degradation modeling approach followed in this work**

Based on the theoretical models like the ones constructed by Sangid and others [SaMS11], [SaMS11] and Zhou and others [ZZYH16], it has been seen that just the crack initiation can be modeled. Additionally, these models are only based on dislocations' activity concepts and are theoretical, not validated with experimental data. Crystal plasticity models were deduced to have some limitations and complexity, where they are mostly applied to single grains.

Indeed, the effects of the aging of polycrystalline structures on the behavior laws of materials are rarely considered in previous models; this is the ultimate objective of this work. In this study, a model which takes into account the experimental observations was aimed to be constructed. This model is a combination model between the physical fracture mechanics approach and physicochemical-microstructural concepts. The model can be achieved by relating the parameters of a famous damage-based model used to interpret the fatigue crack propagation (Cohesive Zone Model) to the most critical physicochemical-microstructural parameters. This linkage provides a deeper understanding of the reliability aspects and overcomes several previous models' limitations. In this way, the main restriction of physical models, the lack of the consideration of microstructural evolution, can be overcome. In fact, this is a continuation of the work of the previous Ph.D. student in our laboratory [Dorn19], where she used the CZM to model the crack evolution, however with constant parameters taken from the literature, without considering the effect of the microstructural changes on the damage progress.

As mentioned previously, the main limitations to overcome in previous models are related to the microstructural evolutions in the granular structure at topside metallic components in power modules. Consequently, it is first essential to analyze the initial microstructure of wires and metallization layers after welding the wire, particularly the changes in the aluminum grains' properties. This is followed by interpreting the evolution of these microstructural properties, such as grains' size, texture, orientation, and disorientation angles upon cycling. Grain reconstruction processes have a considerable influence on the properties of grains, as shown in the previous sections. The role of dislocations generated mainly from the wire welding process in forming cracks in the early cycling stages should also be taken into account. Then, the crack propagation must be interpreted based on the main physicochemical-microstructural changing features. Analyzing the degradation processes microstructurally is highly important, especially since the crack propagation process accompanying grain reconstructions is responsible for the total failure of upper metallic components in power modules. Consequently, predicting the preferable crack pathway across grains and grain boundaries is essential. This was aimed to be achieved by finding links between the parameters of cohesive laws (critical fracture energy and stress) and materials' physicochemical properties that change within the microstructure upon aging. These aspects are not discussed by most of the previous models and will be considered in this approach and detailed starting from the next chapter.

9 CONCLUSIONS

This chapter primarily presented the different parts of a standard power module assembly, with particular attention to the interconnection interfaces between bonding wires and metallization layers. The constitution of wires and metallization layers were presented. Then, the technologies of welding the wires to metallization layers have been detailed. Next, the initial microstructure of wires and metallization layers before the welding procedure was explored. Afterward, the microstructural shapes of deformations that these components face when being deformed were detailed. The next section showed the main microstructural changes that occur after welding the wire on the metallization layer. The following part was devoted to show the degradation modes and mechanisms occurring at topside metallic contacts in standard power module assemblies, because degradations concentrate at such positions. The most common degradation mechanisms are the wire fracture and its detachment from metallization layers, in addition to reconstructions of the metallization and wire grains. Wire fracture and lifting-off mechanisms are microstructurally related, by which they are affected by changes in the grains' structures, and they cause their decohesion when cracks progress. Cracks' formation and propagation were explained in detail since they are the direct reason behind the failure of power modules. In the following, the electrical indicators used to predict topside metallic interconnections' degradation were presented. These indicators monitor the damage during the module's operation and let us know the end of its life. In this way, appropriate and efficient maintenance can be set up with the goal of reducing the costs of power systems. In the last part of this chapter, previous failure prediction models were presented, showing important physicochemical-microstructural modeling attempts. Finally, the approach to follow in this study was introduced.

The work carried out during this Ph.D. study will be presented as follows. First, microstructural analyses are made to interpret the microstructural changes occurring at topside metallic contacts in semiconductor power devices upon cycling. These changes are linked to degradation processes. The next chapter presents a physicochemical-microstructural degradation model specific to the topside metallic contacts. As mentioned previously, many previous models discussed the topside metallic degradation problems of power devices from electrical and mechanical points of view. However, relating these problems to microstructural changes and physicochemical property evolutions is a new way of dealing with such issues. The introduced model was constructed with the help of a physical model, the cohesive zone model (CZM), by relating its damage parameters to physicochemical-microstructural features. In the last chapter, such relations were expressed through simulating the crack evolution using the ANSYS APDL software by putting the physicochemical-microstructural parameters as input data.

CHAPTER II: EXPERIMENTAL MICROSTRUCTURAL AND DEGRADATION ANALYSES FOR TOPSIDE METALLIC CONTACTS IN IGBT POWER MODULES WHEN BEING AGED

1 INTRODUCTION

The first chapter showed that plastic deformations and dislocations in the vicinity of the wire contact with the metallization exist prior to cycling due to the wire welding process. When cycling occurs, grain reconstructions arise, leading to several changes in the properties of materials. This is accompanied by crack propagation which causes the wire lifting-off, the direct cause behind the failure of upper metallic parts of power electronic components.

These degradation processes are better discussed after applying experimental analyses such as SEM, AFM, and particularly by using the EBSD technique, which enables us to interpret the degradation processes within the microstructure. These experimental analyses were done after managing some accelerated cycling tests on SKIM63 IGBT samples at different cycling stages. Accelerated cycling tests were applied by the previous Ph.D. student and are detailed in the following reference [Dorn19]. In the upcoming chapter, these microstructural analyses will be the basis for constructing the cracking model at the wire-metallization interconnection.

2 DESCRIPTION OF DUTS AND POWER CYCLING TESTS

To interpret the degradation processes microstructurally, accelerated cycling tests should be first applied [Dorn19]. Commercial SKIM63 modules from Semikron were chosen to be used in the cycling tests. A SKIM63 module is a three-arm power converter, each composed of two switches, also called DUTs “Device Under Test”, as shown in Figure 39. Each arm is associated with one Direct Copper Bonding (DCB) substrate. A DUT consists of four IGBT chips placed in parallel with two freewheeling diodes which are not considered here. Therefore, each DCB substrate contains a total of twelve components, eight IGBTs and four diodes, as seen in Figure 40. The same chip numbering shown in Figure 40 will be used in further work in this chapter.

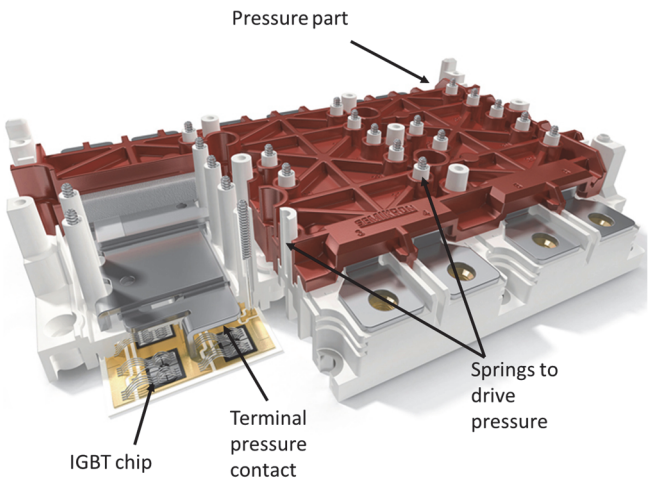

Figure 39: Representation of the SKIM63 module manufactured by Semikron [Semi17].

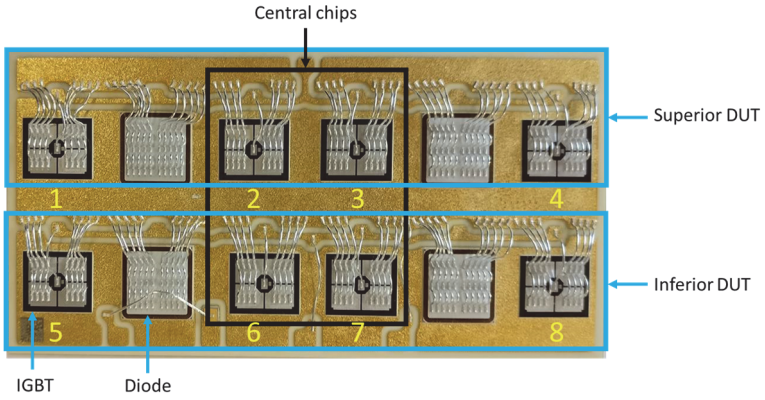

Figure 40: An image showing the two DUTs in the SKIM63 module, including the IGBTs and diodes.

A SKIM63 module has an assembly structure without a base plate. The DCB substrate is placed directly in contact with the cooling system via a thermal grease already pre-deposited by the manufacturer. The mechanical mounting of the DCB substrate on the cooler is done by screws. The electrical contacts for both the power and the control are carried out by a set of pressure and spring systems integrated into the module's structure. The chip deposition (die-attach) is made by silver sintering. This latter process results in better electrical, thermal, and mechanical properties than conventional solders. Reliability tests have shown that modules sintered by silver have lifetimes up to three times longer than modules with standard solders [GöFa10]. The delamination of solders, one of the main degradation mechanisms of power electronics, does not occur in practice or is negligible when using SKIM63 modules. Consequently, wires lifting-off or their fracture, as well as reconstructions inside metallization chips and wires, are the only degradation mechanisms observed during aging. This justifies using such modules in order to focus only on the degradation processes at upper metallic interconnection zones, with the aim of developing a physicochemical-microstructural degradation model for predicting the crack propagation, the process responsible for total failure.

Generally, two types of accelerated cycling tests are used: passive and active cycling. Passive cycling is used more when studying the degradation of large solder joints, typically for the attachment between a DCB substrate and the base plate. However, active cycling generally has a more significant impact on the metallic interconnections close to the chip, and eventually in the die-attach layer. Consequently, only active accelerated cycling tests were performed in the aging tests [Dorn19]. The test bench necessary for such tests is divided into three main parts, a supporting part, a measurement part, and a power and control part, as shown in Figure 41.

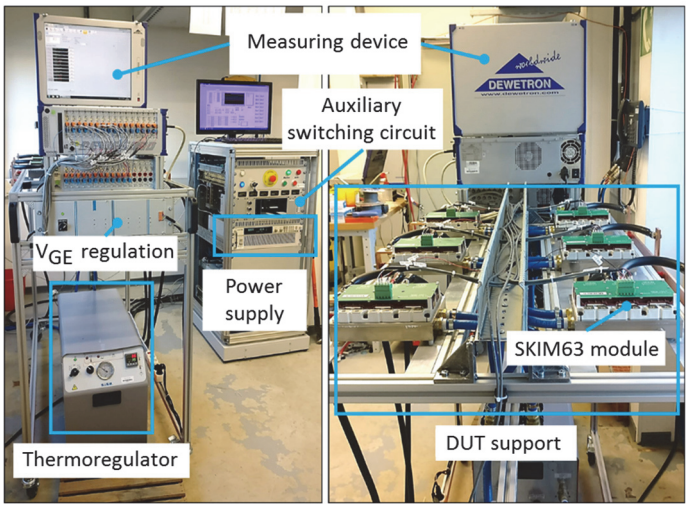

Figure 41: The test bench used for performing the active power cycling tests.

Because these aging tests are accelerated, the imposed junction temperature variations ΔT_j during power cycling are much larger than those usually experienced by the module during normal operations. The

current load, as well as the power-on period (t_{on}) and the power-off period (t_{off}) are adjusted in order to achieve the desired ΔT_j. Auxiliary transistors in series with the DUTs ensure the power load current switching during t_{on} and t_{off} periods, which are respectively the heating and cooling times of DUTs. The impact of the reference temperature corresponding to the initial temperature of the module components is not considered in this study; therefore, this temperature is fixed for all aging tests at 45 °C. Thermal stresses were applied with the following conditions {ΔT_j = 110 °C, $T_{j\,min}$ = 55 °C, t_{on} = 3 s, t_{off} = 6 s}. As mentioned previously, these experiments are detailed in the following reference [Dorn19].

Six devices were aged at a different number of cycles; in other words, the six devices were extracted at different aging stages. This is done in order to perform experimental analyses on the aged samples at different cycling stages and see the microstructural changes and the crack propagation evolution in these samples. It was supposed that the degradation is similar for all tested devices. To verify this assumption, the on-state collector-emitter voltage (V_{CE}), an aging indicator used to quantify the damage in the wire bonds, was measured [DIKD20]. Indeed, this latter is directly impacted by the loss of contact between the wire and the metallization. The failure criterion is usually fixed at a 5% increase in the V_{CE} [KoKS15]. The evolution of averaged V_{CE} on each tested device upon cycling is shown in Figure 42. In this figure, the last measurement of V_{CE} for each device before being removed from the test bench is denoted by a red dot. These points symbolize the level of degradation at the topside interconnections of each of the six tested modules.

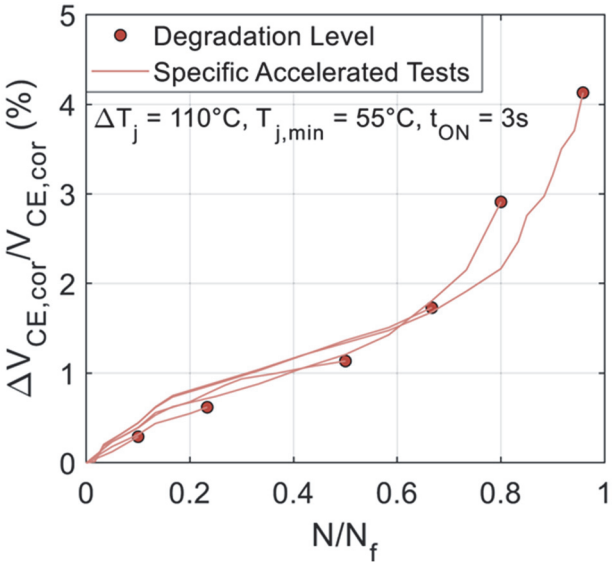

Figure 42: The evolution of $\Delta V_{CE}/V_{CE}$ vs. N_{cycles}/N_f upon cycling [DIKD20].

The results of Figure 42 show that the evolution of V_{CE} follows a distinctive trend. This confirms the hypothesis of a similar and repeatable degradation in all the tested modules. Based on that, it is assumed that the same degradation processes occur in wire and metallization components. Consequently, analyzing one metallic contact is representative of other metallic contacts.

As a result, SEM analyses were performed first to interpret the microstructural changes at the surface of the metallization layer. Micro-section analyses were then conducted at the wire-metallization interface of different samples aged at different cycling stages using a numerical microscope, in order to see the crack propagation evolution upon aging [Dorn19]. In this work, wire-metallization contacts of the cycled samples, which were prepared by the previous Ph.D. student [Dorn19] just to analyze the crack progress and speed, were analyzed using the EBSD technique to reveal the microstructural evolutions with aging in the vicinity of cracks, and then to be able to explain these changes through relating them to physicochemical aspects. Only the four central chips marked in Figure 40 were analyzed using the EBSD technique since they are the most degraded positions. Nanoindentation measurements were performed on these degraded wire samples in order to relate the evolution of physical properties such as Young modulus and hardness to aging. The EBSD analyses and nanoindentation measurements were made by ELEMCA's laboratory in Toulouse-France.

3 SCANNING ELECTRON MICROSCOPIC (SEM) ANALYSES

Scanning Electron Microscopic (SEM) technique was performed for aged metallization chips in order to interpret the microstructural changes at different cycling stages. The resulting SEM images can be seen in Figure 43. These images were all taken at the same metallization position (near the wire) for the same IGBT chip with an identical magnification [Dorn19].

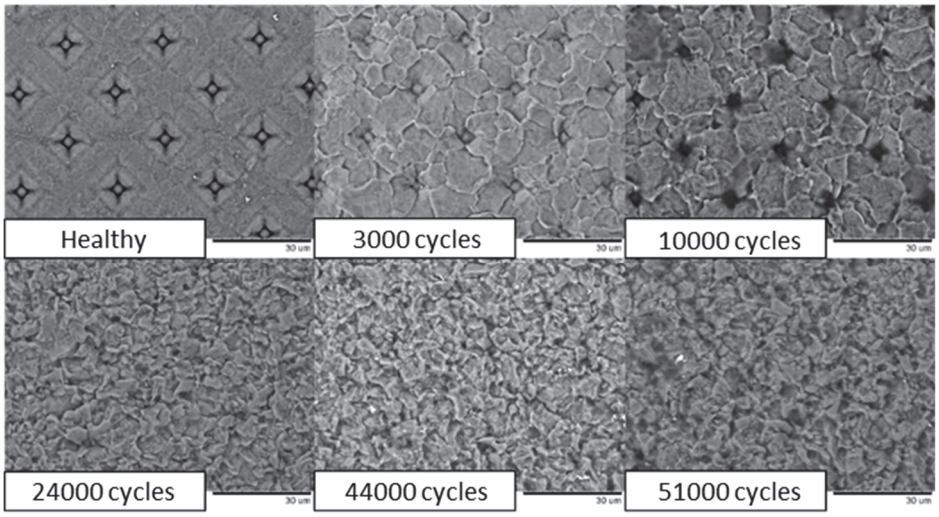

Figure 43: SEM images of the same metallization chips at different aging states [Dorn19].

In the initial state, the multi-elemental cell structure visible in the IGBT metallization chip is in the shape of a checkerboard pattern. This pattern remains visible up to approximately 10,000 cycles due to metallization reconstructions. When reconstructions become intense, this regular structure is no longer detectable. The progressive damage continues, and once 24,000 cycles are reached, the SEM images do not show any more significant degradation evolution inside the metallization. These observations seem to validate the idea that the reconstruction processes of metallization chips mainly occur at the beginning of the aging process, as previously mentioned in the literature [ZAFB19]. The rate of damage in the metallization seems to decrease at advanced cycling stages until reaching a plateau. It should be noted that reconstruction processes are deduced to increase the metallization resistance, as seen in Chapter I [MLLD14], [PØGP15].

Using a numerical microscope, micro-sections were then made at specific parts of aged samples to measure the crack propagation length at the wire-metallization contact at different aging stages. First, the samples are cut using a chainsaw (Secotom-10, Struers) to obtain small IGBT chip samples ready to be used in the analyses. These cuts are made while retaining the silicon gel of the substrate in order to prevent projections from damaging the wires and metallization chips. Subsequently, the gel is removed by immersing the samples in a chemical solvent (Ardrox 2312). The samples are then coated in an epoxy resin, and placed in a vacuum impregnation apparatus (Citovac, Struers) until the resin hardens. After that, for each wire-metallization interface, pre-polishing followed by polishing is carried out on the samples under resin, by which after the end of polishing the first wire-metallization metallic interconnection, polishing is resumed progressively to access the next metallic interface. Thus, this procedure was repeated eight times because each chip possesses eight wires, as presented in Figure 44. Polishing provides a smooth and clean surface to access the wire-metallization interfaces. Grinding is afterward applied to remove the unnecessary materials until reaching the desired location, the wire-metallization contact. Finally, the crack length was measured using a digital microscope (Hirox) [Dorn19]. The same wire numbering shown in Figure 44 will be used in further work in this chapter.

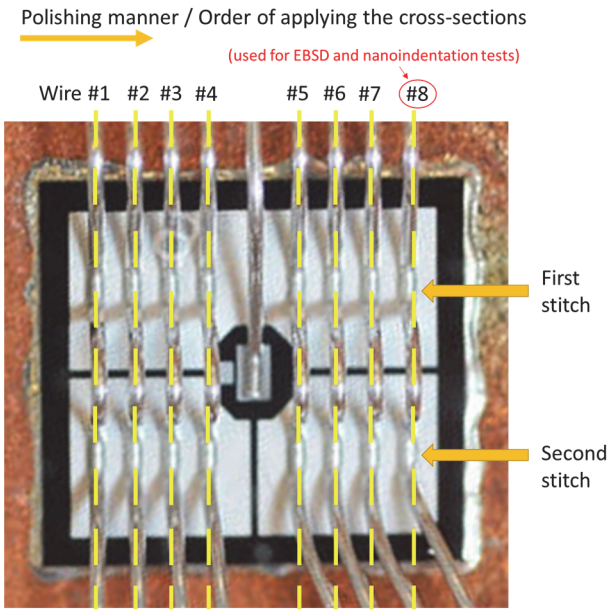

Figure 44: The applied polishing process on wires.

Since it was observed that the cracking manner is identical among all the wires, only one wire-metallization contact per cycled module is enough to present. Figure 45 shows an example of the crack evolution at the wire-metallization interface as a function of the cycling stages, for a wire cycled under the following conditions {ΔT_j = 110 °C, $T_{j\,min}$ = 55 °C, t_{on} = 3 s, t_{off} = 6 s} [Dorn19].

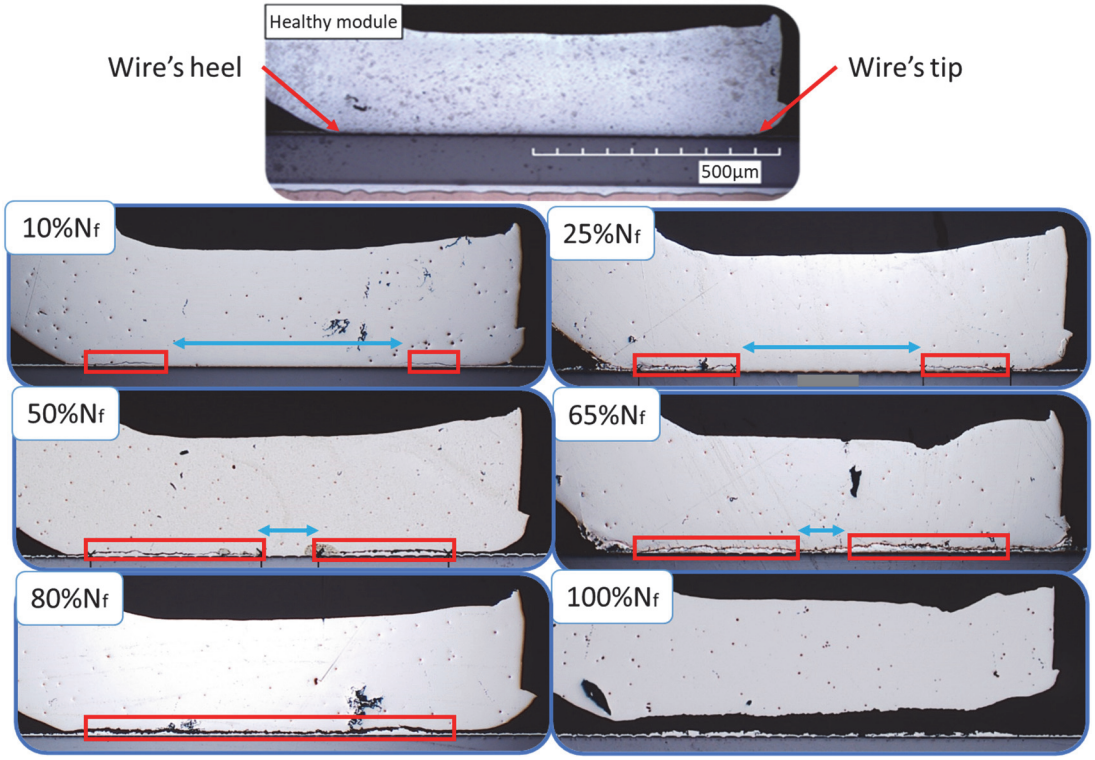

Figure 45: Micro-section analyses showing the cracks evolution at the wire-metallization interface [Dorn19].

Cracking started inside the wire just above the interconnection interface. Cracks are visible at each contact end at 10% N_f, where N_f is the number of cycles to reach failure (≈ 57,500 cycles) for a whole DUT (not for a single wire). Crack's initiation is largely favored at the contact edges, especially at the wire's extremities, due to the presence of initial defects resulting from the ultrasonic wire welding process [AYAE16], and since stress concentrate in such areas upon cycling. It is also deduced that cracks are formed

at the heel position faster than at the tip. This can be realized when looking at the wire's crack path at both wire's tip and heel positions for samples cycled at 10% and 25% N_f. Cracks then continue propagating from both edges toward the center of the bottom wire zone, as observed in the sample cycled at 50% N_f. The crack propagation is not occurring exactly at the wire-metallization interconnection interface; however, it occurs just above the interconnection interface at the bottom parts of the wire. The crack propagation speed at advanced cycling stages seems to be slower than the speed of the crack initiation. At 65% and 80% N_f the crack is almost complete. This is because the N_f value used here is a mean value averaged among several wires as mentioned before; thus, this analyzed wire is damaged more than the average damage of other wires. The reason is that this wire is one of the wires positioned in the central IGBT chips. When N_f is reached, cracks are totally distributed at the entire bottom wire zone, where total separation (lifting-off) occurs. All these observations are coherent with the literature and experimental data [AYAE16], [LCLH07].

4 ATOMIC FORCE MICROSCOPIC (AFM) ANALYSES

Atomic Force Microscopy (AFM) has been frequently used to study surface phenomena because it allows intensive observation of materials' surfaces. AFM can analyze any part of the surface morphological structure in three dimensions. Therefore, this method provides more information about some microstructural processes than other traditional equipment. AFM can calculate critical parameters such as the depth and width of grooves in case of grooving, which takes place mostly when materials are annealed at high temperatures [JiSI99]. AFM also shows the formed hillocks when the metallization layer is subjected to reconstruction processes. Subsequently, this technique is able to obtain the value of the surface roughness. As explained in Chapter I, the increase in surface roughness could signify the formation of cracks [KPWD11]. It also has several effects on the properties of the materials, such as decreasing their strength and chemical stability and increasing their electrical resistance [ZAFB19]. Therefore, AFM is a valuable technique for studying the microstructural changes at the topside metallic parts in semiconductor power devices.

Some AFM analyses were performed to see the topographical changes at the surface of the metallization layer near and far from the bonding wire. Figure 46 (a) shows the three-dimensional surface topography of aluminum cells before cycling. Figure 46 (b) shows aluminum metallization cells close to the wire when N_f is reached. Figure 46 (c) shows aluminum metallization cells far from the wire when N_f is reached.

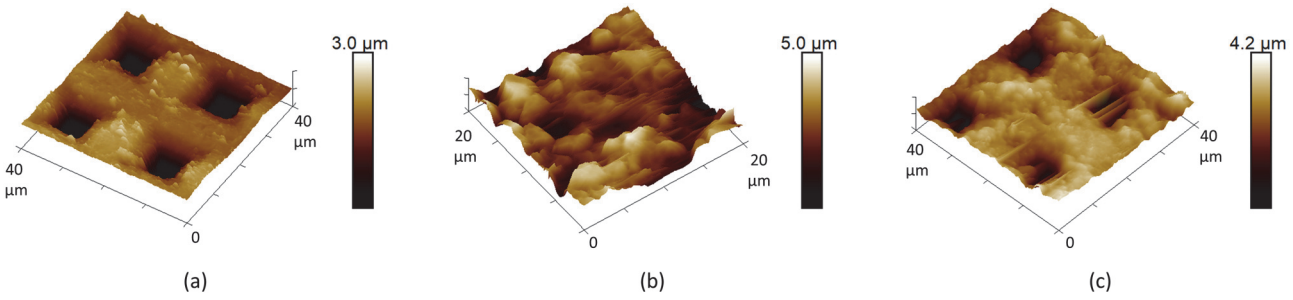

Figure 46: AFM images for (a) non-degraded IGBT metallization cells, (b) degraded IGBT metallization cells near the wire at N_f (c) degraded IGBT metallization cells far from the wire at N_f.

When the sample is healthy, the morphology of the cells is regular. This is not the case with cells near and far from the wire after cycling, where micro-valleys and hillocks are formed. For the cells far from the wire, their structure is more regular than those near the wire, with lower extrusions and surface roughness. The maximum height or depth of the formed hillocks and voids far from the wire was about 4.2 µm; however, this value was about 5 µm for cells near the wire. Additionally, the number of formed hillocks and voids on the metallization surface far from the wire is lower than at the metallization surface near the wire. This is because the interconnection zones are more distorted due to the accumulation of deformations and stress near the metallic interconnections.

5 ELECTRON BACKSCATTER DIFFRACTION (EBSD) ANALYSES

The ESBD technique is one of the most important and used analysis techniques in terms of microstructural outputs. This technique, with the help of any complementary image and structure analysis tool like the ATEX software [BeFu17], is used to characterize the local microstructure by giving the distribution of the size, shape, texture, and orientation of grains. Consequently, the evolution of all these parameters is configured in this EBSD analysis. Moreover, the crack evolution can be microstructurally interpreted when applying this analysis.

In fact, after applying the SEM and AFM microstructural analyses, it was deduced that the microstructural changes and the crack progress occur for all the degraded samples and are synchronous with aging. Based on that, EBSD analyses were carried on in this Ph.D. work to better study these processes on the wire-metallization contacts. The previously degraded IGBT samples that were analyzed microstructurally using SEM and AFM are used in these EBSD tests [Dorn19]. The main hypothesis assumed when doing these analyses is that all wire-metallization contacts degrade in the same manner upon aging.

The modules analyzed using the EBSD technique are aged at the following thermal stress conditions {ΔT_j = 110 °C, $T_{j\,min}$ = 55 °C, t_{on} = 3 s, t_{off} = 6 s} as mentioned previously. Aged samples were withdrawn at different cycling stages. In the EBSD analyses, only the first stitch of the wires as shown in Figure 44 was analyzed, since the second one is not aligned with the polishing plane. Because grinding was applied from left to right to analyze crack propagation, as explained in section #3 (see Figure 44), the last interface in contact with the chip was left to apply the EBSD analyses. This interface is surely not the most degraded interface among the eight others since it is situated on the exterior parts of the chip; however, it nonetheless provides information about the microstructural changes occurring upon aging. The same wire numbering shown in Figure 44 will be used in the following analytical study. In *Table* 3 below, some information about the main conditions of the EBSD tests applied is listed.

Table 3: EBSD tests conditions.

Resolution (Width, Height)	3333 pixels, 667 pixels	Specimen tilt (degrees)	70°
Field (Width, Height)	1 mm, 0.2 mm	EBSD Camera Pixel Grouping Mode	4x4 (336x256 pixels)
Static & Auto Background Noise Correction	On	EBSD camera exposure time	24.4 ms
Tilt axis	Parallel to X	Acceleration voltage	20 kV

5.1 GENERAL ANALYSIS: MICROSTRUCTURAL EVOLUTION'S INTERPRETATION FOR THE WHOLE WIRE AND METALLIZATION COMPONENTS DURING CYCLING

Using the EBSD technique, this first analysis was done to interpret the distribution and evolution of grains' size, morphology, boundary disorientation angles, and texture for wire #8 in chip #7 as labeled in Figure 40 and Figure 44.

- **Grains' sizes analyses**

  Primarily, to identify grains, the definition of a critical disorientation angle is required, so that all boundary segments with an angle higher than the defined angle are considered grain boundaries. This angle is set to be 5° in this analysis, as reported in the literature [GuLe19]. The grain size significantly impacts grains' strength against cracks, where smaller grains acquire higher strength according to the Hall-Petch relationship [HaKS03], [Hans04], [ZZYH16]. For that, it is important to study the evolution of grains' size.

The mapping seen in Figure 47 for (a) a healthy sample, (b) cycled at 10% N_f, (c) cycled at 50% N_f, and (d) cycled at 100% N_f presents the grain size distribution according to a colour code ranging from blue (smallest grains) to red (biggest grains). The size of each grain is determined by calculating the diameter of its equivalent circle.

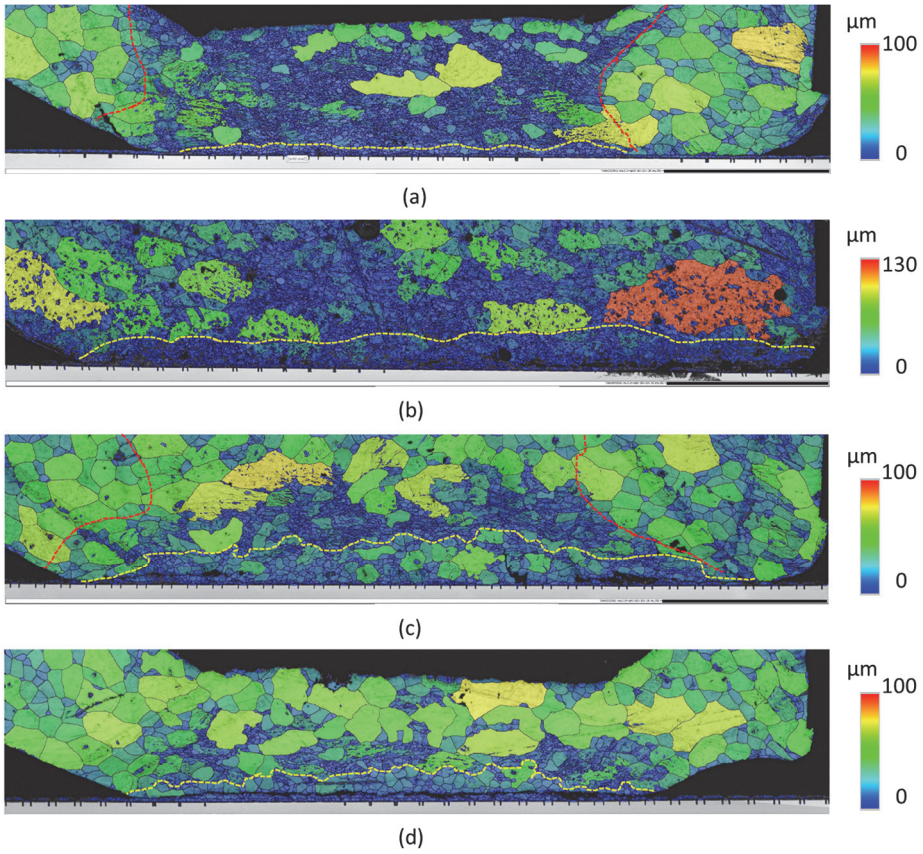

Figure 47: The distribution of grains size in (a) a healthy sample, (b) cycled at 10% N_f, (c) cycled at 50% N_f, and (d) cycled at 100% N_f.

According to the data shown in Figure 47, the following conclusions can be reported. In the healthy sample, the grain size distribution shows that the samples can be divided into three main zones. The first zone (zone A) is outside the contact area at the wire's extremities, in which the grains are not affected by the wire welding process and are randomly arranged with generally big sizes (40-100 µm). The second zone (zone B) is over the wire-metallization interconnection interface, where grains are highly impacted by the ultrasonic forces when welding the wire and are smaller than those in zone A, with a highly random distribution of sizes. The last zone (zone C) is just at the interconnection interface between the wire and the metallization layer, with grains having the smallest sizes (< 10 µm), where the highest impact of ultrasonic forces exists.

Upon cycling, the three zones remain but evolve independently until reaching total failure. The zone outside the contact area at the wire's extremities (zone A) does not seem to change. Inside the wire above the wire-metallization contact (zone B), the microstructure seems to return to its initial state, similar to the microstructural form outside the contact area (zone A), caused by grains reconstructions, resulting in an increase in the size of the grains. This phenomenon is activated by the induced temperatures during the power cycling (55 °C to 165 °C) and is enhanced by the plastic deformations resulting from the wire welding process. Regarding the wire-metallization interface (zone C), it is seen that upon cycling, the size of grains increases. This zone is also a thermally activated zone caused by grains' reconstruction. The causes behind these granular deformations in zone C are the same as for grains in zone B; however, this zone has more significant enhancing factors, especially that such position is the most affected position by the deformations caused by the wire welding process; in addition, major deformations resulting from the power cycling occur there. Such observations in the

three zones are consistent with the information mentioned in the literature [KWBS12], [MKSG08].

- **Grains' morphology analyses**

The EBSD technique explores the morphology of grains as well. It is interesting to study the morphology of grains since the grain boundaries will be changed with the change of the grain's shapes; thus, the boundary characteristics will vary. It was also reported that the grain shape mostly affects the stress tensor's component for each stress state [SaDH11]. Based on these information, the morphology of grains is discussed.

The shapes of grains are identified by superposing an ellipse on each grain. The form factor considered is the ratio of the major axis to the minor axis of the superposed ellipse. Each grain is then coloured from blue to red, depending on the value of this form factor. As the form factor has low values, the grain is more circular. When the form factor is high, the grain is more elliptic. It was reported that the ductility of grains is influenced by their aspect ratio (or form factor) [RaHP13]. A change of the grain aspect ratio during deformations should lead to softening or hardening of the material depending on the specimen and grain orientation. Figure 48 shows the evolution of the morphology of the grains for (a) a healthy sample, (b) cycled at 10% N_f, (c) cycled at 50% N_f, and (d) cycled at 100% N_f.

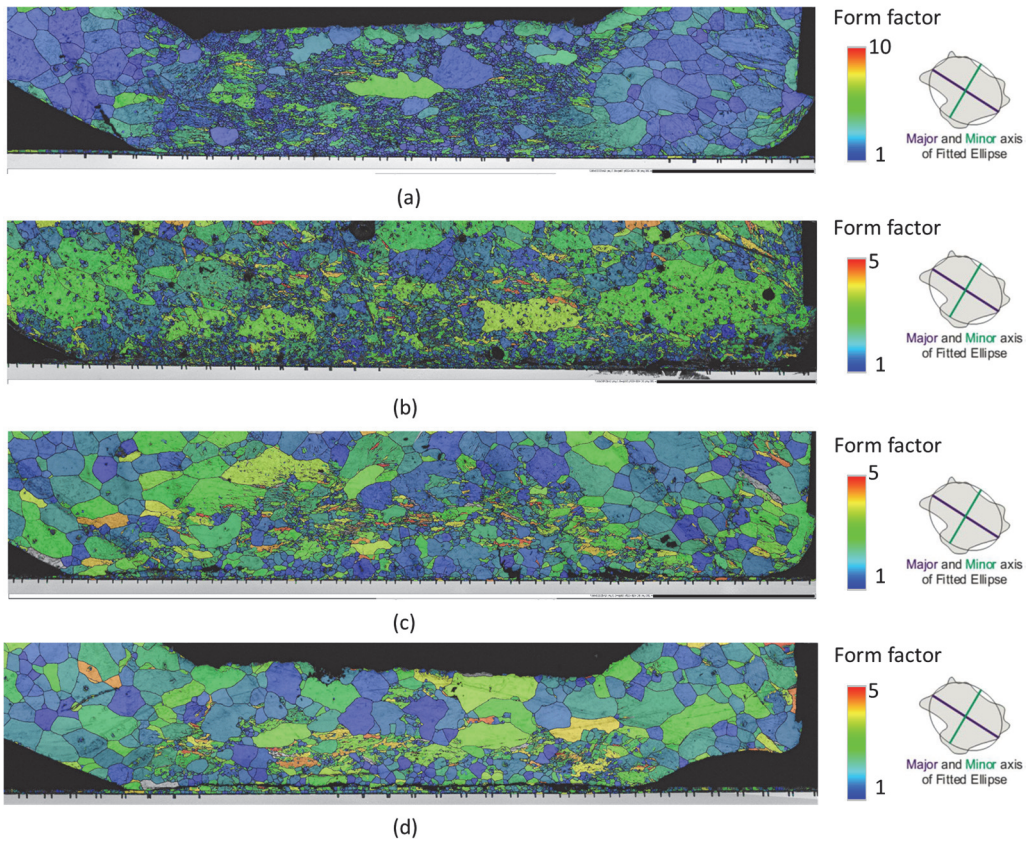

Figure 48: The distribution of grains shape in (a) a healthy sample, (b) cycled at 10% N_f, (c) cycled at 50% N_f, and (d) cycled at 100% N_f.

From Figure 48, it is deduced that grains generally tend to be less equiaxed upon cycling in all zones. This is caused by boundary migrations and grain growth processes. Some grains tend to be more circular when deformations and sub-grains are formed. This is the case for some grains in zone C, especially at the early cycling stages, caused by the rearrangements of dislocations resulting from the wire welding process.

- **Boundary disorientation angles' analyses**

Boundary disorientation angles affect several grain properties. They affect the value of grain boundary energy which in turn impacts the stability of grains [HaGo71]. Disorientation angles also affect the passage of dislocations and movement of deformations upon cycling [DSWN19]. Moreover, they highly affect the crack propagation process [ZZYH16]. Figure 49 shows the distributions of the disorientation angles among grain boundaries for (a) a healthy sample, (b) cycled at 10% N_f, (c) cycled at 50% N_f, and (d) cycled at 100% N_f. Angles in dark and light blue refer to LABs, whereas other colours signify the presence of HABs.

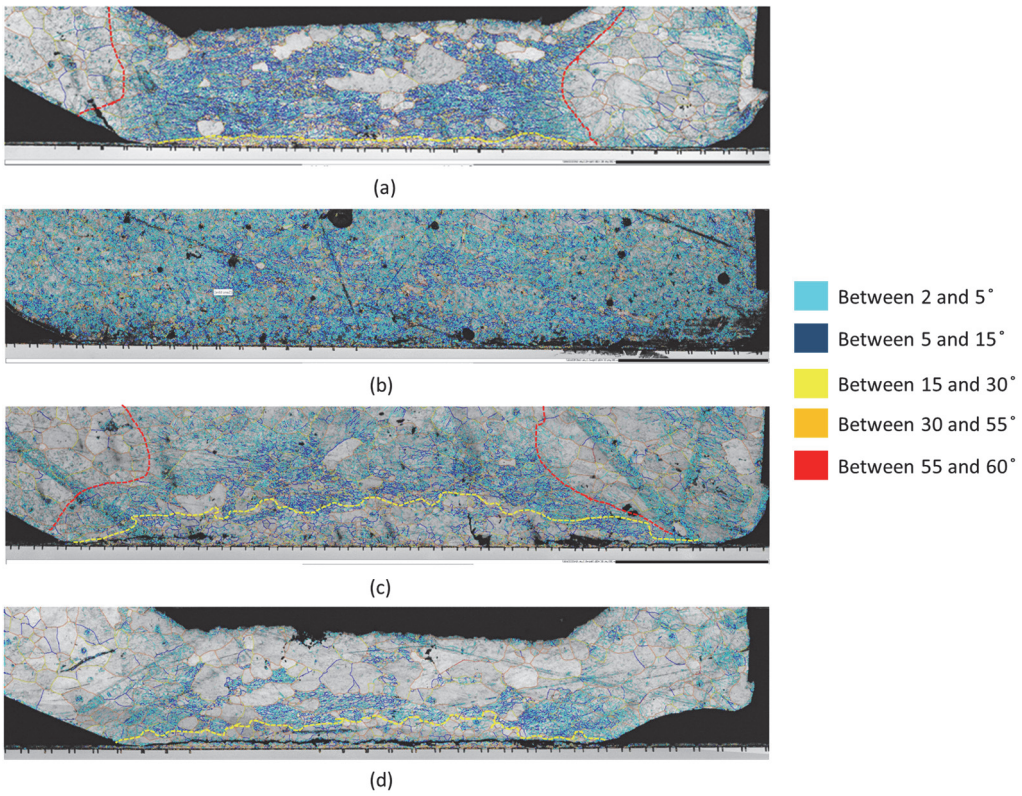

Figure 49: The distribution of grain boundary disorientation angles in (a) a healthy sample, (b) cycled at 10% N_f, (c) cycled at 50% N_f, and (d) cycled at 100% N_f.

A high variation in disorientation angles among neighbor grains is observed in Figure 49. From this image, it is difficult to conclude a general tendency for the evolution of the disorientation angles, especially since the quality of the image corresponding to the sample cycled at 10% N_f is low. It can be deduced that the highest concentration of LABs is always inside zone B. Generally, the concentration of LABs decreases when cycling is advanced. Some HABs become visible in zone C at 50% N_f and when getting closer to N_f. This is verified when looking at the image corresponding to 100% N_f, where the fraction of HABs to LABs is the highest among all the preceding images.

- **Grains' texture analyses**

The grain texture is essential to study since it directly affects the value of surface energy which in turn affects the stability of grains [ZhMX04]. The change in texture means a change in the atomic packing density, thus changing the grains' stability [BWKP18]. Grain's texture is obtained by plotting the IPFs. IPF cartographies corresponding to the x and y directions are plotted for each sample. Figure 50 shows the IPFs evolution for (a) a healthy sample, (b) cycled at 10% N_f, (c) cycled at 50% N_f, and (d) cycled at 100% N_f.

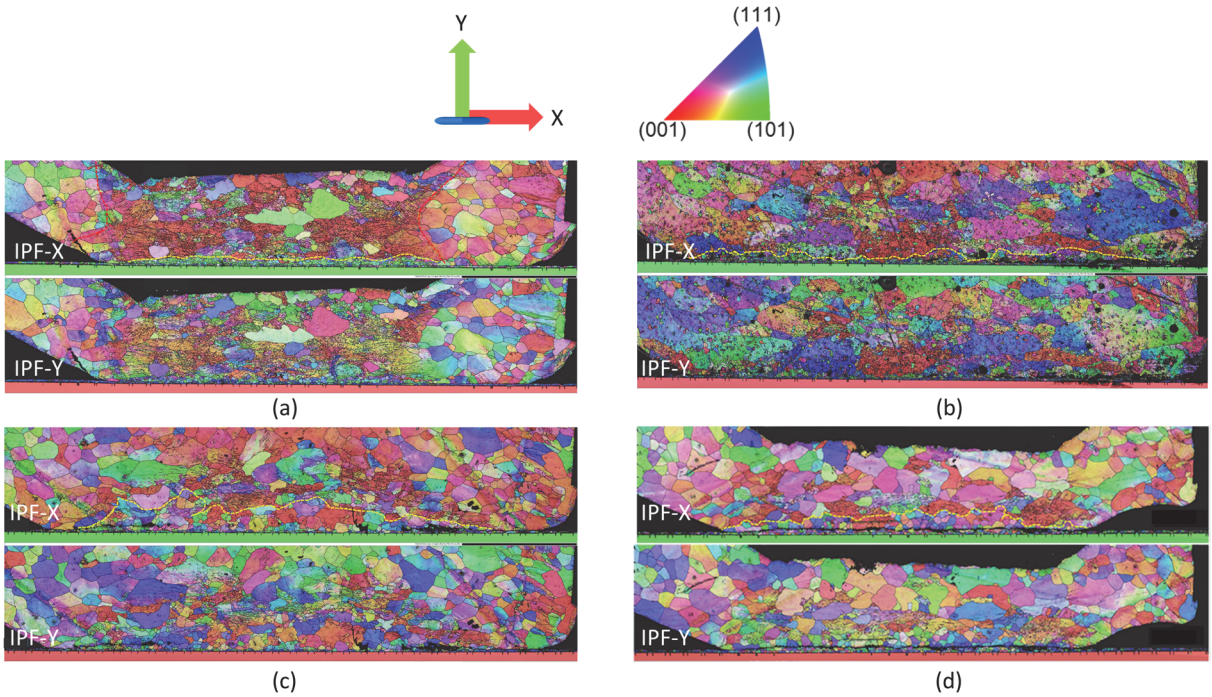

Figure 50: The distribution of grains orientations planes in (a) a healthy sample, (b) cycled at 10% N_f, (c) cycled at 50% N_f, and (d) cycled at 100% N_f.

IPF images show that different textures are present in the sample's microstructure at the initial state. Upon cycling, gains' orientation planes change in all the metallic contact locations, where grains at each position orient differently. The evolution of these orientation planes upon cycling is highly random among all the different samples. Therefore, from these figures, it is not easy to deduce a general manner of grains' orientation behavior upon cycling. The effect of the change in the grains' planes of orientation should be studied locally when examining their contributions to the degradation processes.

Overall, this EBSD analysis shows that interpreting the evolution of the grains' size, shape, texture, and disorientation angles upon cycling is difficult, especially at the wire-metallization interface where cracks are formed. To better analyze the evolution of such parameters, it is necessary to choose a specific zone and work on it. Consequently, partitioning analyses at specific zones are performed in the upcoming sections, where the zone of interest was selected using the ATEX program. In this work, the zone to be selected is just at the wire-metallization contact, where deformations and cracks originate.

5.2 Partitioning analyses I: Interpreting the microstructural changes inside the wire at the metallic topside contact during cycling

Since cracks propagate inside the wire just above the metallization layer, as seen in the literature [AYAE16] and Figure 6, more focus inside this zone should be considered. Partitioning the sample offers a better analysis of the main microstructural features that change upon cycling at the zone of major deformations and crack progress. This first partitioning inside the wire just above the metallization was primarily made to verify and eventually confirm that the planes of orientations of grains change to reduce the surface energy and increase the atomic packing factor. In the next step, this portioning was used to analyze the cracking progress upon cycling by interpreting the evolution of grains' sizes and disorientation angles. The partitioned zone in these analyses is schematized, as shown in Figure 51.

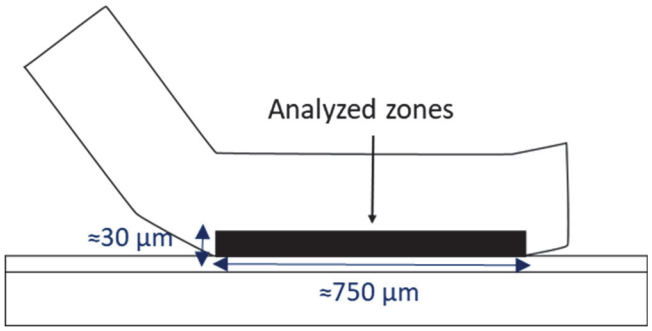

Figure 51: The partitioned zone in the partitioning analyses I.

As mentioned previously, the driving force for materials to reconstruct is reducing the surface energy, which increases their stability [BGHS15], [Buhr18], [TXRW16]. This is the same driving force for the grain growth process [Care95], [SKSM20], [Thom85], [TXRW16]. The higher the packing density, the greater the number of neighbor atoms. This means that the more atomic bonds in these zones, the lower the surface energy. It was seen that for FCC metals such as aluminum, the decreasing order of packing density of crystal faces is for (111), (001), and (101) planes respectively [PBSP17]. The decreasing order of surface energy values for the crystal faces is for (101), (001), and (111) planes respectively [ZhMX04]. Therefore, from the EBSD analyses, it should be noted that the (101) orientation will be less enhanced to be formed since it has the lowest packing density and the highest surface energy. The tendency of grains' orientation should go towards the (111) orientation since it has the highest packing density and lowest surface energy.

Accordingly, EBSD partitioning analyses (as in Figure 51) were performed for different wires in the same position just above the metallization at different cycle numbers to confirm that grains orient in a way to increase the packing density of atoms and decrease the surface energy. The same orientations' colour scale and samples' directions shown in Figure 50 will be considered for all the upcoming IPF maps. The same chips' and wires' numbering in Figure 40 and Figure 44 are used in the following analyses. Starting with Figure 52, this figure shows the IPFs at different cycling stages for wire #8 in chip #2, where (a) is a healthy sample, (b) cycled at 25% N_f, and (c) cycled at 50% N_f.

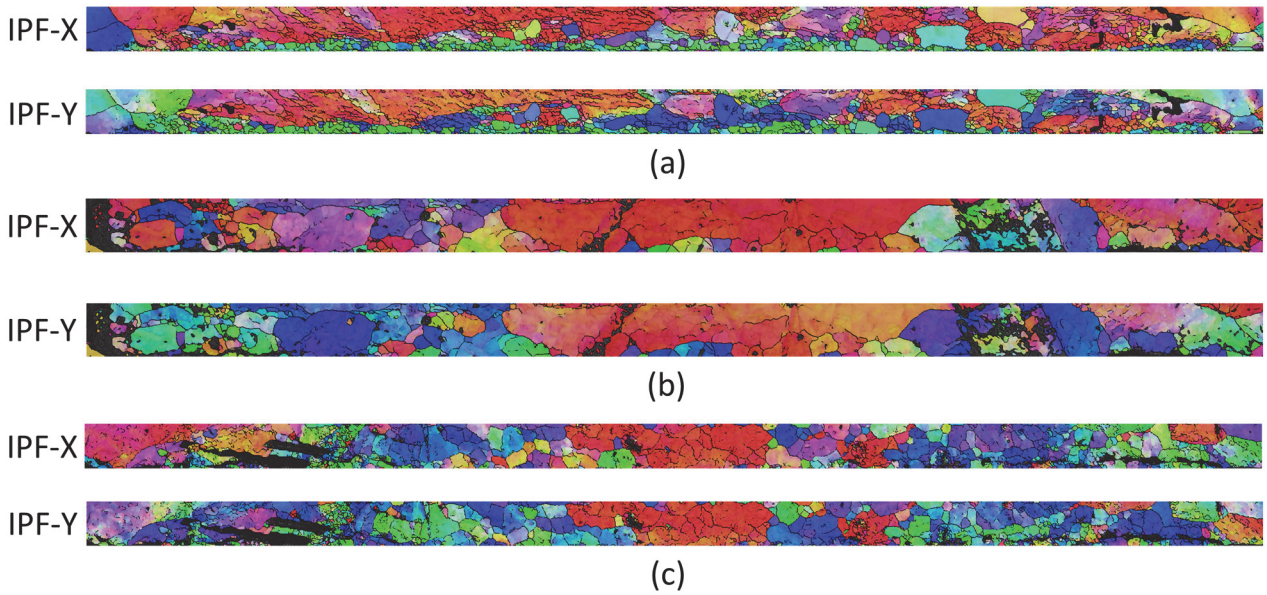

Figure 52: IPFs showing the grains' orientation evolution for wire #8 in chip #2, where (a) is a healthy sample, (b) is cycled at 25% N_f, and (c) is cycled at 50% N_f.

Referring to the IPFs observed in Figure 52, and upon cycling to 25% N_f, we can see that in the x and y directions, the (101) grains' orientation which was dominating at the wire-metallization interface and wire's

center in the healthy state highly decreased. After 50% N_f, more (111) grain orientations are generated in the x and y directions, in addition to the generation of some (001) orientations.

The same analysis was applied for wire #8; however, in chip #7 (a) at a healthy state, (b) cycled at 10% N_f, and (c) cycled at 50% N_f, as observed in Figure 53.

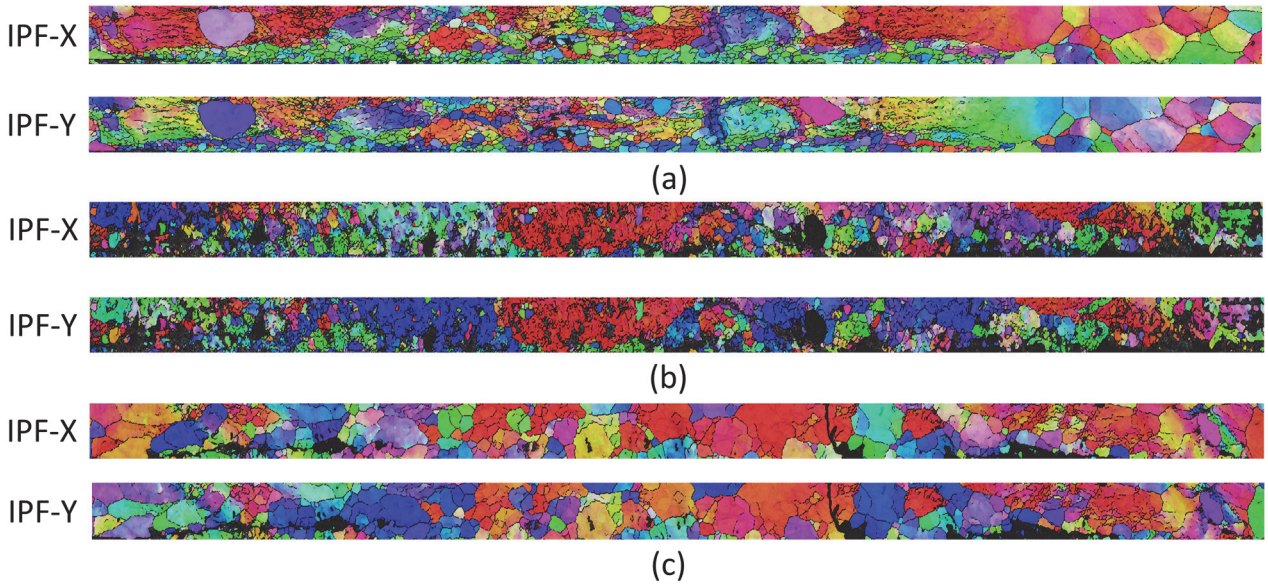

Figure 53: IPFs showing the grains' orientation evolution for wire #8 in chip #7, where (a) is a healthy sample, (b) is cycled at 10% N_f, and (c) is cycled at 50% N_f.

For wire #8 in chip #7, and upon cycling the sample to 10% N_f, a lower frequency of (101) grains' orientation can be deduced when looking at the x and y directions, with an increase in the (111) orientation. When cycling to 50% N_f, the (101) grain orientation highly decreased in both the x and y directions as well, with the generation of (001) and (111) orientations aside.

Figure 54 shows advanced cycling stages for the same wire and chip positions as in Figure 53 (wire #8 in chip #7); however, for a different IGBT SKIM63 sample, where (a) is cycled at 65% N_f and (b) is cycled at 80% N_f.

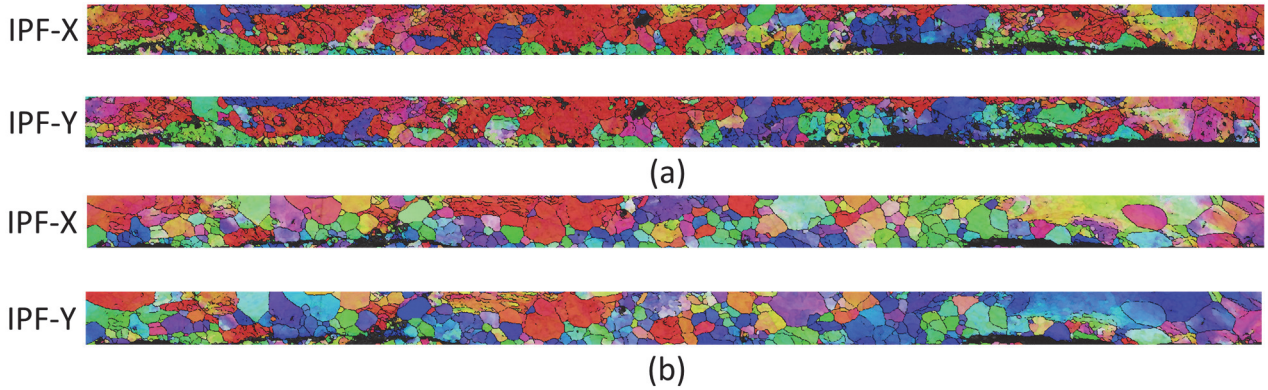

Figure 54: IPFs showing the grains' orientation evolution at advanced stages for wire #8 in chip #7 for a different IGBT sample than the one analyzed in Figure 53, where (a) is cycled at 65% N_f and (b) is cycled at 80% N_f.

Based on Figure 54, and upon cycling the same chip and wire positions as in Figure 53, however, for a different IGBT sample, it can be deduced that more (111) orientations were generated, particularly in the y-direction. In the x-direction, the distribution of orientation planes seems to be random; however, the

frequency of the (101) orientation is shallow, where some (001) orientations have been oriented to the (111) orientation.

All the results presented in Figure 52, Figure 53, and Figure 54 confirm that grains orient in a way to reduce the surface energy and increase the atomic packing density. In this way, it is confirmed that reconstructions reduce the surface energy, increasing grains' stability as reported in the literature [BGHS15], [Buhr18], [TXRW16]. Since it is also reported in the literature that the highest packing density crystal orientation has the lowest surface energy and vice versa [PBSP17], [ZhMX04], this means that grains and in order to stabilize, tend to have denser structures.

Other important outcomes can be extracted from this partitioning by analyzing the evolution of the distribution of grains' sizes and disorientation angles. As mentioned previously, the size of grains significantly impacts grains' strength against cracks [HaKS03], [ZZYH16], by which when the grain size decreases, its strength increases and vice versa. Figure 55 shows the evolution of the number fractions of grain sizes for two wires (in chips #2 and #6) at early cycling stages (reaching 25% N_f), at which the crack speed is maximal, as deduced from Figure 45.

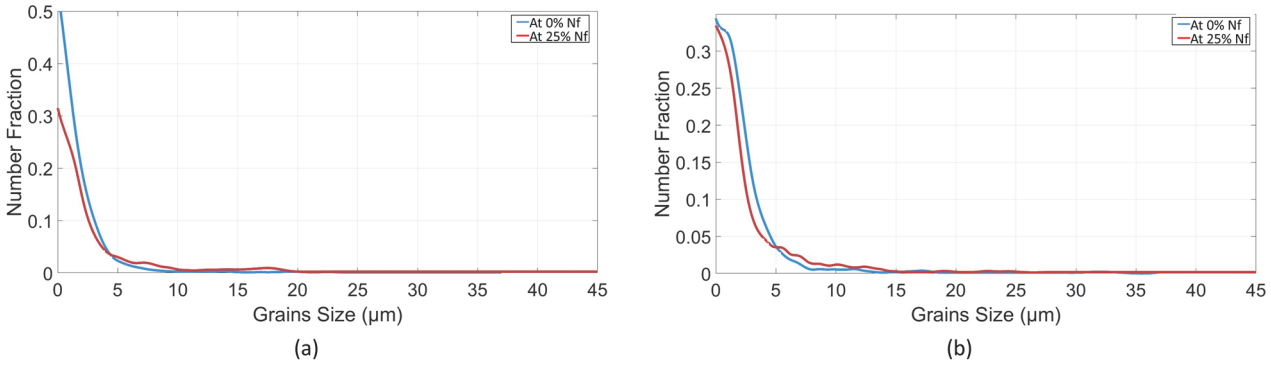

Figure 55: The number fractions' distribution of grain sizes upon cycling wire #8 in chips (a) #2 and (b) #6.

From Figure 55, it can be deduced that rapid crack initiation is synchronous with grain growth because, in both samples, bigger grains are formed upon cycling. The grain growth process is deduced from the existence of smaller fractions of grains having tiny sizes and the presence of small fractions of grains acquiring high sizes, indicating the presence of one or two huge grains. These big grains may occupy a large volume in the microstructure.

Thereafter, the evolution of grain boundary disorientation angles is interpreted at the advanced cycling stages. Disorientation angles influence the formation and propagation of cracks [BGHS15], [DSWN19], [Gour02], [SaMS11]. Figure 56 shows the evolution of disorientation angles' number fractions for two wires (in chips #2 and #6) at advanced cycling stages (65-100% N_f), at which the crack speed is decreasing.

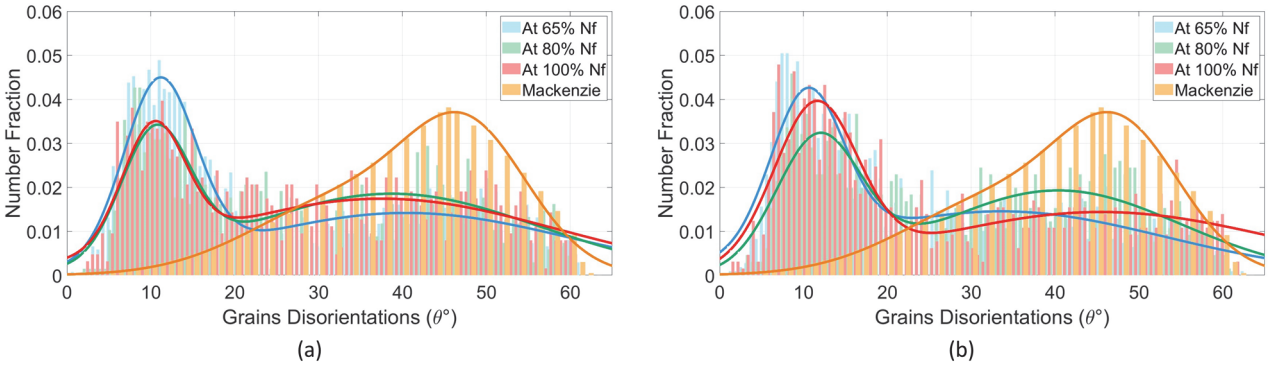

Figure 56: The number fractions' distribution of grain boundary disorientation angles upon cycling wire #8 in chips (a) #2 and (b) #6.

It has been observed in Figure 56 that cracks evolution is synchronous with the decrease in the number fractions of LABs and the increase in the number fractions of HABs in both wire samples when comparing the portion cycled at 65% N_f with that at 80% and 100% N_f. When only comparing the portions cycled at 80% and 100% N_f with each other, it is observed that the sample cycled at 100% N_f (total failure) has higher LAB and lower HAB number fractions. This may be because the cracks themselves induce deformations, especially at 100% N_f, which is the lifting-off moment [LiLD05], [LiPo18]. The rearrangement of deformations to sub-grains at this cycling stage, specifically near the metallic interface, may cause this observation. This is verified by the decrease in the rate of grain growth seen in Figure 49 (c and d) when cycling is at advanced stages. This may result in an increase in the number fraction of LABs.

In the upcoming section, deeper analyses are conducted by studying specific interconnection positions in the vicinity of cracks in order to relate the changes there with the degradation processes. Thus, another partitioning procedure was made.

5.3 PARTITIONING ANALYSES II: INTERPRETING THE MICROSTRUCTURAL CHANGES AT THE HEEL, CENTER, AND TIP POSITIONS INSIDE THE WIRE AT THE METALLIC TOPSIDE CONTACT DURING CYCLING

In order to have a better analysis of the crack propagation behavior, this new partitioning at the positions of cracks' nucleation is necessary. This partitioning is used to deeply interpret the degradation processes and the microstructural and material properties evolution within cycling. The same orientations' colour scale and samples' directions shown in Figure 50 will be considered for all the upcoming IPF maps. The same chips' and wires' numbering in Figure 40 and Figure 44 are used in the following analyses.

5.3.1 Microstructural analysis before cycling

The two most critical positions at the wire-metallization metallic contact are the heel and tip terminal edges, the positions where stress concentrate and cracks initiate. The metallization parts in contact with the wires will be analyzed just in this section for the healthy sample, since it is already known that cracks do not propagate there. Analyzing the wire-metallization healthy contacts is important to configure the initial microstructure. Additionally, the data obtained from the healthy sample will be the reference for the derived data of cycled samples which will be presented in the next section by applying the same partitioning manner for degraded samples at different cycling stages. Moreover, partitioning the healthy sample is helpful for knowing the properties of materials before cycling. These properties will be used later to model the crack's formation in the upcoming chapter.

In this section, the manner of partitioning the healthy sample at both heel and tip metallic contact positions is represented in Figure 57. The same chips' and wires' numbering in Figure 40 and Figure 44 are used in the following analyses. Wire #8 in chip #6 is used in these analyses.

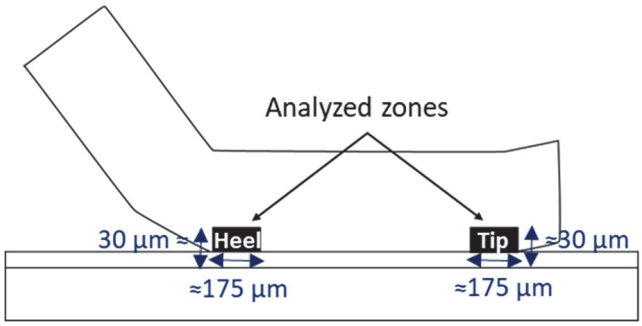

Figure 57: The heel, tip, and center partitioned positions in the partitioning analyses II (healthy state).

- **Partitioning at the heel position:**

The partitioning at the heel position is well shown in Figure 58. The partitioned wire and

metallization samples are just at the heel wire-metallization terminal contact.

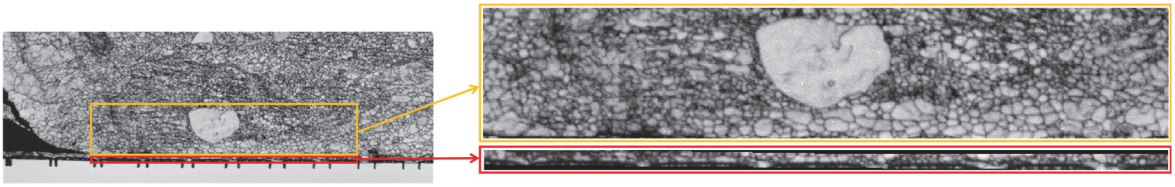

Figure 58: The partitioning made for the healthy sample just at the heel wire-metallization metallic contact.

In this part, the grains' size distribution is interpreted. Then a texture study is performed by plotting the IPFs, followed by Direct Pole Figures (DPFs) to know the present texture components. Texture components provide information at specific zones, whether deformation or recrystallization processes exist at the wire-metallization contact edges before cycling.

A. Grains' size analyses

Figure 59 shows the grain size distribution at the heel metallic interconnection interface for the partitioned metallization and wire portions in the healthy sample.

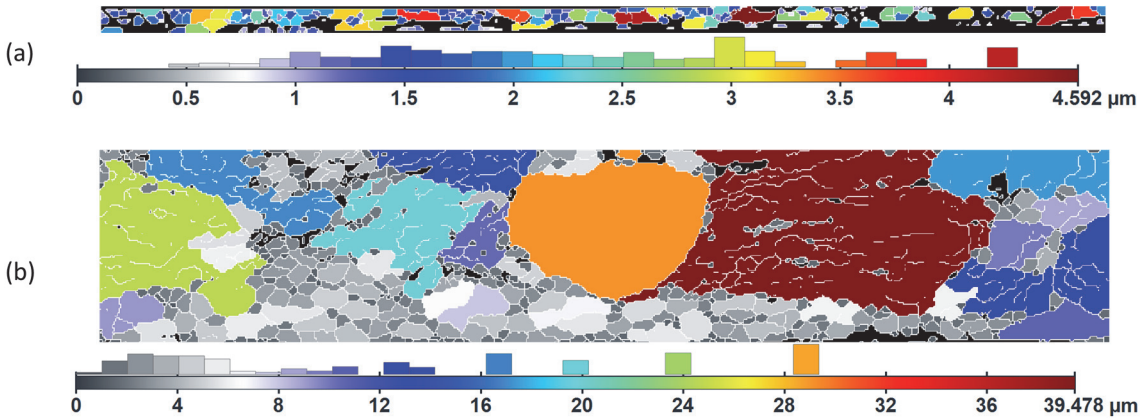

Figure 59: Grains' size distribution at the healthy heel wire-metallization metallic contact for the partitioned (a) metallization and (b) wire samples.

Grains inside the metallization layer have almost the same size between 1-4.5 µm since they compose the metallization thin film's thickness; this results in high-strength grains. However, inside the wire, there is a variety in the size of grains, where it is possible to see tiny grains near big grains reaching 39.5 µm; thus, a wide variety in terms of strength exists [Hans04].

B. Grains' texture analyses

Afterward, IPFs are presented in Figure 60 for the partitioned metallization and wire portions in the healthy sample at the heel metallic interconnection interface.

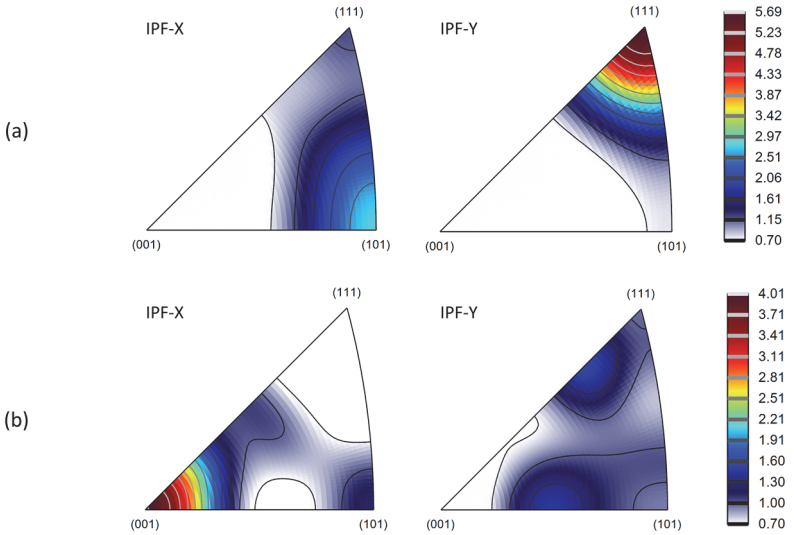

Figure 60: IPFs at the healthy heel wire-metallization metallic contact for the partitioned (a) metallization and (b) wire samples.

The microstructure of the metallization is clearly textured in Figure 60 since it is orientated preferably towards the (111) plane in the y-projection. Concerning the wire portion just at the metallic interconnection interface, the preferred orientation of grains in the x-direction is (001). These orientations are essential to know since they are directly related to material stability, as explained in the previous section. DPFs, which are 3D grain orientation representations, can also be plotted based on the orientations seen in the IPFs in order to give additional information about the existing orientation planes.

The DPFs of the analyzed samples are compared to the ideal and preferred DPFs studied in the literature, which are under the name of “ideal texture components” [BTAA18], [LiBB05], [LPHZ18], [ZhTN92]. Diverse classifications of these ideal texture components exist according to the nature of the material under study, whether it is in a rolled or sheared deformation state, and if the structure corresponds to FCC crystal structure or has another crystal type. In our case, rolled FCC classifications are considered since the deformed material is an FCC metal (aluminum). Each ideal texture component in rolled FCC classifications possesses particular characteristics. For example, the Cube (Cb) and Goss (Gs) textures are associated with recrystallization phenomena [Hu74], [KePi16], [LPHZ18], [NyNa13], [PaCP12], whereas Brass (Bs), Copper (Cu), Taylor (Ty), and (S) type textures are linked to deformation processes [ZhTN92]. Hence, by comparing the DPFs in our samples to those ideal texture components, we can deduce whether the microstructure is arranged in an ideal orientation. This gives information about its properties, whether the material is recrystallized or deformed.

The DPFs at the heel metallic interconnection interface for the partitioned metallization and wire portions in the healthy sample are plotted in Figure 61. These figures confirm what has been seen in the IPFs in Figure 60 about the orientation of grains. From the plotted DPFs, the crystal texture components can be deduced, as shown in Figure 62.

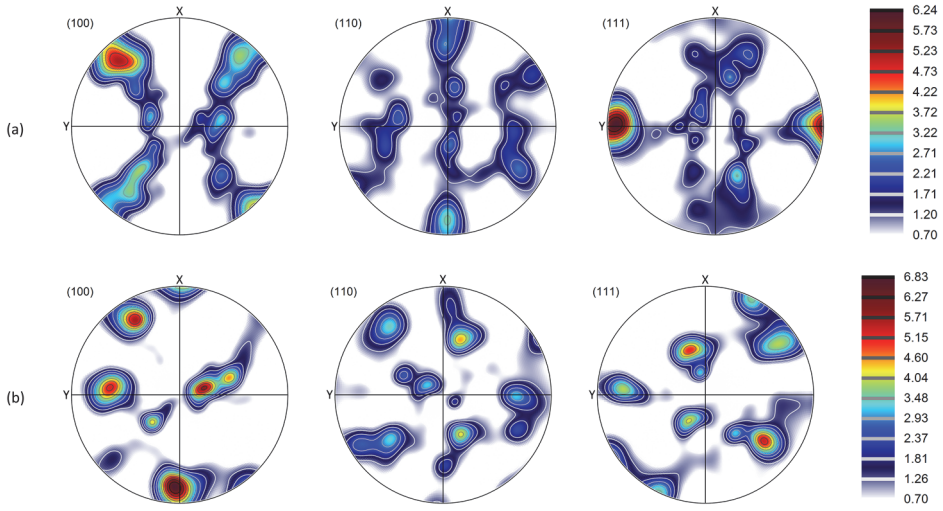

Figure 61: DPFs at the healthy heel wire-metallization metallic contact for the partitioned (a) metallization and (b) wire samples.

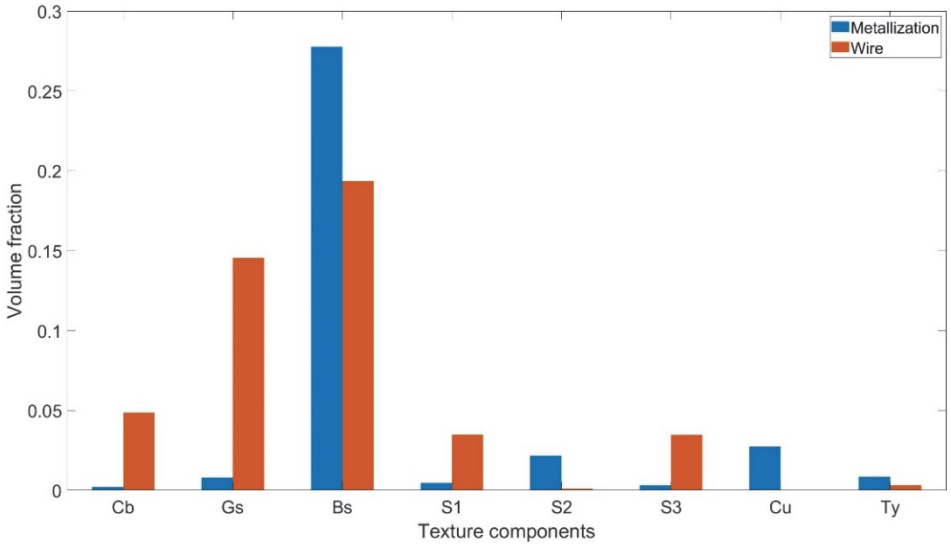

Figure 62: Texture components present at the healthy heel wire-metallization metallic contact for the partitioned (a) metallization and (b) wire samples.

By looking at Figure 61, the grains' orientations observed in Figure 60 are confirmed. The presence of crystal texture components in the microstructure before cycling, as observed in Figure 62, results from the wire welding process. Such texture components are compared to the characteristics of ideal orientations as reported in the literature [KePi16], [LPHZ18], [NyNa13], [PaCP12], [ZhTN92]. It can be deduced that the microstructure of the metallization shows a strong Bs texture. The Bs component has been associated in the literature with deformations [PaCP12], [ZhTN92]. Alternatively, the microstructure of the wire at the interconnection interface exhibits strong Bs, Gs, and Cb textures. Gs and Cb components are generally linked to recrystallized microstructures [NyNa13]. Hence, these results confirm the fact that the initial microstructure of the wire interfacial zone is mainly the result of a thermal-active phenomenon such as recrystallization. Upon cycling, cracks seem to propagate preferably in this zone. This was also reported by Yang and others [YaAJ14]. Hence, Gs and Cb texture components could favor the growth of cracks. This may be evidenced by recrystallization followed by grain growth, resulting in bigger grain sizes and thus weaker grains according to the Hall-Petch law.

- **Partitioning at the tip position:**

  As for the heel, partitioning just at the tip wire-metallization terminal contact is made for the wire

and the metallization components, as seen in Figure 63.

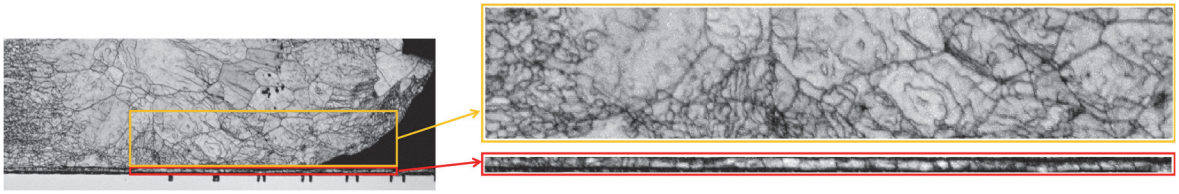

Figure 63: The partitioning made for the healthy sample just at the tip wire-metallization metallic contact.

As for the case of heel partitioning, the grains' size distribution is first interpreted. Then, a texture study is performed by plotting the IPFs, DPFs, and crystal texture components.

A. Grains' sizes analyses

Figure 64 shows the grains' size distribution at the tip metallic interconnection interface for the partitioned metallization and wire portions in the healthy sample.

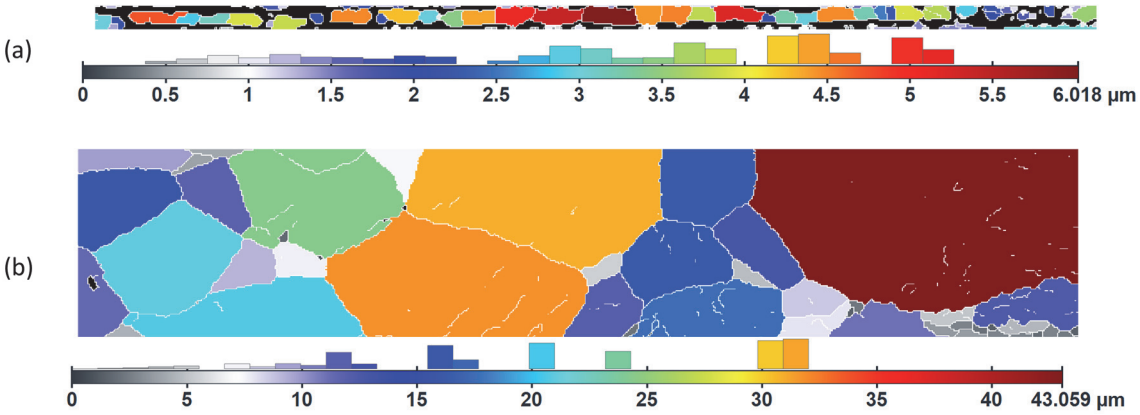

Figure 64: Grains' size distribution at the healthy tip wire-metallization metallic contact for the partitioned (a) metallization and (b) wire samples.

As at the heel position, grains inside the metallization layer have almost the same size since they compose the thickness of a thin film; however, inside the wire, there is variety in the size of grains. For the metallization part, most grains possess a size between 3-6 µm, whereas at the wire interface, the sizes are large (mostly > 10 µm); thus, they acquire lower strength compared to the strength of the grains inside the metallization [Hans04].

B. Grains' texture analyses

IPFs at the tip metallic interconnection interface in the healthy sample are presented in Figure 65 for the metallization and wire partitioned portions.

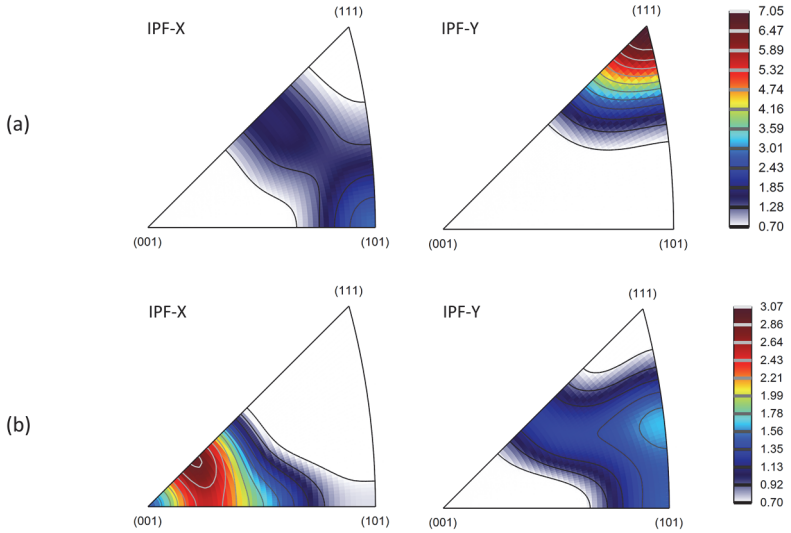

Figure 65: IPFs at the healthy tip wire-metallization metallic contact for the partitioned (a) metallization and (b) wire samples.

From Figure 65, the microstructure of the metallization looks clearly textured by looking at its strong (111) plane orientation in the y-projection. The preferred orientation of grains in the wire portion at the interconnection interface is (001) in the x-direction and (101) in the y-direction. DPFs are then plotted in order to be able to extract the crystal texture components for the grains within the tip portion.

DPFs are shown in Figure 66 at the tip metallic interconnection interface in the healthy sample for the partitioned metallization and wire portions to confirm the IPFs results and deduce the preferred crystal texture components plotted in Figure 67.

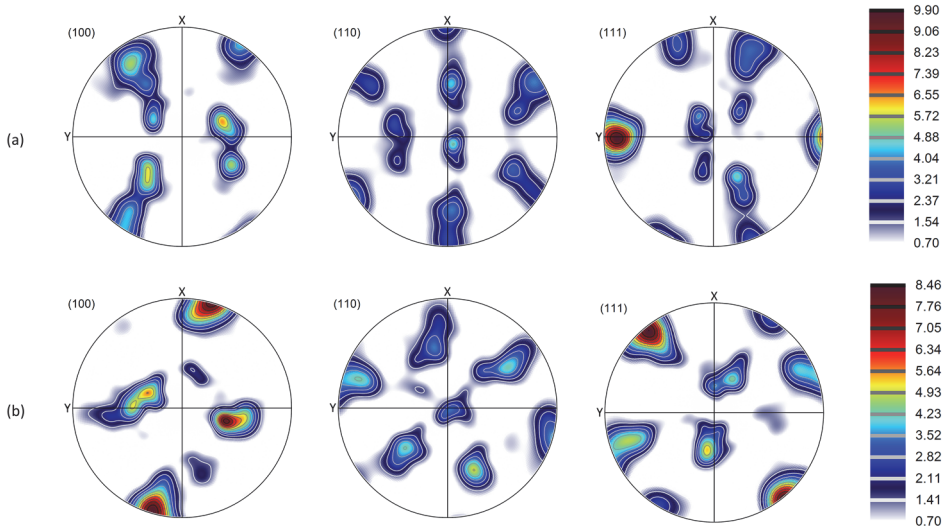

Figure 66: DPFs at the healthy tip wire-metallization metallic contact for the partitioned (a) metallization and (b) wire portions.

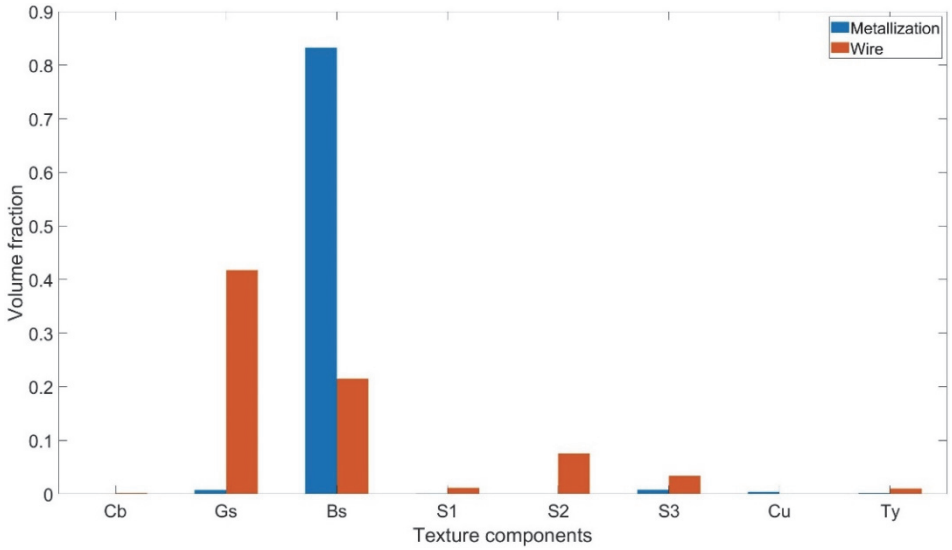

Figure 67: Texture components present at the healthy tip wire-metallization metallic contact for the partitioned (a) metallization and (b) wire portions.

The grain orientations observed in Figure 65 are confirmed in Figure 66. As for the heel portion, the texture components seen in Figure 67 are initially present in the microstructure prior to cycling caused by the wire welding process. A strong Bs texture is observed in the microstructure of the metallization. This Bs component has been associated in the literature with deformations [PaCP12], [ZhTN92]. This was also seen in the heel-partitioned sample. On the other hand, the microstructure of the wire at the interconnection interface exhibits strong Gs and Bs textures, with stronger Gs texture. Such textures signify the existence of both the deformation and recrystallization processes. As for the heel portion, and since the crack nucleates from such positions, the dominant Gs texture component associated with recrystallization is thought to influence the growth of cracks.

From these healthy edge portions, a wide variety in the grain size distribution inside the wire was observed, with the existence of some big grains. This is not the case inside the metallization layer, where grains are almost with equal sizes (< 5 µm). This signifies that metallization chips acquire more strength than wires, referring to the Hall-Petch relationship [Hans04]. Thus, it is reasonable to see the crack inside the wire, not the metallization. Texture components caused by the wire welding process are observed in the healthy state. Deformation and recrystallization components present at the contact between the wire and the metallization layer are other clues for the formation of cracks at the contact sites, especially since the recrystallization components exist inside the wire at both the heel and tip portions. This is because it is reported in the literature that the crack preferably propagates at recrystallized zones [YaAJ14].

5.3.2 Microstructural analysis upon cycling

Based on the previous analyses, and because we aim to see the effect of the microstructural changes on the cracking process that occurs inside the wire just above the metallization layer, aged samples at different cycling stages were analyzed at the crack nucleation vicinity. The same partitioning is applied here as for the healthy sample, at the heel and the tip positions; however, just for the wire without including the metallization, since it is known and deduced that the crack only evolves at the bottom wire parts. A third position at the wire's bottom center was also considered in this section by interpreting the microstructural evolutions that occur there, especially when cracks arrive at the wire's bottom center at advanced stages. This third position was not considered for healthy samples because degradations are the weakest there and are only important when cycling is progressed. By analyzing the microstructural evolution of different samples at different cycling stages inside these three partitioned positions, better interpretations can be constructed. Several important features related to the crack propagation process can be derived from these analyses. The main things to interpret are the evolution of crystal texture components in addition to grains'

texture, sizes, and boundary disorientation angles. This was done by analyzing several samples at different cycling stages. In the following section, wire #8 in chips #6 and #7 was analyzed at different cycling stages. In chip #6, the wire was analyzed at 0 cycles, 10% N_f, and 50% N_f, whereas for chip #7, the wire was analyzed at 65% N_f, 80% N_f, and 100% N_f. The manner of partitioning carried on here for all the samples is represented in Figure 68.

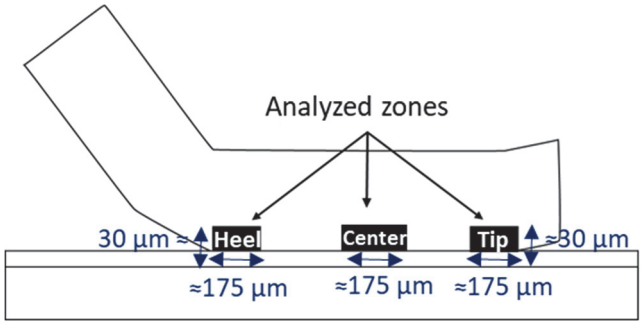

Figure 68: The heel, tip, and center partitioned positions in the partitioning analyses II (upon cycling).

The first discussion to start with is the evolution of the texture components' volume fractions at different cycling stages at the tip, center, and heel positions inside the wire just above the metallization layer.

5.3.2.1 Texture components evolution analysis for wire #8 in chip #7 (0-50% N_f)

In this section, the evolution of crystal texture components is interpreted for wire #8 in chip #7 at the tip, center, and heel positions at 0 cycles, 10% N_f, and 50% N_f. Primarily, the evolution of crystal texture components at the tip position is made, as shown in the figure below.

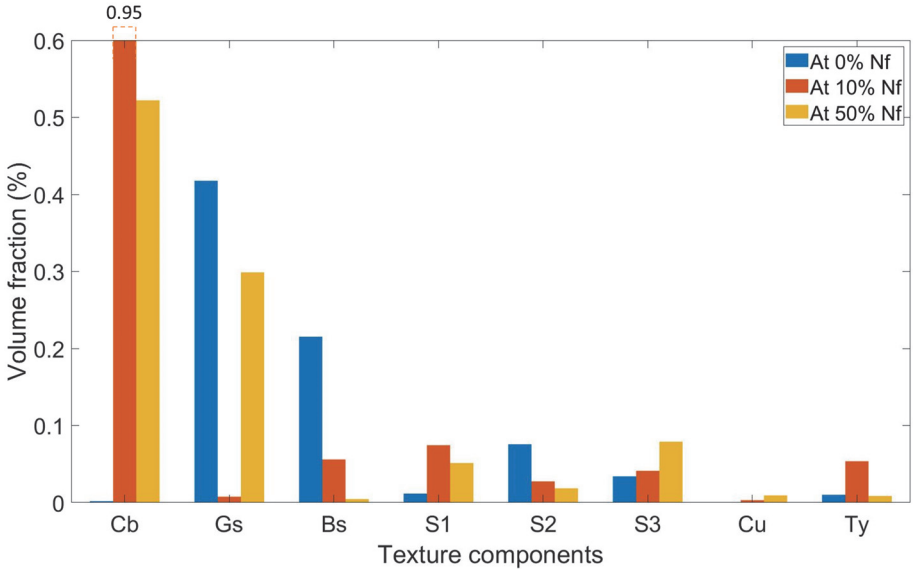

Figure 69: The volume fraction distribution of crystal texture components at the tip position for wire #8 in chip #7 at 0 cycles, 10% N_f, and 50% N_f.

Before cycling, deformation and recrystallization components were present at the tip due to the wire welding forces. After 10% N_f, recrystallization components increased significantly, whereas deformation components generally decreased. This change is due to grains reconstructions, which occur when cycling begins. The high volume fraction of recrystallization components could be a clue for texture. At 50% N_f, recrystallization components remain dominant, with a high increase in the Gs volume fractions. The volume fraction of the deformation components is low at this stage. This is probably because cracks are majorly formed between 10% N_f and 50% N_f; thus, when reaching 50% N_f, cracks are already formed; therefore, stress and deformations have been relieved. Consequently, recrystallization dominates.

The evolution of crystal texture components at the center position is then done, as shown in Figure 70.

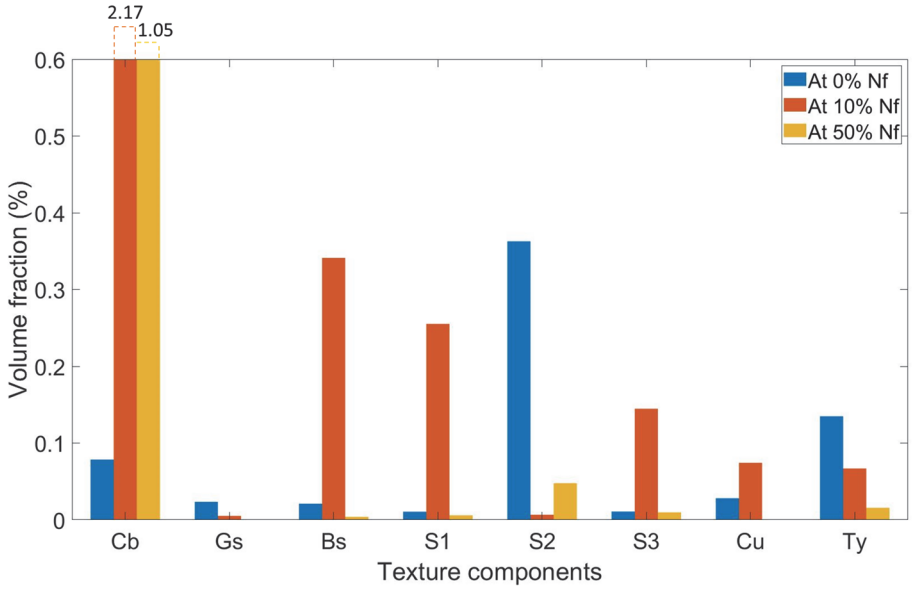

Figure 70: The volume fraction distribution of crystal texture components at the center position for wire #8 in chip #7 at 0 cycles, 10% N_f, and 50% N_f.

For the center position, at 0 cycles, deformation components existed resulting from the welding process, with the presence of very low volume fractions of recrystallization components. Then, after 10% N_f, recrystallization becomes dominant, with a very high increase in the frequency of its components, dominating over deformation ones. This increase is essential to relieve the deformations caused by the welding process. At 50% N_f, recrystallization components highly decreased; however, they are still dominant. This decrease is because the majority of grains had already been recrystallized. Deformation components are null at this stage because deformations are not formed yet.

Finally, the evolution of crystal texture components at the heel position is made, as presented in the figure below.

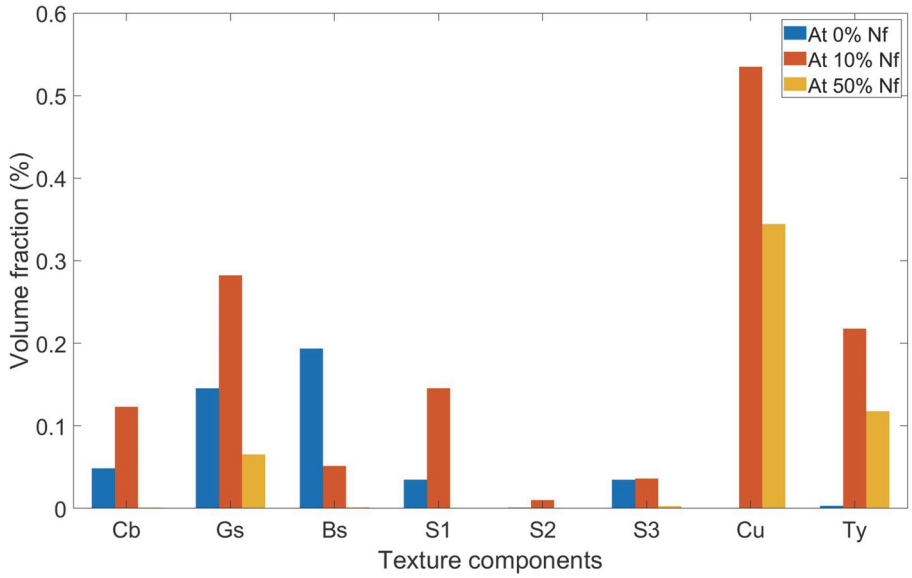

Figure 71: The volume fraction distribution of crystal texture components at the heel position for wire #8 in chip #7 at 0 cycles, 10% N_f, and 50% N_f.

Due to the wire welding process, deformation and recrystallization components exist prior to cycling at the heel position. After 10% N_f, deformation components highly increased and became dominant

over the recrystallization components which increased slightly due to some grains rearrangements. Such an increase in deformation components is expected at the wire's edges, especially the heel, the position for cracks' initiation. At this stage, the volume fraction of deformation components at the heel position is clearly higher than that at the tip. This may also signify that the heel position is subjected to more deformations; thus, cracks first initiate there. At 50% N_f, deformation components remained dominant, but their volume fractions decreased. At this stage, the volume fractions of recrystallization components are highly deceased as well. The dominance of deformations is logical since deformations are highly formed at the heel positions upon cycling. The decrease in their percentages may be due to the formation of cracks that relieve stress and decrease the accumulated deformations.

5.3.2.2 Texture components evolution analysis for wire #8 in chip #6 (65-100% N_f)

As for wire #8 in chip #7, the evolution of crystal texture components is interpreted at the tip, center, and heel positions; however, at 65% N_f, 80% N_f, and 100% N_f. First, the evolution of crystal texture components at the tip position is plotted in Figure 72.

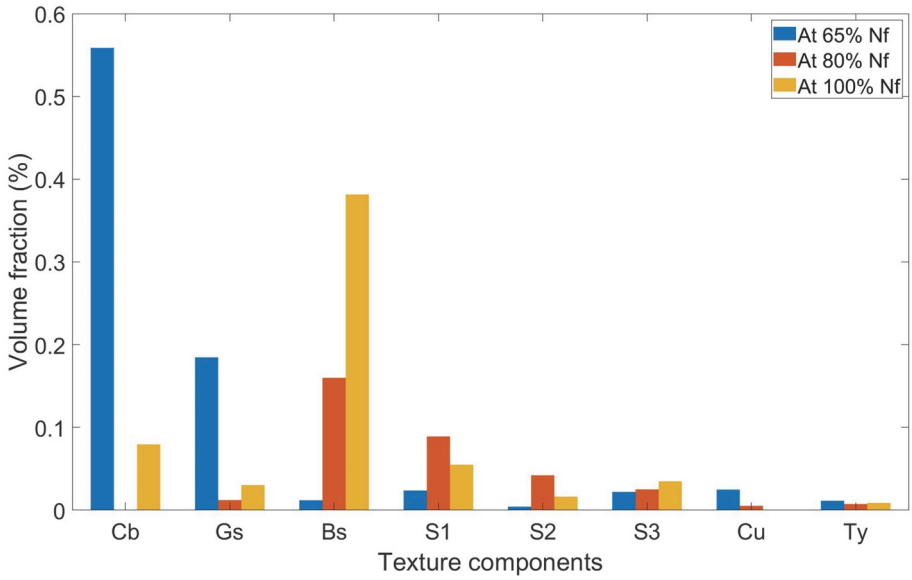

Figure 72: The volume fraction distribution of crystal texture components at the tip position for wire #8 in chip #6 at 65% N_f, 80% N_f, and 100% N_f.

At 65% N_f, recrystallization components dominate at the tip, whereas deformation components are approximately null. Deformations do not seem to have high volume fractions since cracks have already been formed, and stress has been relieved. After 80% N_f, the volume fraction of recrystallization components highly decreased, with an increase in the volume fractions of deformation components. This increase is due to the fact that the cracks themselves may induce deformations, especially at this advanced cycling stage, which is near the lifting-off moment [LiLD05], [LiPo18]. When reaching 100% N_f, the volume fraction of recrystallization components increased slightly. A significant increase in deformation components occurred as well since we just reached the lifting-off moment.

Secondly, as shown in Figure 73, the evolution of crystal texture components at the center position is made.

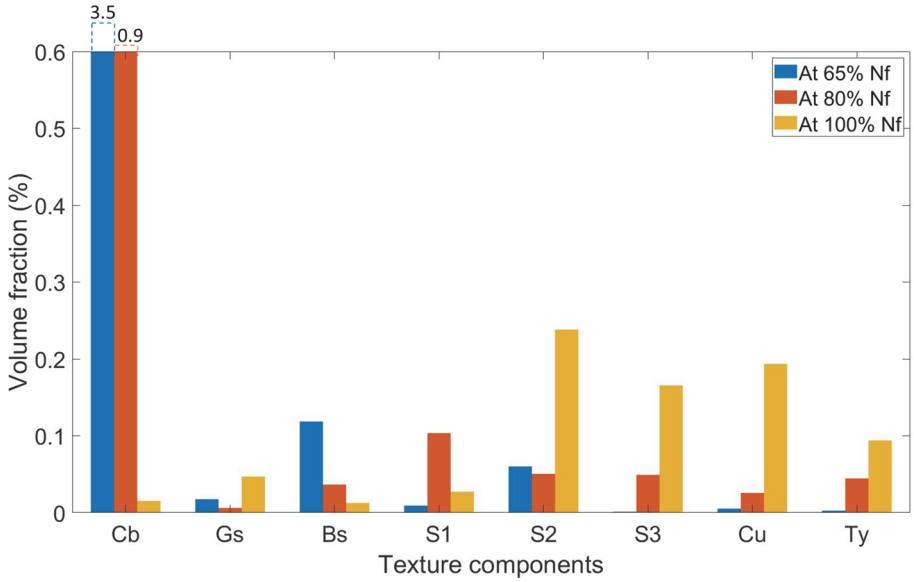

Figure 73: The volume fraction distribution of crystal texture components at the center position for wire #8 in chip #6 at 65% N_f, 80% N_f, and 100% N_f.

Recrystallization components dominate at the center position when the sample is cycled up to 65% N_f. Deformation components are approximately null at that cycling stage. This is logical since cracks did not arrive yet. When reaching 80% N_f, deformation components start appearing. This is because cracks are so near at this moment. Recrystallization components highly decreased at this stage as well. At 100% N_f, deformation components increased and became the dominant components. The increase in such components is logical because cracks have arrived at the center at this moment. Recrystallization highly decreased as well; however, one new component that did not previously exist is formed at this stage with low volume fractions (Gs component). This is because grains reconstruction could result after stress generation to relieve them.

Last but not least, the evolution of crystal texture components at the heel position is made, as shown in Figure 74.

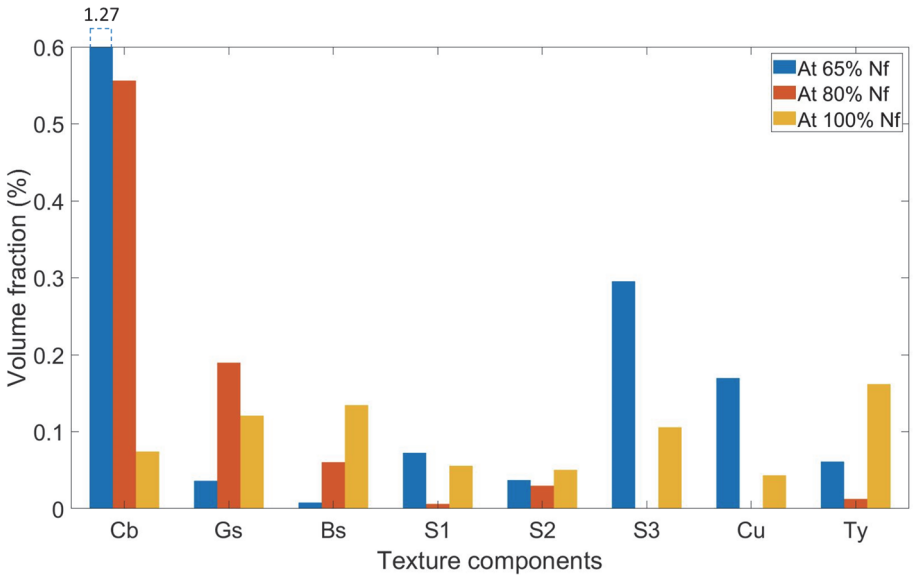

Figure 74: The volume fraction distribution of crystal texture components at the heel position for wire #8 in chip #6 at 65% N_f, 80% N_f, and 100% N_f.

Recrystallization components are dominant over deformations at the heel position when reaching 65% N_f. The deformation components do not have high volume fractions compared to recrystallization

components since cracks are already formed, and stress has been majorly relieved. Recrystallization components are still dominant when cycled up to 80% N_f, even though their volume fraction has decreased. This decrease is probably because most of the grains had been recrystallized. Deformation components still have low volume fractions at this stage. Finally, at 100% N_f, deformations increased and became dominant over recrystallization components which highly decreased due to the impact of cracks in generating stress, especially since it is the moment of the wire's lifting-off.

After analyzing the evolution of the texture components' volume fractions at the wire's tip, center, and heel positions, here come the analyses of the evolution of the distribution of disorientation angles and grain sizes upon cycling. These evolutions were interpreted at different cycling stages for wire #8 in chip #7 (at 0 cycles, 10% N_f, and 50% N_f) and in chip #6 (at 65% N_f, 80% N_f, and 100% N_f) as in the previous analyses. Such evolutions are discussed in detail in the next sections at the wire's tip, center, and heel positions inside the wire just above the metallization layer.

5.3.2.3 The evolution of the distribution of grains' boundary disorientation angles and sizes for wire #8 in chip #7 (0-50% N_f)

For wire #8 in chip #7, IPFs at 0 cycles, 10% N_f, and 50% N_f are plotted for the wire's tip, center, and heel positions. Afterward, the evolution of the distribution of grains' sizes and disorientation angles at those cycling stages are analyzed at the wire's tip, center, and heel positions.

Starting with the tip position, IPFs evolution upon cycling (up to 50% N_f) is plotted in Figure 75, whereas the evolutions of the grains' sizes and disorientation angles are shown in Figure 76.

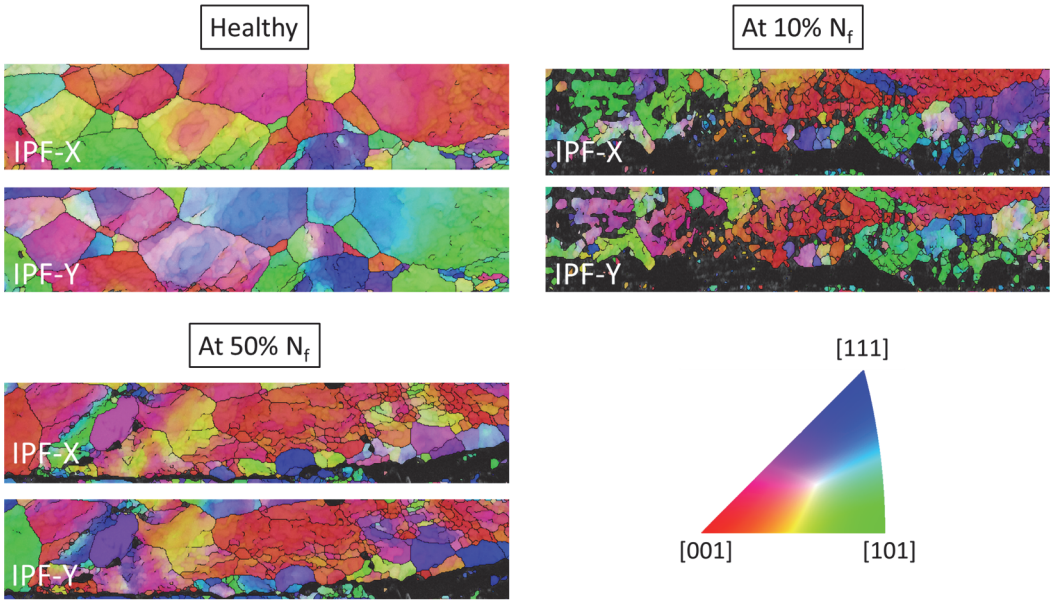

Figure 75: IPFs for wire #8 in chip #7 at the wire's tip at 0 cycles, 10% N_f and 50% N_f.

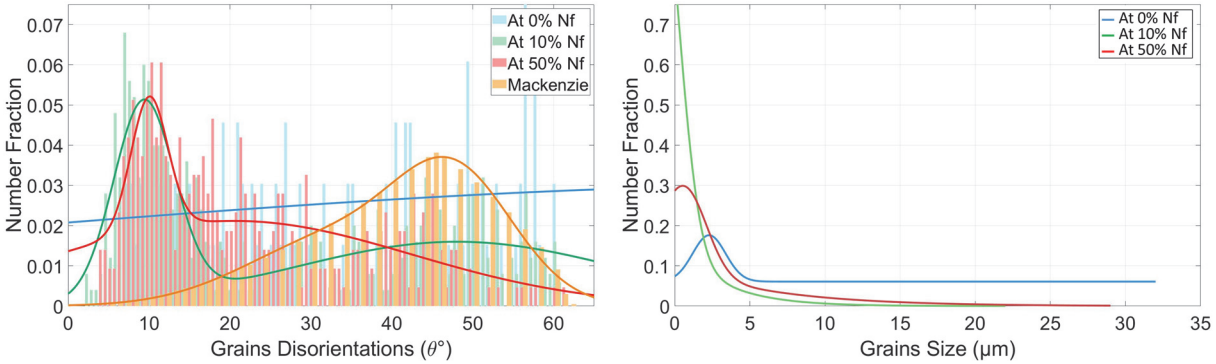

Figure 76: The volume fraction distribution of grains' disorientation angles and sizes for wire #8 in chip #7 at the wire's tip at 0 cycles, 10% N_f, and 50% N_f.

Based on Figure 75 and Figure 76, the following analysis is constructed. First, the Mackenzie distribution is the theoretical disorientation angle distribution for a randomly oriented polycrystal. When crystals are preferentially oriented in specific directions, the polycrystalline material is said to be textured. If the frequency of the actual distribution is higher than the corresponding frequency in the Mackenzie distribution at any disorientation angle, this indicates that the polycrystal is textured [Mack58]. When comparing the disorientation angles distribution to the Mackenzie distribution curve in the tip portion, the healthy portion is deduced to be randomly oriented; however, it may have some texture tendency in some positions since the distribution trend is not so clear. Looking at IPFs for this healthy portion confirms the randomness of the structure; however, the presence of big grains with specific orientations is the reason why one can deduce from the disorientation angles distribution curve a tendency towards texture. Figure 76 shows that the frequency of HABs is higher than that of LABs. Concerning the grain size distribution, grains with big sizes are present (the initial state of grains before welding the wire), besides other small sizes (caused by welding the wire).

Upon cycling to 10% N_f, it is observed that the sample tends to be textured from the disorientation angles distribution. This is clearer when looking at the IPFs. In the IPFs, the right side of this portion is textured towards (001) orientation in both the x and y directions. The left portion is textured towards (101) orientation in the x-direction. The high recrystallization components' volume fractions in Figure 69 also confirm the structure's tendency towards texture. The number of LABs highly increased compared to that in the healthy state. This is an influencer for the propagation of cracks at this location. The majority of grains are small. Big grains observed previously are not present here. This is due to dislocation rearrangements resulting during early cycling and rearrangements of pre-existing deformations caused by the wire welding process. Because the crack formation at this stage is very weak, it is expected that just after the 10% N_f cycling state, a grain growth state should exist after recrystallization, facilitating the crack propagation there. This is because the crack was observed to propagate when the size of grains is bigger, as deduced in Figure 55 and according to the Hall-Petch relationship.

When reaching 50% N_f, the structure is deduced to be textured when comparing the disorientation angles distribution to the Mackenzie distribution, looking at the IPFs (grains orient towards (001) orientation plane), and from the presence of high volume fractions of recrystallization texture components. The number fraction of LABs slightly increases, and that of HABs decreases too, synchronous with the complete formation of cracks at such locations. Regarding the grain size, grains are clearly bigger than before due to grain growth which happens when recrystallization occurs. The expected grain growth process just after 10% N_f is evidenced when looking at the grain size distribution at this cycling stage, where the size of grains is highly bigger than before, at the same stage at which the crack is complete at the tip location.

IPFs and the evolution of the distribution of grains' sizes and disorientation angles are then plotted in Figure 77 and Figure 78 respectively for the center position at 0 cycles, 10% N_f, and 50% N_f.

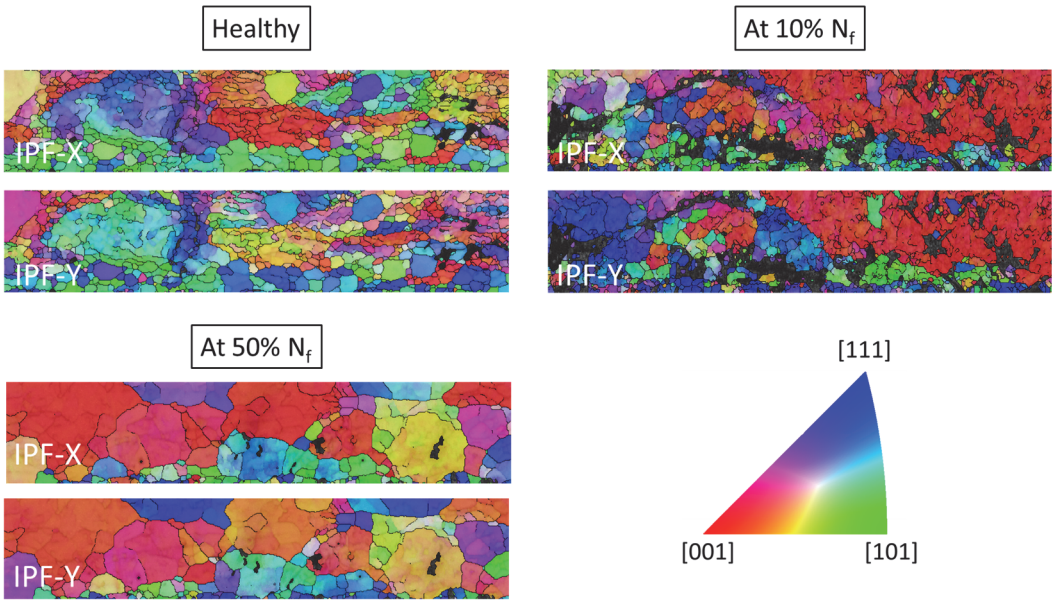

Figure 77: IPFs for wire #8 in chip #7 at the wire's center at 0 cycles, 10% N_f and 50% N_f.

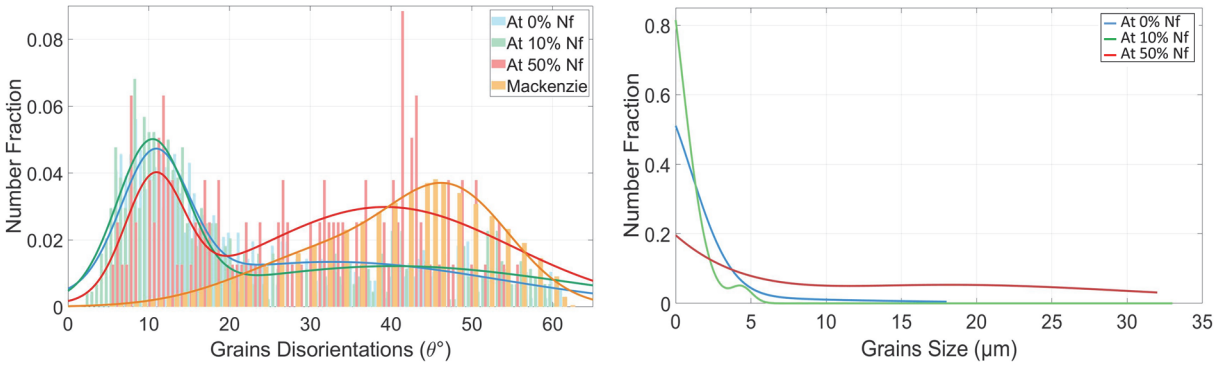

Figure 78: The volume fraction distribution of grains' disorientation angles and sizes for wire #8 in chip #7 at the wire's center at 0 cycles, 10% N_f, and 50% N_f.

When observing the distribution of disorientation angles at the center, the healthy portion is unclear whether it is random or textured. The structure randomness was confirmed when looking at the IPFs. Grains are very small in size, caused by the wire welding process, with no grains having a size > 18 µm.

When this center portion is cycled up to 10% N_f, the structure seems to be textured when looking at the disorientation angles distribution. This was also evidenced by the high frequencies of texture components in Figure 70. IPFs show that the right side of this portion is textured towards the (001) plane in both the x and y directions. The left side of the portion is oriented towards the (111) orientation plane, especially in the y-direction. Most of the grains have smaller sizes than those before cycling. This is maybe because sub-grains are formed at early cycling stages caused by the rearrangement of dislocations generated from the welding process. This hypothesis is strengthened by the high increase in the frequency of LABs and the dominance of recrystallization components.

After 50% N_f, the structure looks textured as well. This is deduced when comparing the disorientation angles distribution to the Mackenzie plot, in addition to looking at the IPFs (grains are mostly oriented towards the (001) plane). Concerning the grain size, bigger grains are observed. This is due to the grain growth which presents after recrystallization. The generation of big grains at this cycling stage is the probable reason behind the high increase in the number fraction of HABs. This is because more abundant big grains surrounded by several smaller grains with high disorientation angles between them exist.

Finally, IPFs and the evolution of the distribution of grains' sizes and disorientation angles are plotted in Figure 79 and Figure 80 respectively for the heel position at 0 cycles, 10% N_f, and 50% N_f.

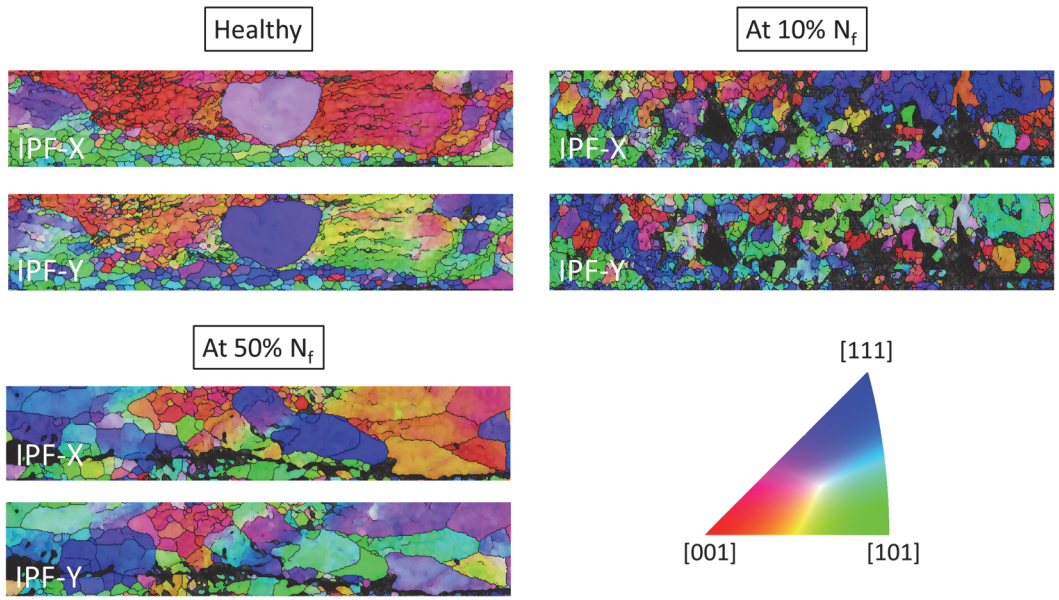

Figure 79: IPFs for wire #8 in chip #7 at the wire's heel at 0 cycles, 10% N_f and 50% N_f.

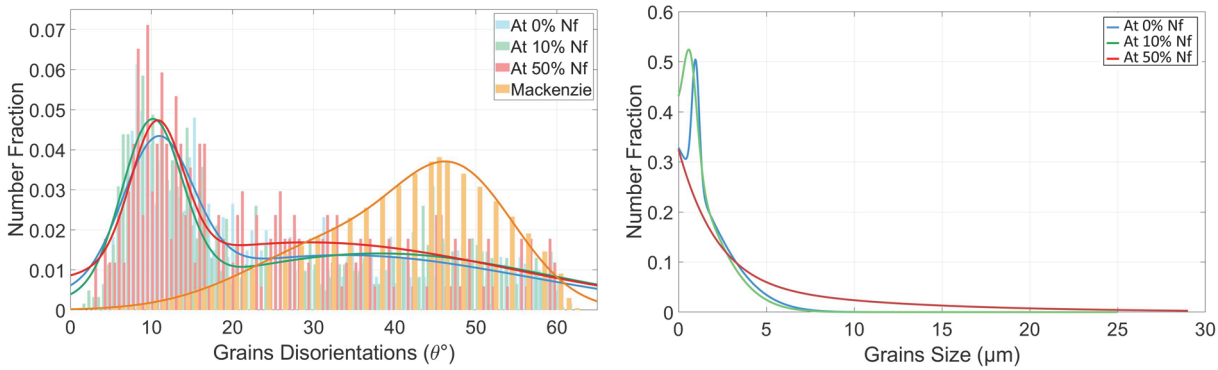

Figure 80: The volume fraction distribution of grains' disorientation angles and sizes for wire #8 in chip #7 at the wire's heel at 0 cycles, 10% N_f, and 50% N_f.

At the heel position, the structure of the healthy portion is not so clear whether it is textured or not when looking at the distribution of disorientation angles. From IPFs, it was seen that some sample locations are textured while others are not. For example, in the x-direction, the topside is oriented towards (001) and the bottom side towards (111). The grains in this portion are mostly small, with a few big grains. The presence of small grains is due to the welding forces, whereas big ones represent the grain's initial state.

At 10% N_f, the structure looks textured from the disorientation angles distribution. When looking at the IPFs, it was clear that certain positions have the same orientations. For example, in the x-direction, the right part is oriented towards (111). In the y-direction, the right side is oriented towards the (101) plane, and the left is oriented towards the (111) plane. The number fraction of LABs increased, and that for HABs decreased compared with that at the healthy state, simultaneously with having a fast crack initiation speed at such positions. Grains are mostly small; however, at the same time, it is expected that between the healthy state and until reaching 10% N_f, a grain growth process phase took place after recrystallization, maybe just before the 10% N_f cycling state. This is because some grains have sizes between 15 and 25 µm. On the contrary, there was only one big grain for the healthy state portion. This grain growth phase is also expected because the evolution of the crack formed at this moment was confirmed to be favored when the size of grains is bigger, as deduced in Figure 55 and according to the Hall-Petch relationship.

The structure still looks textured when the sample is cycled to 50% N_f. This is deduced from the distribution of the disorientation angles. In contrast, the decrease in the texture components' volume fraction in Figure 71 may signify that the structure could have been transformed from textured to random. When looking at IPFs, the structure's texture is unclear. The texture tendency observed in Figure 80 is most probably due to the presence of big grains. Grains are bigger than before. This may be caused by grain growth following recrystallization, deduced from high frequencies of recrystallization texture components at 10% N_f, as pointed out in Figure 71. The grain growth process starting just before 10% N_f is clearer when looking at the grain size distribution at 50% N_f, where the size of grains is highly larger than before. This occurred simultaneously when the crack became complete at the heel position.

5.3.2.4 The evolution of the distribution of grains' boundary disorientation angles and sizes for wire #8 in chip #6 (65-100% N_f)

As for wire #8 in chip #7, IPFs for wire #8 in chip #6 are plotted for the wire's tip, center, and heel positions; however, at 65% N_f, 80% N_f, and 100% N_f. Afterward, the evolution of the distribution of grains' sizes and disorientation angles at those cycling stages are analyzed at the wire's tip, center, and heel positions.

IPFs and the evolution of the distribution of grains' sizes and disorientation angles are first plotted at the tip position at 65% N_f, 80% N_f, and 100% N_f as shown in Figure 81 and Figure 82.

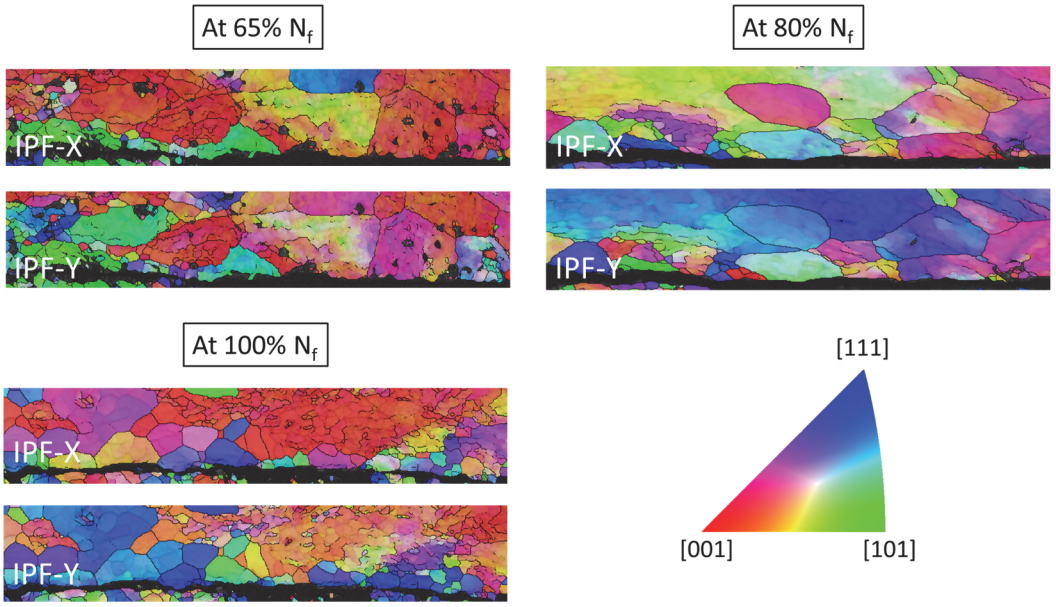

Figure 81: IPFs for wire #8 in chip #6 at the wire's tip at 65% N_f, 80% N_f, and 100% N_f.

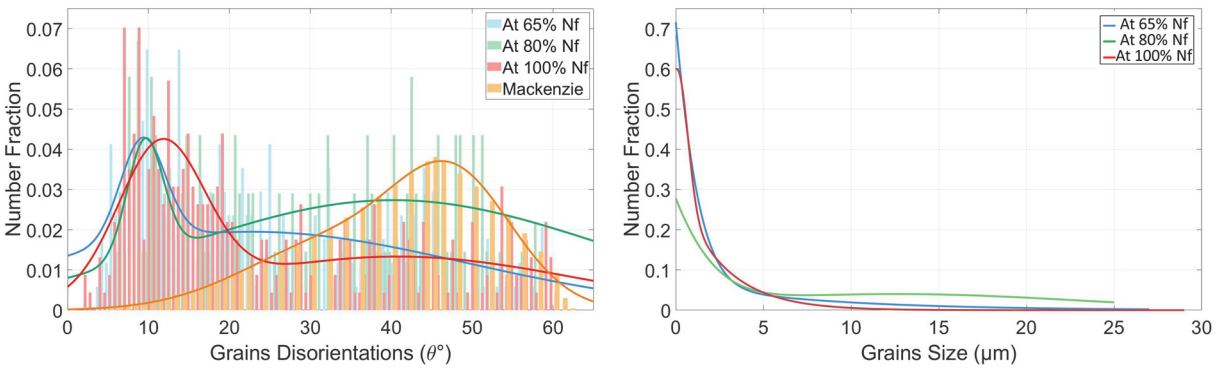

Figure 82: The volume fraction distribution of grains' disorientation angles and sizes for wire #8 in chip #6 at the wire's tip at 65% N_f, 80% N_f, and 100% N_f.

The structure of the tip portion after 65% N_f looks textured when observing the disorientation angles distribution. This is confirmed by the IPFs and verified by the high frequencies of recrystallization texture components in Figure 72. Recrystallization justifies the high frequency of tiny grains compared to the minor frequency of big sizes. These few big grains are mainly due to grain growth caused by the previous recrystallization. At this cycling stage, LABs are dominant, with the presence of some HABs.

Upon cycling to 80% N_f, the structure looks textured as well, deduced from the disorientation angles distribution. From IPFs, it is seen that the presence of very big grain sizes is the cause behind this texture tendency. A shift from LABs to HABs is seen at this moment. This is synchronous with the slowdown in the speed of cracks. Grains are bigger than those in the previous state at 65% N_f. The increase in grain sizes is due to the grain growth process post previous recrystallization.

When reaching 100% N_f, the structure tends to be textured, deduced from the distribution of disorientation angles. From IPFs, some locations were observed to have the same texture. For example, in the x-direction, the right side is textured towards the (001) plane. On the left side in the y-direction, grains are oriented towards (111) and (101) planes respectively. The structure's texture may also be evidenced by the high volume fraction values of the deformation texture components, as shown in Figure 72. Such an increase in the deformation texture components justifies the dominance of small grains. These deformations are most probably caused by the cracks [LiLD05], [LiPo18]. Such deformations could effectively result in lower volume fractions of HABs at this moment compared to that at 80% N_f.

IPFs and the evolution of the distribution of grains' sizes and disorientation angles are then plotted in Figure 83 and Figure 84 respectively for the center position at 65% N_f, 80% N_f, and 100% N_f.

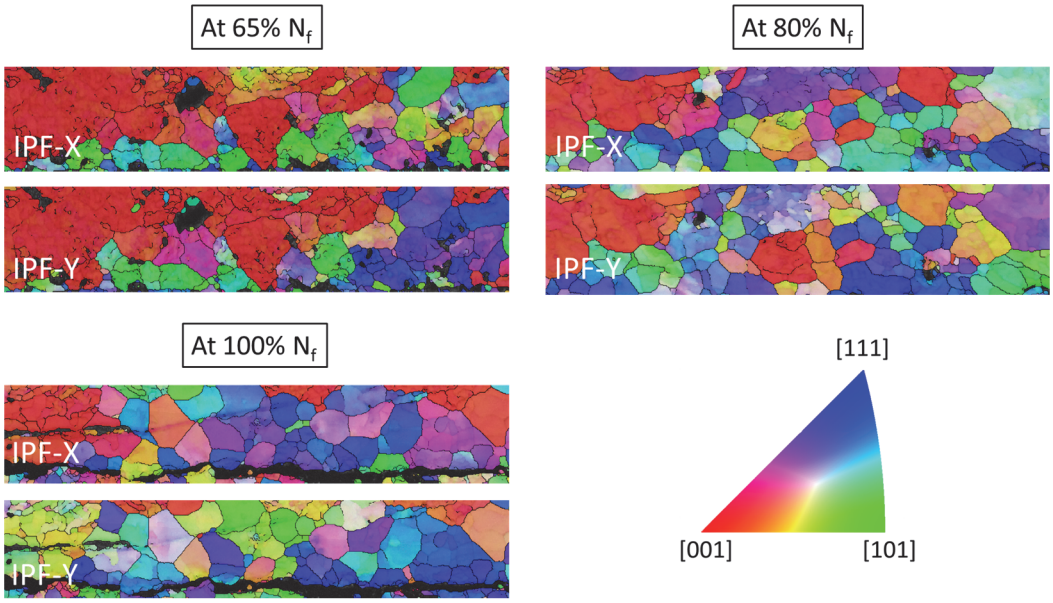

Figure 83: IPFs for wire #8 in chip #6 at the wire's center at 65% N_f, 80% N_f, and 100% N_f.

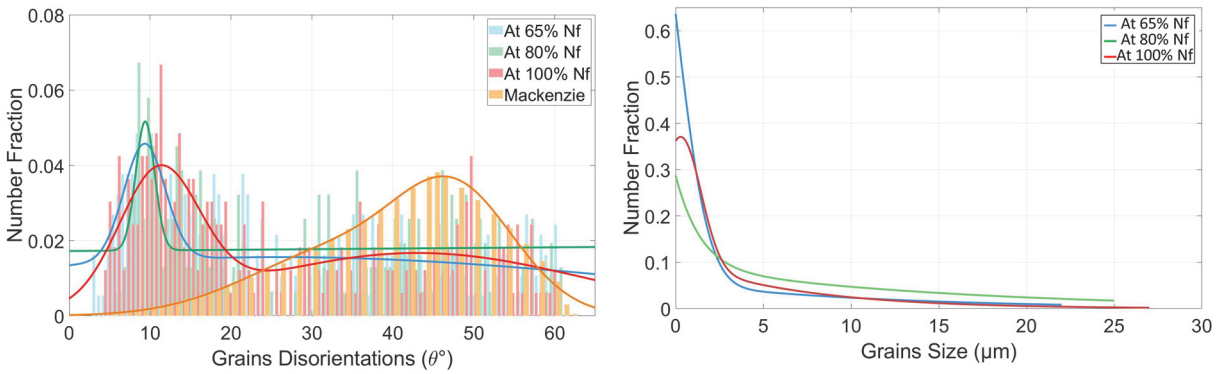

Figure 84: The volume fraction distribution of grains' disorientation angles and sizes for wire #8 in chip #6 at the wire's center at 65% N_f, 80% N_f, and 100% N_f.

The disorientation angles distribution shows that the center portion cycled up to 65% N_f tends to be textured. The high volume fractions of recrystallization components, as seen in Figure 73, and IPFs confirm the texture of this portion. The dominance of recrystallization components justifies the existence of very small grains. Few median grain sizes formed from previous grain growth states are present at this moment.

Upon cycling up to 80% N_f, a very narrow peak is present when looking at the distribution of disorientation angles. This makes the structure's texture not so clear. The high decrease in recrystallization texture components, as seen in Figure 73, and the IPFs plot signify the structure's randomness. The number fraction of tiny grains decreased with the formation of some bigger grains. Grain growth after recrystallization is the probable reason behind the presence of these bigger grains. These grains are the favored ones for the crack passage, which has just arrived at the center position at this moment. Another influencer for the crack passage at those grains is the presence of a higher amount of LABs than that of HABs.

From Figure 83, and upon cycling up to 100% N_f, the structure does not look completely textured; however, it tends to be. This semi-textured structure is confirmed when looking at the IPFs, where the left side in this sample is textured in both the x and y directions, whereas the right side is clearly textured in the x-direction. The sharp decrease in the recrystallization components' volume fractions and the increase in the volume fractions of deformation components, as observed in Figure 73, confirm this semi-texture. Grains are generally small at this moment, caused by deformations that dominate when approaching the module's end of life, especially because deformations concentrate at the center position due to the cracking that happens when reaching the N_f.

Finally, IPFs and the evolution of the distribution of grains' sizes and disorientation angles are plotted in Figure 85 and Figure 86 respectively for the heel position at 65% N_f, 80% N_f, and 100% N_f.

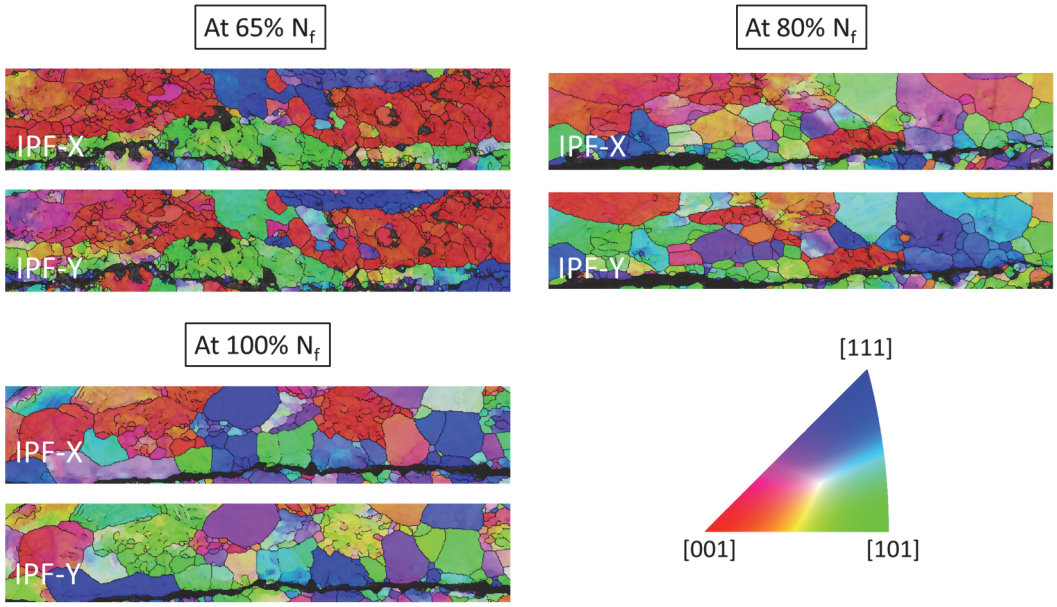

Figure 85: IPFs for wire #8 in chip #6 at the wire's heel at 65% N_f, 80% N_f, and 100% N_f.

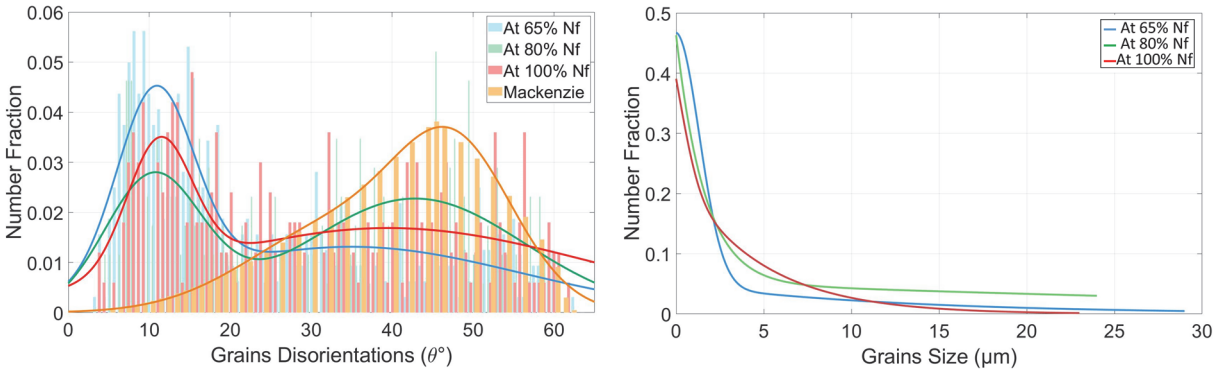

Figure 86: The volume fraction distribution of grains' disorientation angles and sizes for wire #8 in chip #6 at the wire's heel at 65% N_f, 80% N_f, and 100% N_f.

When observing the disorientation angles distributions and IPFs, the heel portion is deduced to be textured at 65% N_f. This is also evidenced by the high volume fractions of recrystallization texture components, as seen in Figure 74. LABs dominate at this moment. Grains are mostly small, with the presence of a few huge grains.

The structure turns random when the sample is cycled up to 80% N_f. This is evidenced when looking at the disorientation angles distribution and IPFs, and is confirmed by the decrease in volume fractions of crystal texture components, as seen in Figure 74. A shift from LABs to HABs is clear at this stage. This is synchronous with the slowdown in the speed of cracks. Grains are bigger than before. This is due to the grain growth process following recrystallization, which dominated at 65% N_f.

Upon reaching 100% N_f, the structure is still random when observing the disorientation angles distribution and IPFs. The increase in the volume fraction of the deformations texture components, as seen in Figure 74, is not enough to change the structure into a textured one since the volume fractions are not so high. Smaller grains existing due to the increase in deformations, most probably induced by the cracks, could be linked to having higher LABs and lower HABs than those at 80% N_f.

5.4 A DISCUSSION ON THE CRACK EVOLUTION

In addition to the crack propagation interpretation made in section #3 (under Figure 45) when showing

some micro-section images for aged samples, some additional points can be mentioned. From the microstructural interpretations in the previous section, different aspects were deduced to influence the crack growth, such as the texture, size of grains, and the local disorientations between grains. Based on the experimental interpretations made in this chapter and the information listed in the literature, the cracking mechanism is summed up as follows.

- **Cracks initiation**

Due to the wire welding process, some deformations exist at the metallic contact sites, especially at the wire extremities, resulting in initial defects [AYAE16]. Stress concentrates at such sites upon cycling. Grains near the interconnection interface are small (< 5 µm), with a majority of LABs. A few HABs exist there, especially at the wire extremities, as observed in Figure 87. Such sites acquiring HABs are preferable locations for cracks' nucleation because HABs are considered obstacles to the migration of dislocations from one grain to its neighbor, causing their accumulation. Upon reaching a particular critical value of stress concentration, cracks initiate [Gour02], [KIKT08], [SaMS11].

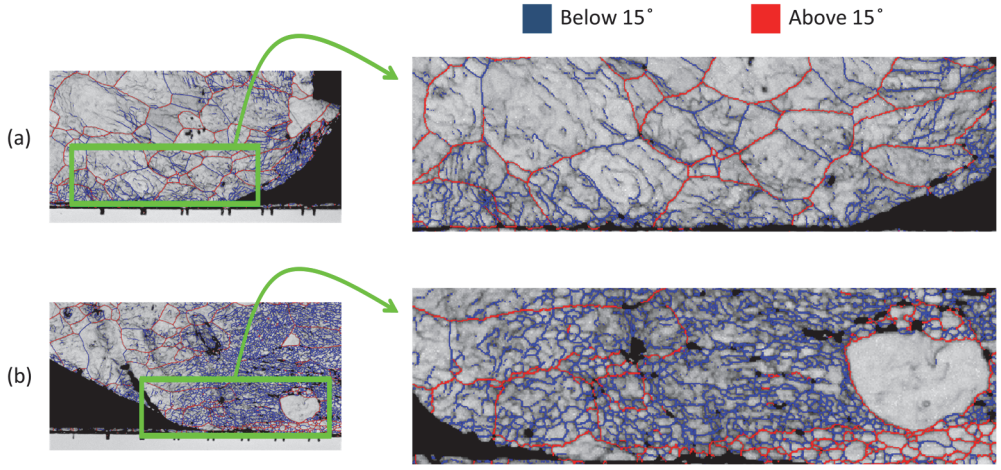

Figure 87: The grain boundary disorientation angles distribution for the healthy sample (a) at the tip position and (b) at the heel position.

Returning to the crack evolution manner seen in Figure 45, cracks were confirmed to initiate from the wire contact ends as observed at 10% N_f, where some HABs are present as illustrated in Figure 87. Other important issues were also deduced. From Figure 45, at 10% N_f, cracks were formed first at the heel position faster than at the tip. Moreover, in Figure 55, Figure 76, and Figure 80, it was deduced that the high crack initiation speed is accompanied by grain growth.

- **Cracks' propagation**

After the nucleation of cracks, their propagation is much easier to occur through LABs, as shown in Figure 87 and reported in the literature [DSWN19]. These boundaries exist inside the wire just above the metallization layer, at the position of the crack evolution observed in Figure 45. The reason behind the progress of cracks through LABs is that such boundaries have poor sliding [DSWN19]. Additionally, cracks can easily penetrate LABs [BGHS15]. It was also deduced that when the cracking speed was the highest, the number of LABs increased, as presented in Figure 76 and Figure 80 after 10% N_f.

As reported in the literature [AYAE16], [LCLH07], cracks were recognized to continue their propagation through grain boundaries and grains above the wire-metallization contact toward the center of the bottom wire zone, as seen in Figure 45, and do not emerge toward large grains inside the wire bulk in the upward direction. At the same time, cracks do not propagate exactly at the interconnection interface where grains are the smallest. Logically, cracks do not propagate through fine grains due to their high strength. So why do they not emerge to the wire bulk, where grains are bigger and thus weaker?

The probable interpretation for this cracking is the formation of high amounts of plastic deformations at the interconnection zones when welding the wire prior to cycling, thereby enhancing the formation of cracks in such positions [PØKG16]. Moreover, the welding process causes the formation of impurities at the interconnection interface, weakening the grains there [GSGL10]. Grain reconstructions occurring at the interconnection sites upon cycling also decrease the contact between neighboring grains, promoting the crack formation [ZAFB19]. Grain growth enhances the crack propagation as well as observed in Figure 55. This is in accordance with the Hall-Petch relationship. This was also reported by Yang and others [YaAJ14]. Therefore, grains' reconstruction is one of the main factors affecting the crack propagation pathway.

Another probable cause is the effect that grain boundaries [DSWN19] and disorientation angles [ZZYH16] may have on hindering the crack progress, especially when looking at the high difference in terms of grain sizes between grains at the metallic interconnection positions and inside the wire bulk [SoAT17]. The increase in the disorientation angle between grains could slow the crack propagation rate by acting as a microstructural hindrance due to the increase in the energy barrier of the crack penetrating the grain boundary; this hinders the crack emission at the crack tip [ZZYH16]. Therefore, the presence of some HABs separating both sites arrests the crack emergence towards the bulk, forcing cracks to propagate just above the metallic interconnection. Moreover, crack closure could occur when migrating from small to big grains. This phenomenon may be caused by several factors, such as the difference in the degree of plasticity between one small grain and its big neighboring, the impurities present, the roughness change between neighboring grains, and other factors [Huss97].

The crack propagation speed at the last cycling stages becomes slower, as presented in Figure 45. This is accompanied by an increase in the frequency of HABs at the interconnection sites, as observed in Figure 56, Figure 82, and Figure 86. Maybe this is due to the role of HABs in resisting cracks' progress [ZZYH16]. Finally, when N_f is reached, cracks are totally distributed at the entire bottom wire zone, where total separation (lifting-off) occurs. All these observations are also coherent with literature and experimental data [AYAE16], [LCLH07].

6 NANOINDENTATION TESTS

Nanoindentation tests were subsequently conducted to determine, locally inside grains, physical and mechanical properties such as the Young modulus (E) and hardness (H). The aim of obtaining these parameters is to see their variation within the same wire among different grains at different locations and to interpret their evolution upon cycling. These values are also used in order to build the physiochemical model in the next chapter.

This technique uses a very fine diamond tip that penetrates the material. This makes it possible to indent fine geometries or thin coatings without being disturbed by the substrate or the mechanical environment around the geometries to be measured. An indenter is pressed into the test object with a defined force curve in nanoindentation tests. When the specified maximum force is reached, the indenter is released in a controlled manner. The penetration depth is recorded during loading and unloading.

Nanoindentation measurements have been carried out on various samples for wire #8 in different chips across a line situated in the middle of the contact area, as presented in Figure 88. Measurements were obliged to be done near the center because most of the samples have too small wire thickness at the wire terminals. In total, fifteen indents are applied on this measurement line, with an increment of ≈ 15 µm between each measurement and the other. The indentation depth ranges between 0.8 to 1 µm. The strain rate was set to be 0.05 s^{-1}, and the Poisson's ratio retained is 0.36.

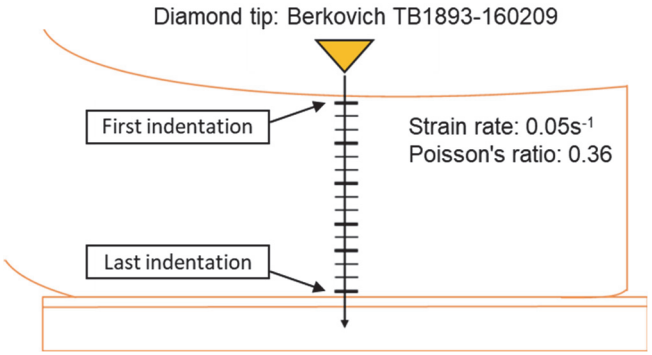

Figure 88: Indents line where the nanoindentation measurements are performed.

After looking at the Young modulus and hardness values, it was seen that these values are highly local, depending on the characteristics of each grain. No general trend can be deduced when plotting the mean value of both parameters for the fifteen indents at each cycling stage. Consequently, to better interpret the values of both parameters, the evolution of both parameters should be interpreted as a function of the number of cycles but by comparing their evolution at the same indentation height, not by taking a mean value. However, this is so difficult to do in a precise way due to several limitations. The main limitation is that not all the measurements are identical, where many nanoindentation cross-sections are not located exactly at the same positions among different samples. The cause for that is the thickness of the wire which may differ among these different samples.

Figure 89 and Figure 90 show the evolution of both Young modulus and hardness parameters as a function of the number of cycles. These parameters were measured approximatively at the same indentation height for samples aged at a different number of cycles. As the height of indentation increases, this means that we are getting closer to the metallic contact. At several cycling stages, wires #8 from chips #2, #3, #6, and #7 (as labeled in Figure 44) were analyzed.

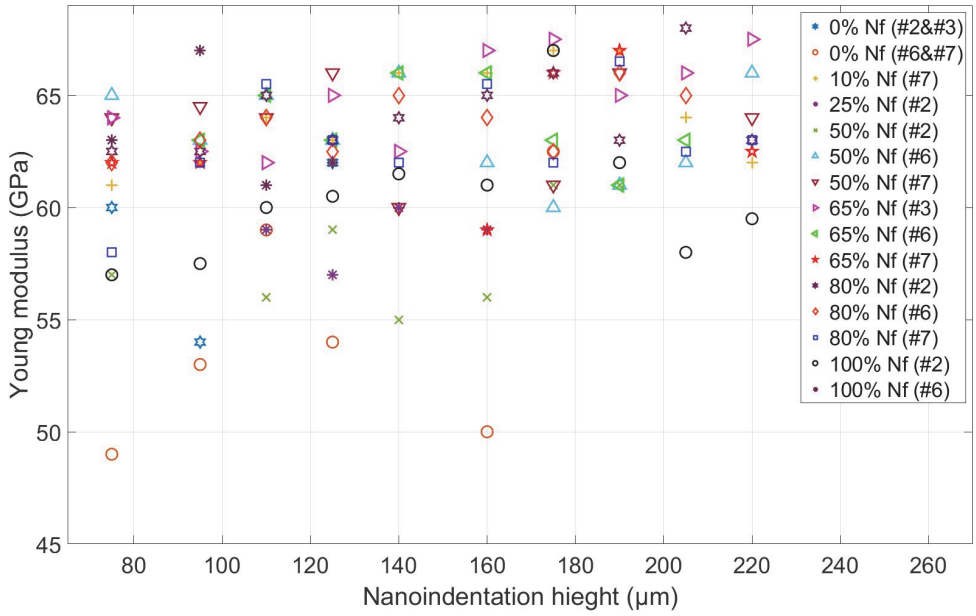

Figure 89: Young modulus (E) evolution with cycling for degraded wires in different chips.

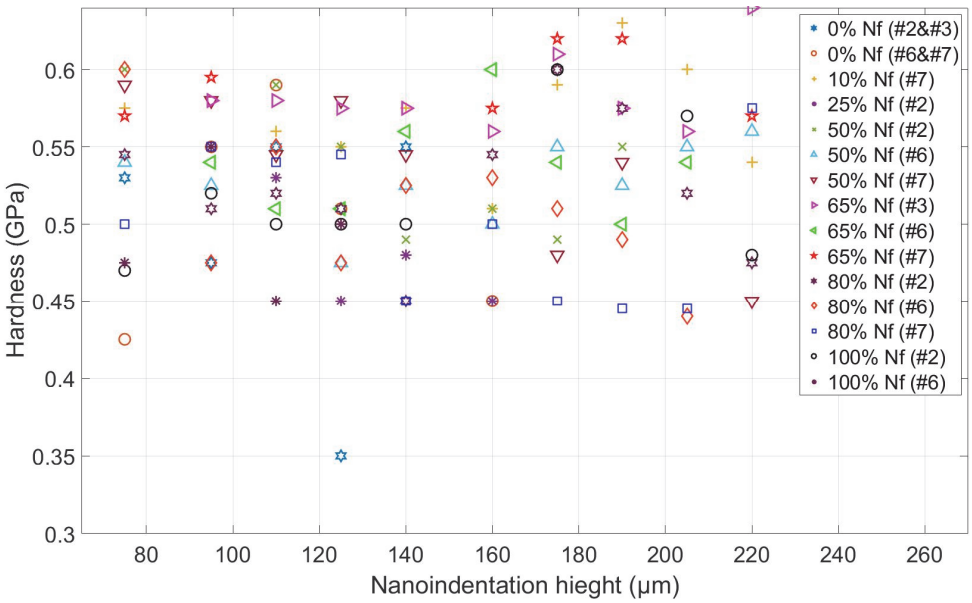

Figure 90: Hardness (H) evolution with cycling for degraded wires in different chips.

From both figures, it is clear that Young modulus and hardness values are highly local, where they depend on the local properties of grains, such as their size. Young modulus and hardness values were deduced to be higher at the metallic interconnection than inside the wire, indicating that aluminum is more rigid at the interface. This is logical because grains are very small when getting closer to the wire-metallization contact. It also seems that Young modulus and hardness values highly vary with cycling. This can be linked to the EBSD data that showed critical reconstruction processes, where for example, the change in the size of grains was so apparent. When comparing the values of Young modulus and hardness for the same wire's positions at different cycling stages, it is concluded that the values mostly decrease upon cycling. This seems to be mainly due to the grain growth process.

7 CONCLUSIONS

To summarize, some microstructural analysis techniques were presented with their outcomes, such as SEM, AFM, and EBSD. EBSD tests with the help of the ATEX software were used for interpreting the evolution of several features, such as the orientation angle of each grain, the disorientation angle between grains, the grain size, the plane of orientation of each grain, and other issues. Since this study focuses on the wire-metallization contact zone where cracks initiate and propagate, these particular positions were discussed microstructurally in detail by partitioning the EBSD data. It was deduced that the grain size globally increases upon cycling. For the texture, it can be concluded that grains orient to increase their packing density and decrease their surface energies. Texture components which enable us to know whether deformation or recrystallization processes are dominant were interpreted as well. Each of these two processes was shown to affect the degradation process in its own way, as explained in the first and second chapters. Moreover, it has been deduced that the crack formation starts from the interconnection edges, initiating from the heel and tip interconnection positions, with a faster speed at the heel than at the tip. The grain growth process and the presence of LABs at the early cycling stages (crack initiation) were accompanied by the maximal crack speed. The shift from LABs to HABs at advanced cycling stages was synchronous with the slowdown in the crack propagation speed. Those interpreted features are so important for building up the physicochemical-microstructural model that will be described in the next chapter.

CHAPTER III: THE PHYSICOCHEMICAL-MICROSTRUCTURAL MODELING APPROACH OF THE CRACK EVOLUTION AT TOPSIDE METALLIC INTERCONNECTIONS

1 INTRODUCTION

In Chapter I, it was shown that the microstructural evolutions are accompanied by degradation processes, particularly the crack evolution which is the driving force of failure. In Chapter II, the main microstructural changes were interpreted upon cycling, and the crack evolution was linked to those changes. Based on that, finding relationships between the crack evolution from one side, and microstructural features and physicochemical properties from another side, is the main thing to do for predicting the crack pathway and its propagation manner.

Accordingly, the combined fracture mechanics - physicochemical and microstructural model is achieved by relating the parameters of a damage-based model in fracture mechanics used to predict the fatigue crack propagation, cohesive zone model (CZM), to the most critical physicochemical-microstructural parameters. After that, the model's parameters are extracted with the help of the ATEX software after applying EBSD analyses on SKIM63 IGBT samples.

First, the CZM approach is described in detail, illustrating its basis on physicochemical concepts. Afterward, the linkage between its parameters and critical physicochemical-microstructural properties is illustrated. Finally, the model used for predicting the crack evolution is built.

2 COHESIVE ZONE MODELS (CZMS) IN FRACTURE MECHANICS

This section describes the CZMs, showing their different types. The appropriate CZM type to predict the formation of the cracks at the metallic contacts was selected. At last, the parameters of the selected CZM were related to critical physicochemical-microstructural parameters.

2.1 DESCRIPTION OF THE CZM

One of the most used models predicting crack propagation is the CZM [Grif21]. It is a multiphysics model in fracture mechanics which can be implemented in finite element tools. In the CZM, the fracture formation is regarded as a gradual phenomenon of separation of intersecting surfaces. In this model, the crack formation and propagation are related to cohesion energies and traction forces, as presented in Figure 91 [PaPa11]. Among the various forms of cohesive laws, the common feature is that the cohesive traction reaches a peak value and then drops toward zero with a gradual increase in the opening displacement. This results in the creation of two free surfaces, which marks the complete formation of a crack. Indeed, during the loading cycle, the opening of the crack will impede the local heat transfer, whereas its closure will permit its restoration partially or fully [BeSD13].

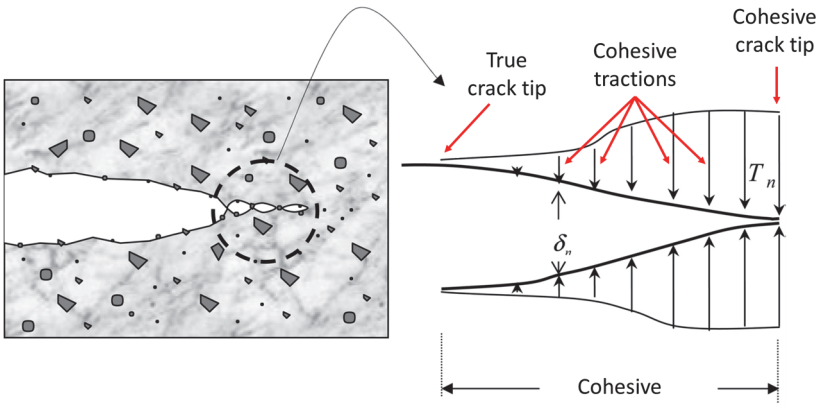

Figure 91: The CZM representation.

The CZM is based on the model proposed by Griffith [Grif21]. Griffith described the initiation and propagation of cracks in the case of brittle fractures in glass in the 1920s. Dugdale [Dugd60] and Barenblatt [Bare62] in the 1960s accounted for the concept of the CZM for brittle materials and investigated the deformation and fracture processes of materials near the crack tip. CZMs became more important following the studies of Irwin [SuJi12]. Based on the results of Griffith, Irwin proposed two approaches to determine the failure criterion; the first is based on the stress fields present at the crack front, and the second is based on the system's interface energy balance when subjected to cracking.

The first approach introduces a new parameter called the stress intensity factor (K), which can describe the stress field in the crack front zone. A singularity point is present at the location of the crack tip, with stresses tending towards infinity. This singularity is obtained in the Linear Elastic Fracture Mechanics (LEFM) domain, in which the behavior law of the material is considered to be evolving in a purely elastic way. In this case, the fracture under monotonic loading occurs when the stress intensity factor (K) reaches the value K_c, called the fracture toughness. This material property is usually determined experimentally and depicts the material resistance against fracture. Thus, in order to apply the stress intensity factor method described above, the inelastic zone must be neglected. However, in reality, the material deforms plastically in the crack front area.

The second approach, based on the energetic balance at the interface, also introduces a new parameter equivalent to the stress intensity factor called the energy release rate (G), which corresponds to the energy rate delivered during cracking. In particular, it is defined as being equal to the decrease in the potential energy of the solid per unit of cracking. When the crack occurs under monotonic loading, this energy release rate G is supposed to be absorbed by the newly created surfaces. Hence, a critical fracture criterion (G_c) similar to the fracture toughness K_c is defined. G_c is also a material property that can be obtained experimentally.

The stress intensity factor K and the energy release rate G are the foundations of the LEFM. However, as mentioned previously, there should be improvements to adapt the plastic deformations in the case of some metals such as aluminum. Thus, new methods have been developed to be able to determine the fracture in conditions where the inelastic zone of the crack front is significant. Additionally, in fatigue crack propagation, the crack growth is due to cyclic and not monotonic loading, as shown previously. In this particular case, and since the crack initiation and propagation differ from a brittle fracture, models have been developed to determine the damage evolution with cycling.

Efforts have been exerted to extend the previously presented notions to the nonlinear domain. The CTOD (Crack Tip Opening Displacement) and J-integral methods are the best-known methods that account for inelastic deformations [SuJi12]. The CTOD noted by δ is based on the crack blunting due to the plastic deformations occurring at the crack tip vicinity. In particular, it represents the opening displacement at the crack tip when considering the blunted crack. On the other hand, the J-integral is a method of calculating the variation of the potential energy at the crack tip for elastic and inelastic deformations. In this manner, the variation of the potential energy at the crack tip, including inelastic deformations, can be seen as a generalized version of the energy release rate G. Associated with these two methods, two critical parameters δ_c (critical crack tip opening displacement) and J_c (critical energy release rate) are defined.

The Paris law is the most commonly developed model that considers the damage evolution with cycling. It relates the crack speed (da/dN) to the stress intensity factor (K) [PaEr63]. For the elastic zone, the J-integral being equivalent to both K and G can be expressed in the Paris law [Rive06]. However, this relation can hardly be generalized for the materials deforming mainly in the plastic zone, when inelastic deformation cannot be neglected. Moreover, the J-integral definition and its domain of validity are based on the deformation theory of plasticity which does not take into account the unloading occurring when a crack grows [GoSø16]. Hence, the J-integral may be used to predict the crack initiation process, but there are some general reservations about its ability to predict crack growth.

The CZM is one of the most important improved models for predicting crack propagation in the case of ductile metals [SuJi12]. The CZM is a more advanced approach for modeling the crack evolution in ductile materials than LEFM and CTOD. This model permits, indeed, to fully describe the behavior of the interface through the build-up of stress during loading until reaching a critical point at which the crack starts to grow, followed by the unloading of the stress at the interface until it becomes a stress-relieved surface. Precisely, this behavior is described by a cohesive traction law in the vicinity of the crack tip, which relates the stress (σ) of the interface to the crack tip opening displacement (δ). However, the difficulty in using the CZM lies in the configuration of this law specific to each cracking scenario, which means it is specific to the geometry of the material, its properties, and the exposed loadings.

This cohesive tensile law has been defined in multiple ways in the literature, depending on the study conditions. In references [GiPM14], [TDCC07], the cohesive laws are presented in a bilinear type, while in references [AbSG05], [GoJD04], they are presented in an exponential type. Examples of cohesive laws are schematized in Figure 92. The definition of these laws depends on the way in which the crack will form, propagate, and vary according to the material properties, geometry, and loadings. Cohesive laws can be obtained analytically via the formulation of a potential characterizing the mechanical response of the interface [Need87].

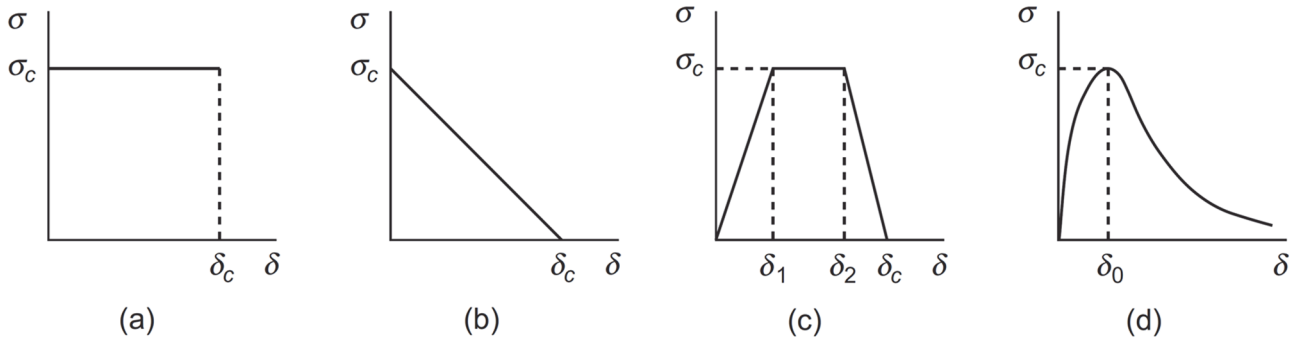

Figure 92: Examples of different cohesive tensile laws: (a) Dugdale's model, (b) the linear model, (c) the trapezoidal model, and (d) the exponential model [SuJi12].

Fracture mechanics defines three fundamental failure modes associated with independent movements of the faces on the sides of a crack. These modes, called mode I, mode II and mixed-mode, are presented in Figure 93. Thus, any crack can be described by one of these elementary modes [Ande05], [SuJi12]. Mode I only considers the normal direction, mode II only includes the tangential direction, whereas the mixed-mode covers both directions.

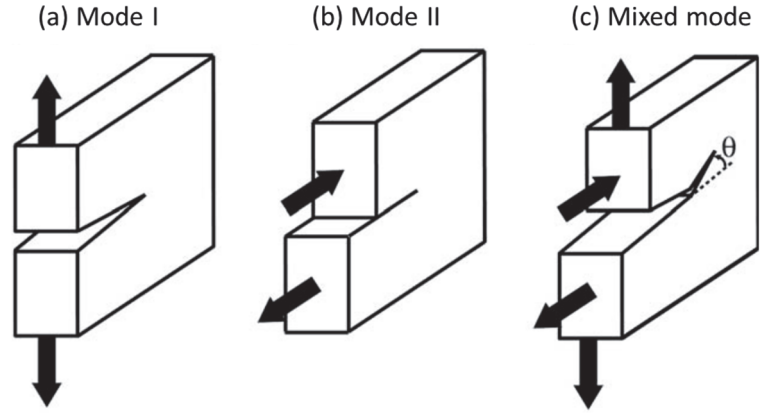

Figure 93: Fundamental fracture modes: (a) Mode I for opening (traction), (b) Mode II for slip (shear in the plane), and (c) Mixed-mode (both traction and slipping).

2.2 CZMs BACKGROUND: THEIR BASIS ON MATERIALS' PHYSICOCHEMICAL PROPERTIES AND INTERNAL STRUCTURE

In this section, the basis of CZMs on the physicochemical and microstructural properties of materials is presented. First, the linkage between the cohesion of materials and their corresponding physicochemical-microstructural properties is shown. Then, the CZMs based on the universal binding energy theory are displayed. Finally, the CZM whose parameters were related to physicochemical-microstructural factors is selected.

2.2.1 The linkage between the cohesion of materials and their physicochemical properties and internal structure

Before showing that the CZM is based on physicochemical and microstructural properties, relationships between such properties and the concept of materials' cohesion are illustrated first by presenting the models of Coffman and others [CoSe08] and Yaghmaee and others [YaRi14].

- **Coffman and other's model** [CoSe08]**:**

One of the important attempts relating the materials' cohesive laws to the geometry and physicochemical properties of grain boundaries was made by Coffman and others [CoSe08]. Cohesive laws are stress-strain curves used in finite element calculations to describe the debonding of interfaces such as grain boundaries. It is difficult to experimentally measure cohesive laws because isolating and measuring the displacements on either side of the grain boundary is so hard. But first, what is the exact meaning of debonding and cohesion?

As known, each material has its particular crystal structure and properties. This results in different materials' nature, type, and bond features. This characterizes the cohesion behavior of the material. Cohesion energy is a basic energetic property of metals, determining most of their other physical properties [KaCY03]. It is the necessary energy to break atomic bonds in the lattice. When metals in contact separate due to the crack formation, in other words, when grains and grain boundary fractures occur, this means that debonding occurs. The debonding of an interface, such as a grain boundary, is described by a cohesive law, giving the displacement across the interface as a function of stress.

According to Coffman and others' work, grain boundary energies and cohesive laws of grain boundary fracture can be extracted in 2D using atomistic simulations with a Lennard-Jones potential for all possible geometries within periodic boundary conditions [CoSe08]. Periodic boundary conditions are a set of boundary conditions chosen for approximating a large system by using a small part called a unit cell. Periodic boundary conditions were used in the y-direction to avoid edge effects that could cause cracks to nucleate at the intersection with the surface. A constrained layer of atoms was used to impose fixed boundary conditions in the x-direction. Using periodic boundary conditions has the disadvantage of only allowing geometries with finite repeat distances. Two rectangular grains were initialized with given rotations that define the grain boundary geometry wished to be analyzed, as presented in Figure 94. In this way, energies and cohesive strengths for grain boundaries were calculated.

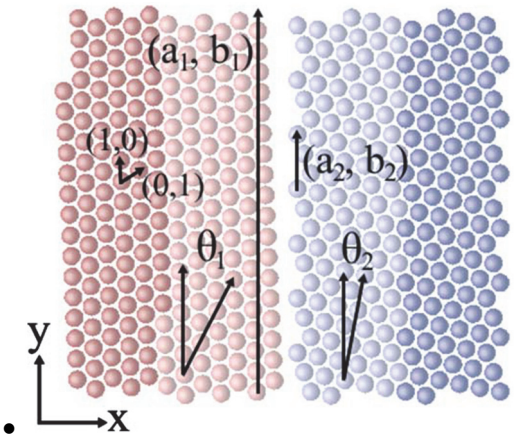

Figure 94: An example of a grain boundary with tilt angles θ_1 and θ_2 and repeat distances $D_1 = |(a_1,b_1)|$ and $D_2 = |(a_2,b_2)|$ [CoSe08].

When analyzing LABs, it was deduced from the simulations that the fracture stress depends on dislocations. At specific boundary disorientation angles, dislocations to generate fracture are absent. At such positions, the cohesive strength highly increases. After plotting the stress distribution vs. the tilt boundary angle for HABs, a discontinuous increase in the fracture stress was deduced when energy cusps were present, as observed in Figure 95. These specific disorientation angles are called special or high symmetric boundaries, with geometries having particularly low repeat distances. In these boundaries, the added flaw is no longer the only nucleation site for fracture. The added dislocation creates a stress field with positive stress on one side and negative stress on the other. The fracture nucleates along the boundary in the region where the stress due to the added flaw is positive. This leads to a linear law for fracture strength as a function of grain boundary tilt angle.

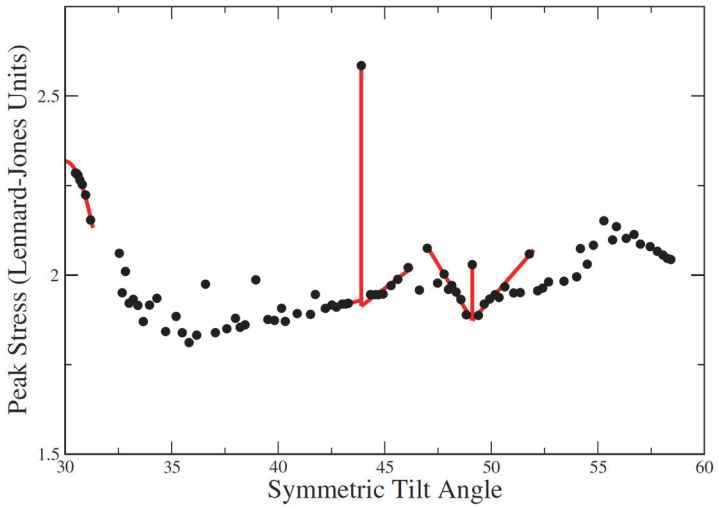

Figure 95: Peak fracture stress vs. tilt angle for HABs. The fracture stress is discontinuous everywhere, with higher values at special tilt HABs [CoSe08].

- **Yaghmaee and other's model** [YaRi14]**:**

This model proposed by Yaghmaee and others transforms bulk molar cohesion energy into inter-atomic bond strengths inside the metallic elements [YaRi14]. The main focus of this work was on the binding strength property expressed by the cohesion energy inside the material. This parameter is classified as an important bulk thermodynamic property. The number of neighboring atoms, the material's crystallography, and the effective length of interaction energies between atoms play dominant roles in strengthening and weakening the binding strength of the material. Therefore, the structural effect of different crystals on their bulk cohesion energy is essential to study.

In this work, and in order to study the effect of the nature of metallic bonds on their physicochemical properties, they first tried to investigate and introduce a mathematical model for transforming the macroscopic molar cohesion energy into microscopic bond strengths between atoms. Then, an algorithm for estimating the nature of the material's bond type, including their properties and lattice scale "cutoff", has been proposed. The number of bond types and the power of the potential function (n-potential; for FCC structures it equals 8) are inserted as input data. The element's crystal structure must also be chosen (BCC, FCC, or HCP). The methodological approach followed by linking the bulk cohesion energy (E_{inner}^{total}) and the fundamental energy scale (E^{av}) is summarized in the equations below. Figure 96 illustrates the way of calculating the bulk cohesion energy of the material (E_{inner}^{total}).

$$E_{inner}^{total} = \frac{1}{2}\sum_{i} ccn(i)\, E_{pair}(i) \tag{9}$$

$$g_{crystal}(i) = \frac{d_i}{d_a} \tag{10}$$

$$E^{av} = 2\, E_{inner}^{total} \sum \frac{ccn(i)}{g_{crystal}^{n-potential}(i)} \tag{11}$$

Where ccn(i) is the cohesive coordination number of atoms in an i^{th} group, $E_{pair}(i)$ is the average cohesive energy (bond strength) between atoms in an i^{th} group and a particular inner atom from which the distances are counted, d_i is the relative atomic distance between the i^{th} group of atoms and a particular inner atom, d_a is the atomic diameter.

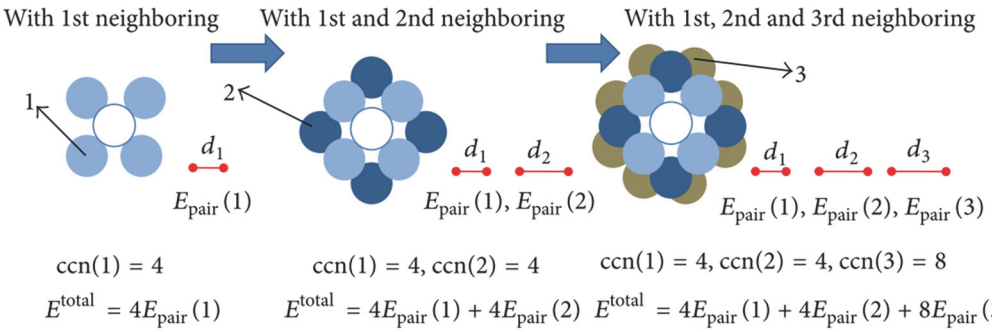

Figure 96: A simple scheme illustrating how atoms' numbers and relative distances vary [YaRi14].

As a result, based on equation (11), the thermodynamic quantity noted by the macroscopic cohesion energy (E_{inner}^{total}) is expressed as the multiplication of a fundamental energy scale (E^{av}) with a complicated function, including the number of atoms with their relative distances and the binding nature based on the material's crystal structures. Therefore, this final equation includes information about the material properties, crystallographic and geometrical characteristics. Although, before any analytical investigation, it is essential to study the crystallography of different structures and evaluate the required mathematical series which represent the atomic distances (d_i) and the number of neighboring atoms ccn(i). Several limitations included in this model must be mentioned. First, homogeneous cohesive energy distribution was assumed in all directions of the crystal cell among each group of atoms with equal distances from arbitrary inner atoms, where the calculated cohesion energy is particularly at zero kelvin. In addition, a better set of cutoff length and potential energy power related to the nature of bond types and crystal structures must be considered separately for each metallic element in the software used in this model.

2.2.2 CZMs built based on the physicochemical universal binding energy theory

All the CZMs are based on stress-displacement behavior laws. Generally, the constitutive laws used are essentially based on mechanical considerations. Consequently, they do not consider the effect of varying grain boundary geometries and physicochemical properties within the material. Recently, several studies have been done to consider such properties. Among the most important CZMs are those established referring to the universal binding energy theory constructed by Rose and others [PaPa11], [RoFS81]. The universal binding energy theory shows the dependency between the metallic bonding energies and their lattice parameters. It was deduced that the lattice parameters are linked to the cubic geometry of material atoms, where each material has its particular lattice parameter. From this theory, cohesive laws and models have been generated [Need87].

- **Universal binding energy theory** [RoFS81], [RoSF83]**:**

Several studies discussing the CZM started from the fact that this model is based on the universal binding energy model. Rose and others generated an atomistic potential relating the metallic binding energies to the lattice parameters by plotting the universal binding energy graph [RoFS81], [RoSF83].

Primarily, it was stated that materials' tension leads to a change in the positions of atoms; thus, there will be a change in the energies between atoms. Therefore, this could be a consequence of the fatigue process. In the next step, they plotted the adhesive binding energies as a function of separation in metallic contacts, as observed in Figure 97. The adhesive binding energy noted by E_{adh} ($a_{interatomic}$) is defined as follows:

$$E_{adh}(a_{interatomic}) = [E(a_{interatomic}) - E(\infty)]/2A_{cross\ sectonal} \quad (12)$$

Where E is the total energy, $a_{interatomic}$ is the distance between the surfaces of metals (interatomic separation distance), and $A_{cross\text{-}sectional}$ is the atomic cross-sectional area.

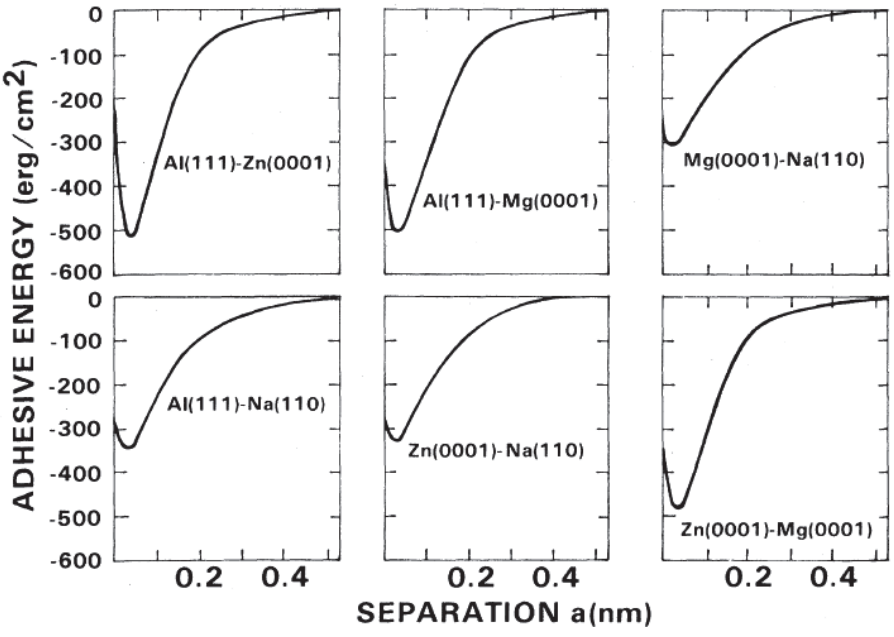

Figure 97: Adhesive binding energy vs. the separation between the surfaces [RoSF83].

After plotting the curves, considerable variations in the depth and shape of the curves were observed. Rose and others tried to scale adhesion and cohesion energies into a universal curve. This scaling was motivated by the expectation that metals with shorter screening lengths would have adhesive energy curves that rise faster with separation. This suggests that for identical metal contacts, the separation is scaled by the Thomas-Fermi screening length (λ_{TF}) [Raim61]. After incorporating the Thomas-Fermi screening length, the new energy equation becomes as follows:

$$E_{adh}(a_{interatomic}) = \Delta E_{eq}.E^*_{adh}(a_{interatomic}{}^*) \quad (13)$$

Where ΔE_{eq} is the equilibrium binding energy. This parameter has the following formula: $\Delta E_{eq} = E_{adh}(a_m)$. $E_{adh}{}^*$ ($a_{interatomic}{}^*$) is the universal energy function that describes the binding energy curve. The scaled separation distance ($a_{interatomic}{}^*$) has the following formula: $a_{interatomic}{}^* = 2(a_{interatomic}-a_m)/(\lambda_{TF1}+\lambda_{TF2})$, a_m is the distance between atomic surfaces at equilibrium, and λ_{TF1} and λ_{TF2} are the screening lengths of bimetallic contacts. The fitting curve of the universal adhesive energy ($E_{adh}{}^*$) against the scaled separation ($a_{interatomic}{}^*$) is given by the following equation, with β = 0.90.

$$E^*_{adh}(a_{interatomic}{}^*) = -(1+\beta a_{interatomic}{}^*)\, e^{(-\beta a_{interatomic}{}^*)} \quad (14)$$

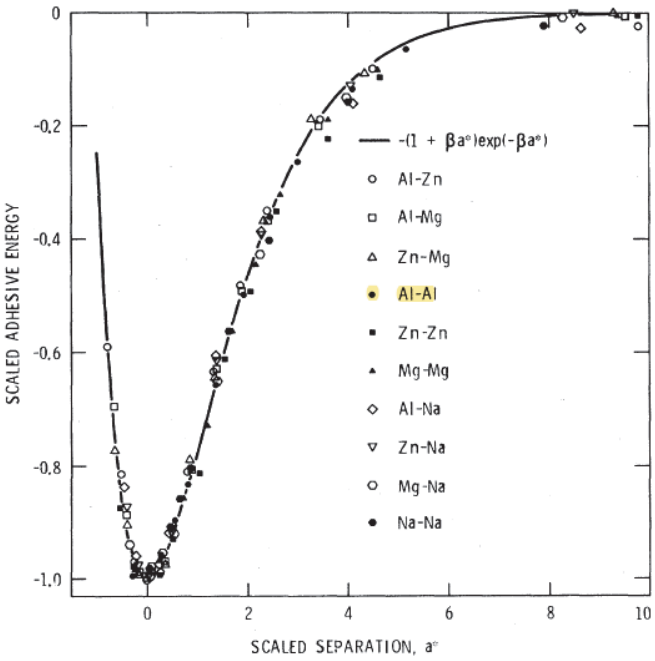

Figure 98: Adhesive energy results [RoFS81].

From Figure 98, the universality of the scaled adhesive energy curve is truly remarkable when looking at the results of ten bimetallic contacts that lie very close to the universal curve. Among these bimetallic contacts is the Al-Al, which corresponds to the wire-metallization metallic contact in the topside components of IGBT semiconductor power devices.

Based on the above equations, a relationship was established between the physicochemical surface energy parameter (γ_s) which depends on the internal structure of the material's atoms (such as its orientation plane [VRSK98], [ZhMX04]), and the cohesive energy property (E_{coh}) as presented in the equation below [RoSF83].

$$\frac{4\pi r_{ws}^2 \gamma_s}{E_{coh}} = 1.7\,\frac{C'_{11}}{2d_{IS}}\,\frac{r_{ws}}{3B} \quad (15)$$

By which $r_{ws} = [(3/4)\,\pi\, n_A]^{1/3}$ is called the Wigner-Seitz radius, n_A is the atom density, B is the bulk modulus, d_{IS} is the interplanar spacing, and C_{11}' is the elastic stiffness constant associated with the direction perpendicular to the interface.

Since $\frac{C'_{11}}{2d}\frac{r_{ws}}{3B}$ is a constant, then $4\pi r_{ws}{}^2\gamma_s \propto E_{coh}$. This relation evidenced the linkage between the cohesion energy of metals and their surface energy values.

- **Approaches linking physicochemical and microstructural features to the CZMs, based on the universal binding energy theory** [KaCY03], [VeCe04]**:**

The introduction of thermodynamic excess variables to describe a cohesive zone offers a precise link between CZMs used in continuum simulations and the properties of the fractured materials. Although the usefulness of the concept of cohesion energy is obvious, however, its is used less than expected. That is because there are no direct experimental or theoretical methods to obtain the absolute value of the cohesion energy, mainly because chemical thermodynamics work with relative and not absolute values. According to its classical definition, the cohesion energy of solid metals at 0 kelvin and 1 bar can be written as presented in the equation below [KaCY03].

$$U^{\circ}_{coh(s,0K)} = \Delta_f \, H^{\circ}_{s(0K)} - \Delta_f \, H^{\circ}_{g(0K)} \tag{16}$$

Where $\Delta_f H^{\circ}_{g(0K)}$ is the enthalpy of the formation of gaseous metals at 0 kelvin (kJ/mol), and $\Delta_f H^{\circ}_{s(0K)}$ is the enthalpy of the formation of solid metals at 0 kelvin (kJ/mol).

From this classical definition, the cohesion energy is only linked to the melting temperature. Although any change in the state of the matter is perfectly described by the relative value of Gibbs' energy change, the cohesion energy in pure metals must also require an absolute scale. When considering Mg and Al metals, they have practically the same melting points (923 and 933 K respectively); however, they acquire at the same time very different cohesion energy values (-146 kJ/mol and -327 kJ/mol respectively). When looking at the crystallographic structure of both metals, it can be seen that they differ in the crystal structure (HCP for Mg and FCC for Al). This would explain a difference in cohesion energies. A free magnesium atom with a relatively stable s^2 electron configuration is much more stable than the free aluminum atom, having a very unstable s^2p^1 electron configuration. This relative difference in the stability of free atoms appears in the definition of the cohesion energy of metals. Based on that, this equation was discussed in Kaptay's work, and an attempt was made to create an absolute scale for the fracture energy of solid metals [KaCY03].

To connect first-principles total energy calculations and continuum models for crack growth, Van der Ven and others defined excess variables that characterize the thermodynamic properties of a cohesive zone [VeCe04]. Their definition of excess variables provides energy partitioning between the cohesive zone and the elastic energy in the surrounding continuum system. Using a supercell approach, they illustrated how excess variables such as energy could be determined from the first-principles total energy calculations. Applying this to the decohesion of FCC aluminum along with a pair of adjacent (111) planes, they have recovered the universal binding curve proposed by Rose and others [RoFS81]. The focus in Van der Ven and others was oriented toward showing how impurities such as hydrogen and oxygen can reduce the cohesive strength of a solid. Only one aspect of crack growth was presented in their work (cleavage). Plasticity around the crack tip caused by the crack growth was not taken into account. Additionally, a short-ranged lattice model containing just nearest-neighbor pair interactions was only considered. Moreover, they used the mean-field approximation, by which the impurity atoms between the separating planes are assumed to be completely disordered [VeCe04].

- **General and unified potential-based CZMs based on the universal binding energy theory** [PaPa11]**:**

General and unified potential-based CZMs are among the most famous CZMs. These models rely on the fact that the CZM is based on the universal binding energy theory. The E_{adh}^{*} parameter listed in the universal binding energy model was noted by Ψ in these CZMs. The resulting universal binding energy function is presented below, where l is the scaled separation associated with the Thomas-Fermi screening length.

$$\Psi = -(1 + l)\, exp(-l) \tag{17}$$

Needleman [Need90] utilized the exponential potential of the above equation with linear shear interaction and obtained the following traction and exponential potential expressions:

$$T_n = \frac{-27}{4}\,\sigma_{max}\left\{\left(\frac{\Delta_n}{\delta_n}\right)\left[1-2\left(\frac{\Delta_n}{\delta_n}\right)+\left(\frac{\Delta_n}{\delta_n}\right)^2\right]+\alpha_s\left(\frac{\Delta_t}{\delta_n}\right)^2\left[\left(\frac{\Delta_n}{\delta_n}\right)-1\right]\right\} \quad (18)$$

$$T_t = \frac{-27}{4}\,\sigma_{max}\left\{\alpha_s\left(\frac{\Delta_t}{\delta_t}\right)\left[1-2\left(\frac{\Delta_n}{\delta_n}\right)+\left(\frac{\Delta_n}{\delta_n}\right)^2\right]\right\} \quad (19)$$

$$\Psi(\Delta_n,\Delta_t) = \frac{9}{16}\,\sigma_{max}\,\delta_n\left\{1-\left[1+\frac{z\Delta_n}{\delta_n}-\frac{1}{2}\alpha_s\left(\frac{z\Delta_t}{\delta_t}\right)^2\right]exp\left(-\frac{z\Delta_n}{\delta_n}\right)\right\} \quad (20)$$

Where $T_{n,t}$ are the normal and tangential tractions, Ψ is the universal binding energy, $\Delta_{n,t}$ are the normal and tangential separation distances respectively, σ_{max} is the normal cohesive strength, τ_{max} is the tangential cohesive strength, $\delta_{n,t}$ are the normal and tangential characteristic lengths respectively, α_s is a shear stiffness parameter, and z = (16/9) exp (1).

When $\Delta_t = 0$, the normal traction (T_n) across the interface as a function of (Δ_n) was plotted for the exponential potential as observed in the figure below [Need90].

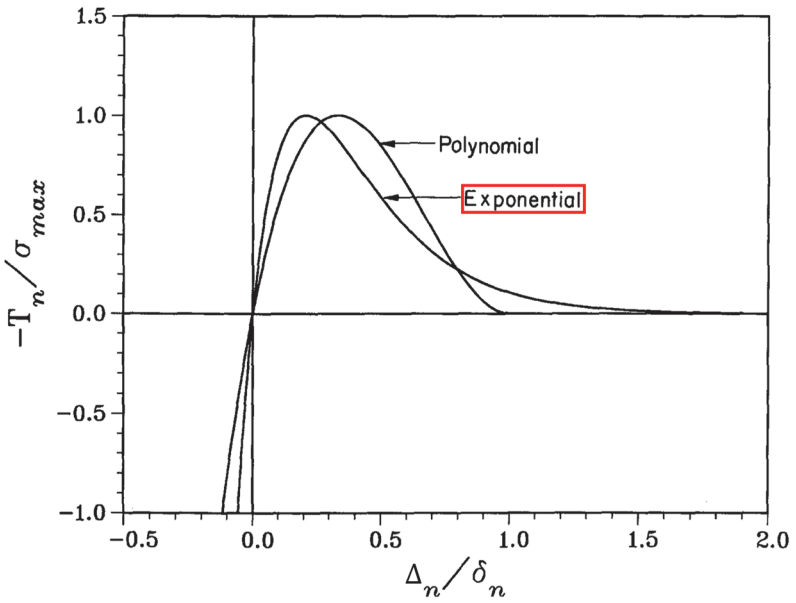

Figure 99: The plot of T_n across the interface as a function of Δ_n (when $\Delta_t = 0$) for the exponential potential bordered in red [Need90].

Based on the above expression, the model was generalized and improved by generating several potential-based models. Three important models are listed as follows:

A. <u>The generalized exponential-periodic potential-based model</u>

The generalized exponential-periodic potential-based model is one of the models proposed by Beltz and Rice [BeRi92], [RiBe94]. It is based on the competition between cleavage decohesion and dislocation nucleation for a slip plane under general loading [PaPa11]. The equation of the universal energy in the generalized exponential-periodic potential-based model is presented as follows:

$$\Psi = 2\gamma_s + 2\gamma_s\, exp^{\left(-\frac{\Delta_n}{\delta_n}\right)}\{[q+(\frac{q-r}{1-r})\frac{\Delta_n}{\delta_n}]\, sin^2\left(\frac{\pi\,\Delta_t}{\delta_t}\right) - [1+\frac{\Delta_n}{\delta_n}]\} \quad (21)$$

By which r is a non-dimensional parameter associated with the length scale Δ_n^* ($r = \Delta_n^* / \delta_n$), where Δ_n^* corresponds to the value of Δ_n after complete shear separation at $T_n = 0$. For the value of q, this parameter represents the ratio of mode II fracture energy to mode I fracture energy or the ratio of the staking energy to twice the surface energy ($q = \gamma_{us} / 2\gamma_s$).

The boundary conditions of this model showed relations between tractions and surface and staking energies. The normal traction (T_n) is linked to the surface energy (γ_s) and tangential traction (T_t) is linked to the stacking energy (γ_{us}). ϕ_n and ϕ_t are respectively the normal and tangential fracture energies [PaPa11].

$$\int_0^{\infty} T_n(\Delta_n, 0) d\Delta_n = 2\gamma_s = \phi_n = \sigma_{max}\, exp\,(1)\, \delta_n \tag{22}$$

$$\int_0^{\delta t/2} T_t(0, \Delta_t) d\Delta_t = \gamma_{us} = \phi_t = \frac{\tau_{max}\, \delta_t}{\pi} \tag{23}$$

Figure 100 demonstrates the generalized exponential-periodic potential function and its traction-separation relationships, where $\phi_n = 2\gamma_s$ = 100 N/m, $\phi_t = \gamma_{us}$ = 200 N/m, σ_{max} = 30 MPa, τ_{max} = 40 MPa, and r = 0 [PaPa11].

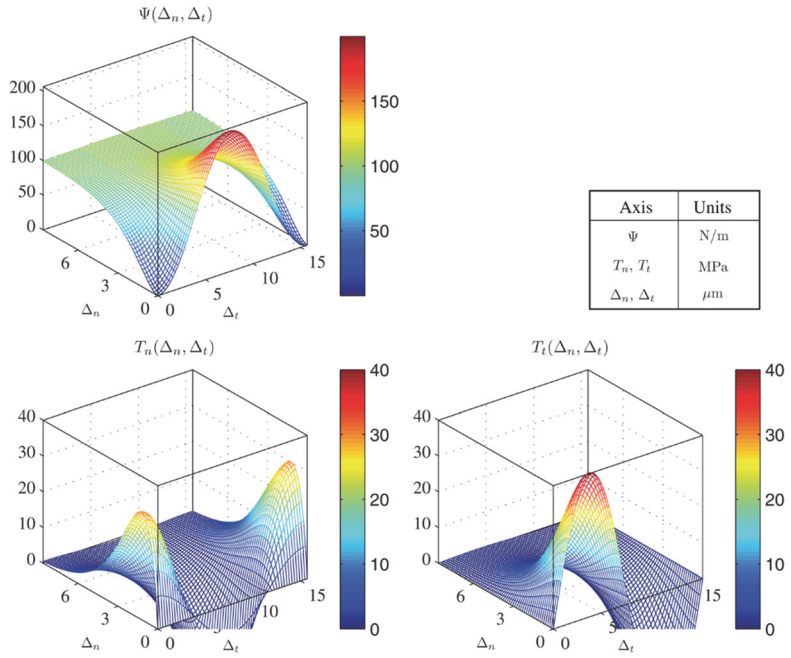

Figure 100: Beltz and Rice generalized exponential-periodic potential and its gradients; ϕ_n = 100 N/m, ϕ_t = 200 N/m, σ_{max} = 30 MPa, τ_{max} = 40 MPa, and r = 0 [PaPa11].

The main limitations of this model are that i) Δ_n^* parameter included in the r parameter is difficult to evaluate, and ii) the potential cannot be utilized for general interfacial shear failure because the periodic function is employed for dislocation's nucleation along the tangential direction.

B. <u>The exponential-exponential-based model</u>

Another model based on the universal energy model is the exponential-exponential-based model. This model is expressed by Xu and Needleman [XuNe93], where it has the following equations:

$$\Psi(\Delta_n, \Delta_t) = \phi_n - \phi_n\, exp(-\frac{\Delta_n}{\delta_n}) \{ [1 - r + \frac{\Delta_n}{\delta_n}] \frac{1-q}{r-1} - \left[q + \frac{(r-q)\Delta_n}{(r-1)\delta_n}\right] exp(-\frac{{\Delta_t}^2}{{\delta_t}^2}) \} \tag{24}$$

Figure 101 illustrates the exponential-exponential potential function and its traction-separation relationships, where ϕ_n = 100 N/m, ϕ_t = 200 N/m, σ_{max} = 30 MPa, τ_{max} = 40 MPa, and r = 0 [PaPa11].

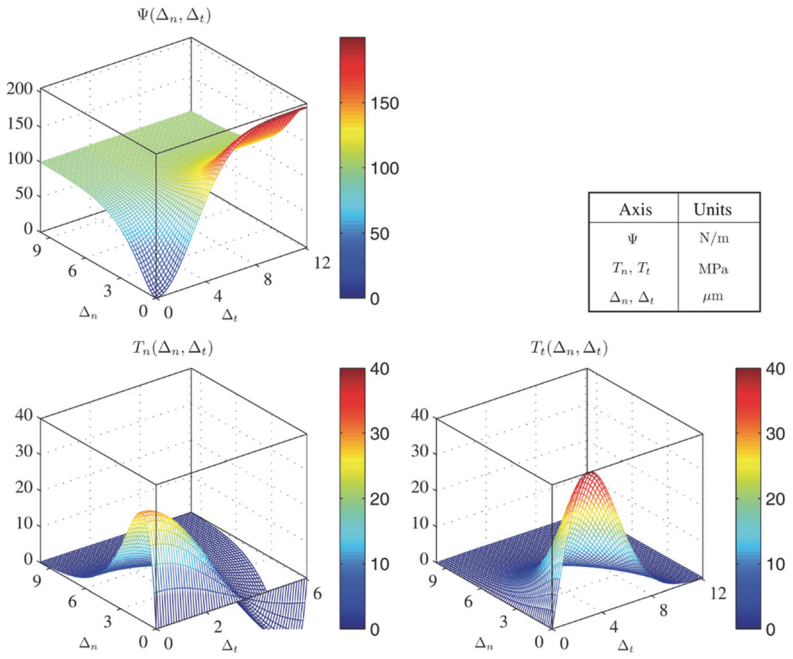

Axis	Units
Ψ	N/m
T_n, T_t	MPa
Δ_n, Δ_t	μm

Figure 101: Xu and Needleman exponential-exponential potential and its gradients; ϕ_n = 100 N/m, ϕ_t = 200 N/m, σ_{max} = 30 MPa, τ_{max} = 40 MPa, and r = 0 [PaPa11].

As for the generalized exponential-periodic potential-based model, the main limitation of this model is that the variable Δ_n^* is hard to determine. In addition, due to the exponential function, the final crack opening width is infinite, which does not resemble macroscopic fracture behavior.

C. The general unified potential-based model

A polynomial-based potential was formulated in conjunction with physical fracture parameters and consistent fracture boundary conditions in order to tackle the limitations of previous potential-based models. In each fracture mode, physical fracture parameters such as fracture energy and cohesive strength are employed. Additionally, shape parameters that characterize various material softening responses (brittle, plateau, and quasi-brittle) are integrated with each fracture mode. The general unified potential-based model obeys the subsequent equation [PaPa11]:

$$\Psi(\Delta_n, \Delta_t) = min\,(\phi_n, \phi_t) + \left[\Gamma_n \left(1 - \frac{\Delta_n}{\delta_n}\right)^{\alpha} \left(\frac{m}{\alpha} + \frac{\Delta_n}{\delta_n}\right)^{m} + \langle \phi_n - \phi_t \rangle\right] * \left[\Gamma_t \left(1 - \frac{|\Delta_t|}{\delta_t}\right)^{\beta} \left(\frac{n}{\beta} + \frac{|\Delta_t|}{\delta_t}\right)^{n} + \langle \phi_t - \phi_n \rangle\right] \quad (25)$$

α and β are shape parameters, whereas $\langle \cdot \rangle$ is the Macaulay bracket, i.e., $\langle x \rangle = \begin{cases} 0, & (x < 0) \\ x, & (x \geq 0) \end{cases}$.

The general unified potential function and its traction-separation under the following conditions: ϕ_n = 100 N/m, ϕ_t = 200 N/m, σ_{max} = 40 MPa, τ_{max} = 30 MPa, and α = 5, and β = 1.3 are shown in Figure 102 [PaPa11].

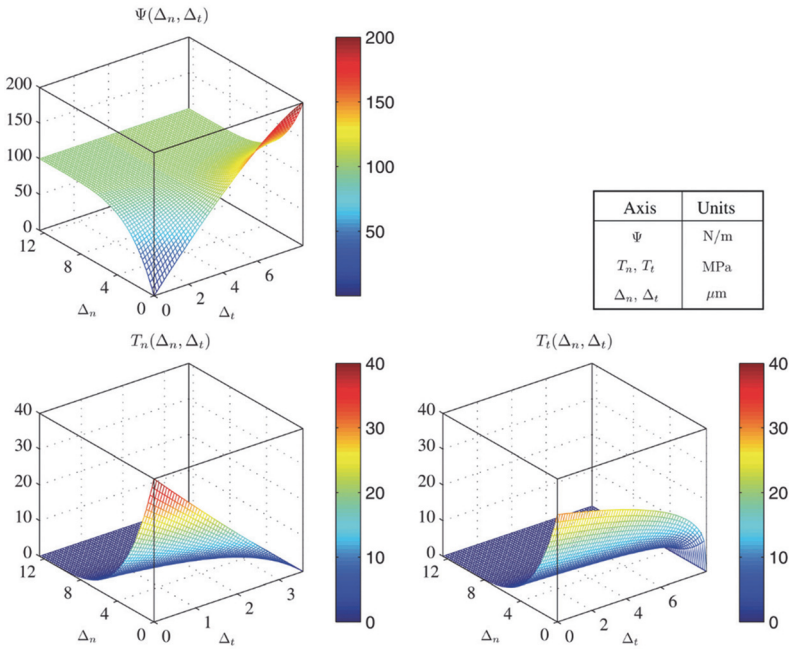

Figure 102: The general unified potential and its gradients; ϕ_n = 100 N/m, ϕ_t = 200 N/m, σ_{max} = 40 MPa, τ_{max} = 30 MPa, α = 5 and β = 1.3 [PaPa11].

The importance of this model is that it provides a consistent constitutive relationship under mixed-mode conditions, demonstrated by assessing the work of separation parameter (W_{sep}). This parameter consists of the work done by the normal traction (W_n) and the work done by the tangential traction (W_t). Consequently, two separation paths were investigated.

In the first path, material particles separate along the normal direction up to $\Delta_n = \Delta_{n,max}$; this is followed by complete tangential failure. Consequently, $\Delta_{n,max} = 0$ indicates the mode II failure while $\Delta_{n,max} = \delta_n$ represents the mode I failure. Thus, while $\Delta_{n,max}$ increases from 0 to δ_n, this means that W_n increases from 0 to ϕ_n while W_t decreases from ϕ_t to 0. Therefore, W_{sep} increases from ϕ_t to ϕ_n. The following expressions evaluate the work of separation of path 1. This path is schematized in Figure 103.

$$W_n = \int_0^{\Delta_n,max} T_n(\Delta_n, 0) d\Delta_n \tag{26}$$

$$W_t = \int_0^{\delta_t} T_t(\Delta_{n,max}, \Delta_t) d\Delta_t \tag{27}$$

$$W_{sep} = \int_0^{\Delta_n,max} T_n(\Delta_n, 0) d\Delta_n + \int_0^{\delta_t} T_t(\Delta_{n,max}, \Delta_t) d\Delta_t \tag{28}$$

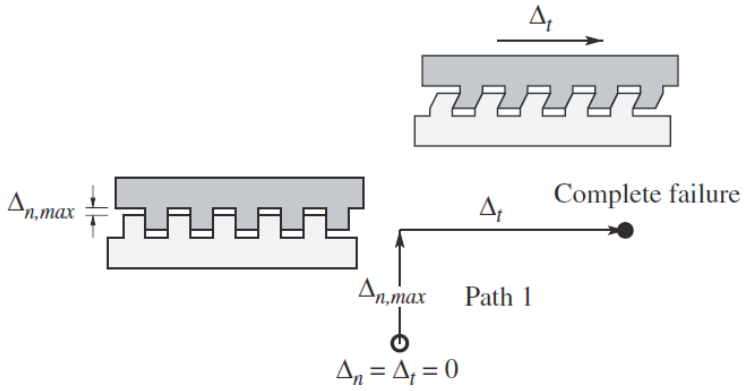

Figure 103: Separation path 1 for the material's debonding process.

In the second path, material particles separate along the tangential direction up to $\Delta_t = \Delta_{t,max}$, then a complete normal failure occurs. Accordingly, the separation path corresponds to mode I failure when $\Delta_{t,max} = 0$ and to mode II failure when $\Delta_{t,max} = \delta_t$. The increase of $\Delta_{t,max}$ from 0 to δ_t leads to the monotonic increase of W_{sep} from ϕ_n to ϕ_t [PaPa11]. The work of separation of path 2 is evaluated by the following expressions. This path is schematized in Figure 104.

$$W_n = \int_0^{\Delta_{t,max}} T_t(0, \Delta_t) d\Delta_t \tag{29}$$

$$W_t = \int_0^{\delta_n} T_n(\Delta_n, \Delta_{t,max}) d\Delta_n \tag{30}$$

$$W_{sep} = \int_0^{\Delta_{t,max}} T_t(0, \Delta_t) d\Delta_t + \int_0^{\delta_n} T_n(\Delta_n, \Delta_{t,max}) d\Delta_n \tag{31}$$

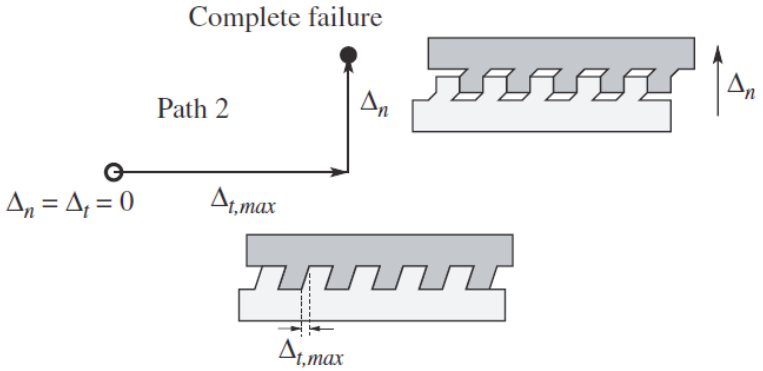

Figure 104: Separation path 2 for the material's debonding process.

This work of separation parameter (W_{sep}) presented in the general unified potential-based model was used in many publications when interpreting decohesion processes in the microscale [LHHO09], [MöBi14], [ZLTC19]. This parameter will be deeply discussed in the upcoming sections when explaining the approach followed in order to relate the CZM elements with critical physicochemical-microstructural properties.

Nevertheless, the presented potential-based models still have several limitations in representing the physical phenomena associated with cohesive fracture. First, these models are proposed under the condition of monotonic separation paths. Thus, unloading/reloading relations should be addressed independently to describe energy dissipations, including fatigue damage. In addition, the reviewed potential functions are rate-independent. In order to account for rate-

dependent fracture behaviors, the potential-based models may need additional development. Moreover, the unified potential-based model is based on four fracture parameters in each fracture mode. The determination of these parameters is a challenging task. Consequently, the upcoming approach is followed.

3 THE COMBINED CZ - PHYSICOCHEMICAL AND MICROSTRUCTURAL METHODOLOGICAL APPROACH FOLLOWED IN THIS STUDY

Starting from the fact that the CZM is based on physicochemical and microstructural concepts, as shown in the previous section, the following approach was thought about. In fact, physical models used to predict the damage evolution, such as the CZMs, utilize parameters independent of the aging state; however, it was observed in the previous chapters that the microstructure evolves with aging, and this evolution surely affects the materials' properties. Therefore, the parameters of these models change as well. The main hypothesis assumed is that evolution of the parameters of these models can be linked to that of the local microstructure within aging. The combined CZ - physicochemical and microstructural model to consider is specific to topside metallic interconnection degradations in power modules. This model is intended to be constructed based on the degradation processes exploration detailed in Chapters I and II. Results showed that the total failure of the module is due to the loss of contact between wires and metallization chips. As explained previously, this loss is due to the formation and propagation of cracks at the wire-metallization interfaces during the module's operation caused by degradation processes. Cracks' formation and propagation occur in accordance with other processes under the title of grains reconstructions, which must also be considered. Therefore, it is essential to mention the diversity of grains' characteristics at the topside metallic contacts. This variety comes from having different material properties, such as the composition and thickness of wires and metallization chips, in addition to the wire welding process that greatly changes the initial structure.

Because the fatigue problem is caused by the crack formation and propagation in topside metallic parts in power devices, our hypothesis is to find relationships between the driving force of the failure problem, i.e., the crack propagation from one side, and physicochemical-microstructural features from another side, in order to predict the crack pathway. The main proposed hypothesis in this approach is that these physicochemical-microstructural characteristics have a significant role in the degradation processes in the metallic contact vicinity. Their evolution's interpretation should make it possible to predict the cracking mechanism. This is corroborated by numerous observations from the carried-on experimental analysis and the listed information in the literature, as presented in the previous chapters. The precise objective of this approach is to use existing relationships from the literature relating the characteristics of the grains (size, disorientation angles, and orientation planes) to thermodynamic and physical parameters (the work of separation of intersecting surfaces, tensile strength, and hardness), benefiting as much as possible from the already obtained EBSD data.

Based on that, the first thing to do is to choose a suitable CZM type for the objectives of this study, which can predict the fatigue crack progress upon cycling. Afterward, the model's parameters are linked to physicochemical-microstructural properties.

3.1 BRIEF DESCRIPTION OF THE SELECTED CZM TYPE

Several ways to define the CZM are proposed in ANSYS APDL [Ansy13], the software used to simulate the crack evolution in the next step. The definition of the CZM varies according to the type of the finite element model used. Two types of elements can be used to model the decohesion of intersecting solid interfaces representing the crack evolution: the interface elements and the contact elements. In this study, contact elements are chosen because they allow the meshing of each solid at the interface independently. This aspect is important for the simulation's calculus at the wire-metallization contact. Associated with these elements, the two proposed modes of cohesive traction laws are bilinear and exponential. In this study, the

bilinear mode, as represented in Figure 105, is chosen because its definition is simpler than the exponential mode. The mode of fracture in this study was set to be a mixed-mode since both normal and tangential deformations exist.

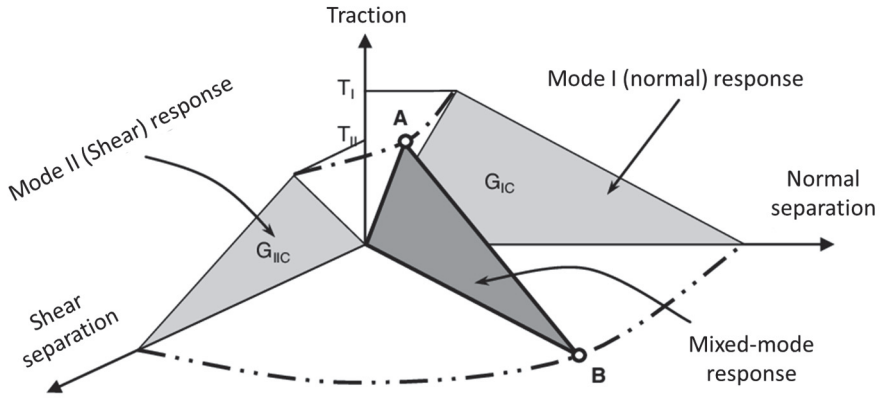

Figure 105: Bilinear cohesive law used in ANSYS APDL for a mixed-mode failure.

The selected CZM is used for bonded materials. This CZM type is based on physicochemical concepts since it was initially established by referring to the universal binding energy theory constructed by Rose and others, as detailed in the previous section [PaPa11], [RoFS81]. As a result, the parameters of the chosen CZM are the critical fracture stress for separation (σ_c) and the critical fracture energy (G_c). This selected bilinear mixed-mode CZM for bonded materials deals with the idea of cycling as proposed by Alfano and Crisfield [AlCr01]. They said that the CZM could reflect cyclic degradations by linearly reducing stiffness using a reduction factor ($1-d_n$), where d_n is the cumulative damage degradation characteristic after n loadings ($0 \leq d_n \leq 1$) [AlCr01]. Under the repeated action of cyclic loads, the cohesive force unit follows the tension-displacement relationship with d_n as the number of cycles increases [RoSi03]. The evolution of d_n can be plotted in the ANSYS APDL program to follow the crack progress.

The graph representing the selected CZM type and the manner of the damage evolution is shown in Figure 106. The CZM concept is summed up as follows. Upon cycling, stress increases. When the stress reaches the critical fracture stress for separation σ_c (see Figure 106), deformations begin to be in the plastic domain, and the crack between two intersecting surfaces initiates. Until reaching this moment, d_n remains null. After reaching σ_c, the stress decreases, and the separation between the interesting surfaces progresses concurrently with the increase in the value of d_n. In the plastic path, if the stress does not decrease to zero from the first cycle, the minimal stress value reached in the first cycle will be the critical stress value for separation in the second cycle. Similarly, if the stress does not decrease to zero in the plastic zone in the second cycle, the minimal value reached in the plastic zone will be the critical stress value for separation in the third cycle. This scenario continues upon cycling until reaching a cycle by which the value of stress in the plastic zone decreases to zero. At this stage, d_n reaches a value of 1, and the crack is complete by reaching the critical separation value δ_c. This means that the critical fracture energy value representing the area of the big triangle that joins the following coordinates: (0,0), (δ_0,σ_c), and (δ_c,0) is reached.

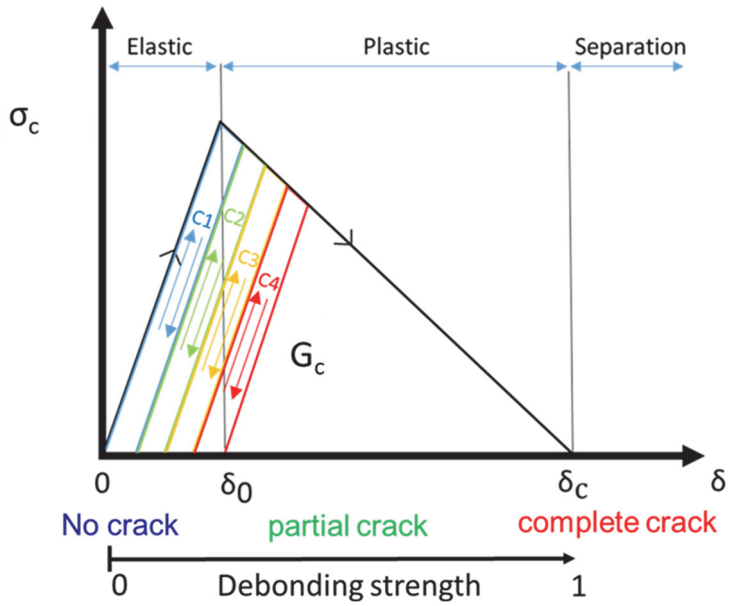

Figure 106: The CZM type used for bonded materials. The number beside the letter C refers to the number of cycles.

To sum up, the CZM is used to model the crack progress since it allows to describe the behavior of the crack in a zone near the front of the crack tip based on the cohesive laws of tractions. In this way, the crack evolution at the topside metallic contact can be simulated when the module is subjected to electrothermal and mechanical loads. In the upcoming section, the work is oriented toward relating the main physicochemical and microstructural properties to the crack propagation process. This original approach combines fracture mechanics and physicochemical-microstructural concepts. Such a combination is achieved by relating the parameters of the CZM, which are the critical fracture stress and fracture energy, with microstructural features and physicochemical properties representing the grains and grain boundaries, such as their sizes and orientations. This combined model aims to predict the crack passage at the interconnection sites in the vicinity of metallization layers and bonded wires according to a physicochemical-microstructural point of view. Based on this model, the evolution of the simulated crack propagation is discussed later within cycling, as will be presented in the next chapter, confirming the model's results experimentally.

3.2 Obtaining the parameters of the selected CZM after relating them to physicochemical-microstructural properties

After selecting the CZM type to be used for simulating the crack evolution at topside metallic contacts in power devices, this section shows the linkage between the model's parameters and critical physicochemical-microstructural factors. As mentioned previously, the selected CZM is applied for the case of debonding surfaces, where its elements should be assigned in accordance with the observations of their local microstructural characteristics. Here comes another reason for preferring this approach over the crystal plasticity approach: the possibility of evaluating the evolution of the thermodynamic parameters of the CZMs with aging. This permits analyzing the effect of aging on the microstructure and its characteristics.

The bilinear mixed-mode CZM parameters to be correlated with physicochemical and microstructural properties are the critical normal stress for separation, the critical tangential stress for separation, the normal critical fracture energy, and the tangential critical fracture energy. After establishing the way of obtaining the CZM parameters, grains at the metallic contact zones are represented by hexagons for modeling the crack evolution there. In this configuration, the edges of hexagons represent the grain boundaries, the most critical sites for cracks' formation and evolution. In order to simulate the crack propagation, CZM elements are defined at the edges of these hexagons, as seen in Figure 107. The CZM parameters should allow predicting the crack formation and propagation.

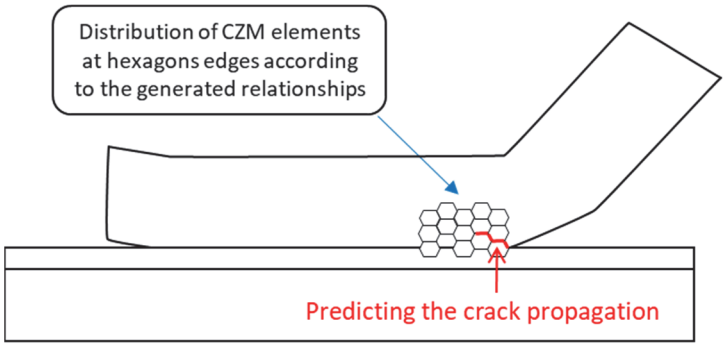

Figure 107: The methodology followed for distributing the CZM elements at the edges of hexagons representing grain boundaries.

The hexagon's geometry was inspired by the honeycomb geometry, which is thought to be the best representative geometry for grains. It is somehow close to their shapes because grains do not have specific regular shapes. Additionally, hexagons offer curvatures at the center of their edges. This looks closer to the morphology of the grains. Moreover, this geometry is flexible to control, by which critical fracture stresses and energies can be easily inserted on its edges. Each hexagon was supposed to have a radius close to the grain size in the actual situation.

In the simulations, the CZM is applied separately on each hexagon edge; therefore, the contact debonding will depend on the stress values at each edge and whether they reach the critical fracture stress value. In this way, the granular decohesion is simulated by using localized CZM parameters after investigating the effects of microstructural parameters on crack formation. Using this model, cracked sites stay in an open state (stay cracked) in further cycling stages. This can also be observed in microstructural images like Figure 45, where cracked sites stay in this state when cycling advances.

Consequently, in order to predict the crack propagation at the metallic interconnection parts, relationships between CZM parameters and critical physicochemical-microstructural features are primarily required. Both CZM's parameters were obtained by combining physicochemical-microstructural equations and experimental data from EBSD and nanoindentation analysis. The two following sections explain the strategy used for calculating the critical energy and stress parameters.

3.2.1 Obtaining the normal and tangential critical fracture energies

First, the work of separation parameter (W_{sep}) is thought to be the best representative parameter of both normal and tangential cohesive energies (critical fracture energies) in the mixed-mode CZM for the case of debonding surfaces between contact grains. At the microscale, grains are the intersecting surfaces, and their intersection regions are the grain boundaries. Several authors used this parameter in the literature when discussing decohesion and fracture processes in the microscale [LHHO09], [MöBi14], [ZLTC19].

The work of separation between adhering surfaces is related to the surface energy (γ_s) of each grain and the grain boundary energy (γ_{gb}) which reflects the excess energy per unit boundary area, or in another definition, the force acting tangentially on the boundary. γ_s and γ_{gb} are schematized in Figure 108.

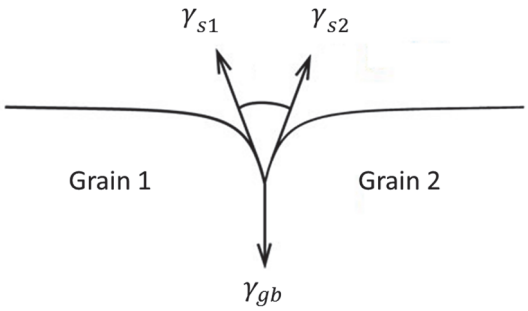

Figure 108: Surface and grain boundary energies representation for neighbor grains.

Both surface and boundary energies are directly related to grain microstructural features. These energy values vary according to the orientation angle of each grain, the disorientation angle between neighbor grains, and the texture of grains. Thus, the surface and grain boundary energies reflect the dependency of the grain's microstructure on the work of separation parameter. The equation representing the work of separation or the cohesion energy between grains is as follows [Gumb99], [MöBi14], [Seah79], [ZLTC19]:

$$W_{sep} = 2\,\gamma_s - \gamma_{gb} \tag{32}$$

If the surface energies of the intersecting grains 1 and 2 are different ($\gamma_{s1} \neq \gamma_{s2}$), then the work of separation equation is as follows.

$$W_{sep} = \gamma_{S1} + \gamma_{S2} - \gamma_{gb} \tag{33}$$

The effect of temperature on critical fracture energy values will be indirectly incorporated by the microstructural changes that take place upon cycling due to temperature changes, modifying orientation planes, orientation angles, and disorientation angles. Such changes affect γ_s and γ_{gb} values; therefore, W_{sep} changes. However, since the maximal temperature reached upon cycling is only about 180 °C (≈ 0.27 of aluminum's $T_{melting}$), this means that aluminum is still in the cold phase. Therefore, the temperature has a minor influence on the energy values upon aging [WCFC19]. The influence of cycling on degradation processes and the changing the material properties is dominant over the effect of temperature itself.

In order to calculate the value of W_{sep}, the values of γ_s and γ_{gb} should be known. For this purpose, some equations were considered. The necessary data for calculating W_{sep} are extracted with the help of EBSD experimental data and the ATEX software. Figure 109 is an EBSD image for a non-degraded IGBT device (SKIM63 module) at the interconnection position between the wire and the metallization layer. This sample was used to extract the necessary data for obtaining γ_s and γ_{gb} values. It was experimentally observed that cracks' formation starts from the interconnection edges of the wires, particularly at the heel position. After a certain number of cycles, cracks initiate at the tip position [Dorn19]. For simplification, and since cracks start from the heel position, the methodology of obtaining γ_s and γ_{gb} values will be applied at the heel position for simulating the formation of the cracks there, in the zone marked in yellow in the figure below. The necessary data for obtaining the critical energy values in such positions will be extracted after portioning this healthy sample at the heel position, using the same partitioning methodology presented in Chapter II in sections #5.3.2.

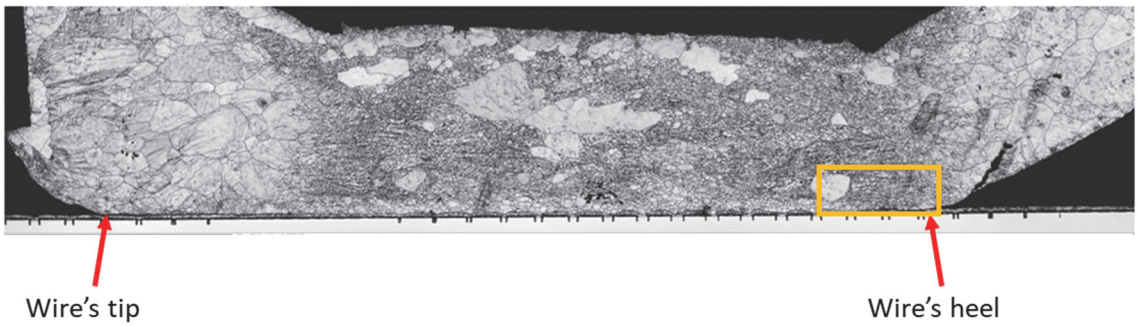

Figure 109: An EBSD image of a non-degraded IGBT sample (SKIM63 module) at the interconnection between the wire and the metallization layer.

Regarding the grain boundary energy (γ_{gb}), this value is more complicated since it is directly related to each grain's orientation angle, specifically the resulting disorientation angle at the intersection of neighbor grains. Upon cycling, the orientation angle of each grain and, therefore, grains' disorientation angles start to change caused by the surface roughening. The driving force for these changes is the dislocation plasticity, not the diffusion processes as previously thought, since the maximum temperature reached in the case of cycling is not so high compared to the melting temperature of aluminum [BWKP18]. Equation (34) represents the direct relationship between the boundary energy (γ_{gb}) and the disorientation angle between neighbor grains ($\Delta\theta$), where k_{HP} is the Hall-Petch constant for aluminum (0.6 J/m^2), and θ_a and θ_b are specific angle values (θ_a = 20° and θ_b = 70° in polycrystalline aluminum [HaGo71], [LHHO09], [ZZYH16]). The disorientation angle ($\Delta\theta$) is schematized in Figure 110.

$$0° < \Delta\theta < \theta_a \; ; \; \gamma_{gb} = \frac{k_{HP}\,\Delta\theta}{\theta_a}$$

$$\theta_a < \Delta\theta < \theta_b \; ; \; \gamma_{gb} = k_{HP} \qquad (34)$$

$$\theta_b < \Delta\theta < 90° \; ; \; \gamma_{gb} = [k_{HP}(90 - \Delta\theta)/90] - \theta_b$$

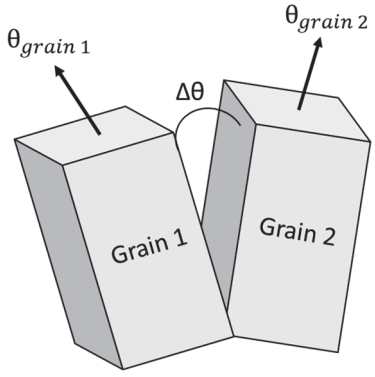

Figure 110: Schematization of orientation angles (θ_{grain1} and θ_{grain2}) of neighbor grains with the resulting disorientation angle ($\Delta\theta$) between them.

Figure 111 shows the orientation of each grain at the selected heel portion. Each of these oriented crystals has its own Euler angles representing the angles of orientations in all directions (phi1, phi, phi2). The diversity in orientation angles results in different disorientation angles between neighbor grains. Figure 112 shows the resulting disorientation angles between neighbor grains. From such data and using the previous equation, the grain boundary energy can be calculated.

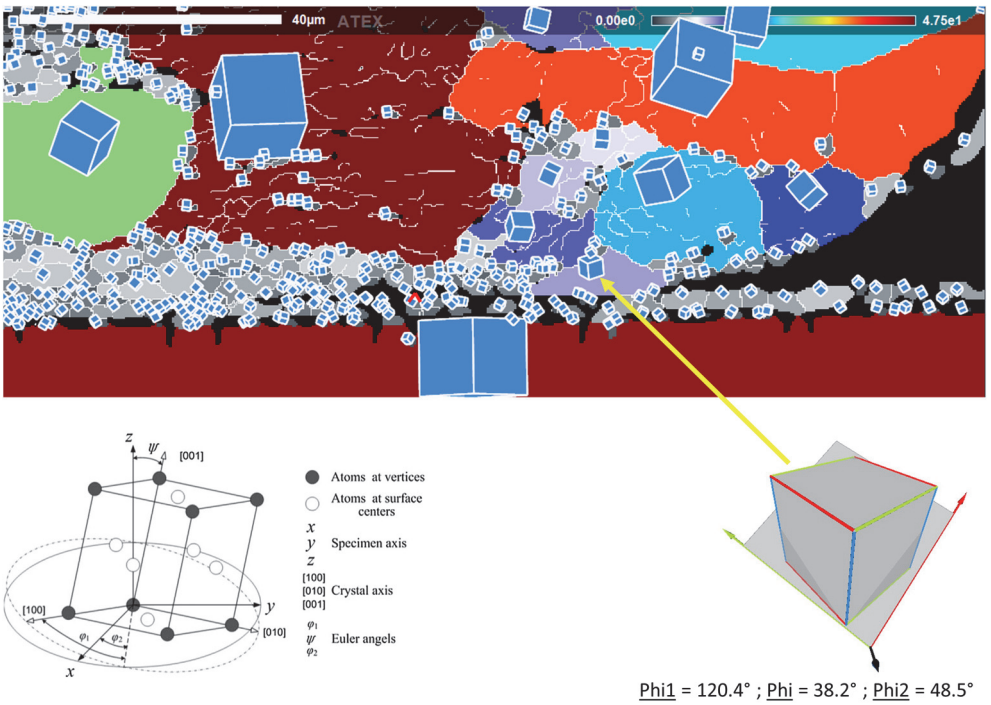

Figure 111: Grains' orientations at the heel position with an example of a grain's Euler angles representing its orientation.

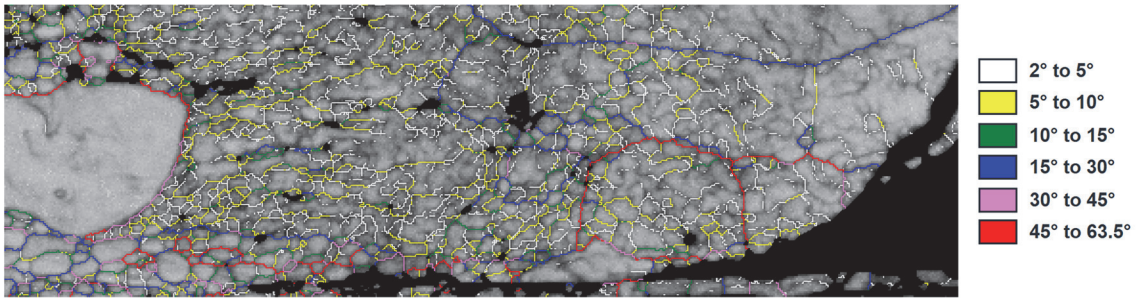

Figure 112: Disorientation angles between grains at the heel position.

From Figure 112, it is deduced that the orientation angle between neighbor grains highly differs from one grain to another. It is also observed that low boundary angles are dominant above the interconnection interface; thus, the boundary energy is mainly low for major boundaries. This is because when the disorientation angle is low, the first case in equation (34) is used to calculate the boundary energy, resulting in low boundary energy values. In this case, and referring to equations (32) and (33), the resulting cohesive energy values are high. On the contrary, when looking at the grains at the wire-metallization interconnection sites, it is observed that the number of boundaries owing higher disorientation angles is greater than those above the contact; thus, the boundary energy values are generally greater at the interconnection sites, referring to equation (34). Therefore, the resulting cohesion energy values are lower, deduced from equations (32) and (33). The values of γ_{gb} obtained using this methodology were compared to the values reported in the literature for the case of aluminum. For example, in the work of Zheng and others [ZLTC19], it was reported that γ_{gb} has a value between 0-0.5 J/m^2. This range is the same as for γ_{gb} calculated using equations (32)-(34).

After knowing how to obtain the grain boundary energy values, it is time to extract the second parameter necessary to calculate the cohesive energy values, which is the surface energy. This parameter is directly related to the texture of the grain, or in other words, to the plane of orientation of each grain. In the case of the upper metallic parts of IGBT modules, the wires and the metallization layers are made up of aluminum atoms with an FCC structure. As mentioned previously, aluminum grains are made of several

aluminum atoms connected to each other. Each grain has its own surface energy caused by its specific atomic distribution; therefore, bonding and cohesive forces and energies differ from one crystal to another.

Upon cycling, the grains or crystals rotate; thus, the crystal orientation changes. This means that the surface energy of each grain will change, affecting the system's total energy. It is seen that upon cycling, grains change their planar orientation in order to achieve the lowest surface energy, as discussed in Chapter II. For the case of aluminum, the surface energy values of (001), (110), and (111) planes are 0.9 J/m^2, 0.972 J/m^2, and 0.62 J/m^2 respectively [ZhMX04]. From these values, it can be deduced that the values of surface energies are greater than grain boundary energies. These reported surface energy values are so near to the values of the surface energy of aluminum in the temperature range between 150-200 °C reported by Levy and others [LeRe70], which is a range near to the cycling conditions carried on in this work for the SKIM63 IGBT modules.

As deduced, the surface energy values are directly related to the planes of the orientation of grains; thus, it is necessary to know the existing planes of orientation in the structure. For this purpose, the Inverse Pole Figure is plotted for grains at the heel position, as seen in Figure 113. This figure shows that grains are favorably oriented in certain directions. Grains at the metallic interconnection zone have a dominance of (101) orientation, whereas the dominant orientation of grains inside the wire bulk is (001).

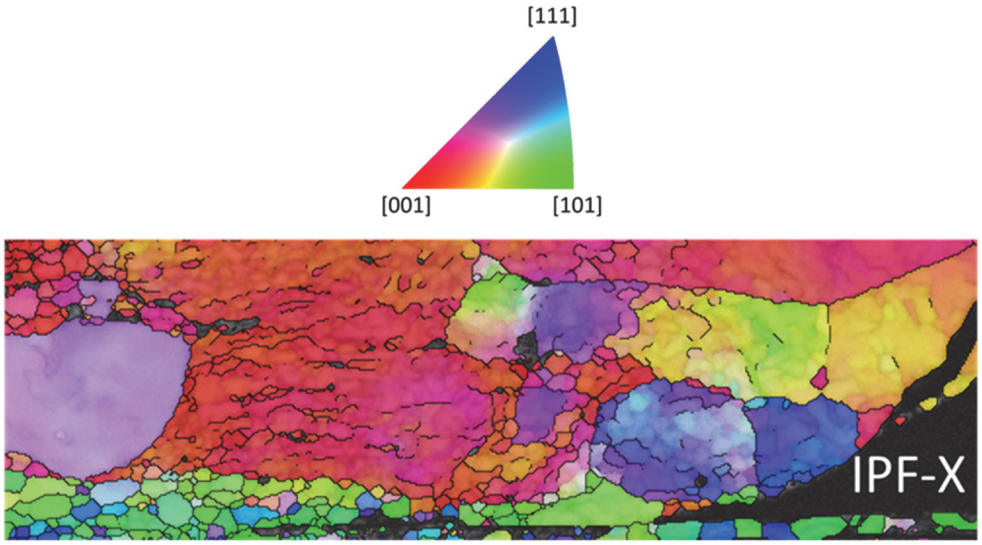

Figure 113: IPF plotted in the x-direction to obtain the grains orientation planes at the heel position.

Finally, after being able to obtain the values of both grain boundary and surface energies, the values of the work of separation parameter representing the cohesive energy can be calculated, referring back to equations (32) and (33). It can be deduced that cohesive energy values generally vary between 0.65 to 1.8 J/m^2. Since the deformation's dominant direction is unknown, as mentioned before, the mixed-mode CZM is used by assuming the same energy values for normal and tangential directions in the simulations. Therefore, the same values of W_{sep} are used in both normal and tangential directions at the grains' hexagonal edges.

3.2.2 Obtaining the normal and tangential critical fracture stresses for fracture

After knowing how to calculate the first cohesive zone parameter, obtaining the critical fracture stress value necessary for the crack formation in normal and tangential directions is the next step. Surely, not all grains have the same strength. Grains in thin metallization films have higher yield strength values than those located inside the wire just above the metallization layer, at the positions of crack formation [HJNS99]. The critical fracture stress value is affected by the grain size since the yield strength of the material is inversely proportional to the size of the grain, as represented by the Hall-Petch equation shown in equation (2) [Arms87], [Hall51], [Kato14]. The size distribution of grains at the portioned heel part can be observed in Figure 114.

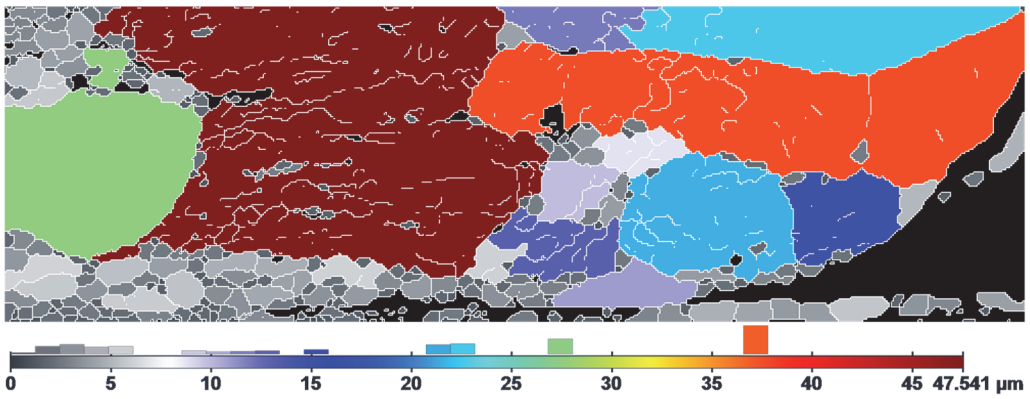

Figure 114: Grains' sizes distributed at the heel position.

In order to calculate the values of the critical contact stress parameter defined in the mixed-mode CZM in the ANSYS APDL software, a linkage was thought about between this mechanical parameter and physicochemical properties since this parameter has a pure mechanical background. The nearest representative parameter to the critical contact stress in the normal direction is the tensile strength. This was also reported in the ANSYS APDL verification manual, where the notion "tensile strength" is written when assuming the value of the critical normal contact stress [Ansy13]. Indeed, tensile strength is a more flexible parameter, where some physicochemical features can be linked to it. Thus, in this work, the tensile strength will be used as a representative parameter of the critical stress in order to relate it to some physicochemical properties.

As for the critical fracture energy, and since the mixed-mode is used with unknown deformations' dominant direction, it is assumed in the upcoming work that both critical tensile and shear stress values for the crack formation are equal. In this way, both directions are offered the same probability to debond. This means that obtaining the tensile strength will be enough because its value will also be applied to the tangential direction. Therefore, in this section, the attempt is to calculate the tensile stress value using physicochemical-microstructural properties.

From reference [PaTy08], hardness values are linked to the values of tensile and yield strength, as shown in equations (35) and (36) below, where σ_{TS} is the tensile strength, H is the hardness value, and n is the strain hardening exponent. These relationships were considered in several publications such as [TKTD15].

$$\sigma_{YS} = \frac{H}{3} * 0.1^n \tag{35}$$

$$\sigma_{TS} = \frac{H}{2.9} * (\frac{n}{0.217})^n \tag{36}$$

Equations (35) and (36) are combined in equation (37) as follows, showing a direct relationship between yield and tensile strength.

$$\sigma_{TS} = \frac{3\sigma_{YS}}{0.1^n} * \frac{1}{2.9} * (\frac{n}{0.217})^n \tag{37}$$

Based on equations (2),(35)-(37), it can be deduced that tensile strength is directly related to the grain size, yield strength, and hardness. Experimentally, it is seen that the grains' size distribution is highly random, so to determine the effect of its random distribution on the mechanical properties of grains, such as their tensile strength, the hardness values are measured. These measurements are applied by performing nanoindentation tests vertically across a non-degraded IGBT sample, as presented in Figure 88. Figure 115 shows the hardness values (in GPa) across a non-degraded wire sample at different indentation heights.

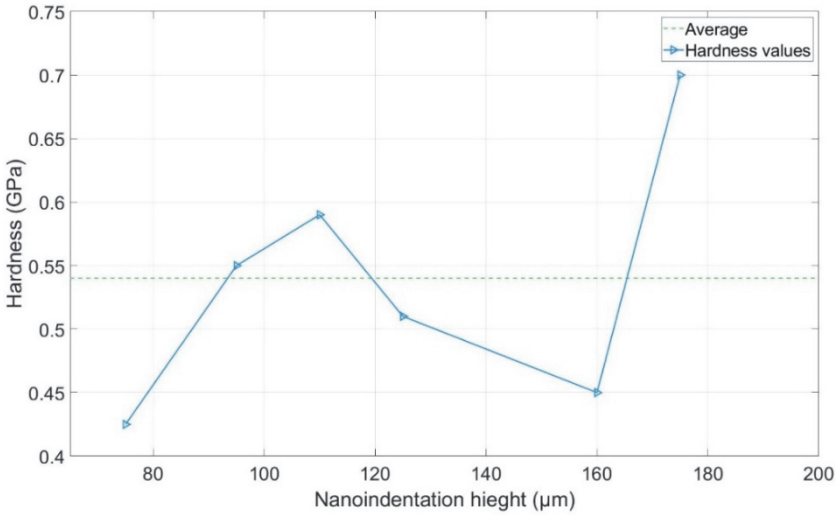

Figure 115: Hardness values measured vertically across a non-degraded wire.

From Figure 115, it can be concluded that hardness values are highly variable depending on each grain's local properties, such as its size and the dislocation density within it. As mentioned in Chapter II, hardness values are much greater when getting closer to the interconnection interface. This is because the grains' sizes near the metallization layer are smaller, caused by the forces exerted upon bonding the wire, in addition to the formation of high dislocation concentration sites inside these grains upon cycling.

Although, even if the hardness measurements were operated through nanoindentation tests, the probable existence of a certain amount of impurities upon welding the wire makes it difficult to precisely know the yield and tensile stress values for aluminum grains theoretically since the strain hardening values for each grain will not be accurately noticed. Moreover, the hardness measurements were not exactly done at the wire edges since the thickness of the wire is very small at such positions after the welding process. In addition, these measurements were not made at the same locations in different wire samples. Thus, the resulting nanoindentation data may not be accurate, especially in terms of the indentation position, because hardness values are highly local. For these reasons, the upcoming methodology was followed to obtain the tensile stress values for grains at the metallic contact, benefiting from the yield stress and hardness values.

The strength values for grains inside the metallization are close since all grains are small with approximately the same sizes. The case is different for the grains inside the wire, where it is impossible to assume relative strength values for grains inside the wire. This is because the grain sizes are highly random inside the wire, by which it is possible to have very big and very small grains in the same sample.

Starting with the yield stress values, it is reported in the literature that for aluminum thin films such as metallization layers, the values are between 100 and 150 MPa [TISM02]. Regarding the tensile stress values representing the critical stresses for debonding in the CZM, and since the strength of the metallization is surely higher than the wire, and because it is also previously known from the literature that cracks will not propagate inside the metallization, approximate values of tensile stress are considered. These values are about 175 MPa for the grains at the metallization layer. This can be deduced when looking at the tensile stress values for different film thicknesses and the ratio of these tensile stress values to their corresponding yield strengths, as reported in the following reference [KCMF09]. This value could also be concluded as an average using equation (37).

For aluminum wires, yield strength values are between 10 and 30 MPa [NaNS00]. To obtain the tensile stress values of grains inside the wire, a relationship was established between hardness and tensile strength, as mentioned by Broll and others [BGHS15]. That article worked on aluminum wires in MOSFETs by doing the same nanoindentation procedure as ours, aiming to obtain the hardness values. Great compatibility was observed when comparing the hardness values reported in that article at the metallic interconnection

sites with the measured values in this work for SKIM63 IGBT samples. These hardness values range between 400-550 MPa. In that paper, the calculated tensile stress values and their corresponding hardness values were reported for different non-degraded wire samples in different regions. The resulting tensile stress values mostly range between 80-110 MPa for the wire positions just above the interconnection with the metallization layer. Since the hardness indentation values reported in that article at the interconnection zones are in the range of the hardness values measured in this work, the tensile stress values reported there in the healthy samples will be considered in the combined CZ - physicochemical and microstructural model as average grains' tensile stress values.

Based on the above, and after knowing how to obtain the CZM parameters, the dependency between the physicochemical-microstructural parameters and the necessary CZM parameters to predict the crack formation and propagation is accomplished. In the next step, those parameters should be assigned in a representative way using the ANSYS APDL program in order to predict the crack passage within the hexagonal edges representing the grain boundaries at the topside metallic contacts. This is explained in the next section.

3.3 THE COMBINED CZ - PHYSICOCHEMICAL AND MICROSTRUCTURAL MODEL TO BE USED FOR SIMULATING THE CRACK EVOLUTION

In order to model very roughly the particle size observed in the microstructure, grains' size variation was considered at the heel partitioned position through the existence of three different grain size zones, where each zone acquires unique grains' sizes. From Figure 116, it is observed that three zones of grains' sizes exist in this healthy SKIM63 sample at the heel position. As noted in the figure below, zone 1 represents grains inside the metallization, zone 2 represents grains in the wire just in contact with the metallization, and zone 3 represents grains above the grains in zone 2, with smaller sizes than those in zone 2.

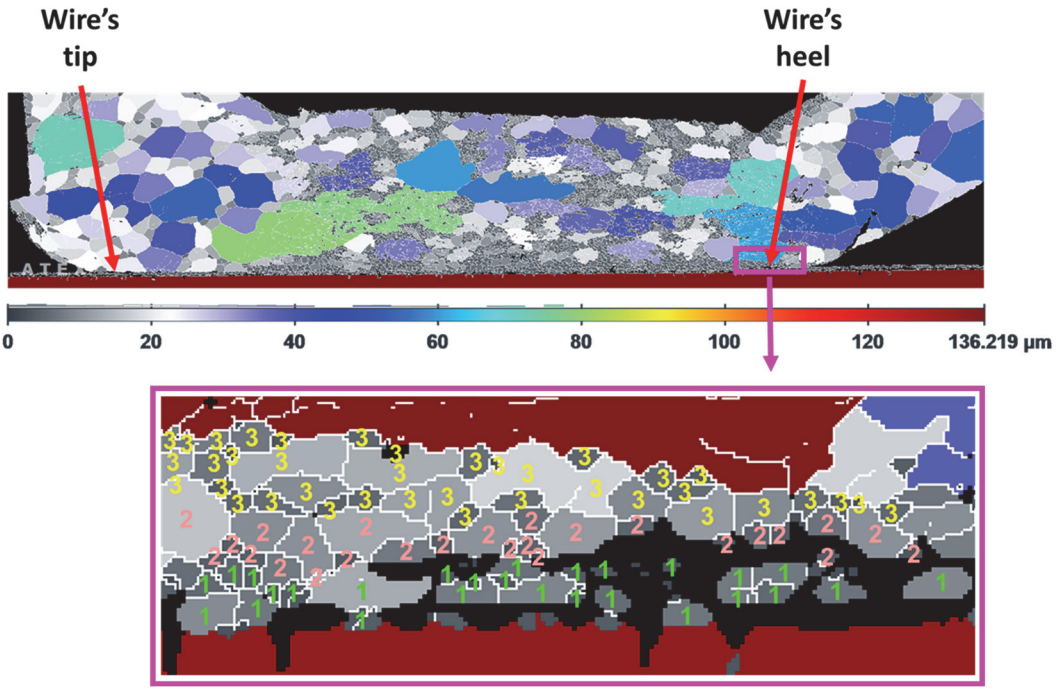

Figure 116: The three grain size zones numbered 1, 2, and 3.

After showing the existence of the three grain size zones, these zones were considered in the simulations when inserting the hexagons that represent grains. Consequently, the three size zones are assumed as follows. The first zone (zone 1) is inside the metallization layer with hexagons' size of about 3 µm, the second zone (zone 2) is inside the wire at the contact interface with the metallization layer owing larger sizes (3.5 µm), and finally, the last zone (zone 3) inside the wire above the second zone with reduced size (2 µm) as schematized in Figure 117. For simplification issues, the hexagons inserted have the same

dimensions (≈ 3.54 µm), close to the grains size in the actual situation. Even if the cell sizes are identical here, different sizes and disorientation angles can be accounted for by using localized CZM parameters in accordance with the characteristics of the local microstructure. This is because, for example, different sizes lead to different strengths in the cells, whereas different disorientation angles lead to different cohesive energies.

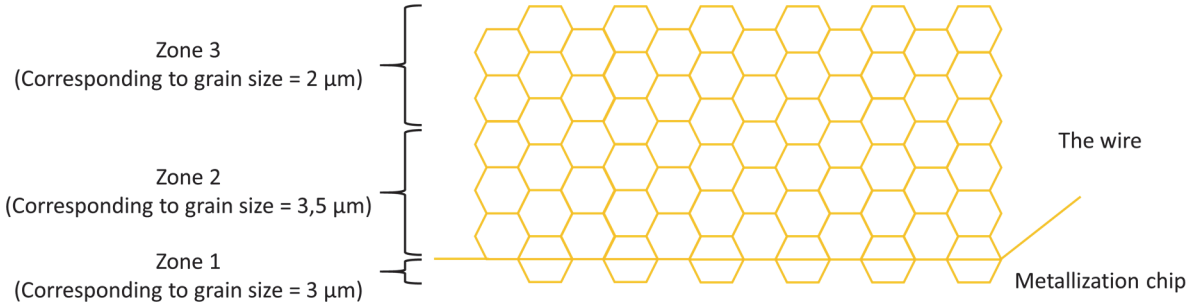

Figure 117: The three size zones observed in Figure 116.

When assigning the CZM elements, it has been assumed that the hexagonal edges in zone 3 acquire higher critical energy values than those at the metallic contact since the disorientation angles are lower in zone 3; thus, the grain boundary energy values are lower as discussed previously when analyzing Figure 112 (≈ 0.15 J/m^2). In addition, since in zone 3 the (001) orientation dominates with some (111) and (101) orientations, the values of surface energy are high (≈ 0.9 J/m^2) [ZhMX04]. Consequently, the average value of W_{sep} there is around 1.8 J/m^2. On the contrary, the disorientation angles at the interconnection zone (zones 1 and 2) are generally high as observed in Figure 112; thus, the grain boundary energy values there are high too (≈ 0.6 J/m^2). Moreover, a mix of orientation planes exists at the interconnection zone (zone 1 and 2) as seen in Figure 113. Therefore, when averaging the surface energy values according to the values listed in the following reference (≈ 0.8 J/m^2) [ZhMX04], the average value of W_{sep} will be around 1 J/m^2. Consequently, for zones 1, 2, and 3, the normal and tangential critical energies are set to be 1 J/m^2, 1 J/m^2, and 1.8 J/m^2 respectively for all the hexagonal edges.

Concerning the critical fracture stress, the metallization layer noted by zone 1 has higher strength than that of the wire, as mentioned in the previous section (σ_{TS} ≈ 175 MPa) [KCMF09]. Metallization layers are thin films with no big variations in grain sizes they have. As a result, the critical fracture stress values for the hexagonal edges inside the metallization layer will have approximately the same term of strength as that for the metallization in the macroscale. In contrast, the wires are thick, having very big grains at the upside positions and very small sizes near the interconnection. Therefore, the situation is totally different when comparing the wire grains with those inside the metallization. One cannot assume relative tensile stress values for different grains inside the wire opposite from that inside the metallization. As mentioned previously, and with the help of the work done by Broll and others [BGHS15], the values of the critical fracture stresses are assigned for the hexagonal edges inside the wire.

In reality, the critical fracture stress values are certainly higher than those generated in the simulations at early cycling. Therefore, these values are reduced when using them in the simulations in order to speed up the debonding and see the crack formation in a few cycles; otherwise, no cracks will be observed in a reasonable computation time (less than 12 hours). Only the values of critical fracture stresses were reduced because they directly impact whether debonding occurs or not since it only occurs when the critical stress is reached. In contrast, the critical fracture energy values only affect the debonding strength; therefore, it is unnecessary to reduce these values when speeding the simulations.

As previously assumed, the hexagonal edges in zone 3 have greater strength than those in zone 2 since they have smaller sizes as observed in Figure 116 and represented in Figure 117. The values of critical fracture stresses are divided by a factor of 2.75 for the hexagons inside the wire. For the metallization layer, the values are divided by a smaller factor of 2.25, because when considering a high factor such as 2.75, deboning inside

the metallization layer will dominate. The reason is that higher stresses are generated inside the metallization layer than in the wire. However, the debonding inside the metallization, not inside the wire, is illogical since the real tensile strengths for the metallization grains are higher than that for the wire grains, and because this propagation manner is not seen in the EBSD plots and the literature [AYAE16], [BGHS15], [Buhr18], [RaTW98]. The chosen reducing factors were selected after applying several simulations using different reducing factors. It was seen that when using higher reducing factor values, the debonding is so fast from the early cycling stages, however, when using lower reducing factor values, the debonding is so slow and it is necessary to apply many cycles to see a crack. As mentioned in the previous section, the tensile strength values range between 80 and 110 MPa for zones 2 and 3. Since zone 3 has bigger hexagons than zone 2, the normal and tangential critical fracture stresses for zones 2 and 3 are set to be 28 MPa (80 MPa/2.75) and 40 MPa (110 MPa/2.75) respectively. For zone 1 inside the metallization, the normal and tangential critical fracture stresses are set to be 80 MPa (175 MPa/2.25).

An additional reason for precisely choosing the 28 MPa and 40 MPa reduced critical fracture stress values for grains inside the wire is mentioned here. As said previously, the size of the hexagons in zone 2 is about 3.5 µm and about 2 µm for the hexagons in zone 3. The strain hardening exponent is reported in the literature in the range of 0.05-0.15 [KaSc10]. For simplification, an average strain hardening value of 0.1 is supposed for these grains. Assuming the 28 MPa tensile stress value for hexagons in zone 2, their corresponding yield strength values can be deduced using equation (37). Then, By subtracting the Hall-Petch equations corresponding to both zones 2 and 3 (using equation (2)), the yield strength value for the hexagons in zone 3 can be deduced by knowing how much the yield strength value for hexagons in zone 3 is greater than that for hexagons in zone 2. It was deduced that the yield strength in zone 3 is higher than in zone 2 by ≈ 10.355 MPa. Therefore, using equation (37), the 40 MPa tensile stress value for zone 3 results.

4 CONCLUSIONS

This chapter showed the different types and modes of the CZM. The basis of CZMs on physicochemical-microstructural properties was then illustrated. Afterward, the appropriate CZM type and mode for building the physicochemical model were chosen from the ANSYS APDL software to simulate the crack propagation in the next chapter. The definition of the selected CZM is based on two parameters: the critical stress σ_c that must be reached at the interface to initiate decohesion, and the energy G_c that allows knowing when the intersecting interfaces will be completely debonded. Both parameters were shown to be linked to physicochemical-microstructural properties. Consequently, direct relationships were presented between critical physicochemical-microstructural properties and the CZM parameters that control the growth of the crack. Finally, the way of introducing such properties to microstructurally model the crack formation at the topside metallic contacts was described.

In the next step, the methodology explained in Chapter III will be applied to predict microstructurally the crack evolution at the wire-metallization contact. Based on the simulations' results, the manner of the crack formation and propagation can be interpreted. The crack evolution manner resulting from the simulations should be compared to that in experimental data.

CHAPTER IV: PREDICTING THE CRACK EVOLUTION AT TOPSIDE METALLIC INTERCONNECTIONS USING THE COMBINED CZM - PHYSIOCHEMICAL AND MICROSTRUCTURAL APPROACH

1 BUILDING UP THE MODEL TO BE USED FOR PREDICTING THE CRACK EVOLUTION IN TOPSIDE METALLIC CONTACTS IN SKIM63 IGBT MODULES

To evaluate the approach presented in Chapter III, an electrothermal-mechanical finite element model, including the CZM parameters calculated using the methodology presented in the previous chapter, has been implemented. This was performed using the ANSYS APDL numerical simulation software. For simplification reasons, only a two-dimensional representation of a single SKIM63 IGBT chip has been modeled.

For constructing this model, a two-dimensional geometry of a SKIM63 IGBT module is primarily created. The dimensions of this module are taken from the following references [Dorn19], [Häus13], [Semi17]. As discussed previously, hexagons are inserted at the interconnection interface between the bonded wire and the metallization layer to represent the grains and possibly predict the crack that passes through them after inserting the CZM elements. Afterward, a material model is established, including each material's electrical, thermal, and mechanical properties in the assembly, in addition to the CZM elements assigned for each hexagon edge. After that, meshing is performed, with small and fine meshing at the zone of interest, the contact between the wire and the metallization layer. Then, the active power cycling is expressed by carrying on an electrothermal simulation in order to obtain the cyclic evolution of the temperature gradients inside the module. The resulting thermal data is used for applying the mechanical simulation necessary to get the stress and strain values at the metallic contact zone responsible for the degradations. The simulated degradations also depend on the CZM parameters, which control the crack passage and growth rate. As discussed before, the CZM is based on thermodynamic considerations, and its parameters are independent of the cycling conditions such as ΔT_j, t_{on}, and t_{off}. This means that only electrothermal-mechanical calculations provide the stress and strain values. The main hypothesis assumed here is that the crack propagation is only allowed at the CZM locations, i.e., at the grain boundaries. This is illustrated by the information reported in the literature [GSGL10], [OnKS00].

The crack evolution seen experimentally in aging tests for SKIM63 IGBT modules under the following conditions {ΔT_j = 110 °C, $T_{j\,min}$ = 55 °C, t_{on} = 3 s, t_{off} = 6 s} must be compared to the simulated crack propagation evolution. Consequently, the same conditions were applied in the simulations as for the experimental tests. Thus, when the simulations are done, and in order to validate them, their results are compared with the microstructural analysis results, particularly those related to the crack evolution manner. In this way, the effect of the microstructural and physicochemical properties on the crack formation and propagation is taken into account in the finite element models through the parameters of the CZM, which were assigned based on their linkage with physicochemical-microstructural properties.

1.1 THE MODEL'S GEOMETRY

First, all the components of the SKIM63 IGBT power module are constructed in two dimensions in the ANSYS APDL program. These components include the wire, the metallization layer, the IGBT chip laying above a silver nano-powder layer, and the DCB substrate. As mentioned in Chapter III (section #3.3), grains observed in Figure 111-Figure 114 at the heel position are represented by hexagons inserted at the upper metallic interconnection interface between the wire and the metallization layer, as schematized in Figure 117. Consequently, the crack formation and propagation can be microstructurally modeled from the debonding of these hexagonal edges. Thus, sixty-one hexagons were put at the heel position. In order to correctly reproduce the heat dissipation occurring when the module is turned off, the SKIM63 IGBT power module is also associated with a cooling system. This bottom side system corresponds to the position where the water circuit runs to cool down the system. The two-dimensional model's geometry is presented in Figure 118. The dimensions of the model's components are summed up in Table 4 [Dorn19], [Häus13].

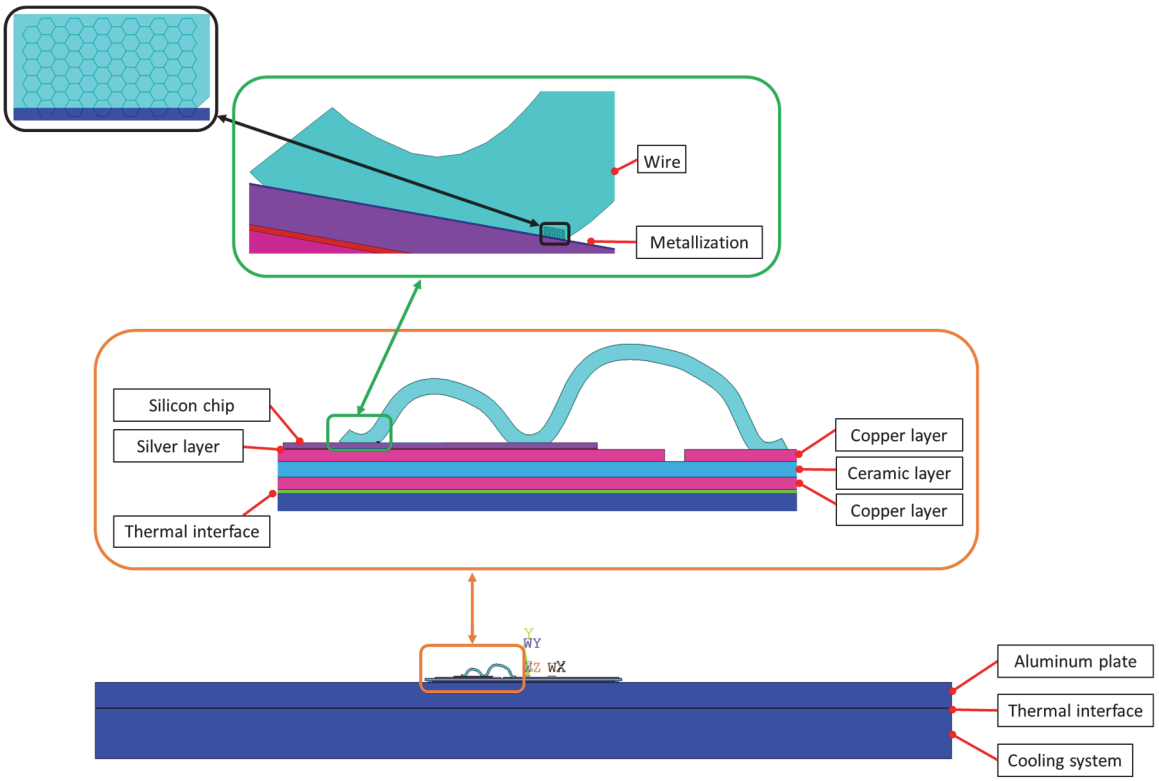

Figure 118: The two-dimensional model's geometry.

Table 4: The dimensions of the model's components [Dorn19], [Häus13].

Material	Length (mm)	Width (µm)
Aluminum wire (Al)	13.9	380
Metallization layer (Al)	6.2	5
Silicon (Si)	7.7	140
Silver (Ag)	7.7	20
Superior Copper (Cu)	36	300
Ceramic (Al_2O_3)	39	380
Inferior Copper (Cu)	36	300
Superior thermal interface (TIM)	38	100
Aluminum plate (Al)	170	5000
Inferior thermal interface (TIM)	170	100
The cooling system (Al)	170	10000

1.2 MATERIAL PROPERTIES OF THE MODEL AND THE CZM PARAMETERS USED

- **Material properties of the model**

The technical documentation of the SKIM63 IGBT modules used when constructing the model's geometry provides the nature of the materials constituting the assembly [Dorn19], [Häus13]. The materials composing the components of the model are listed in Table 5. The bonding wire and metallization layer are made of aluminum, the IGBT chip laying above the silver nano-powder layer is

silicon, the DCB substrate is an assembly of Cu-Al_2O_3 ceramic-Cu layers, and the cooling system components are made of aluminum. Thermal interfaces ensuring good continuity of the heat flow are also incorporated into the module by inserting thermal greases. Subsequently, benefiting from this technical documentation and by using the information listed in the literature, the material properties model for the components of the IGBT device is constructed [Dorn19], [GöFa10], [Häus13], [NaNS00], [ShAl00].

A. Electrical and thermal properties

Starting with the electrical properties, conduction losses are the only considered ones in the active power cycling to obtain the right thermal gradients at the contact level between the wire and metallization film. For simplification, the IGBT chip is modeled by a simple conductive silicon layer characterized by an anisotropic resistivity. This resistivity is defined so that the current flow is only vertical to account for the behavior of the elementary cells constituting the chip. The vertical resistivity is deduced from the IGBT chip's current-voltage (I-V) characteristics [Dorn19].

B. Mechanical properties

Mechanically, the stress-strain behavior at the metallic interconnection level can be decoupled from the behavior of lower layers. The silicon chip under the metallization is considered rigid enough to filter out the deformations coming from lower layers. In other words, based on the significant difference in the behavior between silicon (very rigid) and aluminum composing the metallization and the wire bonding (very ductile), we can assume that the layers under the chip do not influence the stresses and strains inside the metallization and bonding wire located above the chip. Thus, the model can be simplified by only using elastic properties for all materials except the metallization layer and the bonding wire.

Aluminum constituting the wire and metallization chip deforms in an elastoplastic domain in a non-reversible way. These resulting deformations lead to the appearance and accumulation of degradations. Regarding the creep process, it is not considered in this study for two main reasons: i) the creep behaviors of the metallization thin film layer (≤5 µm thick) and bond-wire (around 360 µm diameter) are not well known, and ii) the interaction of creep deformations in the area of interest is very weak. As a result, the electrical, thermal, and mechanical properties of all these materials are summed up in Table 5 below [Dorn19], [GöFa10], [Häus13], [NaNS00], [ShAl00].

Table 5: Material properties used in the model [Dorn19], [GöFa10], [Häus13], [NaNS00], [ShAl00].

Material	Al	Si	Ag	Cu	Al_2O_3	TIM
Specific mass (Kg/m^3)	2700	2330	7350	8960	3780	-
Electrical resistivity (Ω.m)	2.7e-8	R_x >>R_y (1.13e-2)	4e-8	1.7e-8	1e12	1e20
Thermal conductivity (W.m^{-1}.K^{-1})	238	124	250	390	24	2
Thermal capacity (J.Kg^{-1}.K^{-1})	897	750	230	390	830	-
Poisson ratio	0.33	0.3	0.37	0.34	0.2	0.33
Thermal expansion coeff. (ppm/K)	23.5	4.1	19.6	17	8	23.5
Young modulus (GPa)	76	131	6.28	97	370	76

As mentioned in Chapter III, the aluminum material constituting the wire and the metallization is dissimilar in terms of properties in these two components. This is due to the differences in terms of properties between thin films and thick wires caused by the dissimilarity in the grain size distribution and their anisotropic properties and characteristics. In addition, the composition of the metallization layer and the wire are not exactly the same when looking at the percentages of

impurities in both components. About 1% of Si is usually present inside the metallization layer [Dorn19], [Ruff17], whereas the wire is almost 99.99% pure [Dorn19], [NaNS00]. This causes differences in terms of strength between the bonding wire and metallization chips. Based on the previous information, it was assumed that both aluminum materials have the same Young modulus values because they are reported to be the same in the literature. This can be observed when looking at the Young modulus values of thin films reported in the following reference [GSSS11] (about 70 MPa) and Young modulus values corresponding to the wires as seen in reference [Davo17] (also around 70 MPa). However, the major differences between both aluminum materials are yield and tensile strength values. Consequently, the wire's aluminum stress-strain curve is taken from the following reference [NaNS00]. The shape of its curve plot was used for the metallization; however, the only difference is the yield stress value set to be 100 MPa for the metallization, as listed in the following references [Davo17], [GSSS11], [KCMF09], [Ruff17]. The non-linear mechanical properties of wires' and metallization layers' aluminum are presented in the curves below [NaNS00], [ShAl00].

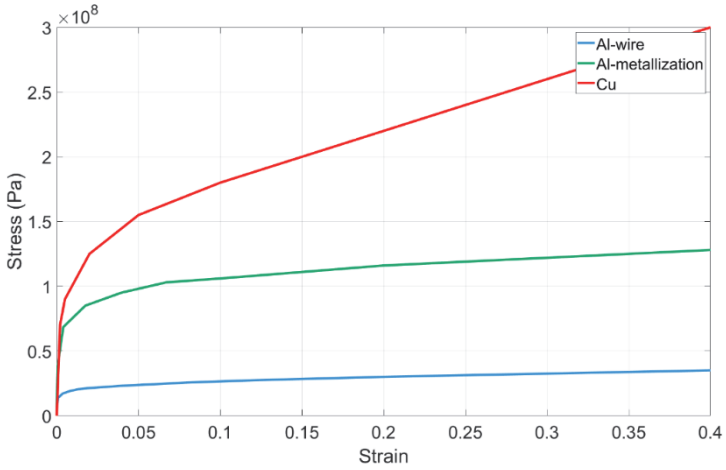

Figure 119: Stress-strain curves for copper, wire's aluminum, and metallization's aluminum.

- **The CZM parameters**

As detailed in Chapter III (section #3.3), the applied CZM is a mixed-mode model. Reduced critical stresses and fracture energies are assumed to have the same magnitudes in the normal and tangential directions. Three hexagonal size zones are considered at the heel contact position, by which zone 1 inside the metallization layer has hexagons with 3 µm size, zone 2 above zone 1 inside the wire just above the metallization with hexagons size around 3.5 µm, and zone 3 above zone 2 with hexagons size of about 2 µm (see Figure 117). The hexagonal edges of each size zone were supposed to have unique CZM parameter values. For zones 1, 2, and 3, the normal and tangential critical fracture stress values are set to be 80 MPa (175/2.25), 28 MPa (80/2.75), and 40 MPa (110/2.75) respectively, and the normal and tangential critical fracture energies are set to be 1 J/m^2, 1 J/m^2, and 1.8 J/m^2 successively (look at the explanation below Figure 117).

2 PROTOCOL AND LOADING CONDITIONS OF THE APPLIED ELECTROTHERMAL AND MECHANICAL SIMULATIONS

After constructing the geometry and the material model of the IGBT device, it is time to define the simulations' boundary conditions. The zone of interest, which comprises the locations of the crack evolution at the topside metallic contacts, is modeled by injecting a constant electric current at the copper track of the DCB substrate in contact with the upper metallic part, followed by applying mechanical constraints at the bottom edges of the DCB substrate. The protocol followed when applying the simulations and the considered boundary conditions are detailed in the following sections.

2.1 THE PROTOCOL FOLLOWED IN THE SIMULATIONS

The applied simulations represent the previously performed accelerated power cycling aging tests. Each cycle consists of a heating phase (by Joule's effect) and a cooling phase (by thermal conduction). Two consecutive simulations were applied using the ANSYS APDL software to represent the power cycling. The first one is electrothermal with a strong coupling to obtain the temperature variations inside the module, reflecting the variations obtained in the aging tests. The resulting thermal stress from this first electrothermal simulation was put as input data in a second mechanical simulation associated with CZM elements of mixed-mode type to estimate the generated stress and strain values and see the formation and propagation of cracks upon cycling. A weak mechanical coupling has been chosen because the mechanical behavior does not significantly affect the thermal results. Therefore, producing a strong coupling that weighs down the calculations is unnecessary. Using weak coupling is forced by the complexity of the model (too many CZMs). These electrothermal and mechanical simulations represent the experimentally performed active power cycling tests done under the same conditions {ΔT_j, t_{on}, t_{off}}. Since the computation time is high, only a few cycles can be reasonably simulated in order to see the first occurring processes and the path of the crack. For simplification reasons, only one bonding wire is considered in the applied simulations instead of the eight existing wires in reality (Figure 40). In addition, the current values put in the simulations are selected to fit the desired ΔT_j values.

However, an important thing that could be thought about when choosing a weak coupling is that cracking may also cause an increase in the temperature, which can accelerate the damage. Therefore, the damage might be underestimated in this case. However, because the simulations only cover the early cycling stages where the crack is very small, then the thermal effect of cracking can be neglected. In addition, since the maximal temperature reached upon cycling is only about 180 °C (≈ 0.27 of aluminum's $T_{melting}$), this means that aluminum is still in the cold phase. Therefore the temperature in the case of aging has a minor influence on the CZM's energy values [WCFC19].

In these 2D simulations, the main focus was to put the appropriate current density values at the IGBT silicon chip that give close ΔT_j and $T_{j\,max}$ values as for the case of real conditions obtained experimentally and if we want to apply 3D simulations. In order to ensure that the 2D simulations with only one chip and one wire can be compared to the case of real 3D geometry with eight wires in each chip, the values of the current densities at the chip must be conserved. In 3D, the current density equals the inserted current (I) divided by the cross-sectional area where the current passes (S^2). However, in 2D, the z dimension is unity (1 m). Therefore the current density at the chip must be the inserted current (I) divided by the length of the chip (7.7 mm).

Three different types of electrothermal-mechanical simulations were performed. The first two simulations, named "Reference simulation" and "Simulation A", were applied by only varying the value of ΔT_j, by which in both simulations t_{on} = 3 s and t_{off} = 6 s. The two ΔT_j variations are ΔT_j = 110 °C for "Reference simulation" {$T_{j\,min}$ ≈ 55 °C, $T_{j\,max}$ ≈ 165 °C} and ΔT_j = 70 °C for "Simulation A" {$T_{j\,min}$ ≈ 55 °C, $T_{j\,max}$ ≈ 125 °C}. Such a variation in the values of ΔT_j was achieved by inserting different current density values at the copper track of the DCB substrate in contact with the upper metallic part. As a reminder, these are 2D simulations; thus, z-dimension is considered in unity, and the current density values are normalized. For ΔT_j = 110 °C, the current density was set to be 7337 Amps/m^2 which corresponds to 56.5 Amps, whereas for ΔT_j = 70 °C, the current density is 5844 Amps/m^2 corresponding to 45 Amps. The third simulation type (named "Simulation B") has exactly the same conditions as "Reference simulation"; however, t_{on} and t_{off} values are changed {$T_{j\,min}$ ≈ 55 °C, $T_{j\,max}$ ≈ 165 °C}. In this third simulation, t_{on} = 6 s and t_{off} = 12 s. In order to have the same temperature fluctuation as in "Reference simulation", the current density value in "Simulation B" was set to be 6935 Amps/m^2, corresponding to 53.4 Amps. Both ΔT_j values (110 °C and 70 °C) were specifically chosen because experimental data for modules degraded at these conditions are already acquired as for the analyzed samples in Chapter II, and simulations in 3D under these conditions are previously made [Dorn19]. Table 6 summarizes the main differences between these three simulations.

Table 6: The conditions of "Reference simulation", "Simulation A", and "Simulation B".

	"Reference simulation"	"Simulation A"	"Simulation B"
Current density	7337 Amps/m^2	5844 Amps/m^2	6935 Amps/m^2
ΔT_j	110 °C	70 °C	110 °C
t_{on}	3 s	3 s	6 s
t_{off}	6 s	6 s	12 s

The inserted current density values were then verified to be in the good range after looking at Figure 120. This can be deduced by comparing the voltage values resulting from the applied simulations and those reported experimentally under the same conditions. For example, regarding "Simulation A" with ΔT_j = 70 °C, the resulting voltage in the simulations when the current is turned on (current density ≈ 5844 Amps/m^2 corresponding to 45 Amps) is about 1.59 v. From experiments, the required current value to do a cycle with ΔT_j = 70 °C should be about 225 Amps [Dorn19]. When extrapolating the I-V curve corresponding to ΔT_j = 70 °C in Figure 120 at I = 225 Amps, the voltage value is around 1.6 v, which is so close to the value obtained in the simulations.

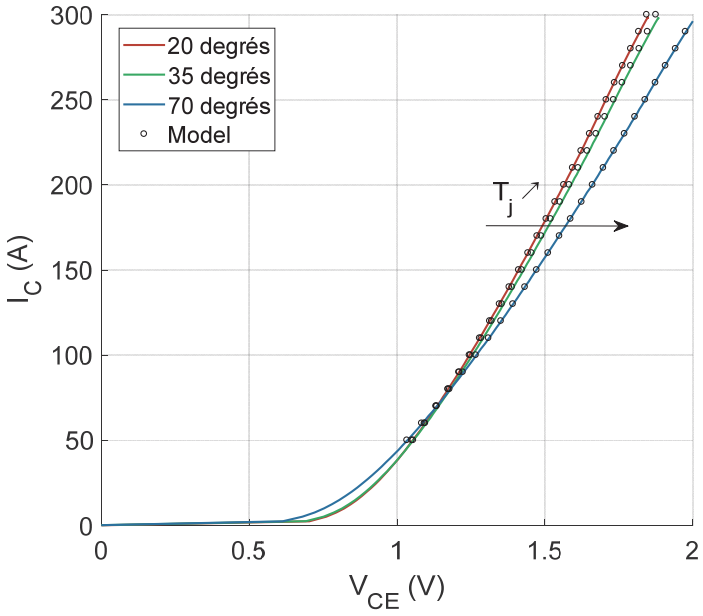

Figure 120: I-V characteristic curve for SKIM63 IGBT modules [Dorn19].

Moreover, under the same cycling conditions {ΔT_j, $T_{j\ min}$, and $T_{j\ max}$}, the current values that were inserted for the case of 3D simulations by the previous Ph.D. student [Dorn19], which are summed up in 7, were compared to those in the 2D simulations applied in this Ph.D. work. For example, in the 3D simulations with ΔT_j = 110 °C, the current value is about 272 Amps. This value corresponds to four chips in parallel. Therefore, the current value for one chip is 272/4 = 68 Amps. This chip is composed of eight wires. On the other hand, in the 2D simulations with ΔT_j = 110 °C, the current value is 56.5 Amps. This current value is distributed only on one wire. So the value of 68 Amps in 3D is compared to 56.5 Amps in 2D. For each wire, the value inserted in 2D (only one wire) is approximately eight times the inserted value in 3D (with eight wires). In this way, the 2D simulations are representatives of those in 3D.

Table 7: Current values used in the 3D simulations to achieve ΔT_j = 110, 90, and 70 °C [Dorn19].

ΔT_j (°C)	110	90	70
I (Amps)	272	256	225

For each of the three simulation types (“Reference simulation”, “Simulation A”, and “Simulation B”), an electrothermal simulation followed by a mechanical simulation were applied. All the equations required for doing the calculations in these simulations can be found in the ANSYS APDL theory reference [Ansy13]. The boundary conditions of these simulations are detailed in the next two sections. The primary data to extract from these simulations are i) the temperature distribution among the different constituents of the power device, ii) the induced deformations over electrothermal-mechanical cycling, and iii) the debonding maps which reflect the crack evolution.

2.2 BOUNDARY CONDITIONS OF THE ELECTROTHERMAL SIMULATIONS

The transient electrothermal simulation is a coupled field simulation with two degrees of freedom, the current and the temperature. Initially, all the model components are considered isothermal with a uniform temperature of 45 °C. Then, two ΔT_j variations were applied as mentioned previously (ΔT_j = 110 °C for “Reference simulation” and “Simulation B”, and ΔT_j = 70 °C for “Simulation A”) by inserting different current densities into the copper track of the DCB in contact with the upper metallic part. A reference voltage of 0 V is applied on the copper track in contact with the emitter to ensure that the current is completely flowing toward the wire. The bottom part of the module was associated with a convection coefficient (h) of 1500 W/m².K and a cooling reference temperature of 45 °C in order to simulate the forced water circulation used in the active power cycling when cooling the IGBT at the t_{off} phase. In general, the convection coefficient depends on the nature of the fluid used, its temperature, the type of flow applied, and the solid/fluid surface. For forced water convection, this value varies between 100 and 15000 W/m².K [Dorn19]. In the model established here, the cooling temperature and the convection coefficient were initially calibrated so that over cycling, $T_{j\,min}$ and ΔT_j are set to be close to the conditions of the experimental aging tests. Figure 121 sums up the boundary conditions used in the electrothermal simulations.

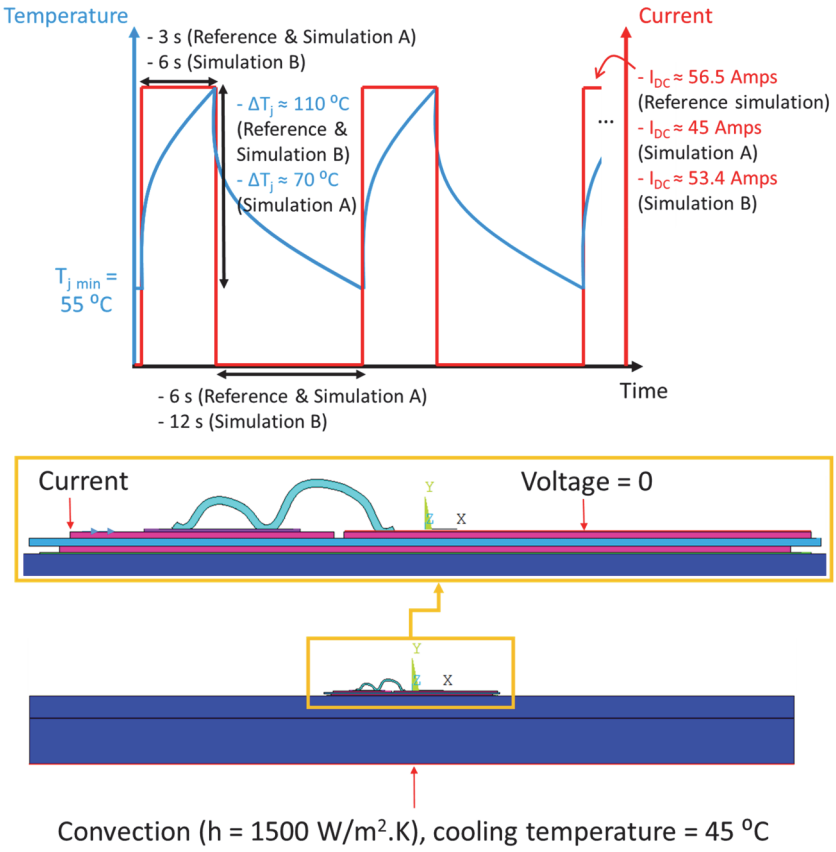

Figure 121: The boundary conditions of the electrothermal simulations.

A total number of 201762 elements and 408836 were implemented in this electrothermal simulation. The mesh sizes in the model’s components are summed up in Table 8.

Table 8: Mesh sizes within the model's components.

Component	Mesh size (µm)
Wire & metallization (away from the interconnection)	2
Silicon layer	50
Silver layer	10
Inferior and superior copper layers	100
Ceramic layer	100
Inferior and superior thermal interfaces	200
Aluminum plate	500
The cooling system	1000

As mentioned previously, the goal of doing this first electrothermal simulation is to obtain the evolution of the temperature fields within the components of the SKIM63 IGBT. In the second step, the obtained thermal results are injected as input data for performing the mechanical simulation.

2.3 BOUNDARY CONDITIONS OF THE MECHANICAL SIMULATIONS

While the whole model was taken into account in the electrothermal simulation, only the upper part of the system is considered in the mechanical simulation. To simplify the simulation's calculus, the model taken into account here is reduced to a single IGBT chip with the DCB substrate because deformations dominate there. This simulation should provide representative results of what happens in the top contact components in the IGBT chip.

As loading conditions, the thermal results obtained from the electrothermal simulation are used as input data. As boundary conditions, the lower vertices of the DCB substrate are constrained by assigning zero displacement values to them. One vertex is constrained in both horizontal and vertical directions, whereas the second one is only constrained in the vertical direction. Such constraints ensure that the DCB substrate can deform in all directions without being able to take off or rotate. These conditions can be better seen in Figure 122.

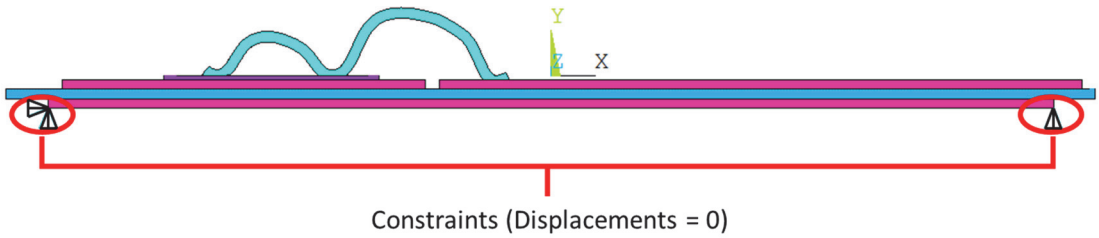

Figure 122: The mechanical constraints applied on the lower edges of the DCB substrate.

In this simulation, all the edges of the inserted hexagons at the wire-metallization contact were assigned as contact elements associated with mixed-mode bilinear CZM parameters, with reduced critical stress values as mentioned previously, to predict the crack progress in an accelerated way. The CZM is applied separately on each hexagon edge; therefore, debonding of contacts will depend on the local stress values at each edge because i) edges have different CZM parameters among the three size zones, and ii) the CZM parameters control the debonding process according to the localized generated stress values caused by cycling. A convergence aid corresponding to an artificial damping value is defined in this mixed-mode CZM (set to be 10 µs). The number of the CZMs applied is 239, reflecting the number of hexagonal edges.

Fine meshing was applied along the wire-metallization contact interface with a length of 0.942 m, especially at the zone where the CZMs will be applied. The meshing size was assumed to be 1 µm. This resulted in a total of 171014 elements and 346491 nodes within this mechanical simulation. This indeed increased the computation time, and sometimes convergence difficulties resulted. Figure 123 shows the fine meshing applied at the interconnection between the wire and the metallization layer, with a zoom-in at the zone where hexagons exist.

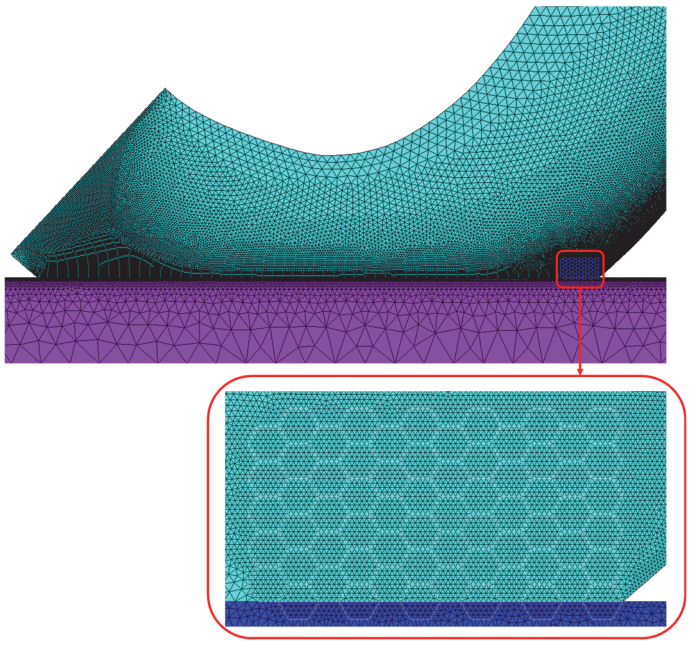

Figure 123: The fine meshing applied to the wire-metallization contact, with a zoomed-in image at the zone of hexagons.

The induced deformations over cycling and the debonding maps which reflect the crack evolution are obtained from this mechanical simulation.

3 MAIN RESULTS OF "REFERENCE SIMULATION"

Following the protocol of applying the electrothermal and mechanical simulations, "Reference simulation" was first applied. From this simulation, the temperature maps at the surface of the IGBT chip were extracted, as well as the resulting stress distribution. Then, the debonding maps for the edges of the hexagons reflecting the crack propagation process are plotted. These results are detailed below.

3.1 MAIN ELECTROTHERMAL RESULTS

The most important outcome of this electrothermal simulation concerns the thermal data. The resulting junction temperature swings averaged on the surface of the IGBT chip are presented in Figure 124 after applying eight power cycles.

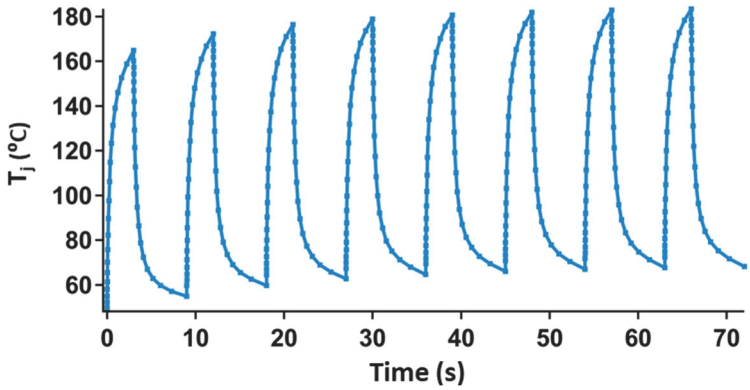

Figure 124: The resulting junction temperature swing averaged on the surface of the IGBT chip after applying eight power cycles.

Regarding the temperature maps' distribution among the model components, it is deduced that the thermal mapping pattern is almost identical within cycling after the end of each heating and cooling phase. Consequently, as an example, the temperature distributions at the end of the heating and the cooling phases in the first power cycle are plotted in Figure 125.

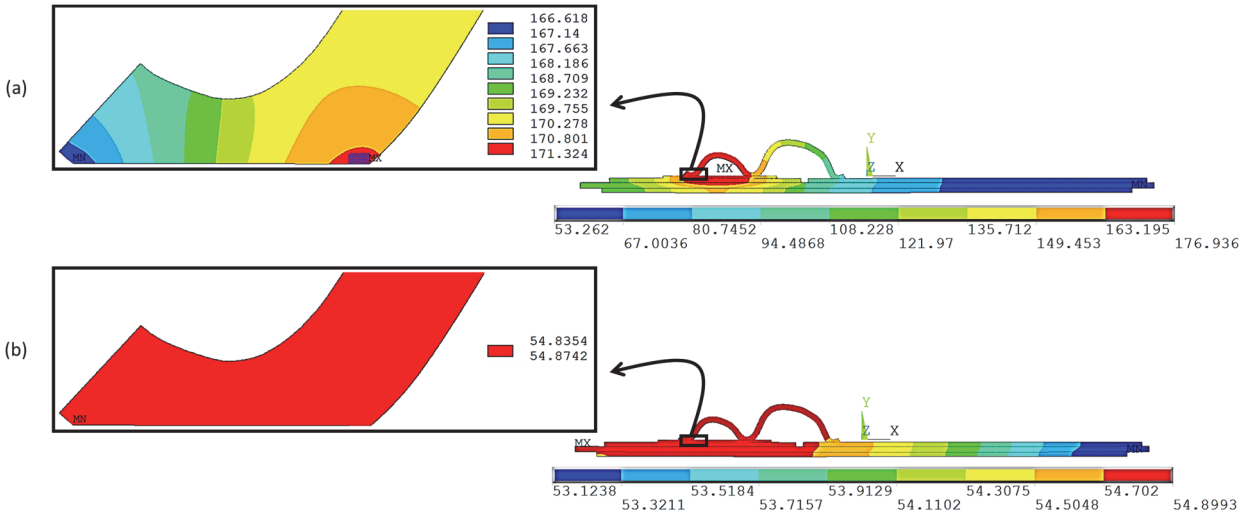

Figure 125: The temperature distribution after the end of the (a) heating and (b) cooling phases in the first power cycle.

Figure 125 shows that the interconnection between the bonded wire and the metallization layer is the position of the highest temperature values. It is also deduced from this figure that the temperature tends to return to its initial state at the end of the cooling phase, by which the variation between the maximal and minimal temperature values at that stage becomes almost null.

3.2 MAIN MECHANICAL RESULTS

The figures below show the distribution of the von mises stress and plastic strain (in MPa) at the end of the heating and cooling phases in the first and the last cycles.

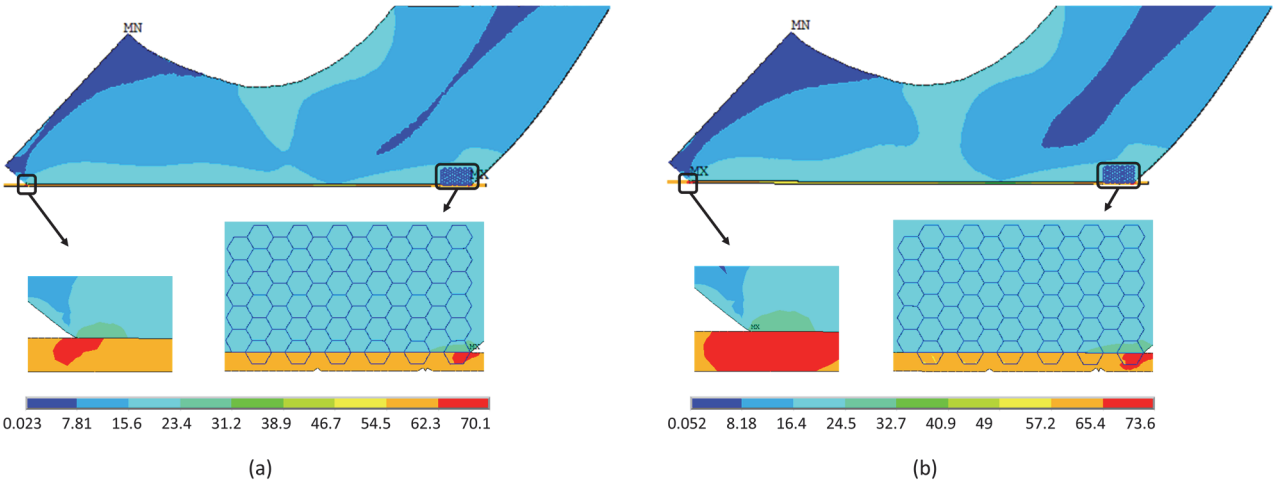

Figure 126: The von mises stress distribution (in MPa) at the wire-metallization contact at the end of the (a) heating phase and the (b) cooling phase in the first power cycle.

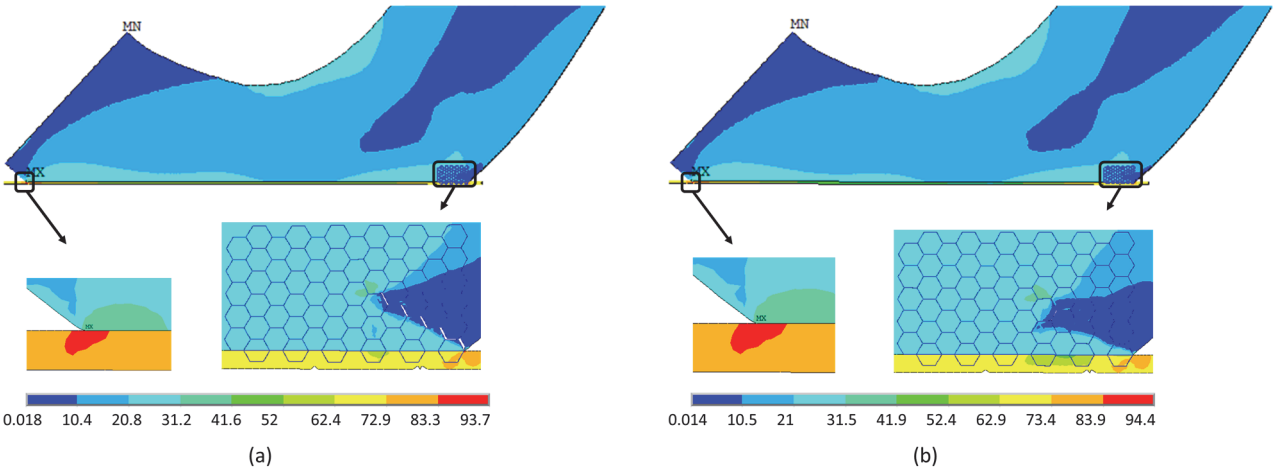

Figure 127: The von mises stress distribution (in MPa) at the wire-metallization contact at the end of the (a) heating phase and the (b) cooling phase in the eighth power cycle.

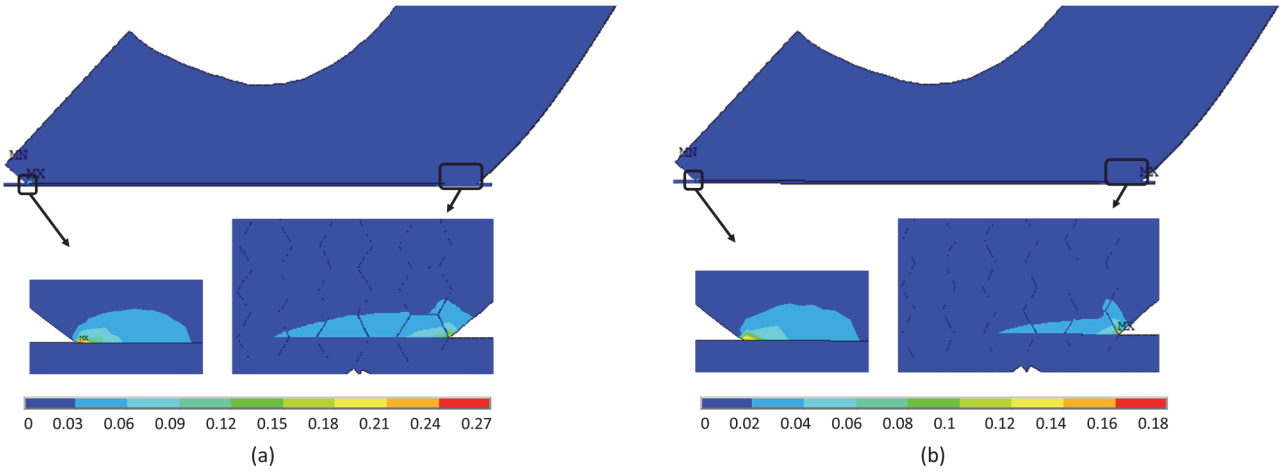

Figure 128: The von mises plastic strain distribution (in MPa) at the wire-metallization contact at the end of the (a) heating phase and the (b) cooling phase in the first power cycle.

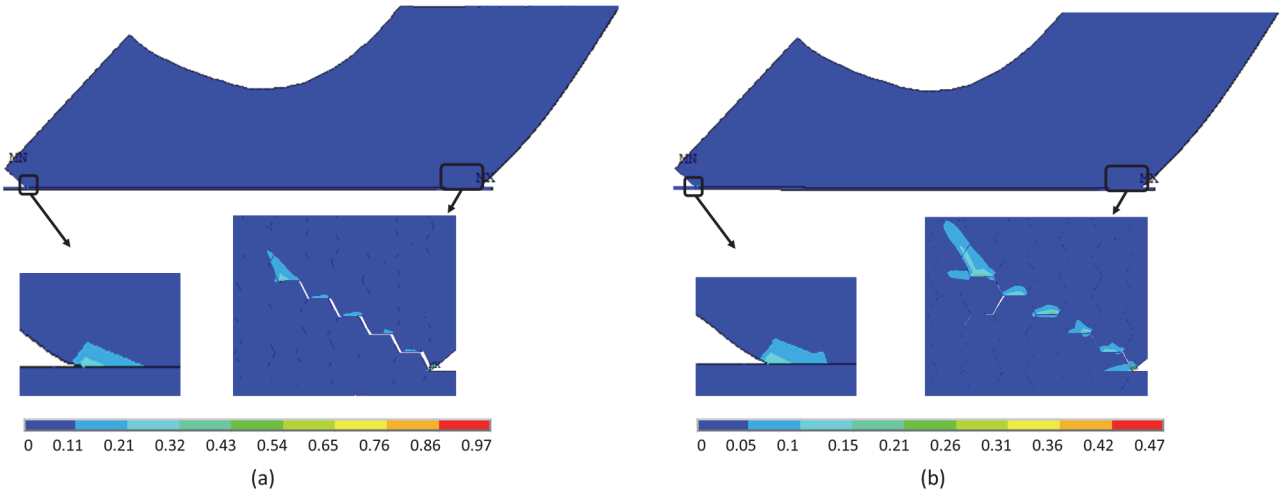

Figure 129: The von mises plastic strain distribution (in MPa) at the wire-metallization contact at the end of the (a) heating phase and the (b) cooling phase in the eighth power cycle.

According to von mises stress distribution seen in Figure 146 and Figure 147, it can be deduced that the maximum von-Mises stress concentrates at the terminal wire edges due to i) the CTE mismatch between silicon that composes the chip and aluminum which composes the metallization and bonding wire, in addition to ii) the high Joule's heating. Regarding the von mises plastic strain distribution presented in Figure 128 and Figure 129, this parameter also concentrates at the terminal wire edges due to the same causes mentioned for the von mises stress. Under continuous temperature fluctuations, its accumulation causes the fatigue failure at the metallic contact zone [TsWu13].

Upon cycling, the values of normal stress (σ_y), shear stress (σ_{xy}), and tangential stress (σ_x) were continuously monitored at the heel position where CZMs are implemented. The importance of analyzing these values is that when one of them reaches the critical fracture stress value put in the CZMs, debonding (cracking) begins. Therefore, these values are essential to analyze when predicting the evolution of the crack. These stress values (in MPa) are plotted in Figure 130, Figure 131, and Figure 132, respectively, at the heel position at the end of the power-off state in the eighth cycle for the three size zones previously presented in Figure 117. The model's x and y directions can be seen in Figure 121 and Figure 122.

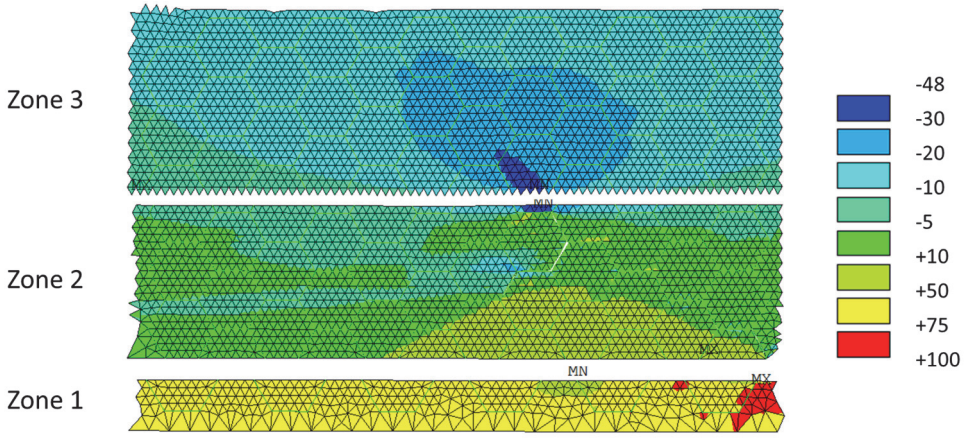

Figure 130: σ_x (in MPa) distribution at the heel position in zones 1, 2, and 3 at the end of the cooling phase in the eighth cycle.

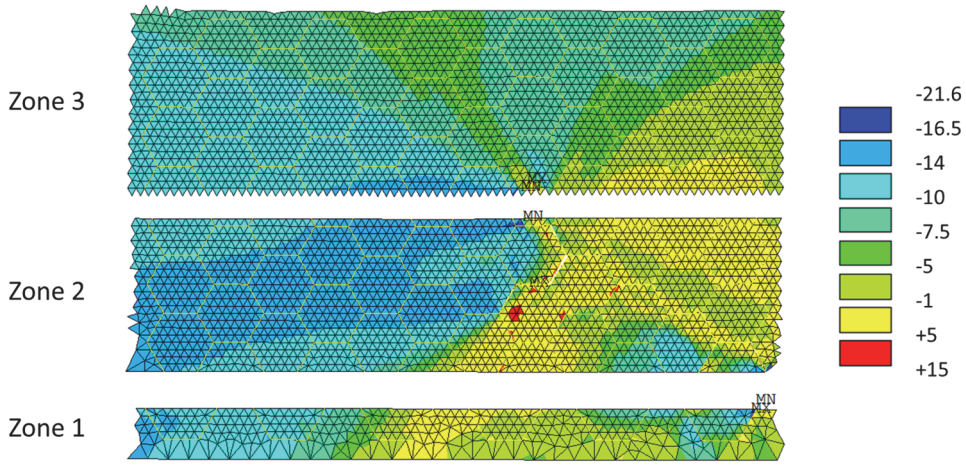

Figure 131: σ_{xy} (in MPa) distribution at the heel position in zones 1, 2, and 3 at the end of the cooling phase in the eighth cycle.

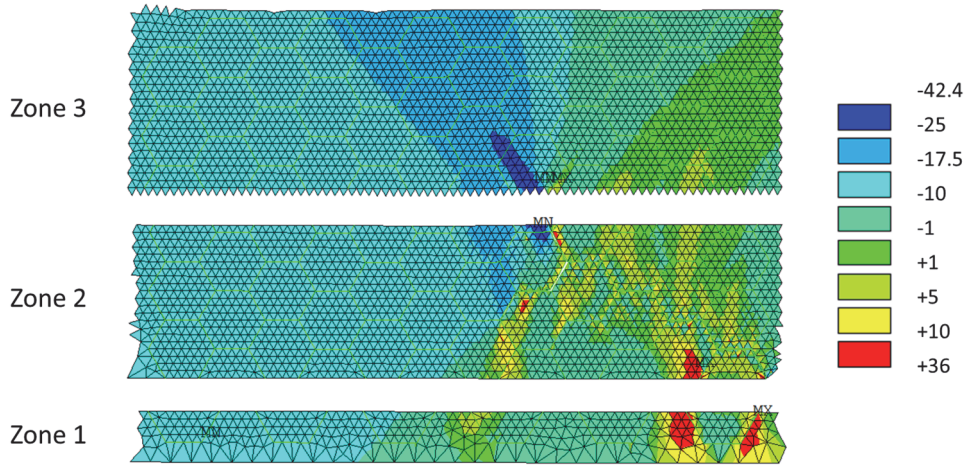

Figure 132: σ_y (in MPa) distribution at the heel position in zones 1, 2, and 3 at the end of the cooling phase in the eighth cycle.

As explained previously, the parameter that allows following the decohesion between intersecting surfaces in ANSYS APDL is called the damage or debonding parameter (d_n). The critical fracture stress value in the CZMs controls the beginning of debonding; thus, the edges of hexagons having critical fracture stress values close to the values of the resulting σ_y, σ_{xy}, or σ_x are expected to start debonding. Based on the stress distribution presented in Figure 130-Figure 132, debonding is expected to occur mainly in zone 2, since the stress values there are higher than those in zone 3, and because the critical fracture stress values in some positions in zone 2 are in the range of the generated stress values, especially in the x-direction. Debonding is unexpected in zone 1 because hexagons in this zone have much higher strength than those in zones 2 and 3, as illustrated previously.

In order to verify these predictions, the debonding maps which show the crack evolution should be plotted. These maps are also of high importance because using them makes it possible to estimate at any element of the interface and any cycling period the percentage of decohesion and thus deduce the crack length evolution within cycling. Surely, it must be remarkable that the debonding maps show the accelerated patterns of crack since reduced critical stress values are used as mentioned previously. It remains so important to find the relation between the stress reduction ratio and the real crack speed. Figure 133 shows the debonding map for hexagons at the heel position after applying eight power cycles.

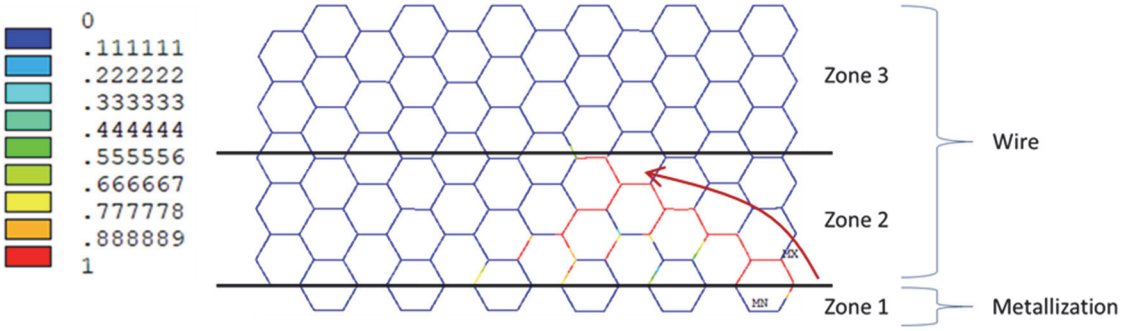

Figure 133: The debonding map at the heel position after eight power cycles.

As expected, debonding mainly occurs inside zone 2, dominantly in the horizontal direction. This justifies the stress distribution in Figure 130-Figure 132, especially in Figure 130, in which σ_x in zone 2 has higher values than those in zone 3, and because the critical fracture stress values are in the σ_x range at some positions in zone 2. The crack starts at the terminal hexagonal edges, just at the metallic interconnection. This evidences that the stress concentrates at these locations, which looks logical when looking at Figure 130-Figure 132. Such locations are also locations for temperature concentration as observed in Figure 125.

In order to support the observation seen in Figure 45 about the faster crack formation at the heel position than at the tip, the same simulations were applied with all the previously mentioned conditions; however, by inserting the sixty-one hexagons at the tip position instead of the heel. The debonding map for the hexagons at the tip position was then plotted after applying eight power cycles as presented in Figure 134.

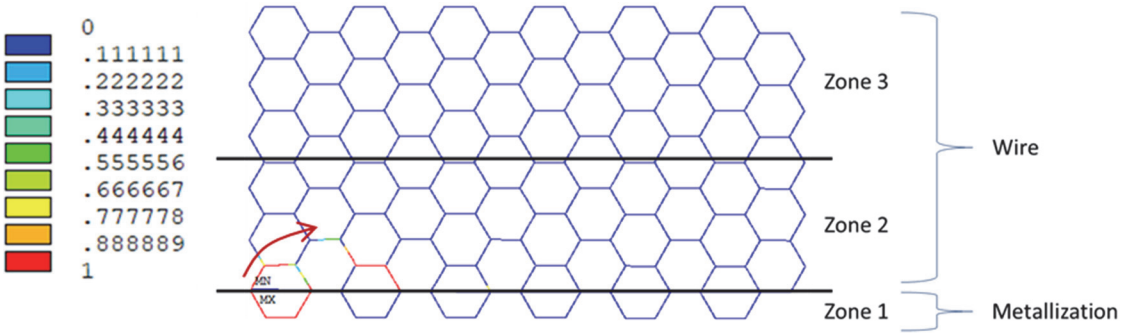

Figure 134: The debonding map at the tip position after eight power cycles.

From this image, it is deduced that the cracking speed is clearly slower than that at the heel position after the same number of cycles under the same conditions. Regarding the similarities between Figure 133 and Figure 134, it can be concluded that in both simulations debonding initiates at the terminal hexagonal edges at the metallic contact and then progresses inside zone 2.

After showing the results observed in "Reference simulation", the same simulation done at the heel position was then repeated, with only varying the ΔT_j values (in "Simulation A") and the power-on duration (in "Simulation B"). The debonding maps were then plotted and compared with those observed in "Reference simulation" in order to configure the effect of ΔT_j and t_{on} on the debonding progress.

4 DEBONDING RESULTS IN "SIMULATION A" AND "SIMULATION B" / EFFECTS OF ΔT_J AND T_{ON} ON DEBONDING

Upon only changing the value of ΔT_j from 110 °C ("Reference simulation") to 70 °C ("Simulation A"), it was deduced that the debonding manner stays the same; however, its speed slows down. This is evidenced by comparing the debonding results at the heel position in "Reference simulation" at the end of the cooling

phase in the fourth cycle with the debonding results at the heel position in “Simulation A” at the end of the cooling phases in the fourth and tenth cycles, as plotted in Figure 135.

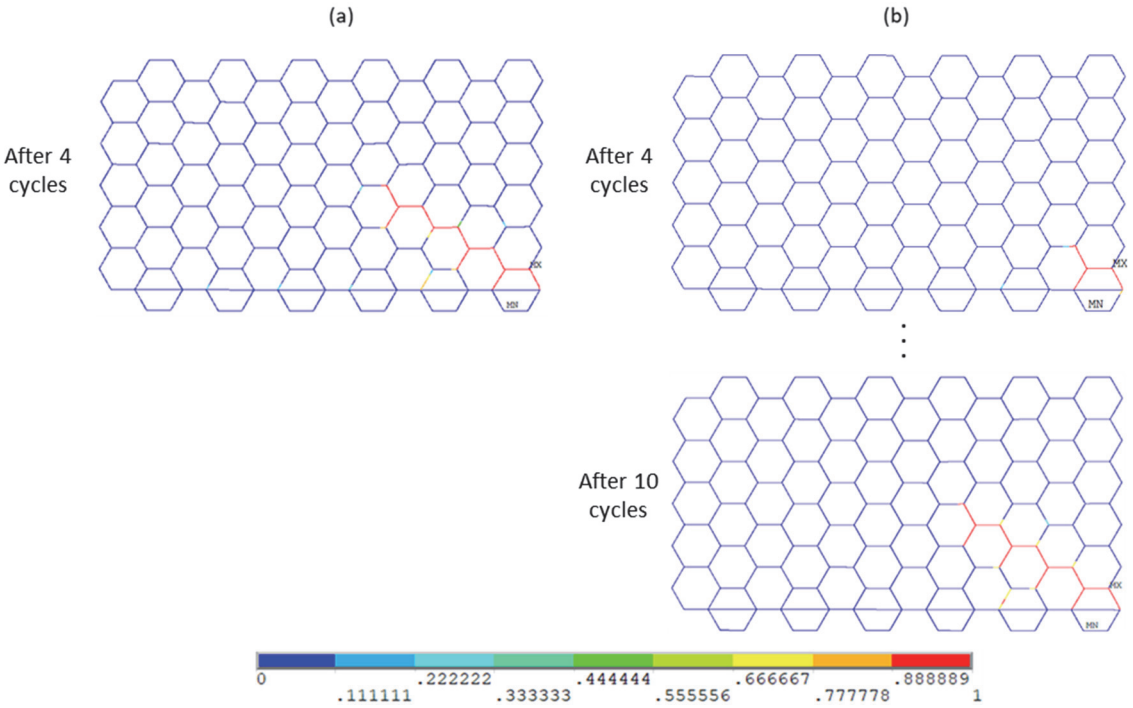

Figure 135: The debonding maps at the heel position in (a) “Reference simulation” (ΔT_j = 110 °C) at the end of the fourth cycle and (b) “Simulation A” (ΔT_j = 70 °C) at the end of the fourth and tenth cycles.

This cracking manner obtained in both simulations is consistent with that reported in the literature even at lower ΔT_j values. Agyakwa and others [AYAE16] deduced that at ΔT_j = 30 °C, the same cracking manner as in our situation occurred (initiating from the wire terminals and propagating inside the wire just above the metallization layer) for an aluminum wire having very close characteristics as in our case (in terms of thickness and purity). Thereafter, it can be deduced that the same cracking manner will result upon changing the junction temperature; however, the only change will be the speed of the cracking.

After showing the effect of changing the junction temperature on the cracking manner, another simulation (“Simulation B”) was applied under the same ΔT_j as in “Reference simulation”, in order to observe the t_{on} effect.

Upon increasing the t_{on} duration from 3 s to 6 s and conserving the same ΔT_j value as in “Reference simulation” (ΔT_j = 110 °C), it was seen that debonding is stronger when having a higher t_{on} duration. Because this simulation takes much more time than “Reference simulation”, only three cycles were made. Afterward, the debonding map resulting in the heel position at the end of the cooling phase in the third cycle is compared with that in “Reference simulation” at the same cycling stage, as shown in Figure 136.

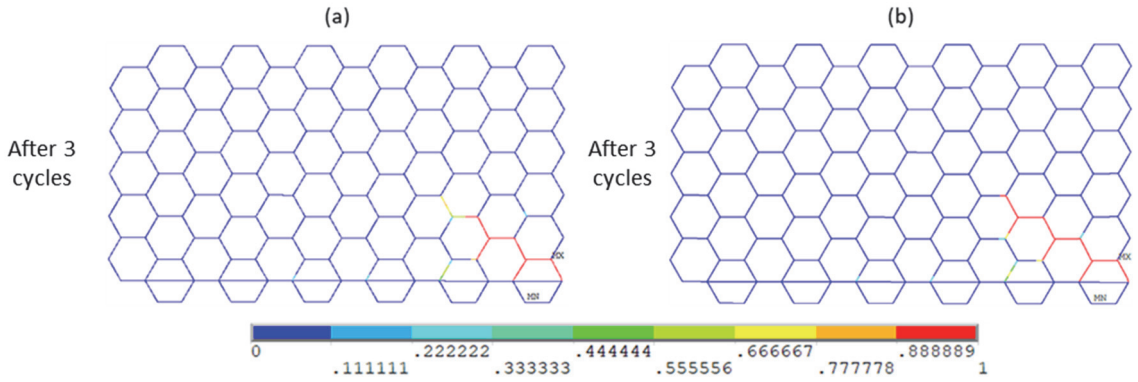

Figure 136: The debonding maps at the heel position at the end of the third cycle in (a) "Reference simulation" (t_{on} = 3 s) and (b) "Simulation B" (t_{on} = 6 s).

The results obtained in both simulations are in agreement with the information reported in the literature [ChBJ17], [Choi16], who mentioned that when t_{on} increases, N_f decreases and the crack evolution becomes stronger and more advanced.

5 A DISCUSSION ON THE RESULTING CRACK EVOLUTION IN THE SIMULATIONS COMPARED TO THAT SEEN EXPERIMENTALLY AND REPORTED IN THE LITERATURE

Based on the cracking patterns seen in Figure 133-Figure 136 and the information reported in the previous chapters about the crack dependency on physicochemical-microstructural features, critical factors that simulations cannot cover must be listed. Apart from the concentration of stress and temperature values at terminal wire edges, the microstructural reason that reinforces the idea of debonding initiation at terminal wire edges is the effect of dislocations' activity. Aluminum is a high stacking fault energy material, which means that the generation of dislocations inside it is much more difficult than in materials acquiring lower stacking fault energy; however, the dislocation's mobility inside it is easier [LiKi20]. Since dislocations with high activity already exist before cycling at the wire edges due to the wire welding process, they will face difficulties when trying to penetrate or eject from HABs, leading to their accumulation. This contributes to the crack initiation. The action of dislocations in forming pile-ups which cause the increase in the stress concentration and lead to cracks' formation at such positions is well described in the previous chapters.

Experimentally, cracking was observed at the zone just above the interconnection between the wire and the metallization, as seen in Figure 45, and not exactly at the wire-metallization interconnection interface. Debonding must not progress inside the metallization layer even though the generated stress values in the simulations are high. This is because all the grains of thin metallization films have small grain sizes; thus, they acquire higher strength referring to the Hall-Petch relationship; therefore, their corresponding critical fracture stress values for debonding are higher.

In the previous simulations, it was deduced that decohesion at the wire's heel position mainly occurs during the heating phase. In contrast, decohesion at the wire's tip position mainly occurs during the cooling phase. Examples from "Reference simulation" show these observations as plotted in Figure 137 and Figure 138.

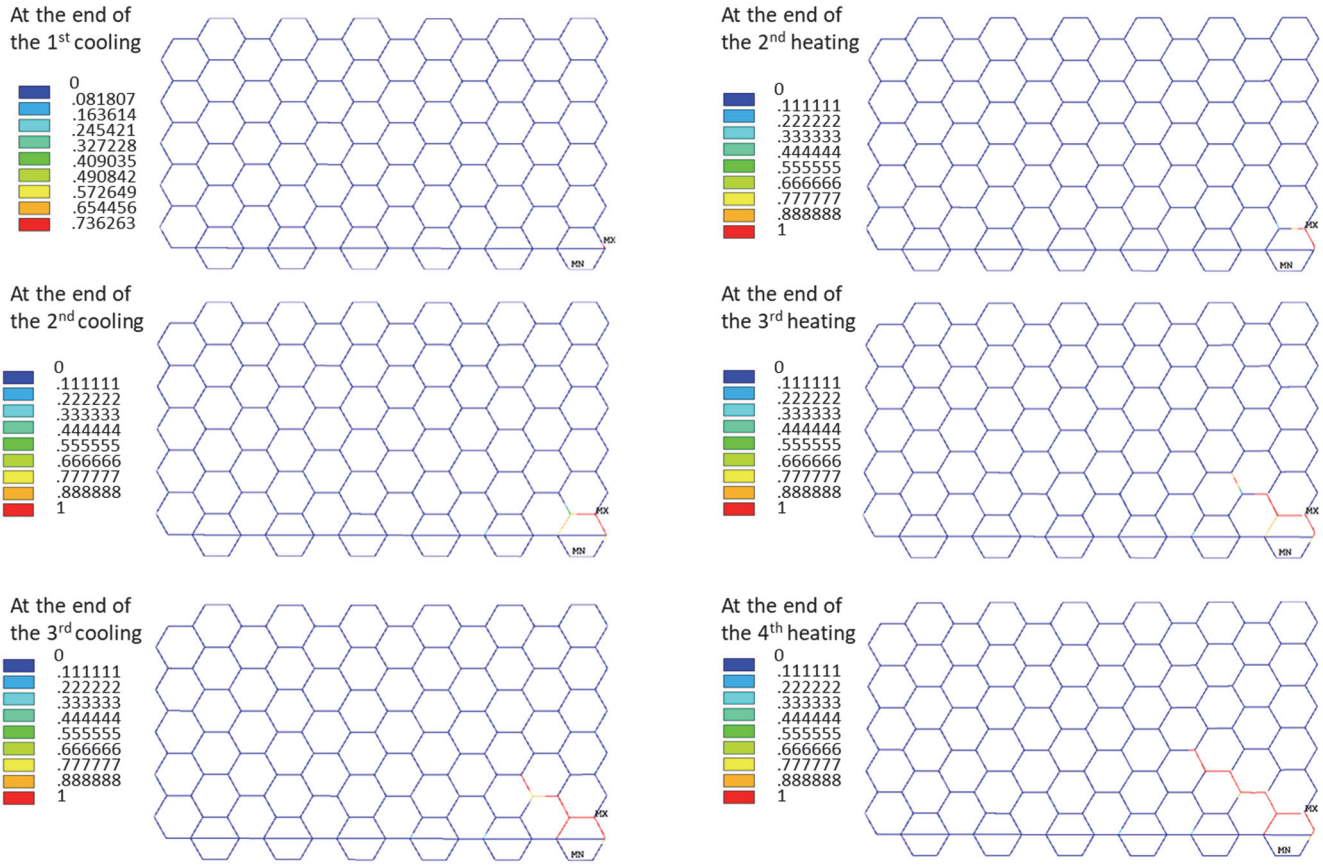

Figure 137: The debonding maps in "Reference simulation" at the heel position.

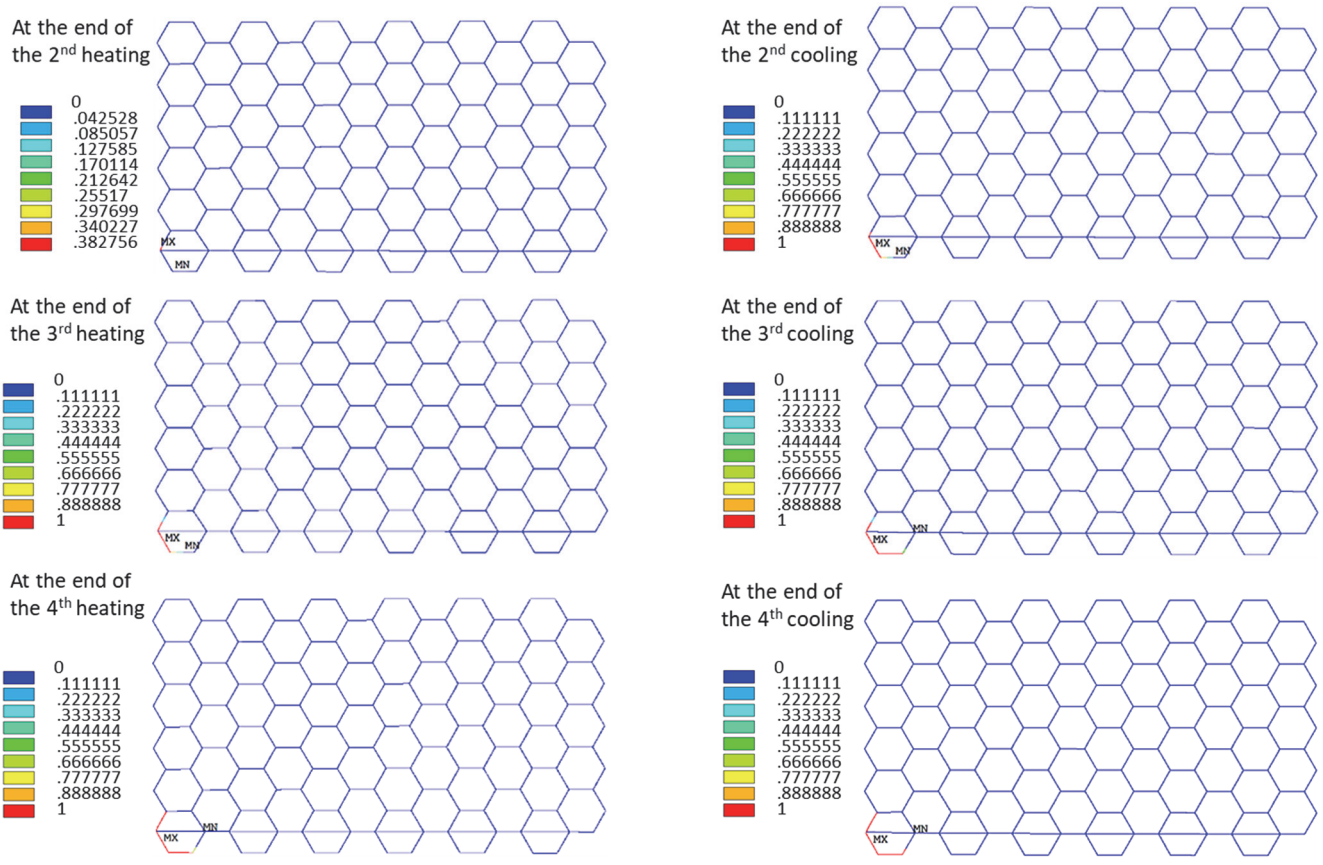

Figure 138: The debonding maps in "Reference simulation" at the tip position.

These results imply that the wire's heel area experiences significant tensile or shear forces during the heating phase compared to the cooling. This trend is reversed at the tip position. Indeed, it is indicated in the literature that compressive forces dominate the wire-metallization contact during heating, while tensile and shear forces are mainly present during cooling [AYAE16], [OnKS00]. According to these observations, whether at the heel or the tip of the wire, decohesion should occur mainly during the cooling phase. However, the entire substrate deforms during the heating phase according to the difference in CTE of the materials composing the assembly. Silicon deforms very little compared to aluminum. The metallization film is very thin, constrained by the silicon chip, and cannot be much deformed. Therefore, the remaining component, the bonding wire, is constrained at its contact with the metallization, and it flexes enormously at the heel part. This is maybe why an opening at the wire's heel is visible at the end of the heating phase. On the contrary, the wire almost returns to its original position at the end of the cooling phase. Therefore, as reported in the literature, tensile and shear forces are generated at the wire's tip at the end of the cooling phase, leading to its opening [AYAE16], [OnKS00].

Conclusions about the debonding behavior reported in the previous sections were summarized as follows. Regarding the debonding evolution pathway, good compatibility was observed when comparing the simulations' results with some experimental data for degraded IGBT semiconductor samples under the same conditions (Figure 45). The crack initiation starting from the terminal edges of the wire in contact with the metallization layer was verified. From the simulations, it was deduced that decohesion at the wire's heel position mainly occurs during the heating phase; however, it mainly occurs during the cooling phase at the wire's tip position. Moreover, the crack propagation just above the interconnection interface was verified in the simulations when looking at Figure 133-Figure 138. From Figure 133 and Figure 134, it was observed that cracks are formed first at the heel position with a faster speed than that at the tip, as observed experimentally when looking at the crack path at both wire's tip and heel positions for samples degraded at 10% and 25% N_f. These observations are coherent with the literature [AYAE16], [LCLH07], [OnKS00].

6 THE PHYSICOCHEMICAL-BASED ANALYTICAL METHOD USED AS A VERIFICATION OF THE SIMULATIONS RESULTS

This section presents an analytical method used to verify the simulations' results. This is done by predicting crack lengths at certain moments, benefiting from the stress values extracted from the simulations' results, and comparing these predicted lengths with the crack lengths resulting in the simulations. This analytical method links the crack length to some physicochemical parameters such as the young modulus, surface energy, critical fracture stress, and critical fracture energy. The equations necessary to obtain the crack length values are listed below. These equations were taken from the following references [MoGS16], [WiZD18] and combined in this section. The parameters listed in equations (38) and (39) are presented in Figure 139.

$$G_c = \frac{\delta_c \, \sigma_c}{2} \tag{38}$$

$$G_d^j = G_c \; - \; \frac{\sigma_m^j \, \delta_c}{2} \tag{39}$$

$$\sigma_c \sqrt{a} = \sqrt{\frac{E \, (2\gamma_s + G_d^j)}{\pi}} \tag{40}$$

Where G_c is the critical fracture energy, δ_c is the critical separation value, σ_c is the critical fracture stress, G_d^j is the dissipated energy at point A', σ_m^j is the stress at point A', a is the crack length, E is the young modulus, and γ_s is the surface energy.

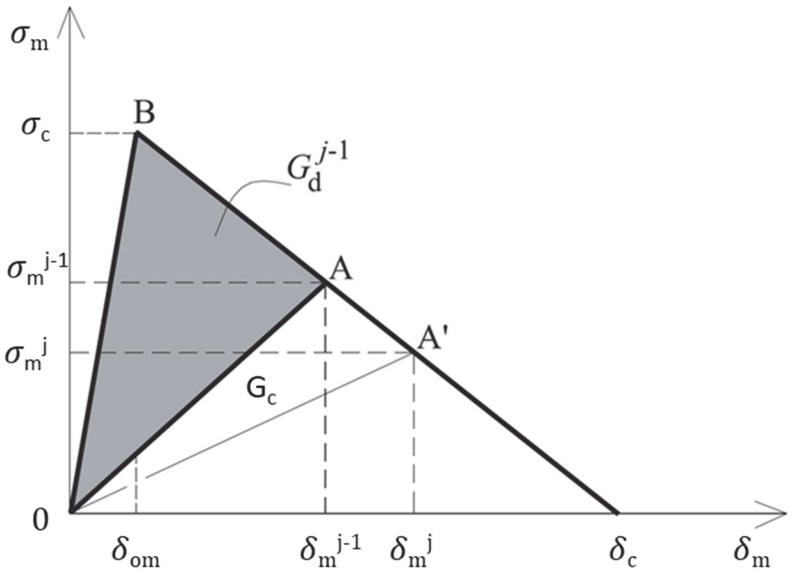

Figure 139: *Mixed-mode (I + II) cohesive law [MoGS16].*

In ANSYS APDL software, one has to put the critical fracture energy and stress values when applying the CZMs. As explained previously, the critical fracture energy values only affect the debonding strength; thus, they are not reduced when using them in these equations. Another reason for not reducing them is that if they were reduced and upon using equation (39), G_d^j will be a reduced value. When using this reduced value in equation (40) which contains real values of material properties such as young modulus and yield strength, difficulties in assigning the appropriate values will be faced. Therefore, only the critical fracture stress values were reduced when used in equations (38) and (39) because they directly impact the occurrence of debonding, by which the latter does not occur unless the resulting stress reaches the critical fracture stress values. In equation (40), because all other values in this equation are real as mentioned before, the critical stress values are not reduced.

G_c is assigned to have a value of 1 J/m^2 as inserted in the "Reference simulation". The real critical fracture stress (σ_c) used in equation (40) is set to be 110 MPa, benefiting from the following reference [BGHS15] as illustrated in section #3.2.2 in Chapter III. As mentioned in the previous paragraph, reduced stress values (σ_c and σ_d^j) are used in equations (38) and (39) as inserted in the "Reference simulation" to obtain the correct δ_c length considered in the CZMs. These reduced stress values are assumed to have the major effect on the resulting δ_c length, more than the effect of both G_c and G_d^j energy values that may acquire on this length value. Same as the conditions of "Reference simulation", the reduced value of σ_c used in equations (38) and (39) is set to be 28 MPa.

The ANSYS APDL program automatically adds the value of stiffness (set to be 0.9e13 MPa/m). Other parameters necessary for calculating the crack length are listed as follows. The Young modulus (E) parameter has a value of about 65 GPa, deduced from the nanoindentation results. The grain just at the heel wire-metallization contact is oriented toward the (111) direction along the x-direction in the healthy analyzed sample, as observed in Figure 140. This particular orientation was mentioned to have a value of γ_s = 0.62 J/m^2 as mentioned in the literature [ZhMX04]. Since the CZM elements are manually inserted, the value of δ_c can be calculated using equation (38). The value of δ_c for the studied hexagonal edges is 7.267e-8 m.

Figure 140: The orientation of the grain (along the x-direction) just at the healthy heel wire-metallization contact.

This analytical method of calculating the crack length at a specific time and position was applied on the first two debonded edges of the heel terminal hexagon just at the wire-metallization interface, in addition to a third debonded edge in the neighbor hexagon, as marked and labeled in Figure 141.

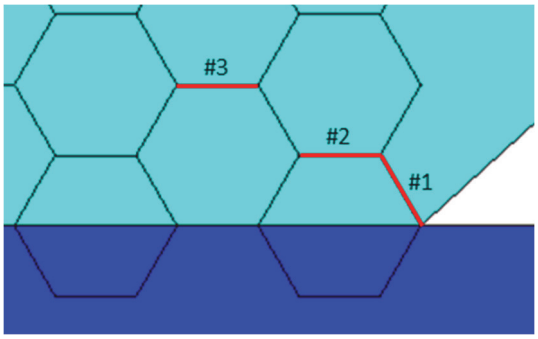

Figure 141: The hexagonal edges labeled #1, #2, and #3 assigned for predicting the crack length.

The crack length is calculated with the help of the simulation results. As listed previously, the length of one cycle is 9 s, 3 s for the heating phase (power-on state), and 6 s for the cooling phase (power-off state). In this analysis, the crack prediction is applied at the early cycling stages (during the power-on state in the second, third, and fourth cycles); however, these early cycling stages are in fact accelerated ones as mentioned previously.

Figure 142 shows the debonding evolution in the first selected hexagonal edge bordered in black.

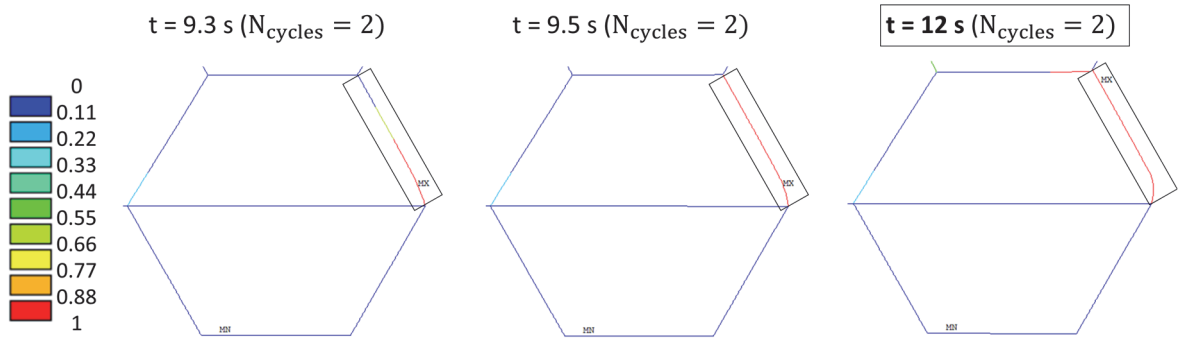

Figure 142: The debonding evolution in the first analyzed hexagon edge.

As seen in Figure 142, the complete debonding of the bordered hexagon edge begins at t = 9.5 s, and it is almost complete at 12 s. At that moment, and by using the previous relationships, the crack length should be around 3.54 µm which is the length of the hexagon edge. The necessary parameter to calculate the crack length value at that moment using equations (38)-(40) is σ_m^j, which is the value of the stress at a specific time after the beginning of debonding (here it is calculated at 12 s). This stress value should be lower than the value of the critical fracture stress put in the simulation, because when debonding starts, stress is relieved. For this purpose, the values of σ_x are extracted at this specific moment for the zone marked in yellow in

Figure 143. The values of σ_x are selected because these values are close to the values of the critical fracture stress; thus, they cause the fracture here. Consequently, the average σ_x value reflects the σ_m^j value around the yellow zone.

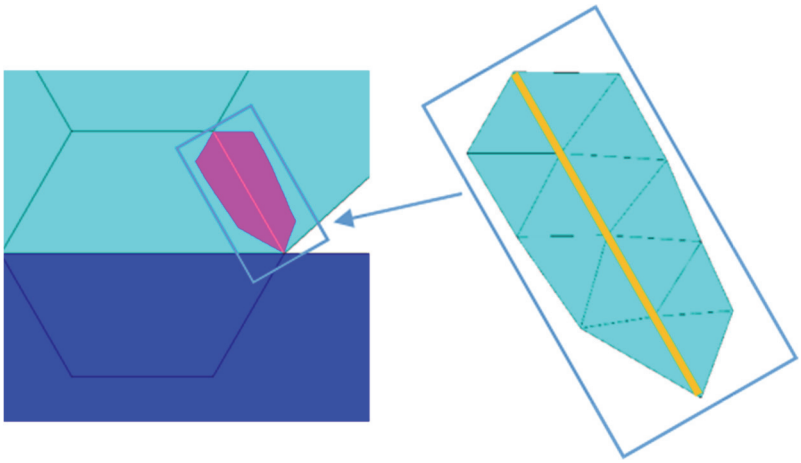

Figure 143: The image at the left shows the selected elements surrounding the first debonded hexagon edge understudy. The image at the right shows the zone marked in yellow at which σ_m^j is extracted.

From the simulation results, the average σ_x value representing σ_m^j around the yellow zone is 4.73 MPa at t = 12 s. Then, using equation (39), $G_d^j = 0.83$ J/m^2. Finally, from equation (40) the value of the crack length (a) is calculated, where a = 3.37 µm which is around 95.26% of the total hexagon edge length which is 3.54 µm. This calculated crack length value is expected as mentioned previously because the crack is complete at this moment and its length is almost the same as the length of the hexagon edge.

Figure 144 presents the debonding evolution in the second selected debonded hexagonal edge bordered in black.

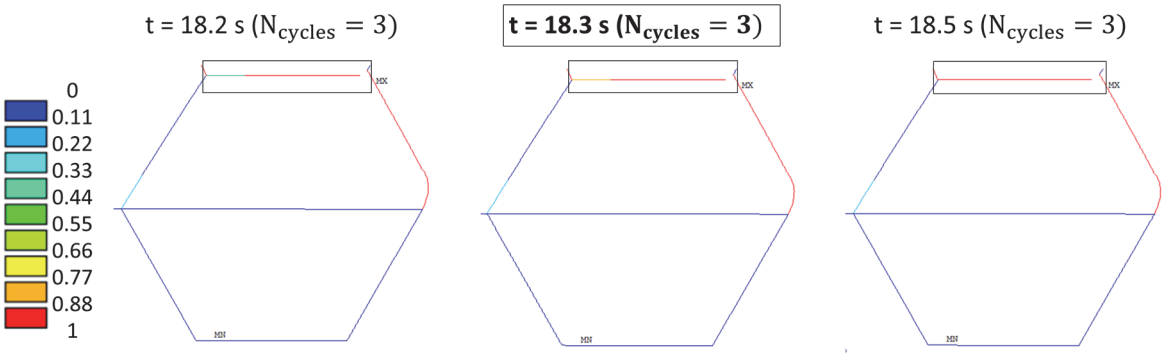

Figure 144: The debonding evolution in the second analyzed studied hexagon edge.

Figure 144 shows that approximately 75% of the hexagon edge is debonded at 18.3 s. At 18.5 s, complete debonding can be observed. For this second debonded hexagon edge, debonding is studied at 18.3 s, just before the complete edge debonding. The values of σ_x at that moment are extracted for the zone marked in yellow in Figure 145. Also for this edge, σ_x values are specifically chosen because these values are close to the values of the critical fracture stress; therefore, they control the fracture on this edge.

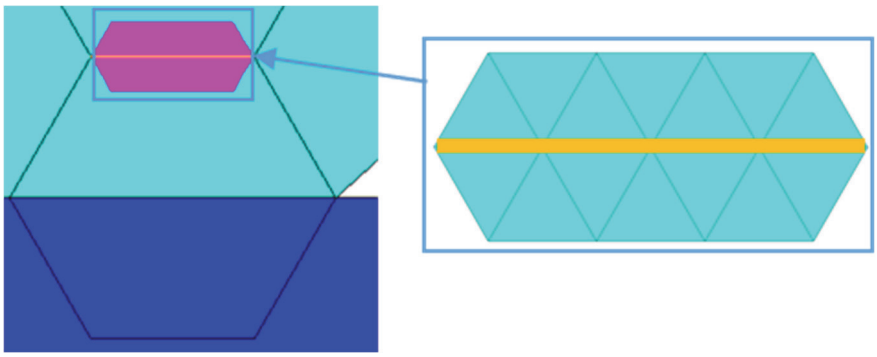

Figure 145: The image at the left shows the selected elements surrounding the second debonded hexagon edge understudy. The image at the right shows the zone marked in yellow at which σ_m^j is extracted.

The simulation results show that the average σ_x value surrounding the yellow zone is 16.91 MPa at t = 18.3 s. Then using equation (39), G_d^j = 0.38 J/m^2. At last, from equation (40) the value of the crack length (a) is calculated, where a = 2.64 µm which is 74.64% of the total hexagon edge length. This calculated crack length is reasoning since at this moment the crack length is almost 75% of the length of the hexagon edge.

Finally, the debonding maps of the third selected debonded hexagonal edge bordered in black are shown in Figure 146.

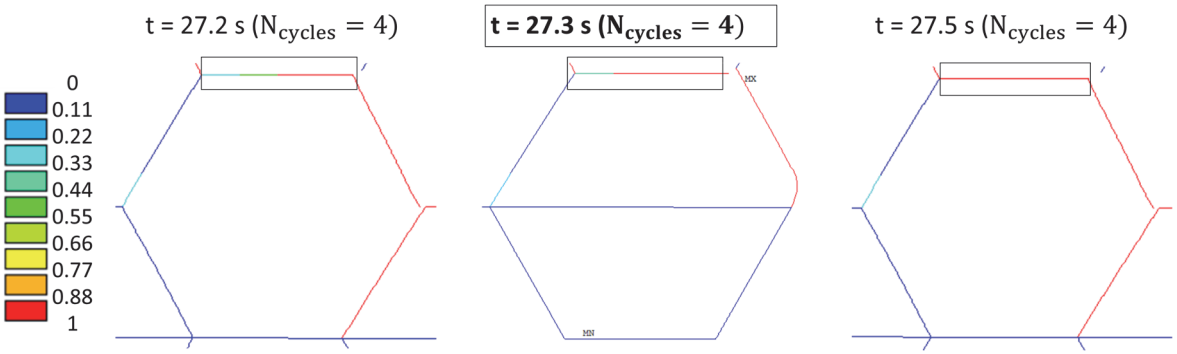

Figure 146: The debonding evolution in the third analyzed hexagon edge.

Approximately 75% of the hexagon edge is debonded at 27.3 s, as observed in Figure 146. At 27.5 s, complete debonding resulted. For this third debonded hexagon edge, debonding is studied at 27.3 s. σ_x values are extracted at this moment for the zone marked in yellow in the next figure. Also for this edge, σ_x values are particularly chosen because they are close to the values of the critical fracture stress; therefore, they control the fracture on this edge.

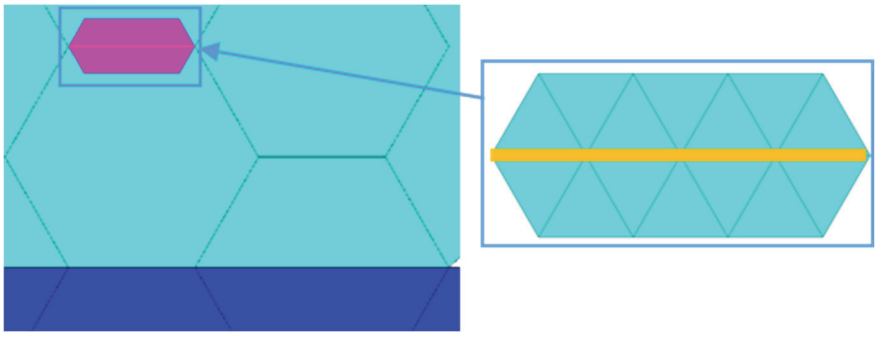

Figure 147: The image at the left shows the selected elements surrounding the third debonded hexagon edge understudy. The image at the right shows the zone marked in yellow at which σ_m^j is extracted.

As a result, the average σ_x value representing σ_m^j around the yellow zone is 16.28 MPa at t = 27.3 s as extracted from the simulation. Then, using equation (39), G_d^j = 0.41 J/m^2. Finally, from equation (40), the value of the crack length (a) is calculated, where a = 2.69 µm which is around 76% of the total hexagon edge length. This calculated crack length is logical because at this moment the crack length is almost 75% of the length of the hexagon edge.

As a result, the crack length values predicted using this method are so close to the values obtained in the simulations. The table below summarizes the crack length values simulated and those predicted using this method.

Table 9: A comparison between the simulated and predicted crack length values using this method.

	Simulated crack length (µm)	Predicted crack length (µm)
First debonding edge	3.54	3.37
Second debonding edge	2.75	2.64
Third debonding edge	2.75	2.69

7 DISCUSSING THE LIMITATIONS THAT THE APPLIED SIMULATIONS DO NOT COVER

After using the numerical simulations for predicting the crack pathway and length, it is also important to discuss their limitations and the assumptions considered. Concerning the CZMs used, some assumptions should be reviewed. The first one supposes that the CZM parameterization is independent of the loading conditions. Thus, when the CZM parameters are calibrated for given {ΔT_j, $T_{j\,min}$, t_{on}, t_{off}} conditions, this means that this CZM can be applied for any other conditions. This might be logical because the CZM elements are just related to materials' properties. Another assumption is that the cracking caused by high ΔT_j values higher than real ΔT_j values is representative of the cracking generated in reality but with an accelerated form. This was an obligatory assumption to reduce the time needed to see the formation of the cracks. This limitation was discussed in section #4 when applying "Simulation A" with ΔT_j = 70 °C and comparing the cracking passage in this simulation with the results of "Reference simulation" with ΔT_j = 110 °C. The crack passage in both simulations was identical.

The most important limitation in these simulations, which may affect the debonding pattern, is that reduced critical fracture stress values were used in the CZMs. From the early cycling stages, the resulting stress values in the simulations caused by cycling are close to the critical fracture stress values. This might, for example, cause debonding in zone 3, especially when using highly reduced critical fracture stress values. Such a cracking manner is not experimentally observed. This abnormal cracking pathway can also be clued while comparing the results of a simulation using real critical fracture stress values with another simulation using reduced critical fracture stress values (such as "Reference simulation"). When looking at the stress values in all directions among these two simulations, it was seen that certain stress values are not reached in zone 3 for 20 cycles when using real critical fracture stress values; however, when using reduced critical stress values, they are reached after only eight cycles! This is probably due to the fast debonding that occurred when using reduced critical fracture stress values for the contact elements in zone 2 touching the contact elements in zone 3, thus changing the stress in the neighborhood and leading to the observed increase in stress in zone 3.

As previously mentioned, the microstructural images showed that the crack propagation pattern is only inside the wire just above the metallic interconnection interface and not inside the wire bulk, even though bigger grains exist there. For the first while, this seems contradictory to the Hall-Petch relation since bigger grains possess lower strength. The probable reason for this cracking pattern is related to the effects of the wire welding process. Primarily, the welding process leads to the formation of a high amount of plastic

deformations at the interconnection interfaces, causing plastic strains prior to cycling [PØKG16]. This results in hardening which enhances the crack formation at the interconnection level, enhancing the crack evolution inside the wire [Buhr18]. It was observed that grains' reconstructions responsible for decreasing the contact between neighbor grains and promoting cracks' formation take place in the hardened sites caused by the wire welding process [ZAFB19]. The welding process also causes the presence of impurities at the interconnection interface, weakening the grains there [GSGL10].

Another influencer for this cracking pathway is the effect that grain boundaries [DSWN19] and disorientation angles [ZZYH16] may have on hindering the crack propagation, especially when looking at the high difference in terms of grain sizes between the grains near the interconnection positions with mostly small sizes and the grains above them which have huge sizes. This may increase the resistance to fracture [SoAT17]. An additional influencer that might be mentioned is the crack closure phenomena [Huss97], which could also result from the changes in surface roughness, plastic constraints, and variations in grains' orientations. Consequently, due to several physicochemical-microstructural factors, the cracking process is much more complicated to predict than saying that it occurs just when stress reaches the fracture stress value at the grain boundary.

Among the presented limitations, some of them will be neglected. The first limitation to be neglected is the crack closure phenomena because if it exists, it will be important at the advanced cycling stages only, not at the early and intermediate cycling stages [Huss97]. In the simulations, only the crack's early stages were modeled. The other limitation that will not be discussed is the presence of impurities because we are not sure whether they are present or not. Therefore, the main limitations to consider are i) the effect of using a reducing factor for critical fracture stress in simulations, as well as ii) the role of grain boundaries and disorientation angles in addition to recrystallization and hardening. These limitations are discussed in detail in the following sections.

7.1 MICROSTRUCTURAL-BASED LIMITATIONS

The effects of grain boundary disorientation angles and the grain hardening process on the crack formation are discussed by applying some EBSD analyses on healthy and degraded wire samples. The main parameters to look for in such analyses are the types of boundaries present, the geometrical necessary dislocations density (GND), the average grain orientations (GOS), and the disorientation average deviation (MAD) maps. These factors were analyzed inside the bottom part of the wire in contact with the metallization, as schematized in Figure 148. This position was studied because it is the cracks' evolution zone.

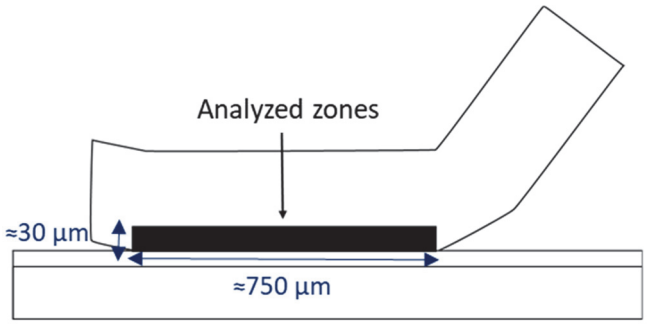

Figure 148: A scheme showing the analyzed portion used to discuss the main limitations that simulations do not cover.

Different samples were analyzed at a different number of cycles. These microstructural analyses were applied to a healthy sample, and when it was degraded at 50% N_f and 100% N_f as shown in Figure 149, Figure 150, Figure 151, and Figure 152.

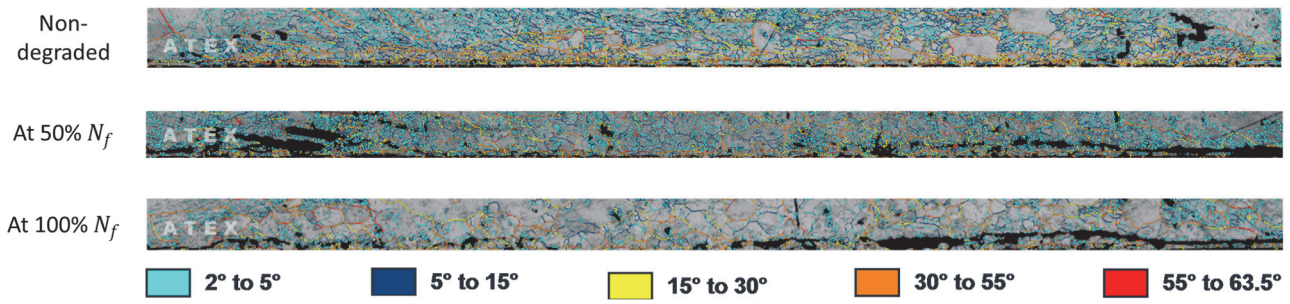

Figure 149: The evolution of boundary angles' distribution upon cycling inside the wire in contact with the metallization.

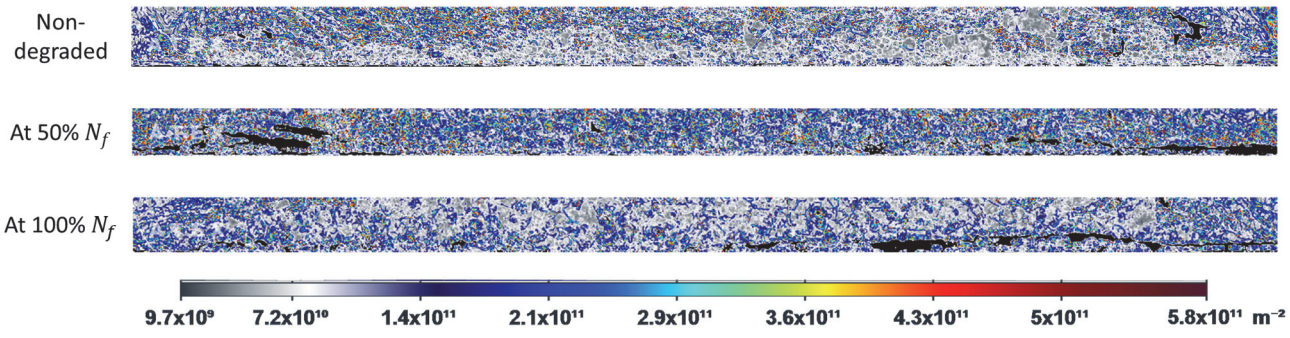

Figure 150: The evolution of GND distribution upon cycling inside the wire in contact with the metallization.

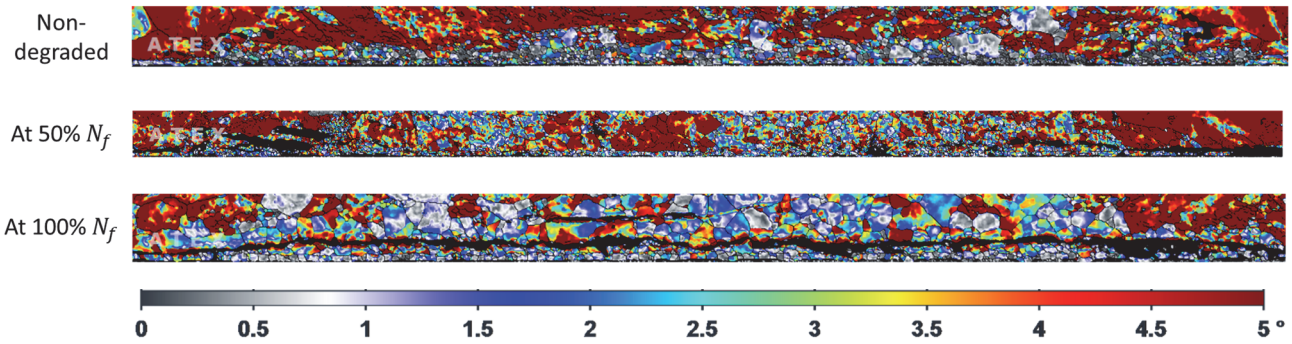

Figure 151: The evolution of GOS distribution upon cycling inside the wire in contact with the metallization.

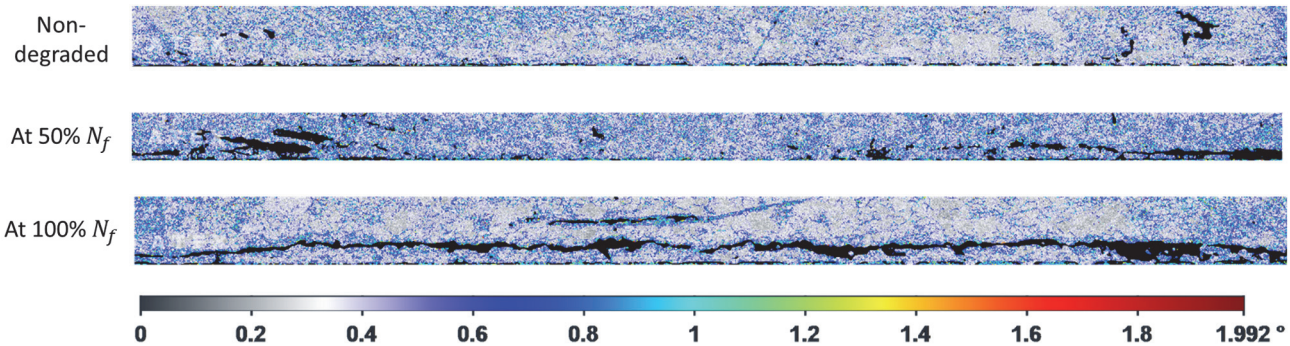

Figure 152: The evolution of MAD distribution upon cycling inside the wire in contact with the metallization.

Each of these properties has its significance. For example, concerning the types of boundary angles, it was observed that the relative frequency of HABs increases upon cycling, especially near the cracks' tip, by which some LABs transform into HABs. Thus, the locations of cracks' progress are the sites where boundaries transform into HABs [PNSS15]. For the GND density, it is seen in the literature that the increase in this parameter means more stress generation. In parallel, it was mentioned that this factor increases upon cycling

near the places of formation of cracks [QHHL04]. Regarding the GOS factor, its increase means the existence of microstructural changes such as recrystallization, sub-grains formation, and dislocations generation [PNSS15], [WWHT19]. It was also deduced that cracks travel along recrystallized grain boundaries [YaAJ14]. About the MAD distributions, it was concluded that this parameter is directly related to the stress intensity factor [RSSQ18]. As a result, these parameters i) may geometrically enhance/hinder the formation of the cracks, ii) increase stress, and iii) give clues about the existence of microstructural evolution processes that affect cracks' formation. The results of these analyses are summed in Table 10.

Table 10: Summary of the evolution of grains' disorientation angles, GND, GOS, and MAD inside the wire in contact with the metallization upon cycling.

Sample's state	Boundary angles	GND density	GOS	MAD
Healthy	LABs are dominant. Low frequency of HABs	Low values, especially at the wire's heel and tip	Generally high values	Low values are dominant
Upon cycling	Generation of HABs	Increases especially at cracks' formation zones	High at zones of cracks' formation	Higher values, majorly at cracks' formation zones
At N_f	High fractions of HABs	High values at zones of cracks' formation	High at zones of cracks' formation	High at zones of cracks' formation

7.2 LIMITATIONS RESULTING FROM SPEEDING UP THE SIMULATIONS

Using reduced critical fracture stress values in the CZMs is the most important limitation to consider since its effect on the crack formation and progress is critical. First, different simulations were performed with different reduced critical fracture stress values. Then, the length of debonded edges initiating from the heel position and growing in the leftward direction towards the tip wire edge was measured upon cycling in these different simulations as schematized in Figure 153. After that, a curve was plotted to show the variation in the crack length with respect to the number of cycles. Finally, using some experimental data from the previous Ph.D. student [Dorn19], the mode of the evolution of the crack (speed and length) was generalized.

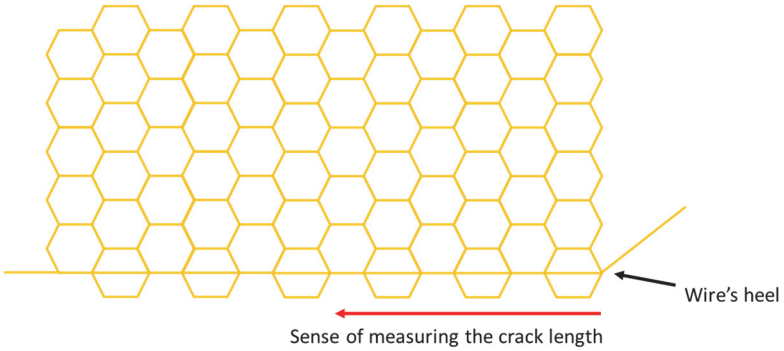

Figure 153: The manner of calculating the crack length.

Table 11 shows the five different undergone simulations. The first one is the same as "Reference simulation". The four additional simulations are named "Simulation 1", "Simulation 2", "Simulation 3," and "Simulation 4". From "Simulation 1" to "Simulation 4", the values of the CZM stress elements were gradually reduced. The critical fracture stress values for the hexagonal edges inside the metallization layer (zone 1) in

"Simulation 3" and "Simulation 4" are put the same. It was impossible to reduce the values in "Simulation 4" because putting a lower value of critical fracture stress leads to a favored debonding inside the metallization. This is an incorrect cracking manner because, in reality, debonding occurs inside the wire just above the metallization layer as shown before.

Table 11: The five applied simulations with their corresponding reduced critical fracture stress values used in the CZMs.

Simulation's name	"Reference simulation"	"Simulation 1"	"Simulation 2"	"Simulation 3"	"Simulation 4"
Critical stress values in zone 1	80 MPa (Real/2.25)	101 MPa (Real/1.8)	90 MPa (Real/2)	62.3 MPa (Real/2.9)	62.3 MPa (Real/2.9)
Critical stress values in zone 2	28 MPa (Real/2.75)	40 MPa (Real/2)	35.5 MPa (Real/2.25)	25 MPa (Real/3.2)	22.9 MPa (Real/3.5)
Critical stress values in zone 3	40 MPa (Real/2.75)	55 MPa (Real/2)	49 MPa (Real/2.25)	34.4 MPa (Real/3.2)	31.4 MPa (Real/3.5)

When observing the debonding maps in "Simulation 3" and "Simulation 4", cracks emerged toward zone 3. The reasons for such an abnormality in the crack propagation pathway were discussed at the beginning of this section, mainly due to using highly reduced values of critical stress. Although in this part, the focus was not oriented towards analyzing the places of the crack propagation, it was on analyzing the evolution of the crack length and speed. To interpret the crack progress evolution in these simulations upon cycling, graphs showing the crack length vs. the number of cycles were plotted for the five simulations, as presented in Figure 154.

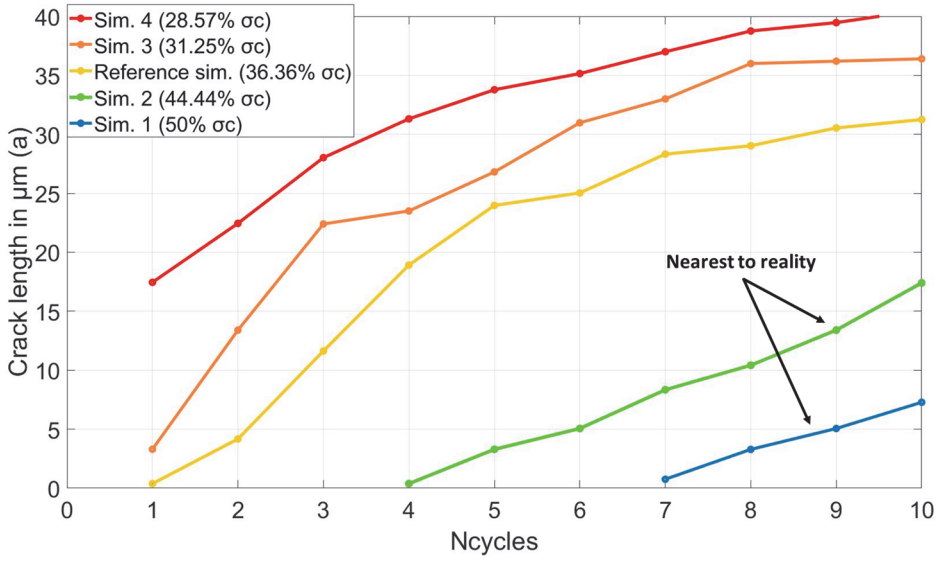

Figure 154: The crack length vs. N_{cycles} plot for "Reference simulation", "Simulation 1", "Simulation 2", "Simulation 3", and "Simulation 4".

In the curves plotted in Figure 154, it is deduced that the crack formation speed is initially high; afterward, it decreases upon cycling. Figure 155 clearly shows the fast crack phase and the linearity of the crack formation plot at the early cycling stages (unit reaching a crack length ≈ 22.5 µm).

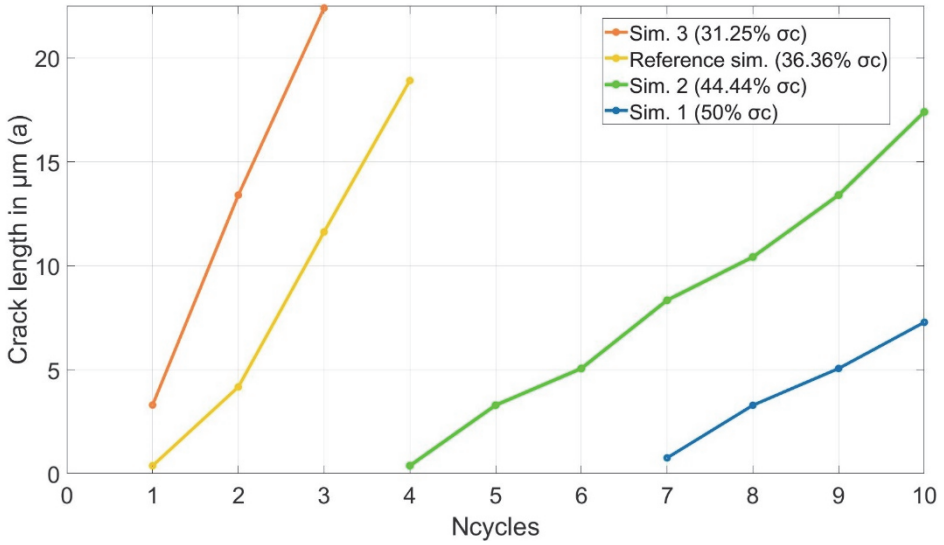

Figure 155: The linear part of the plot shown in Figure 154 for "Reference simulation", "Simulation 1", "Simulation 2", and "Simulation 3".

In order to examine the effect of using different reduced critical fracture stress values on the first linear crack evolution phase (until reaching a crack length ≈ 22.5 µm), the following analysis is made. Figure 156 shows the plot of the N_{cycles} required to reach a crack length ≈ 22.5 µm in simulations using different reduced critical fracture stress values.

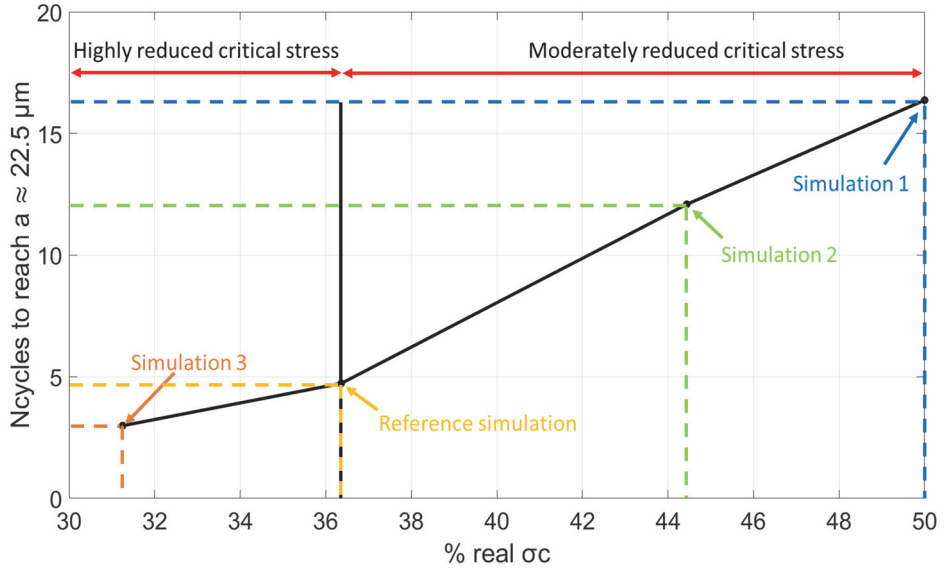

Figure 156: A graph showing the N_{cycles} required to reach a crack length ≈ 22.5 µm in simulations with different reduced critical fracture stress values.

From Figure 156, it can be deduced that upon using high and moderate critical fracture stress reduction, the trend of reaching the crack length ≈ 22.5 µm is different. For moderate reduction, it is observed that there is a linear tendency for the N_{cycles} to reach the crack length ≈ 22.5 µm. For the case of high reduction, the tendency is not the same. The tendency observed in the case of high reduction is less interesting than the previous one because the simulations with moderate critical stress reduction are much closer to reality. Based on this curve, it is assumed that the number of cycles needed to reach a crack length of 22.5 µm, representing the crack linear propagation limit, might be predictable when using a moderately reduced critical stress value.

Because the critical fracture stress values used in "Simulation 1" and "Simulation 2" are the nearest to

reality, and since the crack propagation in these simulations occurs only in zone 2 and does not emerge to zone 3, in addition, because the crack does not start from the first cycle as in real situations, deeper analysis on both simulations was conducted. Based on that, more cycles (thirty power cycles) were applied for "Simulation 1" and "Simulation 2". The crack length evolution upon cycling is presented in Figure 157.

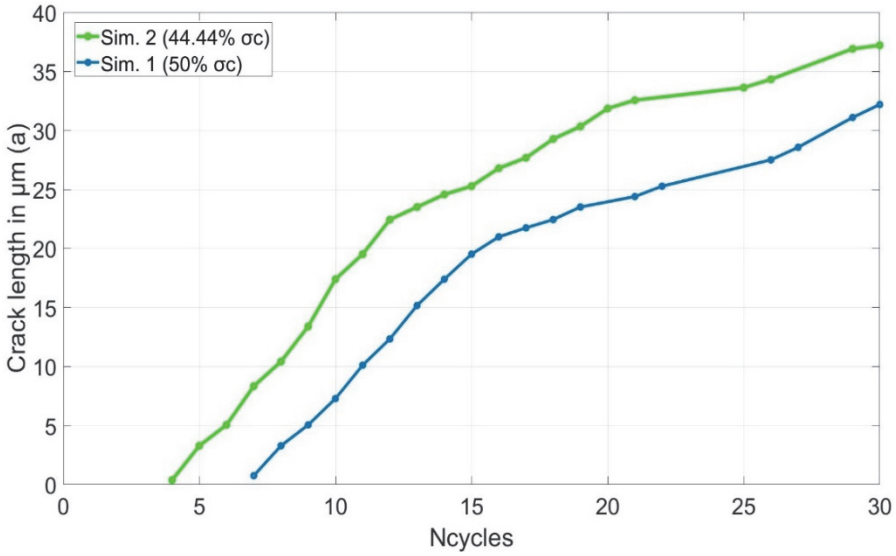

Figure 157: The crack length vs. N_{cycles} plot (up to 30 cycles) for "Simulation 1" and "Simulation 2".

After plotting the crack progress evolution in these simulations, micro-section analyses showing the length of cracks at the wire-metallization interface in SKIM63 IGBT were used. These experimental measurements made by the previous Ph.D. student were utilized to find a correlation between the crack evolution observed experimentally and that resulting in the simulations, furthermore, to see the effect of using reduced stress parameters in the CZMs on the resulting crack length.

Indeed, experimental results showed that the crack does not propagate at a constant speed throughout cycling [DIKD20]. Its progression stages can be divided into two phases, as plotted in Figure 158. A first cracking phase in which the cracking starts and evolves rapidly until it reaches a length between 20 and 30% of the initial contact length at around 10% N_f. Following the first phase, a second phase exists, in which the crack progresses at a slower speed than that in the first phase until it reaches almost 100% of the initial contact length, meaning total rupture of the wire-metallization contact [DIKD20].

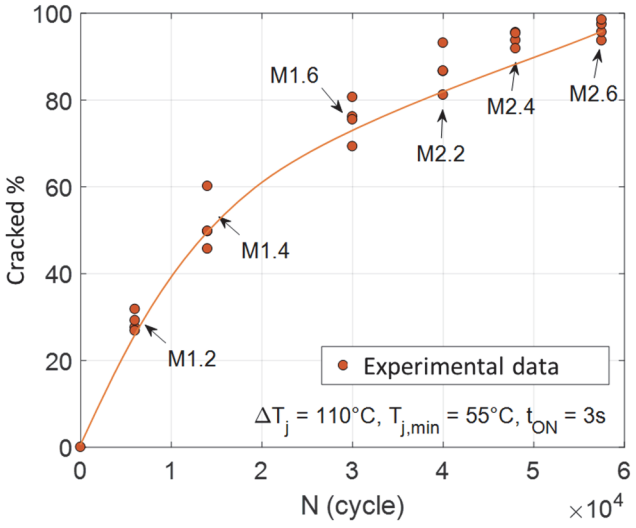

Figure 158: The crack propagation curve reported by Dornic and others [DIKD20], including the fast crack initiation until 10% N_f and the slower crack propagation reaching N_f.

When comparing Figure 154-Figure 157 to Figure 158, it is confirmed that the crack initiation speed is very fast, where it decreases upon cycling. Since it was previously deduced that the crack formation starts faster at the heel position, the crack length was measured there for the sample marked M2 in Figure 159, at the limit separating fast from slow crack propagation speed (at 10% N_f and 20-30% of the crack propagation) [DIKD20]. The crack length at that moment was 96.81 µm [DIKT18].

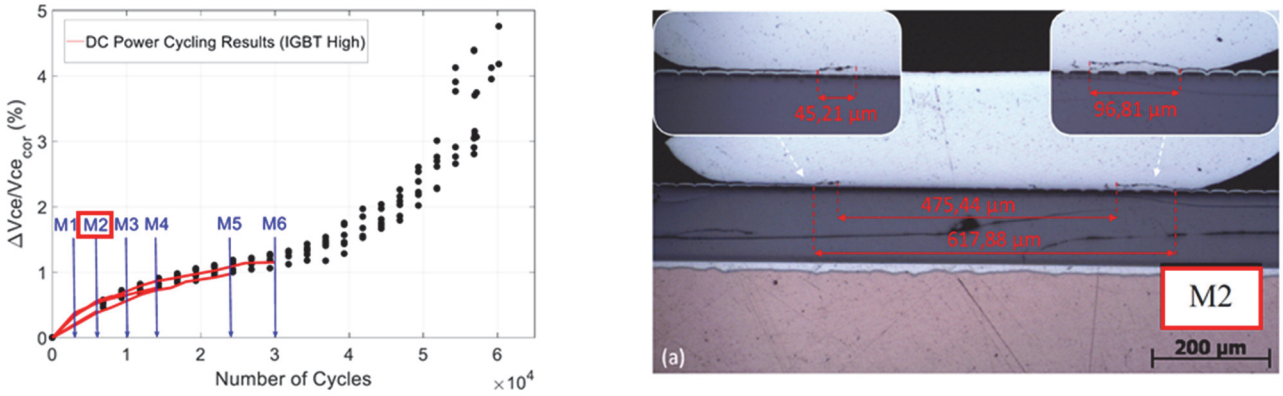

Figure 159: For the sample degraded at 10% N_f under the following conditions {ΔT_j = 110 °C, $T_{j\,min}$ = 55 °C, t_{on} = 3 s, t_{on} = 6 s}, the crack length measured at the wire' heel position is 96.81 µm.

Based on Figure 154-Figure 159, the upcoming conclusions are summed up. Experimentally from Figure 158, before 10% N_f, a fast crack evolution stage is observed. From Figure 159, the crack length at 10% N_f (20-30% of the crack propagation) is deduced to be 96.81 µm. From the simulations' results in Figure 154-Figure 157, it was deduced that there were two phases during the fast crack initiation stage where the crack length at the heel position was still lower than 96.81 µm. In the first phase, the crack propagation is quite linear with cycles until the crack length reaches a value of about 22.5 µm. In contrast, the second phase is rather logarithmic, with a crack speed that grows slower than that at the initiation phase. This second phase starts when the crack size reaches around 22.5 µm.

When exceeding 10% N_f, and because in the simulations a crack length > 96.81 µm was not reached since many cycles are required, in addition to the necessity of adding more hexagons associated with CZM parameters which increases the simulations' complexity, the crack evolution at the advanced cycling stages observed in Figure 158 will be considered. At this advanced cycling phase, the crack propagation evolution also looks logarithmic as for the second cracking evolution phase seen in the simulations (22.5 µm < a < 96.81 µm).

Consequently, upon looking at the simulations and experimental results, we can deduce that the crack initiation phase is so fast. Then, the crack speed decreases within cycling. These observations differ from the expected observations when predicting the crack length evolution using physical models such as the Paris law. Using these laws, a crack speed increase is expected when the crack advances just before reaching N_f.

Returning back to the limitation mentioned at the beginning of this section about the crack formation in zone 3 when applying "Simulation 3" and "Simulation 4", and in addition to the previously mentioned reasons for such a cracking manner (at the beginning of this section), the following analysis was done. Referring to the article done by Zéanh and others [ZDKW08], it was mentioned that the maximum stress can be approximated with a linear function until reaching the mechanical strength. When considering the CZM, the mechanical strength is the critical fracture stress for the beginning of debonding. The hypothesis of the linear stress increase is justified by perfectly cyclic loadings and aluminum's linear elastic properties with linear kinematic hardening behaviors [ZDKW08]. The linear equation is represented in equation (41), where ($\sigma_{initial}$) is the initial stress and (r_σ) is the stress rate.

$$\sigma_{max}\ (\text{MPa}) = \sigma_{initial}\ (\text{MPa}) + r_\sigma\ \ N_{cycles} \qquad (41)$$

A simulation was made using real critical fracture stress values for the three size zones ranging from the wire edge to edge. Then, σ_{max} values for the x, y, and xy directions were plotted vs. N_{cycles} for the entire wire zone in contact with the metallization layer. After that, the N_{cycles} required to reach the critical fracture stress values were predicted. This procedure was done for zones 2 and 3, as marked in Figure 160.

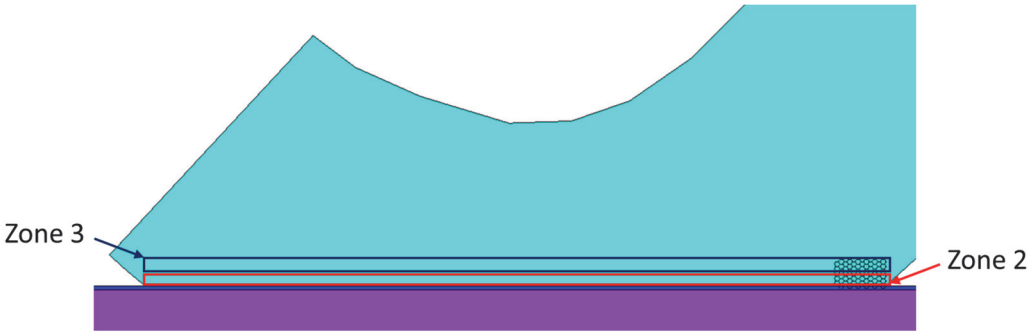

Figure 160: Zones 2 and 3, ranging from the wire edge to edge, selected to predict the N_{cycles} required to reach the critical fracture stress.

For zones 2 and 3, the values of maximum σ_x, σ_y, and σ_{xy} are plotted vs. N_{cycles} for a simulation of twenty cycles using real critical fracture stress values, as shown in Figure 161 and Figure 162 respectively.

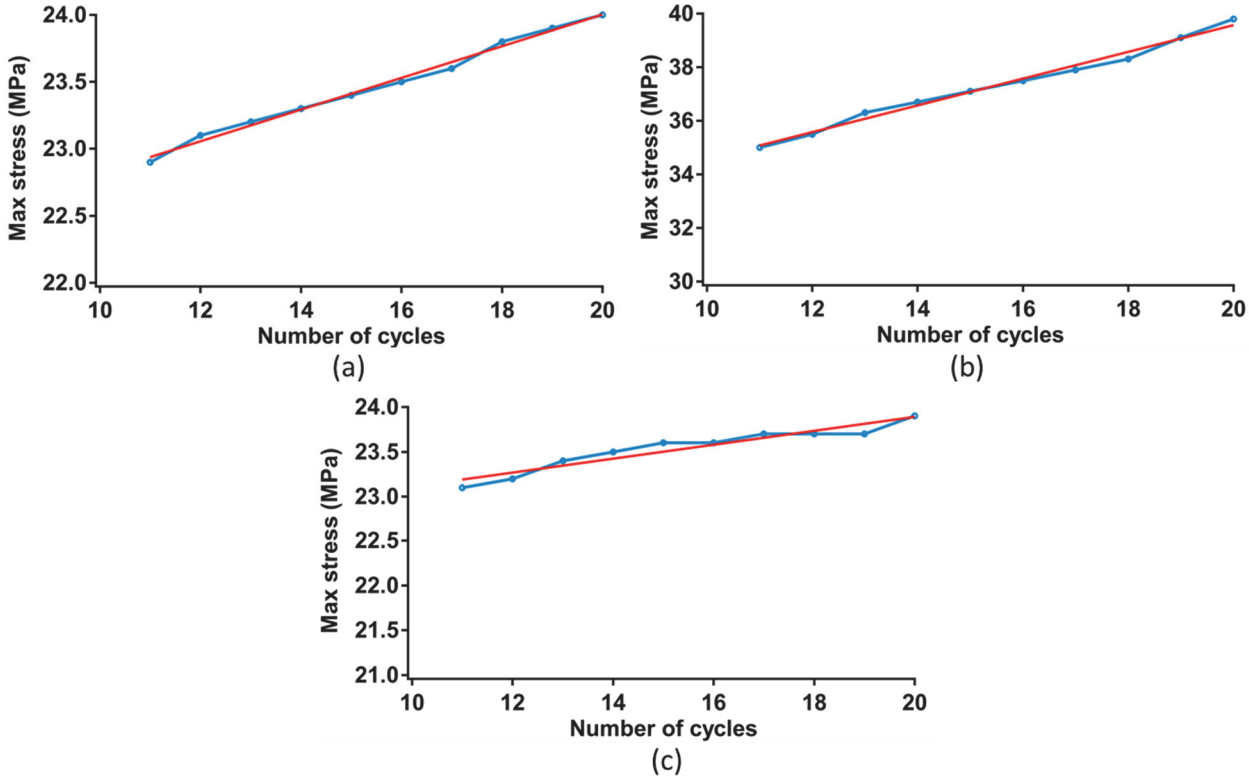

Figure 161: The evolution of (a) maximum σ_x, (b) maximum σ_y, and (c) maximum σ_{xy} vs. N_{cycles} in zone 2.

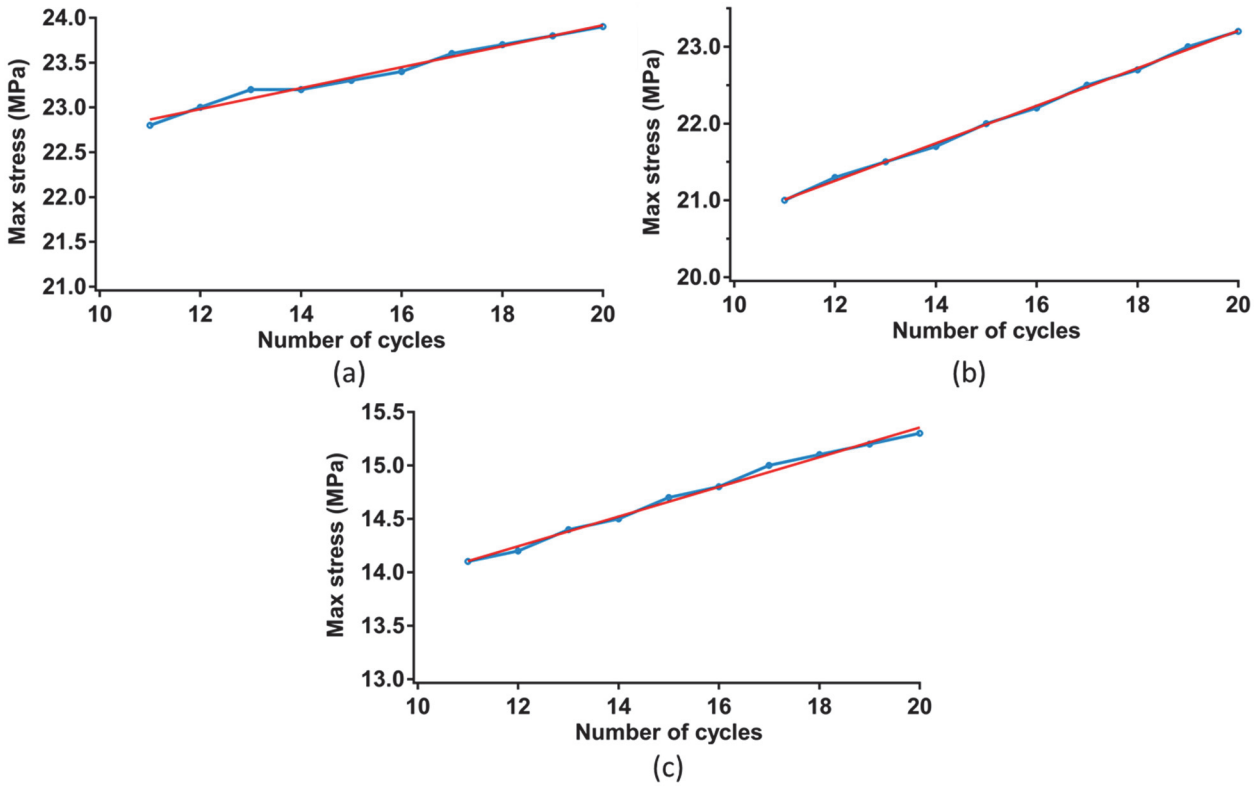

Figure 162: The evolution of (a) maximum σ_x, (b) maximum σ_y, and (c) maximum σ_{xy} vs. N_{cycles} in zone 3.

The tendency of the evolution of the maximal stress values (dots in blue) in all directions is linear in zones 2 and 3 (line in red). Using the linear fitting equations of these curves and equation (41), the N_{cycles} to reach the real critical fracture stress values for the hexagonal edges in zones 2 and 3 were predicted and summed up in Table 12.

Table 12: A table including the critical fracture stresses for zones 2 and 3, in addition to the predicted N_{cycles} to reach these critical fracture stress values in all directions.

Zone	Critical fracture stress (σ_c)	N_{cycles} for σ_x to reach σ_c	N_{cycles} for σ_y to reach σ_c	N_{cycles} for σ_{xy} to reach σ_c
2	80 MPa	494 cycles	101 cycles	744 cycles
3	110 MPa	756 cycles	376 cycles	750 cycles

From these predictions, cracks are supposed to occur primarily in zone 2. When critical fracture stress values are reached, cracks are formed. The formation of cracks relieves the stress near the hexagonal edges in zone 2, which are in contact with those in zone 3. This also probably decreases the generated stress values in zone 3; thus, the hexagonal edges in this zone will not reach their corresponding critical fracture stress values for crack formation. Consequently, the crack will not progress in zone 3.

8 CONCLUSIONS

In summary, CZMs were first implemented at the edges of the hexagons which represent the grain boundaries. In the previous chapter, the parameters of the CZM type used were linked to physicochemical-microstructural properties. Electrothermal-mechanical simulations were applied to model the damage at the wire-metallization interface. The model's conditions were parameterized so that they have the same

conditions as for experimental aging tests. These simulations enable us to predict the cracks' formation process taking place at the wire-metallization interconnection zone.

Three different simulations were made to i) see whether debonding starts from the heel or the tip positions, ii) predict the cracking pathway, iii) examine the effect of only changing the value of ΔT_j on the debonding maps, and iv) see the effect of changing the t_{on} parameter with keeping the same ΔT_j. It was concluded that cracks are first formed at the heel position, where it continues propagating inside the wire just above the metallization layer. The crack speed is faster at the heel than at the tip. The same manner of cracks' formation is seen when only decreasing the value of ΔT_j; however, the speed of cracks becomes slower. When increasing the value of t_{on} with keeping the same ΔT_j, it was observed that debonding is slightly enhanced. In the next step, the debonding maps obtained from these simulations were compared to the manner of crack formation seen experimentally to evaluate the model. Finally, the main limitations resulting from the numerical simulations were debated. Some limitations were discussed based on a physicochemical-microstructural point of view using the EBSD data. The main discussed limitation is using reduced critical fracture stress values in the CZMs to minimize the simulations' calculation time. This limitation was discussed in detail by performing additional simulations.

When applying the simulations, some difficulties were faced. First, obtaining a good representation for the crack propagation requires implementing a very fine mesh at the wire-metallization contact area. This gives rise to several obstacles caused by the increase in the computation time. The number of cycles to be made is another limitation, where a high number of cycles is impossible since the speed of calculus is slow due to the presence of many hexagons associated with CZM parameters at the wire-metallization contact. This forces using reduced critical fracture stress values in the CZMs.

GENERAL CONCLUSIONS AND PERSPECTIVES

This Ph.D. study presented an original CZ - physicochemical and microstructural model for predicting the crack evolution upon cycling. This approach was applied at the level of the upper interconnections of the SKIM63 IGBT power modules, made up of wires and metallization chips.

The first chapter begins by describing the power module assemblies. The purpose of this description is to explain why and how degradations occur. It was shown that the packaging of the module plays a major role in the formation of degradations. In particular, the metallic interconnection interfaces are the most critical areas, especially because of the welding power subjected to wires when bonded to metallization chips. Welding forces lead to grains reconstruction processes and pre-cracks formation at the edges of the wires. These most common degradations within a conventional module assembly are more important when the power device is aged. When power modules are highly aged, the crack propagation accompanied by microstructural changes leads to total failure. To better understand the correlation between the crack progress and the microstructural changes, the evolution of both processes upon aging should be interpreted first. This was better described in the second chapter.

In the second chapter, accelerated cycling tests were applied to SKIM63 IGBT power devices in order to obtain the degradation evolution for given $\{\Delta T_j, T_{j\ min}, t_{on}, t_{off}\}$ conditions. The choice of this module was proved to be appropriate since the only degradations observed were the wires lifting-off and the granular reconstructions inside wires and metallization chips. Therefore, degradations occur only at the level of wires and metallization chips, the zone of interest in this study. Degradations' evolution was directly related to the microstructural evolutions and the changes in the physicochemical properties. SEM and AFM techniques showed that upon cycling, the surface of the metallization layer highly changes, where reconstructions take place. These reconstructions were linked in the literature to the increase in the metallization resistance, as shown in this chapter. In the second step, EBSD tests were applied for different samples at a different number of cycles in order to do a detailed physicochemical-microstructural analysis of the degradation processes occurring. This analysis was conducted at the interconnection zone between the wire and the metallization layer, the positions of cracks initiation and propagation. Regarding the grains' texture transformations, grains orient to increase their packing density and decrease their surface energies. The grain growth process at the early cycling stages and the presence of LABs accompanied the maximal crack speed during its initiation state. The speed of the crack is higher at the wire's heel than at the tip. When cycling advances, a shift from LABs to HABs was deduced to be synchronous with the slowdown in the crack propagation speed.

After realizing the dependency of the microstructural aspects on the degradation processes, particularly the crack evolution, which causes the module's failure since it causes the separation of wires from metallization chips, a physicochemical-microstructural degradation model specific to upper metallic interconnection parts of semiconductor power devices was presented in the third chapter. This model was achieved by relating physicochemical-microstructural properties to the mechanical parameters of the CZM, which is already based on the physicochemical binding energy theory. The critical fracture stress parameter was linked to the grains' size, hardness, and yield strength. On the contrary, the critical fracture energy was linked to the grain's disorientation angles and texture, in addition to the surface and grain boundary energies. Consequently, the parameters of the CZM are calculated based on these constructed relationships. This new way of relating the physicochemical-microstructural features to the crack progress is the novelty of this work. At the end of this chapter, the way of introducing the physicochemical properties to microstructurally model the crack formation at the topside metallic interconnections was described. This modeling was achieved by inserting hexagons representing grains at the terminal edges of the wire-metallization contacts. These edges were assigned as contact pairs associated with localized CZM parameters in accordance with the observations of their local microstructural characteristics. In this way, the granular decohesion can be simulated by investigating the effects of microstructural parameters on crack formation.

Finally, in the last chapter, the previously presented CZM - physicochemical and microstructural relationships were expressed by simulating the crack evolution using the ANSYS APDL software.

Electrothermal-mechanical simulations were performed to model the damage at the wire-metallization interface in the SKIM63 module. The model's conditions were parameterized so that they have the same conditions as for aging tests done experimentally. These simulations allow us to see the temperature distribution in the module and quantify the amplitude of the deformations induced in the area of the wires and metallization chips when thermal stresses are applied. They also enable us to predict the cracks' formation process taking place at the wire-metallization interconnection zone. Simulations with different cycling conditions (different ΔT_j and t_{on}) were applied. It was primarily deduced that the maximal temperature concentrates at the wire-metallization contact. Such contacts are also the concentration center of stress. It was concluded that the crack initiates from the terminal edges of the wire in contact with the metallization. Cracks are first formed at the heel position, where it continues propagating inside the wire just above the metallization layer. The crack speed is faster at the heel than at the tip. Cracking at the heel edge mainly occurs during the power-on state (heating state), whereas at the tip, it mainly occurs during the power-off state (cooling phase). The same manner of cracks' formation is seen when only decreasing ΔT_j; however, the speed of cracks becomes slower. When increasing the t_{on} value with keeping the same ΔT_j, it was observed that debonding is slightly enhanced. The crack evolution results were afterward compared to the data of experimental aging tests performed under the same conditions to see the compatibility between the modeling approach followed in this work and that occurring in the real situation. The same crack's pathway was observed, by which it starts from the wire's terminal edges, initiates faster at the wire's heel than at the tip, and progresses inside the wire just above the metallization layer. The crack length evolution resulting in the simulations was then compared to that seen experimentally. It was observed that when looking at both experimental and simulation data, the crack evolution shows a fast crack initiation stage, and then its speed decreases when cycling advances. This crack evolution is different from that when being predicted using physical models such as Paris law.

Indeed, this newly presented methodology is so interesting since it directly reflects the effect of the physicochemical-microstructural properties of materials on the crack evolution. Some issues may be further developed to better express this methodology. It is so important to see whether the obtained experimental observations are valid at different stress conditions for the same IGBT module and other IGBT module types. It is also important to try applying this mixed fracture mechanics - physicochemical & microstructural approach at different stress conditions for the same IGBT module and other IGBT module types. Additionally, the analytical method presented in section #6 in the last chapter might be developed to benefit from it not only for confirming that the crack length resulting in the simulations is a good value, but also to be able to predict the crack length evolution upon cycling. This might be so interesting by which the crack evolution could be predicted after applying more cycles, which is difficult to be performed using these simulations.

As discussed in the final section of the last chapter, using reduced critical stress values remains the main limitation. As previously explained, this reduction was made to fasten the speed of the crack evolution and be able to see the crack progress from a few cycles. It is still essential to know the relation between reduced and real CZM parameters to estimate the simulation's accelerating factor (estimate the real crack growth speed). To avoid reducing the CZM elements, finding features that can smoothen the calculations in the simulations may be the solution. If this works, several things might be improved. The first one is that it becomes possible to use real CZM elements. Another outcome is that it might be feasible to perform a number of cycles near that in reality and not restricted to eight or ten cycles as in the current situation. Maybe more hexagons can also be added to see whether the crack continues from both edges and reaches the wire's bottom center. Moreover, a general trend for the evolution of the crack speed in all the stages of the crack evolution (including the advanced cycling phases) can be built in this case. Thus, the evolution of the crack speed upon cycling might be compared to that obtained experimentally. However, if the suggestion of finding features that smoothen the calculations does not work, it is then necessary to prove that upon using a certain reduced critical stress value, stress and strain distributions in addition to the debonding maps are representative of those in real situations upon aging the samples. Once these limitations are overcome, this simulation can be improved to be a 3D

simulation. The latter surely provides a better representation of the real degradations than two-dimensional representations.

Another suggestion to improve this methodology may be by using another software that enables us to directly import the EBSD data for healthy and cycled samples, and then apply the meshing on the wire-metallization components to simulate the amount of stress and strain generated caused by aging. This could be a very good way to simulate the microstructural evolutions and the crack progress using the aged samples themselves. For that, more samples can be aged and analyzed using a good-quality EBSD machine. Many improvements can be accomplished using this method, such as directly doing a 3D analysis and using real geometry, not a manually constructed one. Moreover, it is expected to have fewer time calculations because the sample will be analyzed at a specific moment, and there is no transient cycling as in the case of simulations. In this way, the CZM elements can be assigned to the edges of the grains, and then according to the calculated values of the CZM elements, the crack can be predicted at specific locations. This prediction is then compared to the crack evolution observed microstructurally using the EBSD technique for samples aged at more advanced stages. This methodology may also be beneficial to analyze more deeply and accurately the microstructural properties changing within the sample upon aging and relate their change to the stress and deformations generated. This analysis can finally be applied to several wires in several IGBT chips and see if the same tendency of microstructural changes and crack evolution is present.

REFERENCES

[AbSG05] A. Abdul-Baqi, P. J. G. Schreurs, and M. G. D. Geers, “Fatigue damage modeling in solder interconnects using a cohesive zone approach,” *Int. J. Solids Struct.*, vol. 42, no. 3–4, pp. 927–942, 2005.

[AMST15] H. Adachi, Y. Miyajima, M. Sato, and N. Tsuji, “Evaluation of dislocation density for 1100 aluminum with different grain size during tensile deformation by using in-situ X-ray diffraction technique,” *Mater. Trans.*, vol. 56, pp. 671–678, 2015.

[ACYL11] P. A. Agyakwa, M. R. Corfield, L. Yang, J. F. Li, V. M. F. Marques, and C. M. Johnson, “Microstructural evolution of ultrasonically bonded high purity Al wire during extended range thermal cycling,” *Microelectron. Reliab.*, vol. 51, pp. 406–415, 2011.

[AYAE16] P. Agyakwa, L. Yang, E. Arjmand, P. Evans, M. Corfield, and C. M. Johnson, “Damage Evolution in Al Wire Bonds Subjected to a Junction Temperature Fluctuation of 30 K,” *J. Electron. Mater.*, vol. 45, pp. 3659–3672, 2016.

[AkOg17] O. Akyildiz and T. O. Ogurtani, “Thermal Grooving by Surface Diffusion: a Review of Classical Thermo-Kinetics Approach,” *Hittite J. Sci. Eng.*, vol. 4, pp. 7–16, 2017.

[AlCr01] G. Alfano and M. A. Crisfield, “Finite element interface models for the delamination analysis of laminated composites: Mechanical and computational issues,” *Int. J. Numer. Methods Eng.*, vol. 50, pp. 1701–1736, 2001.

[AKGG14] D. Amram, L. Klinger, N. Gazit, H. Gluska, and E. Rabkin, “Grain boundary grooving in thin films revisited: The role of interface diffusion,” *Acta Mater.*, vol. 69, pp. 386–396, 2014.

[Ande05] T. L. Anderson, *Fracture mechanics-Fundamentals and applications*. CRC press, Taylor and Francis Group, ISBN, 2005.

[Ansy13] ANSYS® Mechanical APDL 15.0, *ANSYS Mechanical APDL Theory Reference*. 2013.

[Ansy13] ANSYS® Mechanical APDL 15.0, *ANSYS Mechanical APDL Verification Manual*. 2013.

[ArAJ14] E. Arjmand, P. A. Agyakwa, and C. M. Johnson, “Reliability of thick Al wire: A study of the effects of wire bonding parameters on thermal cycling degradation rate using non-destructive methods,” *Microelectron. Reliab.*, vol. 54, pp. 2006–2012, 2014.

[Arms87] R. W. Armstrong, “The cleavage strength of pre-cracked polycrystals,” *Eng. Fract. Mech.*, vol. 28, pp. 529–538, 1987.

[AwKh19] I. Z. Awan and A. Q. Khan, “Recovery, Recrystallization, and Grain-Growth,” *Chem. Soc. Pakistan*, vol. 41, p. 42, 2019.

[Bare62] G. I. Barenblatt, “The mathematical theory of equilibrium cracks in brittle fracture,” *Adv. Appl. Mech.*, vol. 7, pp. 55–129, 1962.

[BHLL08] R. Bayerer, T. Herrmann, T. Licht, J. Lutz, and M. Feller, “Model for power cycling lifetime of IGBT Modules - Various factors influencing lifetime,” *5th Int. Conf. Integr. Power Syst. CIPS*, pp. 1–6, 2008.

[BeFu17] B. Beausir and J.-J. Fundenberger, “Analysis Tools for Electron and X-ray diffraction, ATEX-software.” Université de Lorraine, Metz, 2017.

[BeRi92] G. E. Beltz and J. R. Rice, “Dislocation nucleation at metal-ceramic interfaces,” *Acta Metall. Mater.*, vol. 40, pp. S321–S331, 1992.

[BeSD13] L. Benabou, Z. Sun, and P. R. Dahoo, “A thermo-mechanical cohesive zone model for solder joint lifetime prediction,” *Int. J. Fatigue*, vol. 49, pp. 18–30, 2013.

[BERK09] T. R. Bieler, P. Eisenlohr, F. Roters, D. Kumar, D. E. Mason, M. A. Crimp, and D. Raabe, “The role of heterogeneous deformation on damage nucleation at grain boundaries in single phase metals,” *Int. J. Plast.*, vol. 25, pp. 1655–1683, 2009.

[BTAA18] S. Boudekhani-Abbas, K. Tirsatine, H. Azzeddine, B. Alili, A. L. Helbert, F. Brisset, T. Baudin, and D. Bradai, “Texture, microstructure and mechanical properties evolution in Fe-x (x = 36 and 48 wt.%) Ni alloy after accumulative roll bonding,” *18th Int. Conf. Textures Mater.*, vol. 375, p. 12034, 2018.

[BPKP16] M. Brincker, K. B. Pedersen, P. K. Kristensen, and V. Popok, “Passive thermal cycling of power diodes under controlled atmospheric conditions - effects on metallization degradation,” *9th Int. Conf. Integr. Power Electron. Syst.*, pp. 5–10, 2016.

[BWKP18] M. Brincker, T. Walter, P. K. Kristensen, and V. N. Popok, “Thermo-mechanically induced texture evolution and micro-structural change of aluminum metallization,” *J. Mater. Sci. Mater. Electron.*, vol. 29, pp. 3898–3904, 2018.

[BGHS15] M. S. Broll, U. Geissler, J. Höfer, S. Schmitz, O. Wittler, M. Schneider-Ramelow, and K. D. Lang, “Correlation between mechanical properties and microstructure of different aluminum wire qualities after ultrasonic bonding,” *Microelectron. Reliab.*, vol. 55, pp. 1855–1860, 2015.

[BGHS15] M. S. Broll, U. Geissler, J. Höfer, S. Schmitz, O. Wittler, and K. D. Lang, “Microstructural evolution of ultrasonic-bonded aluminum wires,” *Microelectron. Reliab.*, vol. 55, pp. 961–968, 2015.

[Buhr18] S. Buhrkal-Donau, “Comparative study of wire bond degradation under power and mechanical cycling tests,” Aalborg University, 2018.

[CaRe18] W. D. Callister and D. G. Rethwisch, *Materials science and engineering: an introduction*, vol. 9. New York: Wiley, 2018.

[Care95] R. Carel, “Grain growth and texture evolution in thin films,” PhD diss., Massachusetts Institute of Technology, 1995.

[ChKC18] S. Chakraborty, P. Kumar, and A. Choudhury, “Phase-field modeling of grain-boundary grooving and migration under electric current and thermal gradient,” *Acta Mater.*, vol. 153, pp. 377–390, 2018.

[CBJI16] U. M. Choi, F. Blaabjerg, S. Jørgensen, F. Iannuzzo, H. Wang, C. Uhrenfeldt, and S. Munk-Nielsen, “Power cycling test and failure analysis of molded Intelligent Power IGBT Module under different temperature swing durations,” *Microelectron. Reliab.*, vol. 64, pp. 403–408, 2016.

[ChBJ17] U. M. Choi, F. Blaabjerg, and S. Jørgensen, “Study on Effect of Junction Temperature Swing Duration on Lifetime of Transfer Molded Power IGBT Modules,” *IEEE Trans. Power Electron.*, vol. 32, pp. 6434–6443, 2017.

[Choi16] U. Choi, “Studies on Igbt Module To Improve the Reliability of Power Electronic Systems,” PhD diss., Aalborg university, 2016.

[Chu96]E. C. Chu, “Temperature-Dependent Yield Properties of Passivated Aluminum Thin Films on Silicon

Wafers," PhD diss., Massachusetts Institute of Technology, 1996.

[Ciap02] M. Ciappa, "Selected failure mechanisms of modern power modules," *Microelectron. Reliab.*, vol. 42, pp. 653–667, 2002.

[CiFi00] M. Ciappa and W. Fichtner, "Lifetime prediction of IGBT modules for traction applications," *IEEE Int. Reliab. Phys. Symp. Proc.*, pp. 210–216, 2000.

[CiMa96] M. Ciappa and P. Malberti, "Plastic-strain of aluminium interconnections during pulsed operation of IGBT multichip modules," *Qual. Reliab. Eng. Int.*, vol. 12, pp. 297–303, 1996.

[CoSe08] V. R. Coffman and J. P. Sethna, "Grain boundary energies and cohesive strength as a function of geometry," *Phys. Rev. B - Condens. Matter Mater. Phys.*, vol. 77, pp. 144111–144121, 2008.

[CoLa70] A. Coucoulas and T. B. Laboratories, "Hot Work Thermosonic Bonding , Facilitating Metal Flow by Restoration Processes," *IEEE Electron. Components Conf*, pp. 549–556, 1970.

[Davo17] K. Davoudi, "Temperature dependence of the yield strength of aluminum thin films: Multiscale modeling approach," *Scr. Mater.*, vol. 131, pp. 63–66, 2017.

[DéRF15] C. Déprés, C. Robertson, and M. Fivel, "3D Discrete Dislocation Dynamics Investigations of Fatigue Crack Initiation and Propagation," *AerospaceLab*, no. 9, pp. 1–8, 2015.

[DSWN19] K. Dharmesh, I. Sridhar, W. Wei, and S. Narasimalu, "Effect of Surface Mechanical Treatments on the Microstructure-Property-Performance of Engineering Alloys," *Materials (Basel).*, vol. 12, p. 41, 2019.

[DIKD20] N. Dornic, A. Ibrahim, Z. Khatir, N. Degrenne, S. Mollov, and D. Ingrosso, "Analysis of the aging mechanism occurring at the bond-wire contact of IGBT power devices during power cycling," *Microelectron. Reliab.*, vol. 114, p. 113873, 2020.

[DIKT18] N. Dornic, A. Ibrahim, Z. Khatir, S. H. Tran, J. P. Ousten, J. Ewanchuk, and S. Mollov, "Analysis of the degradation mechanisms occurring in the topside interconnections of IGBT power devices during power cycling," *Microelectron. Reliab.*, vol. 88–90, pp. 462–469, 2018.

[Dorn19] N. Dornic, "Élaboration et comparaison de deux modèles de durée de vie des fils d'interconnexion des modules de puissance, l'un basé sur les déformations et l'autre sur les dégradations," PhD diss., Université Paris Saclay (COmUE), 2019.

[DoHB93] A. L. Dowson, M. D. Halliday, and C. J. Beevers, "In-situ SEM studies of short crack growth and crack closure in a near-alpha Ti alloy," *Mater. Des.*, vol. 14, pp. 57–59, 1993.

[DrKo03] U. Drofenik and J. W. Kolar, "Teaching thermal design of power electronic systems with Web-based interactive educational software," *18th Annu. IEEE Appl. Power Electron. Conf. Expo.*, vol. 2, pp. 1029–1036, 2003.

[Dugd60] D. S. Dugdale, "Yielding of steel sheets containing slits," *J. Mech. Phys. Solids*, vol. 8, pp. 100–104, 1960.

[DuWA07] F. P. E. Dunne, A. J. Wilkinson, and R. Allen, "Experimental and computational studies of low cycle fatigue crack nucleation in a polycrystal," *Int. J. Plast.*, vol. 23, pp. 273–295, 2007.

[DKCN15] C. Durand, M. Klingler, D. Coutellier, and H. Naceur, "Study of fatigue failure in Al-chip-metallization during power cycling," *Eng. Fract. Mech.*, vol. 138, pp. 127–145, 2015.

[Dura15] C. Durand, "Etude thermomécanique expérimentale et numérique d'un module

d'électronique de puissance soumis à des cycles actifs de puissance," PhD diss., Université de Valenciennes et du Hainaut-Cambresis, 2015.

[Dush71] S. Z. Dushkes, "A Design Study of Ultrasonic Bonding Tips," *IBM J. Res. Dev.*, vol. 15, pp. 230–235, 1971.

[FZJR16] F. Farukh, L. G. Zhao, R. Jiang, P. Reed, D. Proprentner, and B. A. Shollock, "Realistic microstructure-based modelling of cyclic deformation and crack growth using crystal plasticity," *Comput. Mater. Sci.*, vol. 111, pp. 395–405, 2016.

[FeRR18] F. Feyissa, D. Ravi Kumar, and P. N. Rao, "Characterization of Microstructure, Mechanical Properties and Formability of Cryorolled AA5083 Alloy Sheets," *J. Mater. Eng. Perform.*, vol. 27, pp. 1614–1627, 2018.

[FrAs73] H. J. Frost and M. F. Ashby, *A Second Report on Deformation Mechanism Maps*. HARVARD UNIV CAMBRIDGE MA DIV OF ENGINEERING AND APPLIED PHYSICS, 1973.

[GZNT99] H. Gao, L. Zhang, W. D. Nix, C. V Thompson, and E. Arzt, "Crack-like grain-boundary diffusion wedges in thin metal films," *Acta Mater.*, vol. 47, pp. 2865–2878, 1999.

[GeMu93] F. Genin and W. Mullins, "The effect of stress on grain boundary grooving," *Acta Metall. Mater.*, vol. 41, pp. 3541–3547, 1993.

[GeKK92] D. Gerth, D. Katzer, and M. Krohn, "Study of the thermal behaviour of thin aluminium alloy films," *Thin Solid Films*, vol. 208, pp. 67–75, 1992.

[GiPM14] G. Giuliese, A. Pirondi, and F. Moroni, "A Cohesive Zone Model for Three-dimensional Fatigue Debonding/Delamination," *Procedia Mater. Sci.*, vol. 3, pp. 1473–1478, 2014.

[GöFa10] C. Göbl and J. Faltenbacher, "Low temperature sinter technology die attachment for power electronic applications," *6th Int. Conf. Integr. Power Electron. Syst. CIPS*, pp. 16–18, 2010.

[GSGL10] J. Goehre, M. Schneider-Ramelow, U. Geißler, and K. D. Lang, "Interface degradation of Al heavy wire bonds on power semiconductors during active power cycling measured by the shear test," *6th Int. Conf. Integr. Power Electron. Syst. CIPS*, pp. 1–6, 2010.

[Gour02] A. F. Gourgues, "Electron backscatter diffraction and cracking," *Mater. Sci. Technol.*, vol. 18, pp. 119–133, 2002.

[GoSø16] S. Goutianos and B. F. Sørensen, "The application of J integral to measure cohesive laws under large-scale yielding," *Eng. Fract. Mech.*, vol. 155, pp. 145–165, 2016.

[GSSS11] S. Goyal, K. Srinivasan, G. Subbarayan, and T. Siegmund, "Estimating the Yield Strength of Thin Metal Films Through Elastic-Plastic Buckling-Induced Debonding," *IEEE Trans. Device Mater. Reliab.*, vol. 11, pp. 358–361, 2011.

[GoJD04] V. K. Goyal, E. R. Johnson, and C. G. Dávila, "Irreversible constitutive law for modeling the delamination process using interfacial surface discontinuities," *Compos. Struct.*, vol. 65, no. 3–4, pp. 289–305, 2004.

[Grif21] A. A. Griffith, *The phenomena of rupture and flow in solids*, vol. 221. Philosophical Transactions of the Royal Society of London, 1921.

[Gumb99] P. Gumbsch, "Atomistic modelling of diffusion-controlled interfacial decohesion," *Mater. Sci. Eng. A*, vol. 260, pp. 72–79, 1999.

[GuLe19] M. N. Gussev and K. J. Leonard, “In situ SEM-EBSD analysis of plastic deformation mechanisms in neutron-irradiated austenitic steel,” *J. Nucl. Mater.*, vol. 517, pp. 45–56, 2019.

[Hall51]E. O. Hall, “The deformation and ageing of mild steel: II Characteristics of the Lüders deformation,” *Proc. Phys. Soc. Sect. B*, vol. 64, pp. 742–747, 1951.

[HaKI18] T. Hamieh, Z. Khatir, and A. Ibrahim, “Analytical Solutions to the Problem of the Grain Groove Profile,” *Nanosci. Technol. Open Access*, vol. 5, pp. 1–10, 2018.

[HaKS03] T. Hanlon, Y. N. Kwon, and S. Suresh, “Grain size effects on the fatigue response of nanocrystalline metals,” *Scr. Mater.*, vol. 49, pp. 675–680, 2003.

[Hans04] N. Hansen, “Hall-petch relation and boundary strengthening,” *Scr. Mater.*, vol. 51, pp. 801–806, 2004.

[Harm10] G. Harman, *Wire Bonding in Microelectronics*. McGraw-Hill Education, 2010.

[HSPK91] D. O. Harris, R. A. Sire, C. F. Popelar, M. F. Kanninen, D. L. Davidson, L. B. Duncan, J. M. Kallis, D. W. Buechler, P. G. Backes, and F. Reizman, “Fracture Mechanics Life Prediction For Microscale Components – With Application to Wire Bonding,” *29th Annu. Proc. Reliab. Physics. IEEE*, pp. 35–43, 1991.

[HaGo71] G. C. Hasson and C. Goux, “Interfacial energies of tilt boundaries in aluminium. Experimental and theoretical determination,” *Scr. Metall.*, vol. 5, pp. 889–894, 1971.

[Häus13] S. Häuser, *SKiM® 63/93 Technical Explanations*, no. October. 2013, pp. 1–43.

[HePD10] W. Heinz, R. Pippan, and G. Dehm, “Investigation of the fatigue behavior of Al thin films with different microstructure,” *Mater. Sci. Eng. A*, vol. 527, pp. 7757–7763, 2010.

[HJNS97] M. Held, P. Jacob, G. Nicoletti, P. Scacco, and M. H. Poech, “Fast power cycling test for IGBT modules in traction application,” *Proc. Int. Conf. Power Electron. Drive Syst.*, vol. 1, pp. 425–430, 1997.

[HJNS99] M. Held, P. Jacob, G. Nicoletti, P. Scacco, and M. H. Poech, “Fast power cycling test for insulated gate bipolar transistor modules in traction application,” *Int. J. Electron.*, vol. 86, pp. 1193–1204, 1999.

[Hu74] H. Hu, “Texture of Metals.,” *Texture*, vol. 1, pp. 233–258, 1974.

[HLBP14] W. Huai, M. Liserre, F. Blaabjerg, P. De Place Rimmen, J. B. Jacobsen, T. Kvisgaard, and J. Landkildehus, “Transitioning to physics-of-failure as a reliability driver in power electronics,” *IEEE J. Emerg. Sel. Top. Power Electron.*, vol. 2, pp. 97–114, 2014.

[Huss97] K. Hussian, “Short fatigue crack behaviour and analytical models: A review,” *Eng. Fract. Mech.*, vol. 58, pp. 327–354, 1997.

[JaMo83] M. R. James and W. L. Morris, “Fatigue induced changes in surface residual stress,” vol. 17, pp. 1101–1104, 1983.

[JiSI99] M. Jin, E. Shimada, and Y. Ikuma, “Grain boundary grooving by surface diffusion in SrTiO3 bicrystal,” *J. Mater. Res.*, vol. 14, pp. 2548–2553, 1999.

[JoSu96] M. Jono and A. Sugeta, “Crack closure and effect of load variation on small fatigue crack growth behaviour,” *Fatigue Fract. Eng. Mater. Struct.*, vol. 19, pp. 165–174, 1996.

[KaSc10] S. Kalpakjian and S. Schmid, *Mechanical Behavior, Testing, and Manufacturing Properties of*

Materials. Manufacturing Engineering & Technology, 2010.

[KPWD11] K. Kanert, R. Pufal, O. Wittler, R. Dudek, and M. Bouazza, "Modelling of Metal Degradation in Power Devices under Active Cycling Conditions," *12th Intl. Conf. Therm. Mech. Multi-Physics Simul. Exp. Microelectron. Microsystems*, pp. 1–6, 2011.

[KaHo97] Y. S. Kang and P. S. Ho, "Thickness dependent mechanical behavior of submicron aluminum films," *J. Electron. Mater.*, vol. 26, pp. 805–813, 1997.

[KaCY03] G. Kaptay, G. Csicsovszki, and M. S. Yaghmaee, "An absolute scale for the cohesion energy of pure metals," *Mater. Sci. Forum*, vol. 414–415, pp. 235–240, 2003.

[Kato14] M. Kato, "Hall-petch relationship and dislocation model for deformation of ultrafine-grained and nanocrystalline metals," *Mater. Trans.*, vol. 55, pp. 19–24, 2014.

[KePi16] L. A. I. Kestens and H. Pirgazi, "Texture formation in metal alloys with cubic crystal structures," *Mater. Sci. Technol. (United Kingdom)*, vol. 32, pp. 1303–1315, 2016.

[KWBS12] G. Khatibi, B. Weiss, J. Bernardi, and S. Schwarz, "Microstructural investigation of interfacial features in Al wire bonds," *J. Electron. Mater.*, vol. 41, pp. 3436–3446, 2012.

[KIKT08] S. Kobayashi, T. Inomata, H. Kobayashi, S. Tsurekawa, and T. Watanabe, "Effects of grain boundary- and triple junction-character on intergranular fatigue crack nucleation in polycrystalline aluminum," *J. Mater. Sci.*, vol. 43, pp. 3792–3799, 2008.

[KUSM98] J. Koike, S. Utsunomiya, Y. Shimoyama, K. Maruyama, and H. Oikawa, "Thermal cycling fatigue and deformation mechanism in aluminum alloy thin films on silicon," *J. Mater. Res.*, vol. 13, pp. 3256–3264, 1998.

[KoKS15] I. F. Kovačević-Badstuebner, J. W. Kolar, and U. Schilling, "Modelling for the lifetime prediction of power semiconductor modules," *Reliab. Power Electron. Convert. Syst. 5*, pp. 103–140, 2015.

[KoDK10] I. F. Kovačević, U. Drofenik, and J. W. Kolar, "New physical model for lifetime estimation of power modules," *IEEE Int. Power Electron. Conf.*, pp. 2106–2114, 2010.

[KCMF09] H. Kubo, M. Ciappa, T. Masunaga, and W. Fichtner, "Multiscale simulation of aluminum thin films for the design of highly-reliable MEMS devices," *Microelectron. Reliab.*, vol. 49, pp. 1278–1282, 2009.

[LCRX17] W. Lai, M. Chen, L. Ran, S. Xu, N. Jiang, X. Wang, O. Alatise, and P. Mawby, "Experimental Investigation on the Effects of Narrow Junction Temperature Cycles on Die-Attach Solder Layer in an IGBT Module," *IEEE Trans. Power Electron.*, vol. 32, pp. 1431–1441, 2017.

[Lang66] B. Langenecker, "Effects of Ultrasound on Deformation Characteristics of Metals," *IEEE Trans. Sonics Ultrason.*, vol. 13, pp. 1–8, 1966.

[LHGS02] M. Legros, K. J. Hemker, A. Gouldstone, S. Suresh, R. M. Keller-Flaig, and E. Arzt, "Microstructural evolution in passivated Al films on Si substrates during thermal cycling," *Acta Mater.*, vol. 50, pp. 3435–3452, 2002.

[LeCG09] M. Legros, M. Cabié, and D. S. Gianola, "In situ deformation of thin films on substrates," *Microsc. Res. Tech.*, vol. 72, pp. 270–283, 2009.

[LeRe70] M. Levy and M. Regnier, "Mesure des énergies de surface," *J. Phys. Colloq.*, vol. 31, p. pp.C1-159-C1-173, 1970.

[Li17] J. LI, “The contribution of the grain boundary engineering to the problem of intergranular hydrogen embrittlement,” PhD diss., Université de La Rochelle, 2017.

[LiKi20] J. Li and C. Kirchlechner, “Does the stacking fault energy affect dislocation multiplication?,” *Mater. Charact.*, vol. 161, p. 110136, 2020.

[LiBB05] S. Li, I. J. Beyerlein, and M. A. M. Bourke, “Texture formation during equal channel angular extrusion of fcc and bcc materials: Comparison with simple shear,” *Mater. Sci. Eng. A*, vol. 394, pp. 66–77, 2005.

[LHHO09] Z. Li, C. Hou, M. Huang, and C. Ouyang, “Strengthening mechanism in micro-polycrystals with penetrable grain boundaries by discrete dislocation dynamics simulation and Hall-Petch effect,” *Comput. Mater. Sci.*, vol. 46, pp. 1124–1134, 2009.

[LiLD05] J. Lin, Y. Liu, and T. A. Dean, “A review on damage mechanisms, models and calibration methods under various deformation conditions,” *Int. J. Damage Mech.*, vol. 14, pp. 299–319, 2005.

[LiPo18] D. Liu and D. J. Pons, “Crack propagation mechanisms for creep fatigue: A consolidated explanation of fundamental behaviours from initiation to failure,” *Metals (Basel).*, vol. 8, p. 623, 2018.

[Lloy98] J. Lloyd, “Reliability of Copper Metallization,” *Lloyd Technol. Assoc. Inc*, p. 20, 1998.

[LCLH07] W. Loh, M. Corfield, H. Lu, S. Hogg, T. Tilford, and C. M. Johnson, “Wire Bond Reliability for Power Electronic Modules - Effect of Bonding Temperature,” *Int. Conf. Therm. Mech. Multi-Physics Simul. Exp. Microelectron. Micro-Systems*, p. 6, 2007.

[LPHZ18] P. Lohmuller, L. Peltier, A. Hazotte, J. Zollinger, P. Laheurte, and E. Fleury, “Variations of the elastic properties of the CoCrFeMnNi high entropy alloy deformed by groove cold rolling,” *Materials (Basel).*, vol. 11, pp. 1–14, 2018.

[LSSD10] J. Lutz, H. Schlangenotto, U. Scheuermann, and R. De Doncker, *Semiconductor Power Devices, Physics, Characteristics, Reliability*. 2010.

[Mack58] J. K. Mackenzie, “Second paper on statistics associated with the random disorientation of cubes,” *Biometrika*, vol. 45, pp. 229–240, 1958.

[MaDo66] S. S. Manson and T. J. Dolan, “Thermal Stress and Low-Cycle Fatigue,” *J. Appl. Mech.*, vol. 33, p. 957, 1966.

[Mart07] P. A. Martin, “Thermal grooving by surface diffusion: Mullins revisited and extended to multiple grooves,” *Q. Appl. Math.*, vol. 67, pp. 125–136, 2007.

[MLLD14] D. Martineau, C. Levade, M. Legros, P. Dupuy, and T. Mazeaud, “Universal mechanisms of Al metallization ageing in power MOSFET devices,” *Microelectron. Reliab.*, vol. 54, pp. 2432–2439, 2014.

[MaUe06] T. Matsunaga and Y. Uegai, “Thermal Fatigue Life Evaluation of Aluminum Wire Bonds,” *Electron. Syst. Technol. Conf.*, vol. 2, pp. 726–731, 2006.

[MPBB00] M. Mayer, O. Paul, D. Bolliger, and H. Baltes, “Integrated temperature microsensors for characterization and optimization of thermosonic ball bonding process,” *IEEE Trans. Components Packag. Technol.*, vol. 23, pp. 393–398, 2000.

[MeVN12] H. Medjahed, P. E. Vidal, and B. Nogarede, “Thermo-mechanical stress of bonded wires used in high power modules with alternating and direct current modes,” *Microelectron. Reliab.*, vol. 52, pp. 1099–1104, 2012.

[MKSG08] L. Merkle, T. Kaden, M. Sonner, A. Gademann, J. Turki, C. Dresbach, and M. Petzold, “Mechanical fatigue properties of heavy aluminium wire bonds for power applications,” *Proc. - 2008 2nd Electron. Syst. Technol. Conf. ESTC*, pp. 1363–1367, 2008.

[MePP07] M. Mermet-Guyennet, X. Perpiñá, and M. Piton, “Revisiting power cycling test for better life-time prediction in traction,” *Microelectron. Reliab.*, vol. 47, pp. 1690–1695, 2007.

[Mlik20] M. Mlikota, “Multiscale Modelling and Simulation of Metal Fatigue and its Applications,” PhD diss., Faculty of Energy, Process and Biotechnology at the University of Stuttgart, 2020.

[MöBi14] J. J. Möller and E. Bitzek, “Fracture toughness and bond trapping of grain boundary cracks,” *Acta Mater.*, vol. 73, pp. 1–11, 2014.

[MoOl76] A. Motta and D. Olander, “Chapter 8 Grains and Grain Boundaries,” *Light. React. Mater.*, 1976.

[MoGS16] M. F. S. F. de Moura, J. P. M. Gonçalves, and F. G. A. Silva, “A new energy based mixed-mode cohesive zone model,” *Int. J. Solids Struct.*, vol. 102–103, pp. 112–119, 2016.

[Mour12] A. Mouritz, *Strengthening of metal alloys*. Elsevier, 2012.

[Mull61] W. W. Mullins, “Theory of linear facet growth during thermal etching,” *Philos. Mag.*, vol. 6, pp. 1313–1341, 1961.

[MRCL06] D. A. Murdock, J. E. Ramos Torres, J. J. Connors, and R. D. Lorenz, “Active thermal control of power electronic modules,” *IEEE Trans. Ind. Appl.*, vol. 42, no. 2, pp. 552–558, 2006.

[NaNS00] Y. Nagatomo, T. Nagase, and S. Shimamura, “FEM analysis of thermal cycle properties of the substrates for power modules,” *J. Japan Inst. Electron. Packag.*, vol. 3, pp. 330–334, 2000.

[Need87] A. Needleman, “A continuum model for void nucleation by inclusion debonding,” *J. Appl. Mech. Trans. ASME*, vol. 54, pp. 525–531, 1987.

[Need90] A. Needleman, “An analysis of tensile decohesion along an interface,” *J. Mech. Phys. Solids*, vol. 38, pp. 289–324, 1990.

[Need90] A. Needleman, “An analysis of decohesion along an imperfect interface,” *Int. J. Fract.*, vol. 42, pp. 21–40, 1990.

[NKZG16] S. Nik, P. Krantz, L. Zeng, T. Greibe, H. Pettersson, S. Gustafsson, P. Delsing, and E. Olsson, “Correlation between Al grain size, grain boundary grooves and local variations in oxide barrier thickness of Al/AlOx/Al tunnel junctions by transmission electron microscopy,” *Springer Plus*, vol. 5, pp. 1067–1074, 2016.

[NoLa69] K. C. Norris and A. H. Landzberg, “Reliability of Controlled Collapse Interconnections,” *IBM J. Res. Dev.*, vol. 13, pp. 266–271, 1969.

[NyNa13] D. Nyung and H. Nam, “Recrystallization Textures of Metals and Alloys,” *Recent Dev. Study Recryst.*, pp. 3–59, 2013.

[OnKS00] J. Onuki, M. Koizumi, and M. Suwa, “Reliability of thick Al wire bonds in IGBT modules for traction motor drives,” *IEEE Trans. Adv. Packag.*, vol. 23, pp. 108–112, 2000.

[PaEr63] P. Paris and F. Erdogan, “A critical analysis of crack propagation laws,” *J. Basic Eng.*, vol. 85, pp. 528–533, 1963.

[PaPa11] K. Park and G. H. Paulino, “Cohesive zone models: A critical review of traction-separation relationships across fracture surfaces,” *Appl. Mech. Rev.*, vol. 64, p. 20, 2011.

[PNSS15] S. Park, S. Nagao, T. Sugahara, and K. Suganuma, “Heel crack propagation mechanism of cold-rolled Cu/Al clad ribbon bonding in harsh environment,” *J. Mater. Sci. Mater. Electron.*, vol. 26, no. 9, pp. 7277–7289, 2015.

[PBSP17] A. Patra, J. E. Bates, J. Sun, and J. P. Perdew, “Properties of real metallic surfaces: Effects of density functional semilocality and van der Waals nonlocality,” *Proc. Natl. Acad. Sci. U. S. A.*, vol. 114, pp. E9188–E9196, 2017.

[PaCP12] J. De Paula Martins, A. L. M. De Carvalho, and A. F. Padilha, “Texture analysis of cold rolled and annealed aluminum alloy produced by twin-roll casting,” *Mater. Res.*, vol. 15, pp. 97–102, 2012.

[PaTy08] E. J. Pavlina and C. J. Van Tyne, “Correlation of Yield strength and Tensile strength with hardness for steels,” *J. Mater. Eng. Perform.*, vol. 17, pp. 888–893, 2008.

[PeJi09]M. Pecht and Jie Gu, “Physics-of-failure-based prognostics for electronic products,” *Trans. Inst. Meas. Control*, vol. 31, pp. 309–322, 2009.

[PKPU17] K. B. Pedersen, P. K. Kristensen, K. Pedersen, C. Uhrenfeldt, and S. Munk-Nielsen, “Vce as early indicator of IGBT module failure mode,” *IEEE Int. Reliab. Phys. Symp. Proc.*, pp. 1–6, 2017.

[PØGP15] K. B. Pedersen, L. H. Østergaard, P. Ghimire, V. Popok, and K. Pedersen, “Degradation mapping in high power IGBT modules using four-point probing,” *Microelectron. Reliab.*, vol. 55, pp. 1196–1204, 2015.

[PØKG16] K. B. Pedersen, L. H. Østergaard, P. K. Kristensen, P. Ghimire, V. N. Popok, and K. Pedersen, “Degradation evolution in high power IGBT modules subjected to sinusoidal current load,” *J. Mater. Sci. Mater. Electron.*, vol. 27, pp. 1938–1945, 2016.

[Petc53] N. Petch, “The cleavage strength of polycrystals,” *J. iron steel Inst.*, vol. 174, pp. 25–28, 1953.

[Piet10]S. Pietranico, “Analyse de matériaux pour la modélisation des mécanismes de défaillance dans les modules électroniques de puissance,” PhD diss., Ecole normale supérieure de Cachan, 2010.

[PLPB11] S. Pietranico, S. Lefebvre, S. Pommier, M. Berkani Bouaroudj, and S. Bontemps, “A study of the effect of degradation of the aluminium metallization layer in the case of power semiconductor devices,” *Microelectron. Reliab.*, vol. 51, pp. 1824–1829, 2011.

[QHHL04] S. Qu, Y. Huang, H. H. Jiang, C. Liu, P. D. Wu, and K. C. Hwang, “Fracture analysis in the conventional theory of mechanism-based strain gradient (CMSG) plasticity,” *Int. J. Fract.*, vol. 129, no. 3, pp. 199–220, 2004.

[RaKS00] E. Rabkin, L. Klinger, and V. Semenov, “Grain boundary grooving at the singular surfaces,” *Acta Mater.*, vol. 48, pp. 1533–1540, 2000.

[Raim61] S. Raimes, *The wave mechanics of electrons in metals*, vol. 6. North-Holland Publishing Company, 1961.

[RaSW00] S. Ramminger, N. Seliger, and G. Wachutka, “Reliability model for Al wire bonds subjected to heel crack failures,” *Microelectron. Reliab.*, vol. 40, pp. 1521–1525, 2000.

[RaTW98] S. Ramminger, P. Türkes, and G. Wachutka, “Crack mechanism in wire bonding joints,” *Microelectron. Reliab.*, vol. 38, pp. 1301–1305, 1998.

[RMTW99] S. Ramminger, G. Mitic, P. Türkes, and G. Wachutka, “Thermo-mechanical simulation of wire bonding joints in power modules,” *TechConnect Briefs*, vol. Technical, pp. 483–486, 1999.

[RaRa88] V. Randle and B. Ralph, “Grain boundary structure and mechanical properties,” *Rev. Phys. appliquée*, vol. 23, pp. 501–512, 1988.

[RaHP13] G. B. Rathmayr, A. Hohenwarter, and R. Pippan, “Influence of grain shape and orientation on the mechanical properties of high pressure torsion deformed nickel,” *Mater. Sci. Eng. A*, vol. 560, pp. 224–231, 2013.

[Rhea63] G. E. Rhead, “Surface self-diffusion and faceting on silver,” *Acta Metall.*, vol. 11, pp. 1035–1042, 1963.

[RiSa12] S. Ri and M. Saka, “Diffusion-fatigue interaction effect on hillock formation in aluminum thin films under thermal cycle testing,” *Mater. Lett.*, vol. 79, pp. 139–141, 2012.

[RiBe94] J. R. Rice and G. E. Beltz, “The activation energy for dislocation nucleation at a crack,” *J. Mech. Phys. Solids*, vol. 42, pp. 333–360, 1994.

[Rive06] G. a. Riveros, “Numerical Evaluation of Stress Intensity Factors (Ki) J-Integral Approach,” 2006.

[RGTN18] J. A. Rodríguez Martin, C. Gutiérrez, M. Torrijos, and N. Nanos, “Wood and bark of Pinus halepensis as archives of heavy metal pollution in the Mediterranean Region,” *Environ. Pollut.*, vol. 239, pp. 438–447, 2018.

[RoSi03] K. L. Roe and T. Siegmund, “An irreversible cohesive zone model for interface fatigue crack growth simulation,” *Eng. Fract. Mech.*, vol. 70, pp. 209–232, 2003.

[RoFS81] J. H. Rose, J. Ferrante, and J. R. Smith, “Universal binding energy curves for metals and bimetallic interfaces,” *Phys. Rev. Lett.*, vol. 47, pp. 675–678, 1981.

[RoSF83] J. H. Rose, J. R. Smith, and J. Ferrante, “Universal features of bonding in metals,” *Phys. Rev. B*, vol. 28, pp. 1835–1845, 1983.

[REHT10] F. Roters, P. Eisenlohr, L. Hantcherli, D. D. Tjahjanto, T. R. Bieler, and D. Raabe, “Overview of constitutive laws, kinematics, homogenization and multiscale methods in crystal plasticity finite-element modeling: Theory, experiments, applications,” *Acta Mater.*, vol. 58, pp. 1152–1211, 2010.

[RBDL18] R. Ruffilli, M. Berkani, P. Dupuy, S. Lefebvre, and Y. Weber, “Aluminum metallization and wire bonding aging in power MOSFET modules,” *Mater. Today Proc.*, pp. 14641–14651, 2018.

[Ruff17] R. Ruffilli, “Fatigue mechanisms in Al-based metallizations in power MOSFETs,” PhD diss., Université Paul Sabatier-Toulouse III, 2017.

[RSSQ18] S. S. Rui, Y. B. Shang, Y. Su, W. Qiu, L. S. Niu, H. J. Shi, S. Matsumoto, and Y. Chuman, “EBSD analysis of cyclic load effect on final misorientation distribution of post-mortem low alloy steel: A new method for fatigue crack tip driving force prediction,” *Int. J. Fatigue*, vol. 113, pp. 264–276, 2018.

[SaDH11] A. Saai, S. Dumoulin, and O. S. Hopperstad, “Influence of texture and grain shape on the yield surface in aluminium sheet material subjected to large deformations,” *AIP Conf. Proc.*, vol. 1353, pp. 85–90, 2011.

[SKSM20] H. Salama, J. Kundin, O. Shchyglo, V. Mohles, K. Marquardt, and I. Steinbach, “Role of inclination dependence of grain boundary energy on the microstructure evolution during grain growth,” *Acta*

Mater., vol. 188, pp. 641–651, 2020.

[SaMS11] M. D. Sangid, H. J. Maier, and H. Sehitoglu, "The role of grain boundaries on fatigue crack initiation - An energy approach," *Int. J. Plast.*, vol. 27, pp. 801–821, 2011.

[SaMS11] M. D. Sangid, H. J. Maier, and H. Sehitoglu, "A physically based fatigue model for prediction of crack initiation from persistent slip bands in polycrystals," *Acta Mater.*, vol. 59, pp. 328–341, 2011.

[Sant69] C. J. Santoro, "Thermal Cycling and Surface Reconstruction in Aluminum Thin Films," *J. Electrochem. Soc. Solid State Sci.*, vol. 116, pp. 361–364, 1969.

[Scha73] H. Schafft, "Testing and fabrication of wire-bond electrical connections—A comprehensive survey," *Microelectron. Reliab.*, vol. 12, pp. 31–49, 1973.

[Seah79] M. P. Seah, "Adsorption-induced interface decohesion," *Pergamon Press*, vol. 28, pp. 955–962, 1979.

[Semi17] SEMIKRON, *SKiM® 63 Datasheet*. 2017, pp. 1–6.

[ShAl00] J. F. Shackelford and W. Alexander, *Materials Science and Engineering Handbook*. CRC Press Third Edition, 2000.

[SFHR13] V. Smet, F. Forest, J. J. Huselstein, A. Rashed, and F. Richardeau, "Evaluation of Vce monitoring as a real-time method to estimate aging of bond wire-IGBT modules stressed by power cycling," *IEEE Trans. Ind. Electron.*, vol. 60, pp. 2760–2770, 2013.

[SoAT17] P. B. Sob, A. A. Alugongo, and T. B. Tengen, "Cracks Propagation as a Function of Grain Size Variants on Nanocrystalline Materials' Yield Stress Produced by Accumulative Roll-Bonding," *Adv. Mater. Phys. Chem.*, vol. 7, pp. 58–69, 2017.

[SoLi65] R. Soloff and S. Linsley, "Sonic Method of Welding Thermoplastic Parts," U.S. Patent No. 3,224,916, 1965

[SuJi12] C. T. Sun and Z.-H. Jin, *Cohesive Zone Model*. 'Fracture Mechanics' Elsevier, 2012.

[Sze08] S. M. Sze, *Semiconductor devices, physics and technology*. John wiley & sons, 2008.

[TKTD15] X. Tan, Y. Kok, Y. J. Tan, M. Descoins, D. Mangelinck, S. B. Tor, K. F. Leong, and C. K. Chua, "Graded microstructure and mechanical properties of additive manufactured Ti-6Al-4V via electron beam melting," *Acta Mater.*, vol. 97, pp. 1–16, 2015.

[Thom85] C. V. Thompson, "Secondary grain growth in thin films of semiconductors: Theoretical aspects," *J. Appl. Phys.*, vol. 58, pp. 763–772, 1985.

[Thom00] C. V Thompson, "Structure Evolution During Processing of Polycrystalline Films," *Mater. Sci.*, vol. 30, pp. 159–190, 2000.

[Thor77] J. A. Thornton, "High Rate Thick Film Growth.," *Annu. Rev. Mater. Sci.*, vol. 7, pp. 239–260, 1977.

[TXRW16] R. Tran, Z. Xu, B. Radhakrishan, D. Winston, W. Sun, K. Persson, and S. Ping Ong, "Surface energies of elemental crystals," *Sci. data*, vol. 3, pp. 1–13, 2016.

[TsSS04] C. H. Tsau, S. M. Spearing, and M. A. Schmidt, "Characterization of wafer-level thermocompression bonds," *J. Microelectromechanical Syst.*, vol. 13, pp. 963–971, 2004.

[TsWu13] H. K. Tseng and M. L. Wu, “Electro-thermal-mechanical modeling of wire bonding failures in IGBT,” *Proc. Tech. Pap. - Int. Microsystems, Packag. Assem. Circuits Technol. Conf. IMPACT*, pp. 152–157, 2013.

[TISM02] N. Tsuji, Y. Ito, Y. Saito, and Y. Minamino, “Strength and ductility of ultrafine grained aluminum and iron produced by ARB and annealing,” *Scr. Mater.*, vol. 47, pp. 893–899, 2002.

[Tumm01] R. R. Tummala, *Fundamentals of microsystems packaging*. McGraw-Hill Education, 2001.

[TDCC07] A. Turon, C. G. Dávila, P. P. Camanho, and J. Costa, “An engineering solution for mesh size effects in the simulation of delamination using cohesive zone models,” *Eng. Fract. Mech.*, vol. 74, no. 10, pp. 1665–1682, 2007.

[VeCe04] A. Van der Ven and G. Ceder, “The thermodynamics of decohesion,” *Acta Mater.*, vol. 52, pp. 1223–1235, 2004.

[VRSK98] L. Vitos, A. V. Ruban, H. L. Skriver, and J. Kollár, “The surface energy of metals,” *Surf. Sci.*, vol. 411, pp. 186–202, 1998.

[WaMD16] V. V. C. Wan, D. W. MacLachlan, and F. P. E. Dunne, “Integrated experiment and modelling of microstructurally-sensitive crack growth,” *Int. J. Fatigue*, vol. 91, pp. 110–123, 2016.

[WHWL20] C. Wang, Y. He, C. Wang, L. Li, and X. Wu, “Multi-chip IGBT module failure monitoring based on module transconductance with temperature calibration,” *Electron.*, vol. 9, pp. 1–17, 2020.

[WaLB13] H. Wang, M. Liserre, and F. Blaabjerg, “Toward reliable power electronics: Challenges, design tools, and opportunities,” *IEEE Industrial Electronics Magazine*, vol. 7, IEEE, pp. 17–26, 2013.

[WCFC19] Z. Wang, D. Chen, Q. Fang, H. Chen, T. Fan, B. Liu, F. Liu, and P. Tang, “Effects of finite temperature on the surface energy in Al alloys from first-principles calculations,” *Appl. Surf. Sci.*, vol. 479, pp. 499–505, 2019.

[Wata11] T. Watanabe, “Grain boundary engineering: Historical perspective and future prospects,” *J. Mater. Sci.*, vol. 46, pp. 4095–4115, 2011.

[WWHT19] X. Wen, M. Wan, C. Huang, Y. Tan, M. Lei, Y. Liang, and X. Cai, “Effect of microstructure on tensile properties, impact toughness and fracture toughness of TC21 alloy,” *Mater. Des.*, vol. 180, p. 107898, 2019.

[WiZD18] D. Wilson, Z. Zheng, and F. P. E. Dunne, “A microstructure-sensitive driving force for crack growth,” *J. Mech. Phys. Solids*, vol. 121, pp. 147–174, 2018.

[WyGr86] J. W. Wyrzykowski and M. W. Grabski, “The Hall–Petch relation in aluminium and its dependence on the grain boundary structure,” *Philos. Mag. A Phys. Condens. Matter, Struct. Defects Mech. Prop.*, vol. 53, pp. 505–520, 1986.

[XuNe93] X. P. Xu and A. Needleman, “Void nucleation by inclusion debonding in a crystal matrix Void,” *Model. Simul. Mater. Sci. Eng.*, vol. 1, pp. 111–132, 1993.

[YaRi14] M. S. Yaghmaee and R. Riahifar, “In the search of fundamental inner bond strength of solid elements,” *Sci. World J.*, vol. 2014, p. 13, 2014.

[YTYN07] Y. Yamada, Y. Takaku, Y. Yagi, I. Nakagawa, T. Atsumi, M. Shirai, I. Ohnuma, and K. Ishida, “Reliability of wire-bonding and solder joint for high temperature operation of power semiconductor device,” *Microelectron. Reliab.*, vol. 47, pp. 2147–2151, 2007.

[YaPa19] G. Yang and S. J. Park, “Deformation of single crystals, polycrystalline materials, and thin films: A review,” *Materials (Basel).*, vol. 12, p. 2003, 2019.

[YaAJ14] L. Yang, P. A. Agyakwa, and C. M. Johnson, “Calibration of a novel microstructural damage model for wire bonds,” *IEEE Trans. Device Mater. Reliab.*, vol. 14, no. 4, pp. 989–994, 2014.

[YaAJ13] L. Yang, P. A. Agyakwa, and C. M. Johnson, “Physics-of-failure lifetime prediction models for wire bond interconnects in power electronic modules,” *IEEE Trans. Device Mater. Reliab.*, vol. 13, pp. 9–17, 2013.

[YXHL19] L. Yuan, Z. Xia, X. Hu, J. Liu, and Z. Huo, “Failure analysis and process improvement of copper diffusion,” *Microelectron. Reliab.*, vol. 99, pp. 291–294, 2019.

[YAQZ18] X. Yuan, T. An, F. Qin, J. Zhao, and C. Fang, “Mechanisms of power module metallization degradation under ageing,” *19th Int. Conf. Electron. Packag. Technol. ICEPT*, pp. 1322–1325, 2018.

[ZDKW08] A. Zéanh, O. Dalverny, M. Karama, E. Woirgard, S. Azzopardi, A. Bouzourene, J. Casutt, and M. Mermet-Guyennet, “Thermomechanical modelling and reliability study of an IGBT module for an aeronautical application,” *Therm. Mech. Multi-Physics Simul. Exp. Microelectron. Micro-Systems*, p. 7, 2008.

[ZhMX04] J. M. Zhang, F. Ma, and K. W. Xu, “Calculation of the surface energy of FCC metals with modified embedded-atom method,” *Appl. Surf. Sci.*, vol. 229, pp. 34–42, 2004.

[ZAFB19] J. Zhao, T. An, C. Fang, X. Bie, F. Qin, P. Chen, and Y. Dai, “A study on the effect of microstructure evolution of the aluminum metallization layer on its electrical performance during power cycling,” *IEEE Trans. Power Electron.*, vol. 34, pp. 11036–11045, 2019.

[ZLTC19] H. Zheng, X. G. Li, R. Tran, C. Chen, M. Horton, D. Winston, K. A. Persson, and S. P. Ong, “Grain boundary properties of elemental metals,” *arXiv*, vol. 186, pp. 40–49, 2019.

[ZZYH16] P. Zhou, J. Zhou, Z. Ye, X. Hong, H. Huang, and W. Xu, “Effect of grain size and misorientation angle on fatigue crack growth of nanocrystalline materials,” *Mater. Sci. Eng. A*, vol. 663, pp. 1–7, 2016.

[ZhTN92] Y. Zhou, L. S. Tóth, and K. W. Neale, “On the stability of the ideal orientations of rolling textures for F.C.C. polycrystals,” *Acta Metall. Mater.*, vol. 40, pp. 3179–3193, 1992.

[Zöll16] D. Zöllner, “Grain Growth,” *Ref. Modul. Mater. Sci. Mater. Eng.*, pp. 1–29, 2016.

PUBLICATIONS

- M. Shqair, Z. Khatir, A. Ibrahim, M. Berkani, A. Halouani, and T. Hamieh, “A combined physicochemical-microstructural approach to predict the crack path at the topside interconnections in IGBT power devices.” Microelectronics Reliability 132 (2022): 114516.

- M. Shqair, Z. Khatir, A. Ibrahim, A. Halouani and M. Berkani, “Microstructural evolution during the crack propagation at the bond-wire contact area of IGBT power modules upon power cycling.” Microelectronics Reliability 138 (2022): 114635.

- M. Shqair, Z. Khatir, A. Ibrahim, M. Berkani, A. Halouani, and T. Hamieh, “Physicochemical-microstructural approach for modeling the crack passage at topside metallic parts in IGBT semiconductor power electronics.” In 2022 23rd International Conference on Thermal, Mechanical and Multi-Physics Simulation and Experiments in Microelectronics and Microsystems (EuroSimE), IEEE (2022): 1-6.

- A. Halouani, M. Shqair, Z. Khatir, A. Ibrahim, M. Ouhab, “Finite elements analyses of early-stage crack propagation in aluminium wire bonds due to power cycling.” Microelectronics Reliability 138 (2022): 114610.

- A. Halouani, Z. Khatir; M. Shqair; A. Ibrahim; P. Pichon, “An EBSD Study of Fatigue Crack Propagation in Bonded Aluminum Wires Cycled from 55°C to 85°C.” J. Electron. Mater. 51 (2022): 7353-7365.